UC Berkeley
UC Berkeley Electronic Theses and Dissertations

Title
From Coordination Complexes to Conductive Polymers: The Synthesis and Characterization of Anionic Molecules and Materials

Permalink
https://escholarship.org/uc/item/6mk6k0d3

Author
Axelson, Jordan Cole

Publication Date
2016

Peer reviewed|Thesis/dissertation

eScholarship.org Powered by the California Digital Library
University of California

From Coordination Complexes to Conductive Polymers: The Synthesis and Characterization of Anionic Molecules and Materials

By

Jordan Cole Axelson

A dissertation submitted in partial satisfaction of the

requirements for the degree of

Doctor of Philosophy

in

Chemistry

in the

Graduate Division

of the

University of California, Berkeley

Committee in charge:

Professor Jeffrey R. Long
Professor Kenneth N. Raymond
Professor Krishna K. Niyogi

Summer 2016

From Coordination Complexes to Conductive Polymers:
The Synthesis and Characterization of Anionic Molecules and Materials

© 2016

Jordan Cole Axelson

Abstract

From Coordination Complexes to Conductive Polymers:

The Synthesis and Characterization of Anionic Molecules and Materials

by

Jordan Cole Axelson

Doctor of Philosophy in Chemistry

University of California, Berkeley

Professor Jeffrey R. Long, Chair

The field of synthetic chemistry provides an unparalleled opportunity to study the relationship between molecular structure and the physical and chemical properties of a system. Toward this end, this dissertation describes efforts to develop new systems containing negatively charged components with an eye toward applying them to energy storage applications. *Chapter One* begins by explaining the importance of energy storage in harnessing renewable energy sources and how photosynthesis can serve as inspiration for converting solar energy into useful chemical fuels. It also outlines the motivation and core concepts for projects described in later chapters.

Chapter Two is presented in two parts. The first describes the synthesis of a series of ruthenium complexes bearing the pentadentate ligand 2,6-bis[1,1-bis(2-pyridyl)ethyl]pyridine ($PY5Me_2$) and the subsequent electrochemical evaluation of $[(PY5Me_2)Ru(H_2O)]^{2+}$ as a water oxidation catalyst. The second investigates $[(PY5Me_2)Co(H_2O)]^{2+}$ for the same application. While both systems provided initial electrochemical evidence for water oxidation, it was ultimately found that the ruthenium complex served only as a stoichiometric oxidant for water oxidation while the cobalt complex appeared to decompose to a catalytically active side product.

Based on lessons learned in *Chapter Two*, a fresh initiative was undertaken to synthesize new ligand scaffolds that might better support the high-valent metal species necessary to perform water oxidation. Consequently, pentadentate ligands possessing anionic donors were pursued. *Chapter Three* presents the synthesis and characterization of alkali metal salts of the tetraanionic ligand 2,2′-(pyridine-2,6-diyl)bis(2-methylmalonate) ($[PY(CO_2)_4]^{4-}$) via deprotection of the neutral tetrapodal ligand tetraethyl 2,2′-(pyridine-2,6-diyl)bis(2-methylmalonate) ($PY(CO_2Et)_4$). The $[PY(CO_2)_4]^{4-}$ ligand, which features an axial pyridine and four equatorial carboxylate groups, cleanly reacts with a number of divalent first-row transition metals to form the series of complexes $K_2[(PY(CO_2)_4)M(H_2O)]$ ($M = Mn^{2+}$, Fe^{2+}, Co^{2+}, Ni^{2+}, Zn^{2+}). The metal complexes were comprehensively characterized via single-crystal X-ray diffraction, ^1H NMR and UV-Vis absorption spectroscopy, and cyclic voltammetry. Additionally, *Chapter Three* recounts a barrage of synthetic routes that have been attempted in order to generate a new N_4C^- ligand possessing four equatorial pyridine donors and an axial, anionic carbon donor. While this ligand has not yet been successfully isolated in sufficient amounts, the most promising options moving forward are highlighted.

Although the final chapter continues to focus on the synthesis of negatively charged systems, the desired application switches to that of single-ion conducting electrolytes for Li-ion batteries. Hence, *Chapter Four* reports the synthesis of a series of poly(ethylene glycol) (PEG) based network polymers incorporating fluorinated tetraphenylborate nodes into the polymer backbone. The modular nature of the building units for this polymer allowed for a systematic study of the effect of linker length and composition on the conductivity of Li-ions through the material. Whereas long linkers produced flexible materials that were conductive at elevated temperatures, materials made with short linkers were brittle and exhibited no conductivity. However, when loaded with 68 wt% propylene carbonate, materials containing short linkers outperformed those with long linkers, exhibiting conductivity as high as 2.5×10^{-4} S/cm for the polymer made with ethylene glycol. It was also found that the conductivity could be further increased by exchanging the PEG linker for 1,5-pentanediol, which produced conductivity values of 3.5×10^{-4} S/cm.

Table of Contents

Acknowledgements ii
Dedication vi

Chapter One: Coordination Complexes and Conductive Polymers for Energy Storage Applications 1
Section 1.1. The Importance of Energy Storage in Ensuring a Sustainable Energy Future 2
Section 1.2. Water Oxidation: The Bottleneck in Artificial Photosynthesis 2
Section 1.3 Molecular Water Oxidation Catalysts 4
Section 1.4 Energy Storage in Lithium-ion Batteries 7
Section 1.5 References 9
Section 1.6 Supporting Information 12

Chapter Two: Evaluation of $PY5Me_2$ as a Ligand Scaffold for Single-Site Water Oxidation Catalysts 17
Section 2.1 Introduction 18
Section 2.2 Experimental Section 20
Section 2.3 Results and Discussion of Ruthenium $PY5Me_2$ Complexes 24
Section 2.4 Results and Discussion of $PY5Me_2$ Complexes Containing Co^{2+} and Fe^{2+} 29
Section 2.5 Conclusions and Outlook 33
Section 2.6 Acknowledgements 34
Section 2.7 References 34
Section 2.8 Supporting Information 37

Chapter Three: Synthesis and Characterization of a Tetrapodal NO_4^{4-} Ligand and Its Transition Metal Complexes and Synthetic Efforts toward a N_4C^- Tetrapodal Ligand 41
Section 3.1 Introduction 42
Section 3.2 Experimental Section 43
Section 3.3. Results and Discussion of $[PY(CO_2)_4]^{4-}$ and Its Complexes 48
Section 3.4. Results and Discussion of $PY4PhXR_2$ 53
Section 3.5. Conclusions and Outlook 57
Section 3.6 Acknowledgements 58
Section 3.7 References 58
Section 3.8 Supporting Information 62

Chapter Four: Single-Ion Conducting Polymer Networks with Borate Anions and Flexible Linkers 93
Section 4.1 Introduction 94
Section 4.2 Experimental Section 95
Section 4.3 Results and Discussion 100
Section 4.4 Conclusions and Outlook 106
Section 4.5 Acknowledgements 107
Section 4.6 References 107
Section 4.7 Supporting Information 109

Hic sunt dracones.



Map of Islandia by Abraham Ortelius ca. 1590 via Wikimedia Commons. Public Domain.

"Here be dragons." A phrase associated with the edges of medieval ocean maps and unexplored lands filled with monsters and the promise of adventure. While the quest for a PhD may not seem as epic as a story involving one of these fanciful maps at first, the two actually share many of the same plot points. In both cases, the main character sets out on a journey into unknown territory, and though she may have a general knowledge of the path toward the final destination, she has no idea what trials and challenges the road will throw before her. As with any enjoyable tale, the protagonist fortuitously meets a host of characters and companions along the way that help her to tame the wild beasts and maybe even teach her a little magic—especially if chemistry is involved! As a result of the journey and the people who share it, she learns and grows, returning home as someone a little different than when she started.

As I come to the end of my six-year voyage across the seas of graduate school, I want to thank those who have walked with me. Without your encouragement, advice, and companionship I would not have managed to come so far.

First I would like to thank my family. My parents, Jon and Lupe Axelson, have always encouraged my love of learning and instilled in me an appreciation for working hard that has served me well in this endeavor. My sister Taylor is basically just awesome and is a constant inspiring example of someone who is willing to chase after a dream until she grabs ahold of its

tail. Thank you for continuing to believe in me even on the dark days when I doubted myself. I also want to acknowledge my grandparents, Josephine and Abel Perez and Billie and Ken Axelson, who far before I was even born laid the groundwork that allowed me to take the path to a PhD.

I would like to thank my advisor Prof. Jeff Long for giving me the opportunity to explore a variety of different projects during my time at Berkeley and for supporting me in my career direction. A number of other Berkeley faculty have served as mentors as well, namely Prof. Dor Abrahamson, Prof. Robert Bergman, Prof. Marcin Majda, Prof. Peter Marsden, and Prof. Peter Vollhardt. These men have offered me their encouragement, their expertise, and their passion for education, and I can only aspire to be an awesome enough teacher that my students utilize my lessons in chemistry memes (cough, cough… Pete Marsden).

Yet, without the guidance and support of mentors at the University of Illinois at Urbana-Champaign, I would never have ventured west to California. The Chemistry Merit Program was my lifeline during my first two undergraduate years and supplied me with two *amazing* teaching assistants, Dr. Timothy Mui and Dr. Clint Holaday. In addition to calming my somewhat neurotic, overachieving freshman self, Tim once asked me a very important question: why do you work so hard? After informing me that my initial answer, "Because I'm afraid of failing," was not an acceptable response, I had to ponder a bit more. In the end, I told him I work so hard because I know that if I do, I will succeed. Thanks for that lesson in positivity, Tim. Clint pretty much taught me everything I know about introductory organic chemistry, and his example formed the basis of the instructor that I have become. Considering that organic chemistry has such a negative connotation, it should say something about Clint that it was by far my favorite chemistry class and that I still have a strong affinity for the subject today.

The Long Group as a whole has served as my surrogate family over the past six years. I did not have brothers growing up, but I found two in Berkeley, Dr. Jarad Mason and David Zee. Regardless of whether things were research related or not, they have always been there to offer a hug, shoulder, or high-five. David could well be my catalysis twin, as we have braved this subgroup together. I am inspired by his unrelenting work ethic and synthetic savvy and am forever grateful that he introduced me to dim sum, wontons, and Americone Dream. Because Americone Dream makes everything better. I am also thankful for the experience and advice of Dr. Elizabeth Montalvo, Prof. Michael Nippe, and Curtis Wray, who helped me make the transition into graduate school and guided me in the process of becoming an independent researcher. The younger set of Catalysis Subgroup twins, Dianne Xiao and Miguel Gonzalez, has been a delightful addition. I admire Dianne's spunky personality and dedication to her research, and I am excited to see where those two strengths take her. I am fairly convinced that Miguel stole one of those creepy, computer-protecting, magical dinosaur eggs that used to be down in CheXray because I have no other way to explain his X-ray wizardry skills. Without him and the hope he gave me with the first serendipitous crystal structure of a $[PY(CO_2)_4]^{4-}$ complex, *Chapter Three* quite possibly may never have happened.

I am grateful to Conductivity Subgroup as well. They were willing to adopt me late in my graduate school career and train me in the ways of the BeatBox. Dr. Brian Wiers, Michael Aubrey, and Rodi Torres-Govosto have played particularly important roles in getting me up to speed on all things involving impedance spectroscopy and pellet pressing. Prof. Jeff Van Humbeck is credited with inviting me into the Conductivity Subgroup to begin with by passing me the idea for the polymer project described in *Chapter Four*. Additionally, JVH was a fantastic resource for synthetic direction when I ran into dead ends with ligand development.

Outside of the lab, I admire him for his dedication to his family and hope to imitate his work-life balance in the future.

A special shoutout goes to Dr. Katie Meihaus and Dr. Kurt Van Allsburg, who have essentially been my other halves (thirds?) over the course of graduate school. Katie and Kurt have forced me to grow, not just as a researcher, but more importantly as a human being. When I mentioned learning magic earlier, these two are the ones who have diligently pulled it spark by sputtering spark out of me.

Despite involving myself in as much undergraduate mentoring as possible, I had come to believe that the universe would never grant me an undergraduate researcher. In actuality, it had just been waiting to grant me the ideal undergraduate researcher: Brittany "Nova" Gomez. In our brief time together, Brittany proved herself to be assertive, hard working, and a great friend—few people will fashion you a bedazzled sword in honor of graduation. Her upbeat attitude definitely brightened my sixth year.

The rest of the Long Group Ladies are also acknowledged: Dr. Zoey Herm, Dr. Dana Levine, Lucy Darago, Mercedes Taylor, Julia "Jolo" Oktawiec, Rebecca Siegelman, Kristen Colwell, and Rebecca Khoo. Whether it's discussing women in STEM or just a desperate need to get my dance on, I know you gals are there for me.

A number of individuals outside of the Berkeley Chemistry Department have been sources of support for me too. Dr. Megan Cismesia, (soon-to-be Dr.) Thomas Malkowski, Jenna Cameli, David Cramer, Adrienne Moore and Lucas Weiss have all stuck with me since my University of Illinois days. I have greatly appreciated their periodic check-ins and the ability to share both the frustrations and victories of post-undergrad life. Thomas in particular has been my west coast comrade, and even though we are on opposites sides of the state it has been a comfort to pass through graduate school together. Maxwell Dilks has been a near constant companion and source of encouragement over the past three years. His knack for finding ridiculously silly and adorable cat gifs is unmatched and extremely heartening on days when science refuses to cooperate. My First Pres crew (Caroline Davis, Kristin Codiga, Tisha Waki, Mika Pritchard-Berman, Brian Howard, Jason Gorski, Kristin Henderson, Emily Hopcian and so many others) has supplemented my social life and given me the opportunity to enjoy swimming in the frigid Pacific Ocean, snowboarding in the mountains in Tahoe, and running away from zombies in the Central Valley. My friends from CWOW Rena Crocker, Dana Lundblad, and Kim Winkleman are wonderfully strong women, and I am so happy to have found a group who loves 6 am Wednesdays mornings as much as I do. Samuel Tourek and Carol Masters-Salnave have lent me their ears and experience at times when I needed a fresh perspective, and Chase Martin has literally brought magic into my life. (No really, he's actually a magician.) On days when approaching the bench seemed like the least exciting option available, Lucas Smith and David Gygi have inspired me with their bottomless enthusiasm for the scientific endeavor and optimistic outlook on life in general. Their work ethic and dedication to their research never fail to remind me that science can be a wondrous and beautiful thing. A thanks also goes to Con Bro Chill, a musical staple of my graduate school career. Whenever I needed some good vibes and upbeat tunes to lift my spirits, Connor, Sam, Ty, and Steve delivered with their ridiculous antics, shiny outfits, and overwhelming energy. Neon Army knows how to party.

Finally, I would like to recognize all of the students I have had the privilege to work with both at UC Berkeley and the University of Illinois. It is through my interactions with them that I feel I have truly begun to develop a deeper understanding of chemistry.

As an avid collector of quotes, I will finish by sharing some lines that have strongly resonated with me as a graduate student. May those who come after find insight in them as well.

"Make New Mistakes. Make glorious, amazing mistakes. Make mistakes nobody's ever made before."

Neil Gaiman

"The most essential factor is persistence—the determination never to allow your energy or enthusiasm to be dampened by the discouragement that must inevitably come."

James Whitcomb Riley

"Desire is the key to motivation, but it's determination and commitment to an unrelenting pursuit of your goal—a commitment to excellence—that will enable you to attain the success you seek."

Mario Andretti

"If you want to build a ship, don't drum up the men to gather wood, divide the work and give orders. Instead, teach them to yearn for the vast and endless sea."

Antoine de Saint

"We can know only that we know nothing. And that is the highest degree of human wisdom."

Leo Tolstoy

"The difference between what we do and what we are capable of doing would suffice to solve most of the world's problems."

Mahatma Gandhi

"It always seems impossible until it's done."

Nelson Mandela

"Go then, there are other worlds than these."

Jake Chambers, *The Gunslinger*

Dedicated to

Dad, Mom, Tay
&
to the families I have
found along the way.

Chapter One

Coordination Complexes and Conductive Polymers for Energy Storage Applications

"On the arid lands there will spring up industrial colonies without smoke and without smokestacks; forests of glass tubes will extend over the plains and glass buildings will rise everywhere; inside of these will take place the photochemical processes that hitherto have been the guarded secret of the plants, but that will have been mastered by human industry which will know how to make them bear even more abundant fruit than nature, for nature is not in a hurry and mankind is. And if in a distant future the supply of coal becomes completely exhausted, civilization will not be checked by that, for life and civilization will continue as long as the sun shines!"

- Giacomo Ciamician

Section 1.1 The Importance of Energy Storage in Ensuring a Sustainable Energy Future

Two of the most pressing challenges facing humanity today include curbing anthropogenic climate change and reducing our dependence on the finite supply of fossil fuels.[1–4] Because CO_2 emissions from the combustion of fossil fuels for energy generation have been correlated to the global rise in Earth's surface temperature over the past 50 years, these issues have become inextricably linked.[5–7] Motivation for finding solutions to these challenges is further enhanced due to projections that world energy consumption will grow by 48% between 2012 and 2040, with the corresponding CO_2 emissions increasing 34% from 32.3 billion metric tons in 2012 to 43.2 billion metric tons in 2040.[8]

Consequently, initiatives have been put forth to encourage the growth of technologies capable of harnessing alternative energy sources such as wind, hydroelectric, and solar. Solar is a particularly appealing option since the current world consumption of 15 terawatts easily could be satisfied by the more than 100,000 terawatts of sunlight that strike the Earth.[9] While the field of photovoltaics continues to make gains in converting sunlight to electricity, reaching efficiencies of 46% for multi-junction cells,[10,11] the fact stands that the amount of sunlight reaching a photovoltaic device can greatly depend on time of day, local weather conditions, and physical location of the cell. Furthermore, one must consider the change in consumer demand for energy over the course of a day or a year as well as applications that demand mobility like the transportation industry, which are particularly dependent on the high energy density provided by fossil fuels. In order to mediate light availability and energy demand, the issue of energy storage becomes an important factor in establishing a secure energy future.

Section 1.2. Water Oxidation: The Bottleneck in Artificial Photosynthesis

Nature captures solar energy in the form of chemical fuels via photosynthesis. Indeed, fossil fuels represent the last vestiges of sunlight that was captured by this process millions of years ago! In plants, the tandem protein assemblies Photosystem I and Photosystem II utilize photons to convert water and CO_2 into carbohydrates and O_2. During this process, a photoexcited chromophore oxidizes an oxo-bridged Mn_4Ca cluster in Photosystem II, which in turn serves as the catalyst for the oxidation of water to O_2. The electrons liberated by this reaction are passed

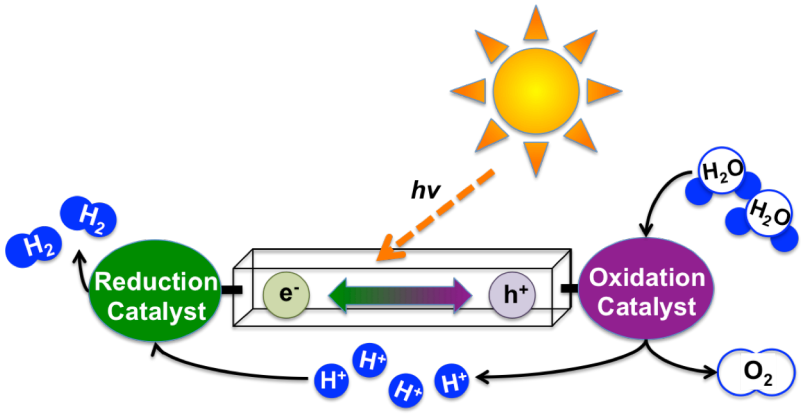


Figure 1.1. Schematic for an artificial photosynthetic device. Sunlight generates an electron-hole pair. Utilizing the holes, the oxidation catalyst converts water to O_2 while the reduction catalyst produces H_2 from protons and electrons.

along an electron transport chain to Photosystem I, where they are used to reduce nicotinamide adenine dinucleotide phosphate ($NADP^+$) to NADPH. NADPH in turn goes on to be used as a reductant in a variety of biological processes including carbon fixing reactions of the Calvin-Benson cycle that produce carbohydrates.[12–14]

Inspired by this process, scientists have worked to develop artificial photosynthetic systems that convert sunlight directly into chemical fuels as shown in Figure 1.1.[15–20] In these devices, a photosensitizer or semiconductor employs photons to generate a charge separation with holes moving toward an oxidation catalyst that converts water to O_2 and electrons moving toward a reduction catalyst used to generate H_2 or a carbon based fuel. Part of the appeal of this modular design comes from the ability to study and optimize the individual components before combining them into a single device.

Although the schematic in Figure 1.1 seems straightforward, in actuality, the realization of such a system is quite challenging. Designing an effective water oxidation catalyst is particularly difficult: in fact, this component is viewed as the bottleneck in building artificial photosynthetic systems.[1,4,21] Whereas most redox properties involve only one or two electron transfers, water oxidation involves an intricate dance of four electrons and four protons as well as O–O bond formation. As shown by Equation 1.1, the oxidation of water is thermodynamically demanding, requiring a minimum potential of 1.23 V versus SHE, or ΔG of ~237 kJ mol^{-1}.

Equation 1.1. $O_2 + 2H_2 \rightarrow 2H_2O \qquad E^0 = 1.23$ V vs. SHE at pH 0

In addition to the thermodynamic price that must be paid for this reaction, a kinetic penalty due to the high activation barrier for the oxidation increases the necessary potential even more and is referred to as *overpotential*. Finally, a water oxidation catalyst must be oxidatively, chemically, and hydrolytically robust in order to withstand the high potentials, reactive intermediates, and aqueous environments to which it is exposed.

A tool that can be used to facilitate water oxidation is proton-coupled electron transfer (PCET). PCET is a concerted process during which an electron and proton are transferred together during a single redox event, thereby permitting an accumulation of redox equivalents in a catalyst while avoiding highly charged, high-energy intermediates.[22–24] Seeing as PCET would be particularly advantageous when applied to chemical transformations involving multiple electron and proton transfers, it is unsurprising that it is ubiquitous in biological processes, especially in photosynthesis which entails 24 electrons and 24 protons in its entirety.[24] In accordance with the Nernst equation, the redox potentials of systems in which PCET occurs possess a pH dependence as shown by Equation 1.2, in which $E_{1/2}$ is the observed redox potential, E^0 is the standard potential of the reaction, and n_{H^+} and n_{e^-} are the number of protons and electrons transferred, respectively.[25]

Equation 1.2. $$E_{1/2} = E^0 - \left(0.059\text{ V} \times \frac{n_{H^+}}{n_{e^-}}\right)\text{pH}$$

Thus for each unit increase in pH, the potential for the redox reaction decreases by 0.059 V. In order to determine in what pH range PCET operates, electrochemical techniques can be used to generate a Pourbaix diagram, which displays the dependence of the potential on the pH. In the example diagram shown in Figure 1.2, the sloped region indicates that PCET occurs from pH 3-11 and, consequently, that the pK_a values of M^{3+}–OH_2 and M^{2+}–OH_2 are 3 and 11, respectively.

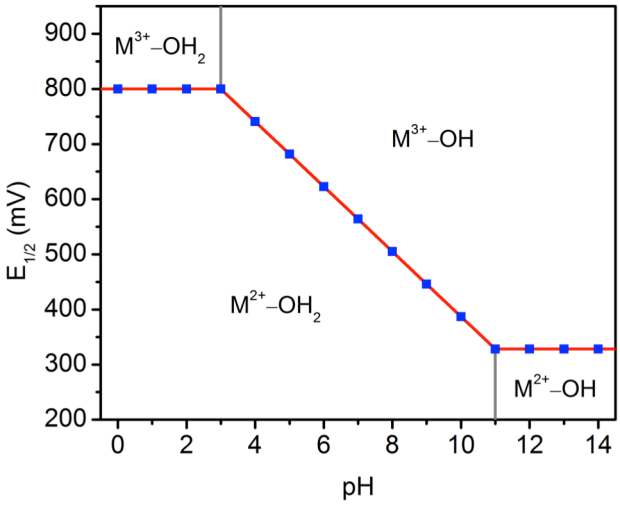


Figure 1.2. Example Pourbaix diagram that shows speciation based on potential and pH.

Section 1.3 Molecular Water Oxidation Catalysts

There are two classes of catalysts: homogeneous and heterogeneous. Because heterogeneous catalysts are insoluble in the reaction medium, they are often favored in industrial applications due to the ease with which they can be separated from products or unreacted starting materials. Heterogeneous catalysts studied for water oxidation in particular are composed of metal oxides or hydroxides, materials that show good stability under the highly oxidizing conditions this application demands.[26,27] Although the organic ligands used in homogeneous catalysts are more prone to oxidative decomposition, they do have an advantage over heterogeneous catalysts in that they provide well-defined coordination environments for the metal ions, allowing for more straightforward analysis of the structure of the catalytic species, identification of important intermediates, and elucidation of the reaction kinetics and mechanism using standard characterization techniques such as NMR, X-ray, and UV-visible absorption spectroscopies. The organic ligands themselves also afford a useful handle for optimizing the reactivity of the catalyst through systematic synthetic tailoring of the ligand scaffold through electronic or steric alterations and for controlling the secondary coordination sphere. Furthermore, while only the outer surface of a heterogeneous catalyst is available to take part in a reaction, in principle each metal center or metal cluster of a homogeneous species can participate.[4,26,28,29]

Though electrolysis of water at metal electrodes to form O_2 and H_2 has been known since the 1700s[29,30] and nature has utilized the oxo-bridged Mn_4Ca cluster in Photosystem II for 2 billion years,[31] interest in homogeneous water oxidation catalysts has surged only in recent decades. Indeed, it was not until 1982 that Meyer et al. published their work on the first molecular water oxidation catalyst, the ruthenium blue dimer (Figure 1.3a).[32] For a time after, in part due to the fact that nature employs a metal cluster at the active site of Photosystem II, the belief persisted that only multinuclear systems could build up sufficient redox equivalents to perform the four electron oxidation of water to O_2.[4,21] However this paradigm was overturned in 2005, when Zong and Thummel published the first evidence of water oxidation by a series of mononuclear ruthenium species[33]. As a result of this work a cascade of new mononuclear ruthenium and iridium water oxidation catalysts have been designed.[4] Yet, the vast majority of

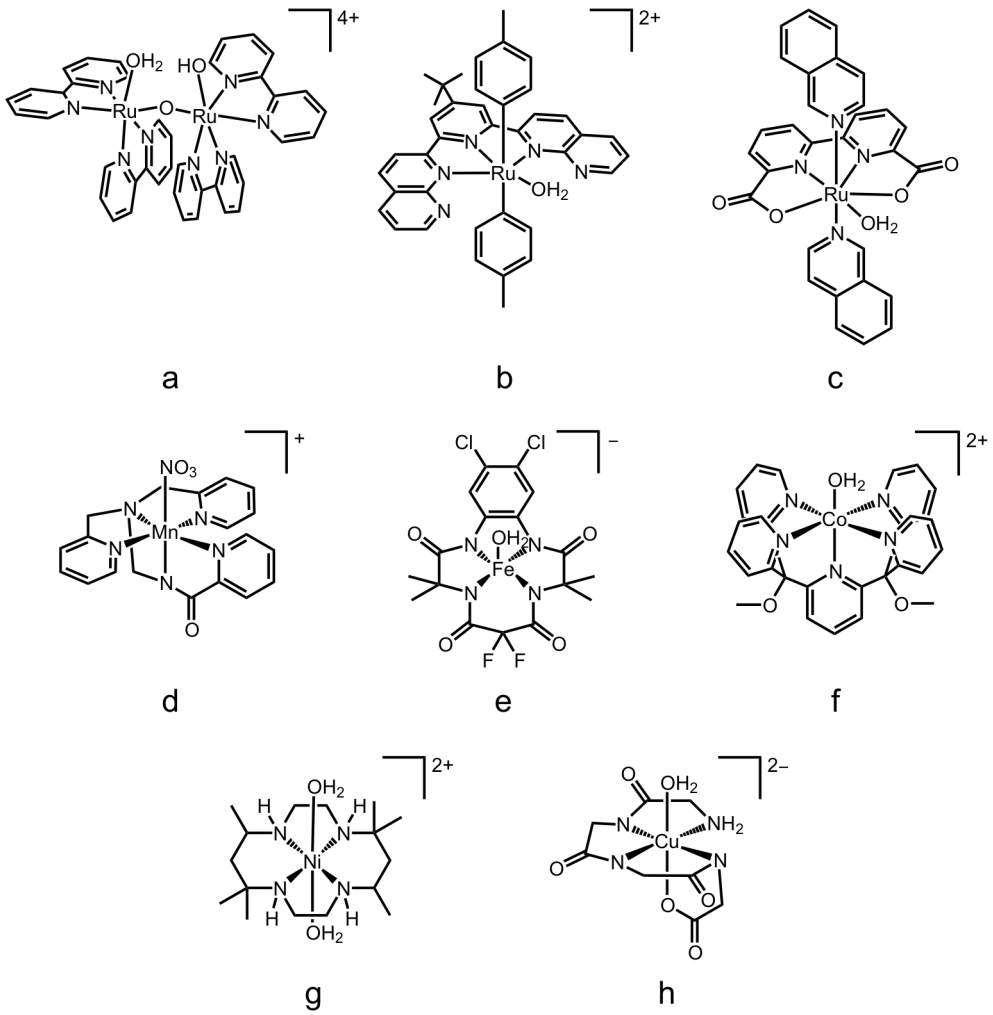


Figure 1.3. Notable molecular water oxidation catalysts. (a) *Cis*,*cis*-[{Ru(bpy)$_2$(H$_2$O)$_2$}$_2$O]$^{4+}$, the ruthenium blue dimer. The first molecular water oxidation catalyst.[32] (b) *Trans*-[Ru(4-*tert*-butyl-2,6-di([1',8']-naphthyrid-2'yl)pyridine)(4-Me-py)$_2$(H$_2$O)]$^{2+}$, one of the first mononuclear water oxidation catalyst published by Zong and Thummel.[33] (c) [Ru(2,2'-bipyridine-6,6'-dicarboxylate)(isoquinoline)$_2$], the first water oxidation catalyst with a turnover frequency matching that of Photosystem II.[34] (d) [Mn(*N*,*N*-bis(2-pyridylmethyl)-amine-*N*-ethyl-2-pyridine-2-carboxamide)(NO$_3$)]$^+$, the first mononuclear manganese water oxidation catalyst.[35] (e) One of a series of Fe^{3+} tetraamido macrocyclic (TAML) complexes published by Ellis et al., the first iron-based water oxidation catalysts.[36] (f) [Co(2,6-(bis(bis-2-pyridyl)methoxymethane)pyridine)(H$_2$O)]$^{2+}$, the first well-defined molecular water oxidation catalyst containing cobalt.[37] (g) [Ni(5,5,7,12,12,14-hexamethyl-1,4,8,11-tetraazacyclotetradecane)(H$_2$O)$_2$]$^{2+}$, the first homogeneous nickel-based water oxidation catalyst.[38] (h) A Cu^{2+} complex formed with a triglycylglycine macrocyclic ligand, the first well-defined copper complex capable of water oxidation.[39]

these precious metal catalysts are extremely slow, with turnover frequencies of less than 1 sec^{-1}.[4] It was not until 2012 that Sun and co-workers published a ruthenium complex with a turnover frequency rivaling that of Photosystem II (>300 sec^{-1}, Figure 1.3c).[34] More recently, mononuclear catalysts made with first row transition metals have been found,[4,29] and those distinguished as the first examples for manganese,[35] iron,[36] cobalt,[37] nickel,[38] and copper[39] are shown above.

In reviewing just the few catalysts shown in Figure 1.3, it can be noticed that a number of them possess anionic ligands. In studies that examined the effects of appending electron withdrawing and electron donating moieties to the ligand scaffold, it was found that strongly donating or anionic ligands are able to lower the potentials needed for oxidation by stabilizing the high-valent metal species formed. Not only can this shift have the beneficial effect of decreasing the overpotential of the reaction, it can also serve to lower the catalytically active redox potential to a range that can be paired successfully with photosensitizers, a feat that neutral ligand sets often fail to accomplish.[3,4,34,40]

Especially when dealing with the more labile first row transition metal complexes, polydentate ligands can be used to curtail deactivation by ligand dissociation. In this respect, a pentadentate ligand would be particularly appealing, as it would maximize the benefits of the chelate effect while retaining an open coordination site for substrate binding.[41] One particular family of ligands, tetrapodal ligands, can bind metals in an κ^5 fashion, forming a square pyramidal coordination cap.[42] Although a number of ligands from this family are known to

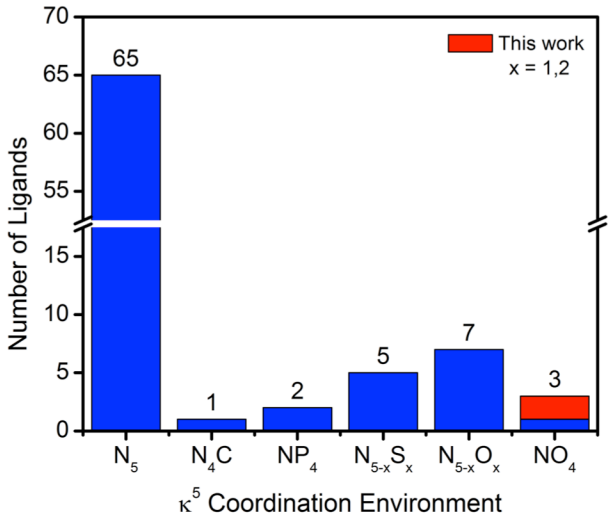


Figure 1.4. Tetrapodal ligands grouped by their κ^5 coordination environment (x = 1,2).

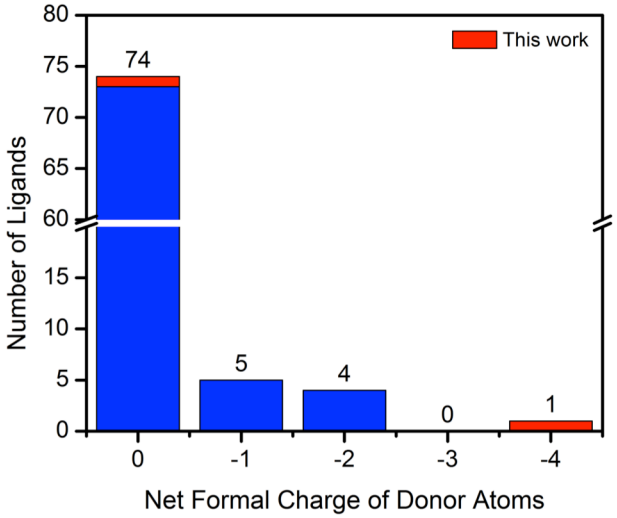


Figure 1.5. Tetrapodal ligands grouped by the net formal charge of their coordinating atoms.

support high-valent metal species,[37,43–45] they have not yet been extensively investigated for the application of water oxidation. Additionally, as shown by Figures 1.4 and 1.5, the vast majority of this ligand family consists of fully nitrogen-based coordination environments, and very few possess anionic donors.[46] Considering the benefits that such ligands could offer, the design and evaluation of new tetrapodal ligands bearing anionic, non-nitrogen donors represents an exciting but uncharted area of research, not only for water oxidation but for other applications requiring the generation of high-valent metal species.

As mentioned previously, despite the benefits associated with the study of homogeneous water oxidation catalysts, they are prone to oxidative decomposition because of their organic ligands as well as to deactivation by ligand dissociation. For this reason, care must be taken to adequately evaluate and accurately identify the true catalytic species in the reaction solution. While in some cases side products may be innocuous, in others freed ions may agglomerate into catalytically active nanoparticles or heterogeneous films on the electrode surface or the ligand may be modified in situ to generate more reactive species. Thus, it is imperative to perform control experiments to show that the molecule in question exhibits unique reactivity compared to free metal salts, that the structure of the molecule remains intact over the course of the experiment, and that no catalytically active particles or films are formed. Fortunately, most of these control experiments are rather straightforward and can be performed with standard laboratory equipment such as UV-visible-NIR, NMR spectrometers, and electrochemical techniques. For more information on this subject, the interested reader is referred to accounts from the literature.[47–51,27,52]

Keeping this information in mind, Chapter Two of this dissertation will delve into the field of water oxidation and discuss the evaluation of mononuclear ruthenium and cobalt complexes bearing the tetrapodal ligand 2,6-bis[1,1-bis(2-pyridyl)ethyl]pyridine ($PY5Me_2$) for this application. Chapter Three will go on to detail efforts toward synthesizing new tetrapodal frameworks possessing NO_4^{4-} and N_4C^- coordination environments, and while Chapter Four continues with the theme of synthesizing anionic species, it will branch into an independent project involving energy storage in batteries, which is introduced below.

Section 1.4 Energy Storage in Lithium-ion Batteries

Nearly all high-capacity batteries used in applications ranging from cell phones to electric vehicles are based on Li-ion technology due to its high gravimetric energy capacity. Currently, commercial Li-ion batteries depend on the intercalation and insertion of Li-ions into the battery electrodes, which are separated by a porous plastic film soaked in a liquid electrolyte solution. These solutions usually consist of a lithium salt dissolved in an organic carbonate solvent.

Despite being the standard for energy storage in electric vehicles and personal electronics, Li-ion technology is far from flawless. For example, the organic solvents used to dissolve the lithium salts are flammable, volatile, and corrosive.[53,54] In the event of an internal short circuit, during an electric vehicle collision or due to penetration by dendrites[53,55,56] over the course of many charge-discharge cycles, these solvents are particularly hazardous as they are a primary source of combustible fuel. As a result, extensive mechanical protection as well as thermal and electric control and management systems must be applied to the battery pack to monitor for thermal runaway. Although these safeguards are necessary, they increase the weight of the battery pack, in turn decreasing its specific energy capacity and inflating the cost of production.

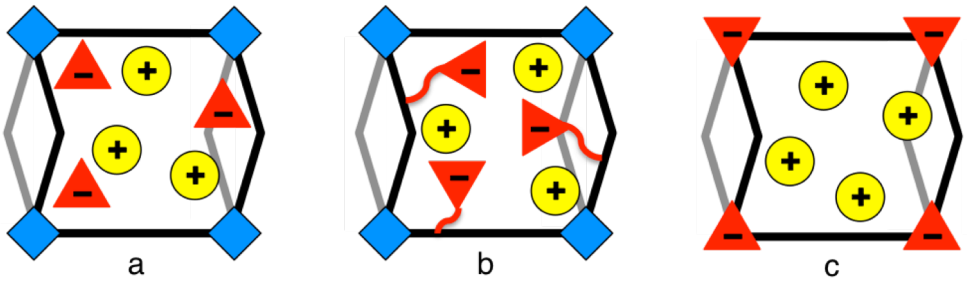


Figure 1.6. Framework designs for incorporating charged species. (a) A framework filled with a binary salt, similar to current liquid electrolyte systems. (b) A framework containing anionic moieties anchored to the linker component, and (c) a framework containing anionic nodes. The latter two frameworks represent strategies for generating single-ion conducting electrolyte systems.

Another problem that arises with liquid electrolytes is that both the Li-ion and its counter anion contribute to the observed ionic conductivity. The unrestricted movement of the anions reduces cell lifetimes and cycling performance by depleting anion concentration near the anode and generating concentration gradients within the cell, which is predicted to promote the growth of dendrites.[57,58] If metallic Li anodes are truly to be used, as has been proposed in order to increase energy capacity in second generation lithium batteries, the suppression of dendrite formation is of paramount importance.[53,55,56] Additionally, anion decomposition at the surface of the cathode interferes with the formation of the electrode-electrolyte interface, a process that ultimately defines the upper limit of a cell's voltage and thusly the energy density and power density of the battery.[54,59,60]

To address these issues, the Long Group has worked to develop new and robust molecular-organic frameworks (MOFs)[61–63] and porous aromatic frameworks (PAFs)[64] that could serve to replace liquid electrolytes. MOFs and PAFs are porous materials made by combining linker and node units to produce three-dimensional, highly interconnected solids. Due to their modular assembly, these materials are synthetically tunable, allowing for the potential to not only optimize ion transport but also to embed charged moieties in the framework itself (Figure 1.6). For example, anionic components could be tethered to the linkers or anions could be incorporated into the backbone of the framework itself. The resulting charged host lattices function as single-ion conductors when impregnated with Li^+ and are of particular interest, as they would eliminate the problems associated with mobile anions. However, the MOF and PAF electrolytes generated thus far are all brittle materials, which do not lend themselves to straightforward formation of films that could easily be integrated into commercial cells.

Due to the robust nature of the fully covalent network found in the PAF previously generated in the Long Group, the PAF was chosen as the source of inspiration for the development of a synthetically tunable, second-generation material that would exhibit more desirable mechanical properties in addition to high Li^+ conductivity. Chapter 4 will conclude this dissertation by describing the synthetic alterations that were undertaken to convert the PAF into a flexible polymer network and the electrochemical characterization that was performed to evaluate the conductive properties of the resulting product.

Section 1.5 References

(1) Cook, T. R.; Dogutan, D. K.; Reece, S. Y.; Surendranath, Y.; Teets, T. S.; Nocera, D. G. *Chem. Rev.* **2010**, *110*, 6474–6502.

(2) Dasgupta, S.; Brunschwig, B. S.; Winkler, J. R.; Gray, H. B. *Chem. Soc. Rev.* **2013**, *42*, 2213–2214.

(3) Kärkäs, M. D.; Johnston, E. V.; Verho, O.; Åkermark, B. *Acc. Chem. Res.* **2014**, *47*, 100–111.

(4) Kärkäs, M. D.; Verho, O.; Johnston, E. V.; Åkermark, B. *Chem. Rev.* **2014**, *114*, 11863–12001.

(5) Allakhverdiev, S. I.; Casal, J. J.; Nagata, T. *Photochem. Photobiol. Sci.* **2009**, *8*, 137–138.

(6) Carlowicz, M. Global Temperatures. NASA. http://earthobservatory.nasa.gov/Features/WorldOfChange/decadaltemp.php (accessed Jul 2, 2016).

(7) Climate Change Indicators in the United States. United States Environmental Protection Agency. https://www3.epa.gov/climatechange/science/indicators/weather-climate/temperature.html (accessed Jul 2, 2016).

(8) Conti, J. J. *International Energy Outlook 2016*; DOE/EIA-0484(2016); Energy Information Administration: Washington, DC, 2016.

(9) Cho, A. *Science* **2010**, *329*, 786–787.

(10) New world record for solar cell efficiency at 46%. Fraunhofer ISE. https://www.ise.fraunhofer.de/en/press-and-media/press-releases/press-releases-2014/new-world-record-for-solar-cell-efficiency-at-46-percent (accessed Jul 2, 2016).

(11) Best Research Cell Efficiencies. National Renewable Energy Laboratory. http://www.nrel.gov/ncpv/images/efficiency_chart.jpg (accessed Jul 2, 2016).

(12) Berg, J. M.; Tymoczko, J. L.; Stryer, L. *Biochemistry*, 5th ed.; W H Freeman: New York, 2002.

(13) Bassham, J. A. Photosynthesis. Encyclopædia Britannica. https://www.britannica.com/science/photosynthesis/The-process-of-photosynthesis-carbon-fixation-and-reduction (accessed Jul 2, 2016).

(14) Tachibana, Y.; Vayssieres, L.; Durrant, J. R. *Nat. Photonics* **2012**, *6*, 511–518.

(15) Barber, J.; Tran, P. D. *J. R. Soc. Interface* **2013**, *10*, 20120984.

(16) Ager, J. W.; Shaner, M. R.; Walczak, K. A.; Sharp, I. D.; Ardo, S. *Energy Environ. Sci.* **2015**, *8*, 2811–2824.

(17) Bonke, S. A.; Wiechen, M.; MacFarlane, D. R.; Spiccia, L. *Energy Environ. Sci.* **2015**, *8*, 2791–2796.

(18) Verlage, E.; Hu, S.; Liu, R.; Jones, R. J. R.; Sun, K.; Xiang, C.; Lewis, N. S.; Atwater, H. A. *Energy Environ. Sci.* **2015**, *8*, 3166–3172.

(19) Janna Olmos, J. D.; Kargul, J. *Int. J. Biochem. Cell Biol.* **2015**, *66*, 37–44.

(20) Liu, C.; Colón, B. C.; Ziesack, M.; Silver, P. A.; Nocera, D. G. *Science* **2016**, *352*, 1210–1213.

(21) Roeser, S.; Farràs, P.; Bozoglian, F.; Martínez-Belmonte, M.; Benet-Buchholz, J.; Llobet, A. *ChemSusChem* **2011**, *4*, 197–207.

(22) Huynh, M. H. V.; Meyer, T. J. *Chem. Rev.* **2007**, *107*, 5004–5064.

(23) Gagliardi, C. J.; Vannucci, A. K.; Concepcion, J. J.; Chen, Z.; Meyer, T. J. *Energy Environ. Sci.* **2012**, *5*, 7704–7717.

(24) Weinberg, D. R.; Gagliardi, C. J.; Hull, J. F.; Murphy, C. F.; Kent, C. A.; Westlake, B. C.; Paul, A.; Ess, D. H.; McCafferty, D. G.; Meyer, T. J. *Chem. Rev.* **2012**, *112*, 4016–4093.
(25) Gileadi, E. *Electrode Kinetics for Chemists, Chemical Engineers, and Materials Scientists*; VCH Publishers, Inc.: New York, 1993.
(26) Cole-Hamilton, D. J.; Tooze, R. P. In *Catalyst Separation, Recovery and Recycling*; Catalysis by Metal Complexes; Springer Netherlands, 2006.
(27) Fukuzumi, S.; Hong, D. *Eur. J. Inorg. Chem.* **2014**, *2014*, 645–659.
(28) Brimblecombe, R.; Dismukes, G. C.; Swiegers, G. F.; Spiccia, L. *Dalton Trans.* **2009**, 9374–9384.
(29) Blakemore, J. D.; Crabtree, R. H.; Brudvig, G. W. *Chem. Rev.* **2015**, *115*, 12974–13005.
(30) Dau, H.; Limberg, C.; Reier, T.; Risch, M.; Roggan, S.; Strasser, P. *ChemCatChem* **2010**, *2*, 724–761.
(31) Najafpour, M. M.; Moghaddam, A. N.; Allakhverdiev, S. I.; Govindjee. *Biochim. Biophys. Acta BBA - Bioenerg.* **2012**, *1817*, 1110–1121.
(32) Gersten, S. W.; Samuels, G. J.; Meyer, T. J. *J. Am. Chem. Soc.* **1982**, *104*, 4029–4030.
(33) Zong, R.; Thummel, R. P. *J. Am. Chem. Soc.* **2005**, *127*, 12802–12803.
(34) Duan, L.; Bozoglian, F.; Mandal, S.; Stewart, B.; Privalov, T.; Llobet, A.; Sun, L. *Nat. Chem.* **2012**, *4*, 418–423.
(35) Young, K. J.; Takase, M. K.; Brudvig, G. W. *Inorg. Chem.* **2013**, *52*, 7615–7622.
(36) Ellis, W. C.; McDaniel, N. D.; Bernhard, S.; Collins, T. J. *J. Am. Chem. Soc.* **2010**, *132*, 10990–10991.
(37) Wasylenko, D. J.; Ganesamoorthy, C.; Borau-Garcia, J.; Berlinguette, C. P. *Chem. Commun.* **2011**, *47*, 4249–4251.
(38) Zhang, M.; Zhang, M.-T.; Hou, C.; Ke, Z.-F.; Lu, T.-B. *Angew. Chem. Int. Ed.* **2014**, *53*, 13042–13048.
(39) Zhang, M.-T.; Chen, Z.; Kang, P.; Meyer, T. J. *J. Am. Chem. Soc.* **2013**, *135*, 2048–2051.
(40) Tong, L.; Wang, Y.; Duan, L.; Xu, Y.; Cheng, X.; Fischer, A.; Ahlquist, M. S. G.; Sun, L. *Inorg. Chem.* **2012**, *51*, 3388–3398.
(41) Grohmann, A. In *Advances in Inorganic Chemistry*; van Eldik, R., Olabe, J. A., Eds.; Advances in Inorganic Chemistry; Academic Press, 2004; Vol. 56, pp 179–210.
(42) Grohmann, A. *Dalton Trans.* **2010**, *39*, 1432–1440.
(43) Que, L. *Acc. Chem. Res.* **2007**, *40*, 493–500.
(44) McDonald, A. R.; Guo, Y.; Vu, V. V.; Bominaar, E. L.; Münck, E.; Que, L. *Chem. Sci.* **2012**, *3*, 1680–1693.
(45) Wang, L.; Duan, L.; Ambre, R. B.; Daniel, Q.; Chen, H.; Sun, J.; Das, B.; Thapper, A.; Uhlig, J.; Dinér, P.; Sun, L. *J. Catal.* **2016**, *335*, 72–78.
(46) See Table S1.1 for the references included in Figures 1.4 and 1.5.
(47) Widegren, J. A.; Finke, R. G. *J. Mol. Catal. Chem.* **2003**, *198*, 317–341.
(48) Schley, N. D.; Blakemore, J. D.; Subbaiyan, N. K.; Incarvito, C. D.; D'Souza, F.; Crabtree, R. H.; Brudvig, G. W. *J. Am. Chem. Soc.* **2011**, *133*, 10473–10481.
(49) Grotjahn, D. B.; Brown, D. B.; Martin, J. K.; Marelius, D. C.; Abadjian, M.-C.; Tran, H. N.; Kalyuzhny, G.; Vecchio, K. S.; Specht, Z. G.; Cortes-Llamas, S. A.; Miranda-Soto, V.; van Niekerk, C.; Moore, C. E.; Rheingold, A. L. *J. Am. Chem. Soc.* **2011**, *133*, 19024–19027.
(50) Wasylenko, D. J.; Palmer, R. D.; Schott, E.; Berlinguette, C. P. *Chem. Commun.* **2012**, *48*, 2107–2109.

(51) Vickers, J. W.; Lv, H.; Sumliner, J. M.; Zhu, G.; Luo, Z.; Musaev, D. G.; Geletii, Y. V.; Hill, C. L. *J. Am. Chem. Soc.* **2013**, *135*, 14110–14118.
(52) Stracke, J. J.; Finke, R. G. *ACS Catal.* **2014**, *4*, 909–933.
(53) Xu, K. *Chem. Rev.* **2004**, *104*, 4303–4418.
(54) Lian, F.; Guan, H.; Wen, Y.; Pan, X. *J. Membr. Sci.* **2014**, *469*, 67–72.
(55) Agrawal, R. C.; Pandey, G. P. *J. Phys. Appl. Phys.* **2008**, *41*, 223001–223019.
(56) Quartarone, E.; Mustarelli, P. *Chem. Soc. Rev.* **2011**, *40*, 2525–2540.
(57) Chazalviel, J. N. *Phys. Rev. At. Mol. Opt. Phys.* **1990**, *42*, 7355–7367.
(58) Rosso, M.; Gobron, T.; Brissot, C.; Chazalviel, J. N.; Lascaud, S. *J. Power Sources* **2001**, *97–98*, 804–806.
(59) Sumathipala, H. H.; Hassoun, J.; Panero, S.; Scrosati, B. *Ionics* **2007**, *13*, 281–286.
(60) Bouchet, R.; Maria, S.; Meziane, R.; Aboulaich, A.; Lienafa, L.; Bonnet, J.-P.; Phan, T. N. T.; Bertin, D.; Gigmes, D.; Devaux, D.; Denoyel, R.; Armand, M. *Nat. Mater.* **2013**, *12*, 452–457.
(61) Wiers, B. M.; Foo, M.-L.; Balsara, N. P.; Long, J. R. *J. Am. Chem. Soc.* **2011**, *133*, 14522–14525.
(62) Aubrey, M. L.; Ameloot, R.; Wiers, B. M.; Long, J. R. *Energy Environ. Sci.* **2014**, *7*, 667–671.
(63) Ameloot, R.; Aubrey, M.; Wiers, B. M.; Gómora-Figueroa, A. P.; Patel, S. N.; Balsara, N. P.; Long, J. R. *Chem. Eur. J.* **2013**, *19*, 5533–5536.
(64) Van Humbeck, J. F.; Aubrey, M. L.; Alsbaiee, A.; Ameloot, R.; Coates, G. W.; Dichtel, W. R.; Long, J. R. *Chem. Sci.* **2015**, *6*, 5499–5505.
(65) Allen, F. H. *Acta Crystallogr. B* **2002**, *58*, 380–388.
(66) Bruno, I. J.; Cole, J. C.; Edgington, P. R.; Kessler, M.; Macrae, C. F.; McCabe, P.; Pearson, J.; Taylor, R. *Acta Crystallogr. B* **2002**, *58*, 389–397.

Section 1.6 Supporting Information

Table S1.1. List of tetrapodal ligands collected during a survey of the Cambridge Structural Database.[a]

CCD Refcode	Reference	Net charge	Donor atoms	Ligand name
ROCDUK	Widger, L. R.; Davies, C. G.; Yang, T.; Siegler, M. A.; Troeppner, O.; Jameson, G. N. L.; Ivanović-Burmazović, I.; Goldberg, D. P. *J. Am. Chem. Soc*. **2014**, *136*, 2699–2702.	0	N4S	$N3Py^{amide}SR$
HIVXAN	Widger, L. R.; Jiang, Y.; McQuilken, A. C.; Yang, T.; Siegler, M. A.; Matsumura, H.; Moënne-Loccoz, P.; Kumar, D.; de Visser, S. P.; Goldberg, D. P. *Dalton Trans*. **2014**, *43*, 7522-7532.	0	N4S	N3PySR
FIPQIF	Inomata, Y.; Gochou, Y.; Nogami, M.; Howell, F. S.; Takeuchi, T. *J. Mol. Struct.* **2004**, *702*, 61-70.	0	NO4	Bis-Tris, hihm, LH_5
MONKIK	Stamatatos, T. C.; Abboud, K. A.; Christou, G. *Dalton Trans*. **2009**, 41-50.	2−	NO4	Bis-Tris:LH_3
CAWPOG	Zimmermann, C.; Heinemann, F. W.; Grohmann, A. *Eur. J. Inorg. Chem.* **2005**, *2005*, 3506–3512.	0	NP4	$PY(PPh_2)_4$
HERTUU	Kohl, S. W.; Heinemann, F. W.; Hummert, M.; Weißhoff, H.; Grohmann, A. *Eur. J. Inorg. Chem.* **2006**, *2006*, 3901–3910.	0	NP4	$PY(PMe_2)_4$
SARRUA	McDonald, A. R.; Guo, Y.; Vu, V. V.; Bominaar, E. L.; Münck, E.; Que, L. *Chem. Sci*. **2012**, *3*, 1680-1693.	2−	N3O2	^{n}Bu-P2DA
SARSAH	McDonald, A. R.; Guo, Y.; Vu, V. V.; Bominaar, E. L.; Münck, E.; Que, L. *Chem. Sci*. **2012**, *3*, 1680-1693.	2−	N3O2	P2DA
KENYUZ	Baranyai, Z.; Uggeri, F. Maiocchi, A.; Giovenzana, G. B.; Cavallotti, C.; Takacs, A.; Toth, I.; Banyai, I.; Benyei, A.; Brucher, E.; Aime, S. *Eur. J. Inorg. Chem.* **2013**, 147–162.	2−	N3O2	H2AAZTA
VARVOA	Sharrad, C. A.; Lüthi, S. R.; Gahan, L. R. *Dalton Trans*. **2003**, 3693-3703.	0	N3S2	EtN_4S_2amp
AMUQIJ	Smith, J. M.; Long, J. R. *Inorg. Chem*. **2010**, *49*, 11223–11230.	1−	N4C	PY4Im
QIDNOG	Ligtenbarg, A. G. J.; Oosting, P.; Roelfes, G.; La Crois, R. M.; Lutz, M.; Spek, A. L.; Hage, R.; Feringa, B. L. *Chem. Commun*. **2001**, 385-386.	1−	N4O	
UHEGOD	Borzel, H.; Comba, P.; Hagen, K. S.; Lampeka, Y. D.; Lienke, A.; Linti, G.; Merz, M.; Pritzkow, H.; Tsymbal, L. V. *Inorg. Chim. Acta* **2002**, *337*, 407-419.	0	N4O	
YIMLAI	Comba, P.; Tarnai, M.; Pritzkow, H.; Wadepohl, H. Anorganisch-Chemisches Institut, Universität Heidelberg, Heidelberg, Germany. Private communication, 2007.	1−	N4O	
DODWUQ	Au-Yeung, H. Y.; Chan, J.; Chantarojsiri, T.; Chang, C. J. *J. Am. Chem. Soc.* **2013**, *135*, 15165–15173.	1−	N4O	
AXIKUN	Sharrad, C. A.; Cavigliasso, G. E.; Stranger, R.; Gahan, L. R. *Dalton Trans*. **2004**, 1166-1172.	0	N4S	N_4Samp
DODNER	McQuilken, A. C.; Ha, Y.; Sutherlin, K. D.; Siegler, M. A.; Hodgson, K. O.; Hedman, B.; Solomon, E. I.; Jameson, G. N. L.; Goldberg, D. P. *J. Am. Chem. Soc*. **2013**, *135*, 14024–14027.	1−	N4S	N3PYS
ZOYZUI	Lubben, M.; Meetsma, A.; Wilkinson, E. C.; Feringa, B.; Que, L. *Angew. Chem. Int. Ed*. **1995**, *34*, 1512-1514.	0	N5	N4Py
REPSIO	Grohmann, A.; Knoch, F. *Inorg. Chem.* **1996**, *35*, 7932–7934.	0	N5	PYN_4
NIQBEU	Jonas, R. T.; Stack, T. D. P. *J. Am. Chem. Soc.* **1997**, *119*, 8566–8567.	0	N5	PY5
GUGCEQ	Dietz, C.; Heinemann, F. W.; Grohmann, A. *Eur. J. Inorg. Chem.* **1999**, *1999*, 2147–2156.	0	N5	$(nac)_2ŸPYN_4$
GUGCIU	Dietz, C.; Heinemann, F. W.; Grohmann, A. *Eur. J. Inorg. Chem.* **1999**, *1999*, 2147–2156.	0	N5	$(cin)_4ŸPYN_4$
VEQPIQ	Favius, B.; Geue, R. J.; Hazell, R. G.; Jackson, W. G.; Larsen, F. K.; Qin, C. J.; Sargenson, A. M. *J. Chem. Soc., Dalton Trans*. **1999**, 3961-3972.	0	N5	N5
QENBIU	Zimmermann, C.; Heinemann, F. W.; Grohmann, A. *Eur. J. Inorg. Chem.* **2001**, *2001*, 547–555.	0	N5	

CCD Refcode	Reference	Net charge	Donor atoms	Ligand name
QENBOA	Zimmermann, C.; Heinemann, F. W.; Grohmann, A. *Eur. J. Inorg. Chem.* **2001**, *2001*, 547–555.	0	N5	
UHEFOC	Borzel, H.; Comba, P.; Hagen, K. S.; Lampeka, Y. D.; Lienke, A.; Linti, G.; Merz, M.; Pritzkow, H.; Tsymbal, L. V. *Inorg. Chim. Acta* **2002**, *337*, 407-419.	0	N5	
UHEGAP	Borzel, H.; Comba, P.; Hagen, K. S.; Lampeka, Y. D.; Lienke, A.; Linti, G.; Merz, M.; Pritzkow, H.; Tsymbal, L. V. *Inorg. Chim. Acta* **2002**, *337*, 407-419.	0	N5	
ILUGOL	Comba, P.; Hauser, A.; Kerscher, M.; Pritzkow, H. *Angew. Chem. Int. Ed*. **2003**, *42*, 4536-4540.	0	N5	
ILUHAY	Comba, P.; Hauser, A.; Kerscher, M.; Pritzkow, H. *Angew. Chem. Int. Ed*. **2003**, *42*, 4536-4540.	0	N5	
ILUHIG	Comba, P.; Hauser, A.; Kerscher, M.; Pritzkow, H. *Angew. Chem. Int. Ed*. **2003**, *42*, 4536-4540.	0	N5	
TABNOA	Roelfes, G.; Vrajmasu, V.; Chen, K.; Ho, R. Y. N.; Rohde, J.-U.; Zondervan, C.; la Crois, R. M.; Schudde, E. P.; Lutz, M.; Spek, A. L.; Hage, R.; Feringa, B. L.; Münck, E.; Que, L. *Inorg. Chem*. **2003**, *42*, 2639–2653.	0	N5	$TACNPy_2$
AVINUO	Speck, A. L.; Schoondergang, M. F. J.; Feringa, B. L. Department of Organic and Molecular Inorganic Chemistry, University of Groningen, Groningen, The Netherlands. Private Communication, 2004.	0	N5	
IROHOM	van den Heuvel, M.; van den Berg, T. A.; Kellogg, R. M.; Choma, C. T.; Feringa, B. L. *J. Org. Chem*. **2004**, *69*, 250–262.	0	N5	
IROHUS	van den Heuvel, M.; van den Berg, T. A.; Kellogg, R. M.; Choma, C. T.; Feringa, B. L. *J. Org. Chem*. **2004**, *69*, 250–262.	0	N5	
NALKIV	Comba, P.; de Laorden, C. L.; Pritzkow, H. *Helv. Chim. Acta* **2005**, *88*, 647-664.	0	N5	
NALKOB	Comba, P.; de Laorden, C. L.; Pritzkow, H. *Helv. Chim. Acta* **2005**, *88*, 647-664.	0	N5	
NALKUH	Comba, P.; de Laorden, C. L.; Pritzkow, H. *Helv. Chim. Acta* **2005**, *88*, 647-664.	0	N5	
NALLES	Comba, P.; de Laorden, C. L.; Pritzkow, H. *Helv. Chim. Acta* **2005**, *88*, 647-664.	0	N5	
NAXSOV	Wong, E. L.-M.; Fang, G.-S.; Che, C.-M.; Zhu, N. *Chem. Commun.* **2005**, 4578–4580.	0	N5	$PY5(OH)_2$
XAKKOK	Zhou, X.; Hockless, D. C. R.; Willis, A. C.; Jackson, W. G. *J. Mol. Struct*. **2005**, *740*, 91.	0	N5	
VIQWIC	Born, K.; Comba, P.; Daubinet, A.; Fuchs, A.; Wadepohl, H. *J. Biol. Inorg. Chem*. **2007**, *12*, 36–48.	0	N5	
EGOCIN	Atanasov, M.; Busche, C.; Comba, P.; Hallack, F. E.; Martin, B.; Rajaraman, G.; van Slageren, J.; Wadepohl, H. *Inorg. Chem.* **2008**, *47*, 8112–8125.	0	N5	
WOJKUC	Bentz. A.; Comba, P.; Deeth, R. J.; Kerscher, M.; Seibold, B.; Wadepohl, H. *Inorg Chem*. **2008**, *47*, 9518-9527.	0	N5	
WOJLAJ	Bentz. A.; Comba, P.; Deeth, R. J.; Kerscher, M.; Seibold, B.; Wadepohl, H. *Inorg Chem*. **2008**, *47*, 9518-9527.	0	N5	
WOJLEN	Bentz. A.; Comba, P.; Deeth, R. J.; Kerscher, M.; Seibold, B.; Wadepohl, H. *Inorg Chem*. **2008**, *47*, 9518-9527.	0	N5	
POBYIP	Comba, P.; Kerscher, M.; Lawrance, G. A.; Martin, B.; Wadepohl, H.; Wunderlich, S. *Angew. Chem. Int. Ed.* **2008**, *47*, 4740-4743.	0	N5	
POBZIQ	Comba, P.; Kerscher, M.; Lawrance, G. A.; Martin, B.; Wadepohl, H.; Wunderlich, S. *Angew. Chem. Int. Ed.* **2008**, *47*, 4740-4743.	0	N5	
POBZOW	Comba, P.; Kerscher, M.; Lawrance, G. A.; Martin, B.; Wadepohl, H.; Wunderlich, S. *Angew. Chem. Int. Ed.* **2008**, *47*, 4740-4743.	0	N5	
MOBBUB	Freedman, D. E.; Jenkins, D. M.; Iavarone, A. T.; Long, J. R. *J. Am. Chem. Soc.* **2008**, *130*, 2884–2885.	0	N5	$PY5Me_2$
COMKOF	Morin, T. J.; Linderman, S. V.; Bennett, B.; Gardinier, J. R. *Inorg. Chem*. **2008**, *47*, 7468–7470.	0	N5	pz_4lut

CCD Refcode	Reference	Net charge	Donor atoms	Ligand name
IWIQIP	Soo, H. S.; Komor, A. C.; Iavarone, A. T.; Chang, C. *J. Inorg. Chem*. **2009**, *48*, 10024–10035.	0	N5	$N4Py^{2NpNH}$
IWIQUB	Soo, H. S.; Komor, A. C.; Iavarone, A. T.; Chang, C. *J. Inorg. Chem*. **2009**, *48*, 10024–10035.	0	N5	$N4Py^{2PhNH}$
UDAXII	Atanasov, M.; Comba, P.; Hanson, G. R.; Hausberg, S.; Helmle, S.; Wadepohl, H. *Inorg Chem*. **2011**, *50*, 6890-6901.	0	N5	
ITOKEI	Comba, P.; Wadepohl, H.; Wiesner. *Eur. J. Inorg. Chem.* **2011**, 2610-2615.	0	N5	
ITOKIM	Comba, P.; Wadepohl, H.; Wiesner. *Eur. J. Inorg. Chem.* **2011**, 2610-2615.	0	N5	
AWETUS	Morin, T. J.; Wanniarachchi, S.; Gwengo, C.; Makura, V.; Tatlock, H. M.; Linderman, S. V.; Bennett, B.; Long, G. J.; Grandjean, F.; Gardinier, J. R. *Dalton Trans*. **2011**, *40*, 8024-8034.	0	N5	$pz^{4Me}{}_4$lut
AWEVAA	Morin, T. J.; Wanniarachchi, S.; Gwengo, C.; Makura, V.; Tatlock, H. M.; Linderman, S. V.; Bennett, B.; Long, G. J.; Grandjean, F.; Gardinier, J. R. *Dalton Trans*. **2011**, *40*, 8024-8034.	0	N5	pz*$_4$lut
AWEVII	Morin, T. J.; Wanniarachchi, S.; Gwengo, C.; Makura, V.; Tatlock, H. M.; Linderman, S. V.; Bennett, B.; Long, G. J.; Grandjean, F.; Gardinier, J. R. *Dalton Trans*. **2011**, *40*, 8024-8034.	0	N5	pz**$_4$lut
EVUTUL	Sun, Y.; Bigi, J. P.; Piro, N. A.; Tang, M. L.; Long, J. R.; Chang, C. J. *J. Am. Chem. Soc.* **2011**, *133*, 9212–9215.	0	N5	CF_3PY5Me_2
EVUVAT	Sun, Y.; Bigi, J. P.; Piro, N. A.; Tang, M. L.; Long, J. R.; Chang, C. J. *J. Am. Chem. Soc.* **2011**, *133*, 9212–9215.	0	N5	NMe_2PY5Me_2
YEGBOD	Atanasov, M.; Comba, P.; Helmele, S. *Inorg. Chem*. **2012**, *51*, 9357–9368.	0	N5	
GENMIX	Atanasov, M.; Comba, P.; Helmle, S.; Muller, D.; Neese, F. *Inorg. Chem*. **2012**, *51*, 12324–12335.	0	N5	
WANDIA	Boyd, J. P.; Irran, E.; Grohmann, A. *Dalton Trans.* **2012**, *41*, 2477-2485.	0	N5	
NESXAM	Clegg, J. K.; Harrowfield, J. M.; Kim, Y.; Lee, Y. H.; Madalan, A.; Thuéry, P.; Woo, A . *Aust. J. Chem*. **2012**, *65*, 734-749.	0	N5	
REVZEY	Draksharapu, A.; Li, Q.; Logtenberg, H.; van den Berg, T. A.; Meetsma, A.; Killeen, J. S.; Feringa, B. L.; Hage, R.; Roelfes, G.; Browne, W. R. *Inorg. Chem*. **2012**, *51*, 900–913.	0	N5	MeN4Py
VEBCUC	Jozwiuk, A.; Ünal, E. A.; Leopold, S.; Boyd, J. P.; Haryono, M.; Kurowski, N.; Escobar, F. V.; Hildebrandt, P.; Lach, J.; Heinemann, F. W.; Wiedemann, D.; Irran, E.; Grohmann, A. *Eur. J. Inorg. Chem.* **2012**, *2012*, 3000–3013.	0	N5	
SEBMET	Prakash, J.; Kodanko, J. J. *Inorg. Chem*. **2012**, *51*, 2689–2698.	0	N5	$N4PyCO_2Me$
WIQQUK	Comba, P.; Hunoldt, S.; Morgen, M.; Pietzsch, J.; Stephan, H.; Wadepohl, H. *Inorg. Chem*. **2013**, *52*, 8131–8143.	0	N5	
WIQRAR	Comba, P.; Hunoldt, S.; Morgen, M.; Pietzsch, J.; Stephan, H.; Wadepohl, H. *Inorg. Chem*. **2013**, *52*, 8131–8143.	0	N5	
WIQREV	Comba, P.; Hunoldt, S.; Morgen, M.; Pietzsch, J.; Stephan, H.; Wadepohl, H. *Inorg. Chem*. **2013**, *52*, 8131–8143.	0	N5	
TIQQAN	Kolanowski, J. L.; Jeanneau, E.; Steinhoff, R.; Hasserodt, J. *Chem. Eur. J.* **2013**, *19*, 8839 – 8849.	0	N5	
FIFLEN	Sahu, S.. Widger, L. R.; Quesne, M. G.; de Visser, S. P.; Matsumura, H.; Moënne-Loccoz, P.; Siegler, M. A.; Goldberg, D. P. *J. Am. Chem. Soc*. **2013**, *135*, 10590–10593.	0	N5	$N4Py^{2Ph}$
KOQDUR	Comba, P.; Rudolf, H.; Wadepohl, H. *Dalton Trans*. **2015**, *44*, 2724–2736.	0	N5	
KOQFAZ	Comba, P.; Rudolf, H.; Wadepohl, H. *Dalton Trans*. **2015**, *44*, 2724–2736.	0	N5	
KOQFED	Comba, P.; Rudolf, H.; Wadepohl, H. *Dalton Trans*. **2015**, *44*, 2724–2736.	0	N5	
KOQFIH	Comba, P.; Rudolf, H.; Wadepohl, H. *Dalton Trans*. **2015**, *44*, 2724–2736.	0	N5	
TUBHEF	Lo, W. K. C.; McAdam, C. J.; Blackman, A. G.; Crowley, J. D.; McMorran, D. A. *Inorg. Chim. Acta* **2015**, *426*, 183–194.	0	N5	2PyN2Q

CCD Refcode	Reference	Net charge	Donor atoms	Ligand name
OGUQEO	Jurss, J. W.; Khnayzer, R. S.; Panetier, J. A.; El Roz, K. A.; Nichols, E. M.; Head-Gordon, M.; Long, J. R.; Castellano, F. N.; Chang, C. J. *Chem. Sci.* **2015**, *6*, 4954–4972.	0	N5	eq-PY4PZMe$_2$
OGUREP	Jurss, J. W.; Khnayzer, R. S.; Panetier, J. A.; El Roz, K. A.; Nichols, E. M.; Head-Gordon, M.; Long, J. R.; Castellano, F. N.; Chang, C. J. *Chem. Sci.* **2015**, *6*, 4954–4972.	0	N5	PY3PZ2Me$_2$
OGUQOY	Jurss, J. W.; Khnayzer, R. S.; Panetier, J. A.; El Roz, K. A.; Nichols, E. M.; Head-Gordon, M.; Long, J. R.; Castellano, F. N.; Chang, C. J. *Chem. Sci.* **2015**, *6*, 4954–4972.	0	N5	ax-PY4PZMe$_2$
JUKMAF	Mitra, M.; Nimir, H.; Demeshko, S.; Bhat, S. S.; Malinkin, S. O.; Haukka, M.; Lloret-Fillol, J.; Lisensky, G. C.; Meyer, F.; Shteinman, A. A.; Browne, W. R.; Hrovat, D. A.; Richmond, M. G.; Costas, M.; Nordlander, E. *Inorg. Chem.* **2015**, *54*, 7152–7164.	0	N5	
JUKSUF	Mitra, M.; Nimir, H.; Demeshko, S.; Bhat, S. S.; Malinkin, S. O.; Haukka, M.; Lloret-Fillol, J.; Lisensky, G. C.; Meyer, F.; Shteinman, A. A.; Browne, W. R.; Hrovat, D. A.; Richmond, M. G.; Costas, M.; Nordlander, E. *Inorg. Chem.* **2015**, *54*, 7152–7164.	0	N5	

[a]The survey was conducted within the Cambridge Structural Database (v5.37)[65] utilizing the CCDC ConQuest V 1.18[66] software and was restricted to tetrapodal ligands forming mononuclear complexes and exhibiting a κ^5 coordination mode. Consequently, metal-ligand complexes contained in clusters were disregarded. If a ligand fulfilling these criteria was found to exhibit different charge states in its crystal structures due to deprotonation, it was counted toward each charge state in Figure 2 for which it qualified. Additionally, the net formal charges shown in Figure 2 are based *only* on the charges of the atoms in the immediate coordination environment of the metal.

Chapter Two

Evaluation of $PY5Me_2$ as a Ligand Scaffold for Single-Site Water Oxidation Catalysts

"The natural world around us shows the way to relief. All of life is maintained by the sun, by the air, by water, by the earth and its resources… If there is any one thing that people do have in common, it is the gift of sunlight. But as the early Christians said, 'If the sun were not hung so high, someone would have claimed it long ago.'"

- Eberhard Arnold

Section 2.1 Introduction

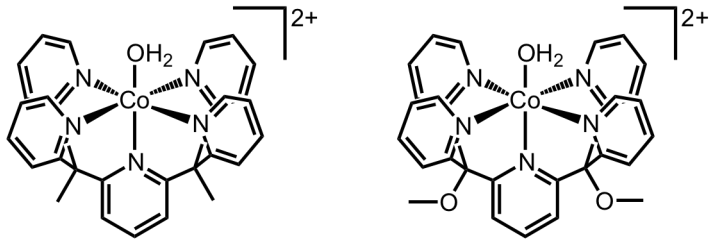
World energy demand is projected to increase from 549 quadrillion Btu in 2012 to 815 quadrillion Btu in 2040, a jump of 48%.[1] In order to meet this continuously growing demand for energy and simultaneously aid the fight against climate change by reducing society's dependence on fossil fuels, the scientific community has set itself to developing technologies that will generate sustainable chemical fuels from the sun and abundant feedstocks like water or CO_2.[2,3]

In order to convert water and CO_2 into useful combustible forms such as H_2, hydrocarbons, or alcohols, these feedstocks must be reduced. A plentiful source of electrons for these reductions can be obtained from the oxidation of water to O_2, a route nature has harnessed in the design of the water-oxidizing complex in plants, Photosystem II, which contains an oxo-bridged Mn_4Ca-cluster in its active site.[4] Nevertheless, the oxidation of water is no trivial task and currently is considered the rate determining step in the development of artificial photosynthetic systems.[5–7] In addition to forming a new O–O bond, O_2 generation involves an intricate mechanism that requires the removal of four electrons as well as four protons. Due to the high activation energy of this endothermic reaction, it also necessitates a catalyst in order to be viable on an industrial scale, and the catalyst must be robust in order to withstand the harshly oxidizing conditions to which it is exposed as previously shown in Equation 1.1. Indeed, even Photosystem II must be repaired every 20-30 minutes under high intensity light.[8–10]

Since the seminal work of Meyer that established the blue dimer, a dinuclear ruthenium polypyridyl complex, as the first homogeneous water oxidation catalyst,[10,11] extensive development and study of new ruthenium polypyridyl complexes have been undertaken.[5,7] However, these systems continue to be plagued by decomposition pathways including ligand dissociation and oxidative degradation of methylene groups in the ligand backbone.[12–15] Thus, approaches to combat these side reactions are vital for ensuring the structural integrity of the system over time. For this reason, complexes bearing polydentate ligands are attractive targets, as they should be more resistant to ligand dissociation as a result of the chelate effect than related complexes containing mono-, bi-, or tri-dentate ligands.

The ligand 2,6-bis[1,1-bis(2-pyridyl)ethyl]pyridine ($PY5Me_2$), which the Long Group has previously utilized in the study of molecular magnetism[16–18] and water reduction,[19–23] is an attractive candidate for supporting water oxidation. As shown in Figure 2.1, it is a pentadentate, pentapyridyl scaffold that forms a square pyramidal coordination cap around metal ions, leaving the sixth position open for binding of an exogenous ligand such as water. Furthermore, $PY5Me_2$ does not possess any methylene groups, rendering it more resistant to oxidative degradation. Due to the abundance of molecular polypyridyl ruthenium species available for comparison, a ruthenium $PY5Me_2$ complex would hold great promise for evaluating this ligand scaffold for water oxidation.

Although a ruthenium complex would serve as an ideal initial case study, the high cost of this precious metal ($1.60 per g)[24] would encumber its use on an industrial scale. On the other hand, first row transition metals such as iron and cobalt, which have had some success as molecular catalysts for the oxidation of water,[5,7] can be purchased at significantly lower, and more desirable prices of less than $0.03 per gram for cobalt[24] and less than $0.001 per gram for iron.[25]



$[(PY5Me_2)Co(H_2O)]^{2+}$ $[(PY5)Co(H_2O)]^{2+}$

Figure 2.1. One of the cobalt $PY5Me_2$ complexes shown by Sun et al. to act as a water reduction catalyst (left).[20] The cobalt PY5 system shown by Wasylenko and co-workers to operate as a homogenous water oxidation catalyst (right).[26]

Two articles published in 2011 provide additional support for exploring first-row transition metal systems containing $PY5Me_2$. The first reported water oxidation by a cobalt complex bearing the pentapyridyl ligand 2,6-(bis(bis-2-pyridyl)methoxymethane)pyridine (PY5),[26,27] of which the iron analogue had been developed originally by Stack and co-workers as a model complex of lipoxygenases.[28,29] As shown in Figure 2.1, PY5 possesses the same pentapyridyl backbone as $PY5Me_2$, but instead of methyl groups at the quaternary carbons, it has methoxy groups. The extremely similar structures shared by PY5 and $PY5Me_2$ imply that their cobalt complexes would likely exhibit similar activity in regard to water oxidation. The second study described a series of cobalt $PY5Me_2$ complexes that performed catalytic water reduction to H_2.[20] Interestingly, this study revealed that the potential required for catalysis could be shifted to less negative potentials by appending an electron withdrawing group to the 4-position of the axial pyridine. Because the syntheses of the $PY5Me_2$ derivatives had already been established, their cobalt complexes could be immediately evaluated to determine if the potential needed for catalytic water oxidation could be rationally controlled in a similar manner. As an added point of interest, if the cobalt $PY5Me_2$ complex should prove to be a successful water oxidation catalyst, at the time of this work[30,31] and to the best of the author's knowledge it would prove to be the first molecular species to facilitate both the reduction of water to H_2 as well as the oxidation of water to O_2 according to the reactions shown in Equations 2.1 and 2.2.

Equation 2.1. $2H_2O + 2e^- \rightarrow H_2 + 2OH^-$

Equation 2.2. $2H_2O \rightarrow O_2 + 4H^+ + 4e^-$

Thus in the subsequent account, syntheses and structural characterization of the ruthenium complexes $[(PY5Me_2)RuCl]^{2+}$ (**1**), $[(PY5Me_2)Ru(CH_3CN)]^{2+}$ (**2**), and $[(PY5Me_2)Ru(H_2O)]^{2+}$ (**3**) are described along with the first-row transition metal complex $[(PY5Me_2)Fe(H_2O)]^{2+}$ (**4**). Electrochemical characterization was performed on the ruthenium complexes as well on the cobalt series $[(PY5Me_2)Co(H_2O)]^{2+}$ (**5**), $[(NMe_2PY5Me_2)Co(H_2O)]^{2+}$ (NMe_2PY5Me_2 = 4-dimethylamino-2,6-bis(1,1-di(pyridin-2-yl)ethyl)pyridine) (**6**), and $[(CF_3PY5Me_2)Co(H_2O)]^{2+}$ CF_3PY5Me_2 = 4-trifluoromethyl-2,6-bis(1,1-di(pyridin-2-yl)ethyl)pyridine) (**7**). Finally, **3** and **5** have been evaluated for water oxidation ability, and their performance is discussed herein.

Section 2.2 Experimental Section

All experiments were performed under a nitrogen atmosphere using standard glovebox or Schlenk line techniques unless specified otherwise. All reagents were purchased from commercial vendors and used without further purification unless otherwise noted. Deionized water was purified by a Millipore Milli-Q UF Plus purification system. Acetonitrile, dichloromethane, diethyl ether, methanol, and tetrahydrofuran were dried by a VAC solvent purification system. Acetone (HPLC grade, Fisher Scientific) and ethanol (200 proof, 99.5+% from Sigma-Aldrich) were used as received. Dimethyl sulfoxide-D6 was purified by distillation and then stored over 4A molecular sieves. Acetonitrile-D3 was dried over K_2CO_3 for 24 hours, distilled, and stored over 3A molecular sieves. $PY5Me_2$;[17] NMe_2PY5Me_2, CF_3PY5Me_2, and the Co^{2+} complexes **5**, **6**, and **7**;[20] and $[(PY5Me_2)CoI]I$[18] were synthesized as previously described.

Synthesis of [(PY5Me$_2$)RuCl]Cl (1Cl). A 100 mL Schlenk flask was charged with 0.315 g (1.52 mmol) of anhydrous $RuCl_3$ and 0.683 g (1.54 mmol) of $PY5Me_2$. Then, 50 mL of anhydrous ethanol and 15 mL of deionized, degassed water were cannula transferred to the flask, and the solution was held at reflux for two days. Once cooled, all solvent was removed by reduced pressure and the flask was returned to the glovebox. The residue was suspended in 50 mL methanol and filtered. The filtrate was collected and solvent removed under reduced pressure. The resulting residue was suspended in acetonitrile and filtered. The solid was collected, dissolved in a minimal amount of methanol, and recrystallized by diffusion of diethyl ether. The gold-colored crystals that formed were suitable for X-ray analysis. Yield 0.122 g (13%). IR (neat, cm^{-1}): 3259(m), 3066(m), 3014(m), 2975(m), 2930(m), 2814(m), 1631(w), 1590(m), 1459(s), 1426(s), 1401(s), 1386(s), 1300(m), 1168(m), 1112(m), 1030(s), 903(m), 861(m), 841(m), 770(s), 758(s), 743(s), 648(s), 630(s), 588(s), 532(s), 505(s). ^{1}H NMR (400 MHz, DMSO) δ 9.67 (dd, *J* = 5.8, 1.8 Hz, 4H), 8.04 (m, 7H), 7.96 (td, *J* = 7.8, 1.5 Hz, 4H), 7.53 (ddd, *J* = 7.3, 5.8, 1.4 Hz, 4H), 2.76 (s, 6H). Anal. Calcd. for $C_{29}H_{25}Cl_2N_5Ru{\cdot}2(HOCH_3)$: C, 54.71; H, 4.93; N, 10.26%. Found: C, 54.56; H, 4.67; N, 10.32%.

Synthesis of [(PY5Me$_2$)Ru(CH$_3$CN)](O$_3$SCF$_3$)$_2$ (2(O$_3$SCF$_3$)$_2$). Into a 20 mL vial were weighed 19.5 mg (0.032 mmol) of **1** and 20.7 mg (0.081 mmol) of $Ag(O_3SCF_3)_2$. After the addition of 15 mL of dichloromethane, the vial was wrapped in foil and left to stir at room temperature for 2 days. The reaction mixture was then filtered through a pipet packed with Celite to remove AgCl. The filtrate was collected and the solvent was removed under reduced pressure. The residue was dissolved in a minimal amount of acetonitrile, and the yellow product was recrystallized by diffusion with diethyl ether, which yielded crystals suitable for X-ray analysis. Yield 15.2 mg (54%). IR (neat, cm^{-1}): 3128(w), 1596(m), 1576(w), 1466(m), 1440(m), 1408(m), 1251(s), 1223(s), 1147(s), 1067(m), 1027(s), 862(m), 841(m), 788(m), 757(s), 745(s), 704(m), 632(s), 572(s), 528(m), 516(s). ^{1}H NMR (400 MHz, DMSO) δ 9.63 (dd, J = 5.2, 1.8 Hz, 4H), 8.16 (m, 7H), 8.07 (td, *J* = 8.3, 7.9, 1.5 Hz, 4H), 7.61 (ddd, *J* = 7.2, 5.7, 1.4 Hz, 4H), 2.82 (s, 3H), 2.80 (s, 6H). Anal. Calcd. for $C_{33}H_{28}F_6N_6O_6RuS_2$: C, 44.85; H, 3.19; N, 9.51%. Found: C, 44.66; H, 3.30; N, 9.39%.

Synthesis of [(PY5Me$_2$)Ru(H$_2$O)](O$_3$SCF$_3$)$_2$ (3(O$_3$SCF$_3$)$_2$). Into a 20 mL vial were weighed 49.0 mg (0.080 mmol) of **1**Cl and 64.9 mg (0.253 mmol) of $Ag(O_3SCF_3)_2$. After adding 15 mL of dichloromethane, the vial was wrapped in foil and left to stir at room temperature for 2 days. The reaction mixture was filtered through a pipet packed with Celite to remove AgCl. The filtrate was collected and the solvent was removed by reduced pressure. The resulting residue was removed from the glovebox, and 15 mL of deionized water were added in air. The

suspension was sonicated for 10 minutes followed by stirring overnight. After the solution was vacuum filtered, the product was isolated from the filtrate with the aid of a rotary evaporator. The product was recrystallized by diffusion of diethyl ether into a mixture of 6 mL of acetone and a minimal amount of water to dissolve the complex (~0.1 mL). X-ray quality crystals were obtained by dissolving the yellow powder in a minimal amount of distilled, deionized water and slow evaporation in air. Yield 40.0 mg (58%). IR (neat, cm^{-1}): 3147(m), 1597(m), 1574(w), 1464(m), 1439(m), 1402(m), 1389(m), 1286(s), 1232(s), 1218(s), 1175(s), 1152(s), 1025(s), 858(m), 838(m), 794(m), 765(s), 757(s), 632(s), 573(s), 514(s), 506(s). ^{1}H NMR (400 MHz, DMSO) δ 9.45 (dd, *J* = 5.9, 1.7 Hz, 4H), 8.06 (m, 11H), 7.63 (ddd, *J* = 7.3, 5.7, 1.4 Hz, 4H), 7.52 (s, 2H), 2.78 (s, 6H). Anal. Calcd. for $C_{31}H_{27}F_6N_5O_7RuS_2 \cdot H_2O$: C, 42.37; H, 3.33; N, 7.97%. Found: C, 42.43; H, 3.27; N, 7.92%.

Synthesis of [(PY5Me$_2$)FeI]I. Directed by the method used to make [(PY5Me$_2$)CoI]I,[18] 318 mg (1.03 mmol) of FeI_2 and 459 mg (1.04 mmol) of PY5Me$_2$ in 40 mL of THF were evenly split between two 20 mL vials and left to stir at room temperature for two days, producing a precipitate. The reaction mixture was vacuum filtered, and the solid rinsed with THF until the solvent passing through the frit was clear. Drying the product *in vacuo* yielded 0.747 g (97%) of bright yellow powder. IR (neat, cm^{-1}): 3422(w), 3100(m), 2982(w), 1592(s), 1475(m), 1462(s), 1448(s), 1433(s), 1406(m), 1292(m), 1248(w), 1225(w), 1164(m), 1151(m), 1058(s), 1014(s), 983(w), 903(w), 863(m), 790(m), 768(s), 748(s), 699(w), 647(m), 634(s), 625(s), 574(m), 513(m). ^{1}H NMR (400 MHz, DMSO) δ 8.44 (dd, *J* = 4.9, 1.9 Hz, 4H), 7.62 (t, *J* = 7.9 Hz, 1H), 7.53 (td, *J* = 7.8, 1.7 Hz, 4H), 7.15 (dd, *J* = 7.3, 4.8 Hz, 4H), 6.97 (d, *J* = 7.9 Hz, 2H), 6.79 (d, *J* = 8.0 Hz, 4H), 2.06 (s, 6H). Anal. Calcd. for $C_{29}H_{25}FeI_2N_5$: C, 46.24; H, 3.35; N, 9.30%. Found: C, 46.71; H, 3.30; N, 8.78%.

Synthesis of [(PY5Me$_2$)Fe(H$_2$O)](O$_3$SCF$_3$)$_2$ (4(O$_3$SCF$_3$)$_2$). Into a 20 mL vial were massed 103 mg (0.137 mmol) of [(PY5Me$_2$)FeI]I and 82.4 mg (0.321 mmol) of $Ag(O_3SCF_3)_2$. After 10 mL of dichloromethane were added, the vial was wrapped in foil, and the solution was left to stir at room temperature for three days. The mixture was vacuum filtered and the filtrate was concentrated to dryness *in vacuo*. The green-yellow residue was capped with a rubber septum, brought out of the glovebox, and 10 mL of distilled, deionized water were added via syringe. The solution was left to stir at room temperature for 15 hours. Then, the brown filtrate was isolated by vacuum filtration in a N_2 filled glovebag, and the solvent was removed using a rotary evaporator. The product was purified by diffusion of diethyl ether into a mixture of 4.0 mL of acetone and a minimal amount of water to dissolve the complex (~0.1 mL).. Dark red, X-ray quality crystals were obtained by slow evaporation of an aqueous solution of the product. Yield 47.0 mg (42%). IR (neat, cm^{-1}): 3165(m), 3116(m), 3077(w), 1675(w), 1598(m), 1577(w), 1466(m), 1458(m), 1442(m), 1411(m), 1389(w), 1287(s), 1232(s), 1219(s), 1177(s), 1154(s), 1063(m), 1026(s), 958(m), 862(m), 798(m), 765(s), 701(m), 686(m), 632(s), 574(s), 514(s), 508(s), 484(s). ^{1}H NMR (400 MHz, DMSO) δ 8.45 (dd, *J* = 5.0, 1.9 Hz, 4H), 7.64 (t, *J* = 8.0 Hz, 1H), 7.55 (td, *J* = 7.8, 2.0 Hz, 4H), 7.17 (dd, *J* = 7.4, 4.8 Hz, 4H), 6.99 (d, *J* = 7.9 Hz, 2H), 6.81 (d, *J* = 8.1 Hz, 4H), 2.07 (s, 6H). Anal. Calcd. for $C_{31}H_{27}F_6FeN_5O_7S_2$: C, 45.65; H, 3.34; N, 8.59%. Found: C, 45.48; H, 3.23; N, 8.60%.

Alternative Synthesis of 4(O$_3$SCF$_3$)$_2$. Following the same method used for metalation of the Co^{2+} complexes,[20] a 20 mL vial was charged with 201 mg (0.567 mmol) of $Fe(O_3SCF_3)_2$ and 253 mg (0.571 mmol) of PY5Me$_2$. The vial was capped with a rubber septum, removed from the glovebox, and injected via syringe with 4 mL of degassed, deionized water followed by 16 mL of degassed acetone. The reaction was left to stir at room temperature for 3 days. In a N_2 filled

glovebag, the reaction solution was vacuum filtered, and the filtrate was concentrated to dryness. As before, the product was purified by recrystallization by diffusion of diethyl ether into a mixture of acetone and water. Yield 239 mg (52%). Anal. Calcd. for $C_{31}H_{27}F_6FeN_5O_7S_2$: C, 45.65; H, 3.34; N, 8.59%. Found: C, 45.41; H, 3.45; N, 8.39%.

Synthesis of [(PY5Me$_2$)Co(OH)](O$_3$SCF$_3$)$_2$ (5a(O$_3$SCF$_3$)$_2$). Into a 20 mL vial were weighed 101 mg (0.134 mmol) [(PY5Me$_2$)CoI]I and 80.2 mg (0.312 mmol) of Ag(O$_3$SCF$_3$)$_2$. Then, 10 mL of dichloromethane were added, the vial was wrapped in foil, and the solution was left to stir at room temperature for three days. The mixture was vacuum filtered and the filtrate was concentrated to dryness *in vacuo*. The pale orange residue was brought out of the box, and 10 mL of distilled, deionized water were added to the solution in air. The reaction was left to stir at room temperature overnight in air. By morning, the suspension had turned pink. The filtrate was isolated by vacuum filtration, and the solvent was removed using a rotary evaporator. Purple crystals were obtained by diffusion of diethyl ether into a solution of 3.5 mL of acetone and 0.5 mL of water. However, the crystals used for X-ray analysis were formed by diffusion of diethyl ether into methanol. Yield 63.1 mg (58%). IR (neat, cm^{-1}): 3506.2w, 3425m, 3297w, 3138w, 3090w, 3013w, 1680w, 1656w, 1599m, 1476w, 1461m, 1449m, 1393w, 1282s, 1257s, 1223s, 1184m, 1175m, 1154s, 1104m, 1069m, 1026s, 917w, 867m, 846w, 786s, 765s, 756m, 741w, 661w, 626s, 590s. ^{1}H NMR (400 MHz, CD_3CN) δ 9.61 (dd, J = 6.2, 1.6 Hz, 4H), 8.25 (m, 3H), 8.03 (td, J = 8.1, 1.4 Hz, 4H), 7.94 (dd, J = 8.1, 1.6 Hz, 4H), 7.67 (ddd, J = 7.5, 6.1, 1.5 Hz, 4H), 2.78 (s, 6H). ESI-MS (*m/z*): $\{[(PY5Me_2)Co(OH)](O_3SCF_3)\}^+$, 668.1. Calcd. for $C_{31}H_{26}CoF_6N_5O_7S_2 \cdot H_2O$: C, 44.56; H, 3.38; N, 8.38%. Found: C, 44.45; H, 3.38; N, 8.35%.

Alternative Synthesis of (5a(O$_3$SCF$_3$)$_2$). 5a was also synthesized from **5**. Co(O$_3$SCF$_3$)$_2$ (156 mg, 0.438 mmol) and PY5Me$_2$ (195 mg, 0.441 mmol) were weighed into a 20 mL vial and capped with a rubber septum. Once removed from the glovebox, 13 mL of degassed acetone and 1.5 mL of degassed, deionized water were added by syringe, and the reaction was left for stir at room temperature for 18 hours. A needle was then inserted into the golden yellow solution, and air was bubbled into the vial continuously until all solvent had evaporated (about 3 hours). The vial was charged with 9 mL of deionized water and bubbled overnight with stirring. The solution was filtered, and the pink filtrate was concentrated to a powder on a rotary evaporator. The solids were dissolved in 1 mL of deionized water and diluted with 5 mL of acetone with the aid of sonication. Recrystallization was performed by diffusion of diethyl ether into the solution to give purple crystals. Yield 207 mg (58%). Calcd. for $C_{31}H_{26}CoF_6N_5O_7S_2 \cdot 3H_2O$: C, 42.72; H, 3.70; N, 8.03%. Found: C, 42.73; H, 3.79; N, 7.87%

Physical Measurements. IR spectra were collected on a PerkinElmer Spectrum 400 FT-IR/FT-FIR Spectrometer. ^{1}H and ^{13}C NMR spectra were collected on a Bruker AVB- 400 MHz instrument and analyzed using MestReNova software (version 7.0.0-8331, Mestrelab Research S.L.). All spectra were referenced to solvent signals. Elemental analysis was performed at the Microanalytical Laboratory at the University of California, Berkeley. Mass spectrometry was performed at the QB3/Chemistry Mass Spectrometry Facility at the University of California, Berkeley using an orthogonal acceleration quadrupole time-of-flight (Q-tof) mass spectrometer with an electrospray ionization (ESI) source operated in positive ion mode (Q-tof Premier, Waters, Milford, MA). Mass spectra were processed using MassLynx software (version 4.1, Waters).

Crystal Structure Determination. Structures for **1**, **2**, **3**, **4**, and **5a** were determined by X-ray diffraction performed on single crystals coated with Paratone-N oil and mounted on Kaptan loops. Crystals were frozen at a temperature of 100 K by a stream of N_2 during the experiments.

Data were collected using either a Bruker SMART diffractometer equipped with an APEX detector using MoKα (λ = 0.71073) radiation (**1**, **5a**) or a Bruker QUAZAR diffractometer equipped with an APEX-II detector using MoKα (λ = 0.71073) radiation (**2**, **3**, **4**). Raw data were integrated and corrected for Lorentz and polarization effects using Bruker APEX2 V. 2009.1.[32] Absorption corrections were applied using SADABS.[33] Space group assignments were determined by examination of systematic absences, E-statistics, and successive refinement of the structures using SHELXL-97.[34] All structures were solved by direct methods using SIR-2004.[35] None of the crystals showed significant decay during data collection. Thermal parameters were refined anisotropically for all non-hydrogen atoms. Hydrogen atoms were placed in ideal positions and refined using a riding model for all structures with the exceptions of **3** and **4**, in which the placements of the hydrogen atoms of the coordinated water molecule were identified from the electron density map. Solvent disorder for the structure of **5a** was extensive. Consequently, SQUEEZE[36] was used to account for unassigned electron density. Olex2[37] was used to perform additional calculations.

Electrochemical Analysis. Experiments were performed using the BAS CV-50W Voltammetric Analyzer and software. Cyclic and square wave voltammetry experiments in aqueous solution utilized a three-electrode system composed of a glassy carbon working electrode, Ag/AgCl reference electrode, and platinum wire auxiliary electrode, while aqueous controlled potential electrolysis experiments (CPE) (pH 7) utilized an FTO working electrode (0.5 cm^2), Ag/AgCl reference electrode, and platinum mesh auxiliary electrode. CPE experiments were performed in a two-compartment cell under N_2 with continuous stirring, in which the chambers were separated by a glass frit. For experiments performed in aqueous solution at pH 1, 0.1 M HNO_3 was used as the electrolyte. A 0.1 M phosphate buffer was used for pH 7-11. Redox potentials obtained versus Ag/AgCl were subsequently referenced to SHE by shifting the values obtained by +195 mV.

Evolution of O_2 during CPE experiments with **5** was confirmed using a custom-build apparatus composed of a round-bottom flask (working volume = 13.8 mL) fitted with a threaded side arm into which the O_2 probe was inserted. Prior to initiating electrolysis, the headspace was purged with N_2 for at least 20 minutes or until the O_2 reading stabilized. During the CPE experiment, the fluorescence optical probe (Ocean Optics FOXY-OR125-AFMG) was submerged in solution adjacent to the working electrode, and O_2 levels were evaluated every 10 sec with a multifrequency phase fluorimeter (Ocean Optics MFPF-100). Sensor data was analyzed using the TauTheta Host Program and converted to "percent O_2" with OOISensors software. Control experiments established standard deviations for the O_2 readings to be ± 3% of the total moles of O_2 detected.

When electrochemical experiments were performed in acetonitrile and 0.1 M ammonium hexafluorophosphate, the three-electrode system was composed of a glassy carbon working electrode, a platinum auxiliary electrode, and a silver wire pseudo reference. A platinum working electrode was used only in the case of **1**. Experiments in acetonitrile were referenced to the ferrocene 3+/2+ couple.

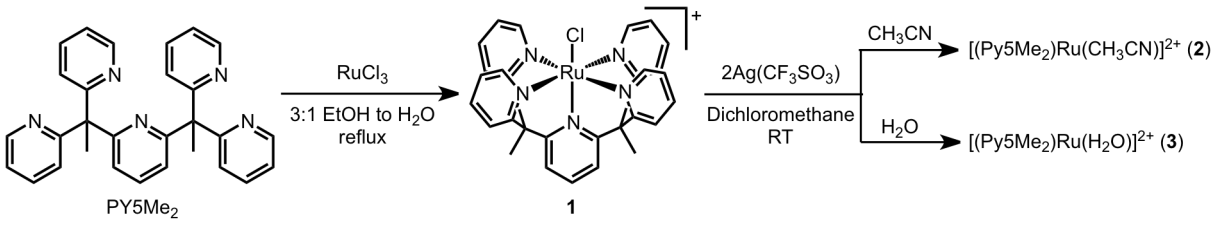
Manometry Experiments. A Testo 521 differential pressure manometer with an operating range of 1-100 hPa and accuracy within 0.5% of the measurement was used to perform manometry measurements. The manometer was coupled to thermostatted reaction vessels for dynamic monitoring of the headspace pressure above each reaction. The secondary ports on the manometer were connected to thermostatically controlled reaction vessels containing the same solvents and headspace volumes as the reaction sample vials. A Pfeiffer Omnistar GSD 301C

mass spectrometer was used for dynamic monitoring of gases formed during the experiment. (The spectrometer was calibrated for gases of interest by injecting equal concentrations of O_2 and CO_2 into the instrument, for which a response ratio of 1:2 was observed.) During a typical experiment, 16.04 mL degassed vials containing a suspension of catalyst in 0.1 M triflic acid (1.5 mL) were connected to the apparatus by capillary tubing. Then, a degassed solution of ceric ammonium nitrate (0.5 mL) at pH=1 (triflic acid, 200 equivalents) was added to the reaction vessel via a Hamilton gastight syringe.

Section 2.3 Results and Discussion of Ruthenium $PY5Me_2$ Complexes

Synthesis and Structure of Ruthenium $PY5Me_2$ Complexes. A ruthenium $PY5Me_2$ complex was initially pursued due to the plethora of ruthenium polypyridyl systems that have been found to act as molecular water oxidation catalysts. The depth of this particular field would provide a substantial foundation on which to evaluate $PY5Me_2$ as a ligand scaffold for this application. Similar to the method employed by Lee et al.,[38] Scheme 2.1 shows that $[(PY5Me_2)RuCl]Cl$ (**1**Cl) was produced by refluxing $RuCl_3$ and $PY5Me_2$ for two days in a mixture of 3:1 absolute ethanol to degassed, deionized water. The final product was isolated as a yellow solid through a series of washes and filtrations followed by purification by recrystallization from methanol and diethyl ether. Despite attempts to optimize these reaction conditions, the yield for **1**Cl remained low, only 13%. Since establishing this route, two new reports have put forth alternative reaction conditions that give **1** in 41%[39] and 74%[40] yields.

Scheme 2.1 Synthesis of divalent ruthenium complexes **1**, **2**, and **3**.



One reaction that competes with O_2 evolution from water is that of oxidation of Cl^- to Cl_2. To prevent any interference by this side reaction, the chloride anions were abstracted in a second step by exposing **1**Cl to two equivalents of $Ag(CF_3SO_3)$ under N_2. A number of conditions screened for this synthesis resulted in no reaction or incomplete conversion (i.e. methanol or acetonitrile at room temperature; dimethyl sulfoxide at 110 °C, 170 °C or 200 °C). However, performing the reaction in anhydrous dichloromethane at room temperature resulted in complete conversion as determined by ^1H NMR. After removing the AgCl byproduct by filtration through Celite and evaporation of the dichloromethane, the liberated sixth coordination position could be filled by either acetonitrile or water by exposing the crude product to the corresponding solvent. Pure $[(PY5Me_2)Ru(CH_3CN)](O_3SCF_3)_2$ (**2**$(O_3SCF_3)_2$) was isolated in 54% yield after recrystallization by diffusion of diethyl ether into acetonitrile, while $[(PY5Me_2)Ru(H_2O)](O_3SCF_3)_2$ (**3**$(O_3SCF_3)_2$) was obtained in 58% yield by slow diffusion of diethyl ether into a mixture of acetone and water. Both aquo and acetonitrile analogues were found to be golden yellow in color. Recently, **3** has also been generated by two slightly different routes that involve refluxing the same starting materials in purely aqueous solutions. They afford **3** in similar yields (52%[39] and 67%[40]) to the route reported here.

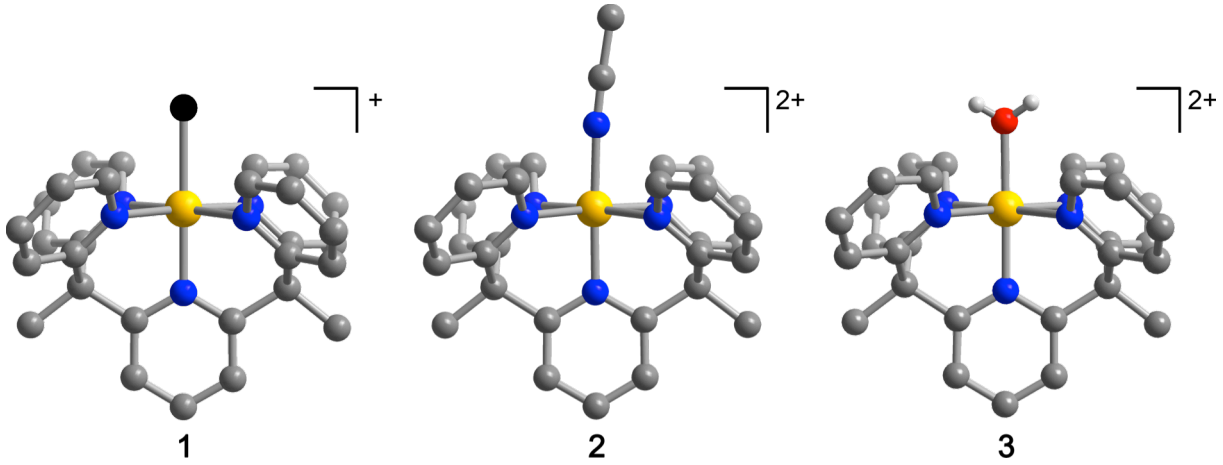


Figure 2.2. Single crystal X-ray structures of ruthenium PY5Me$_2$ complexes. Yellow, red, blue, gray, black, and light gray spheres represent Ru, O, N, C, Cl, and H atoms, respectively. Water H atoms were identified from the electron density map. All other H atoms and counterions were omitted for clarity.

Table 2.1. Crystallographic data for ruthenium PY5Me$_2$ complexes with selected bond lengths (Å) and angles (deg).

Complex	**1**Cl	**2**$(CF_3SO_3)_2$	**3**$(CF_3SO_3)_2$
Empirical Formula[a]	$C_{33}H_{41}Cl_2N_5O_4Ru$	$C_{37}H_{34}F_6N_8O_6RuS_2$	$C_{31}H_{27}F_6N_5O_7RuS_2$
Crystal System	Orthorhombic	Monoclinic	Triclinic
Space Group	*Pnma*	$P2_1/n$	$P\bar{1}$
Ru–N_{avg}, Å	2.061(3)	2.0687(17)	2.0573(14)
M–X,[b] Å	2.4082(15)	2.0391(18)	2.1228(13)
X–Ru–N_{ax}, deg	179.86(14)	177.56(7)	178.13(5)
PY-tilt,[c] deg	90.000(6)	96.483(8)	92.957(1)
OOP,[d] Å	0.0462(1)	0.0509(8)	0.0259(7)

[a] Empirical formulas include outer sphere solvent molecules. [b] X represents the exogenous ligand: Cl in **1**, MeCN in **2**, and H_2O in **3**. [c]The PY-tilt is defined as the angle between the least squares planes generated by the four equatorial pyridine donors and the atoms of the axial pyridine ring and was calculated using Olex2. [d]The out-of-plane (OOP) distortion is defined as the displacement of the metal center from the least-squares plane generated by the four equatorial pyridine atoms and was calculated using Olex2.

^{1}H NMR indicated that all three ruthenium complexes were d^6, low-spin, diamagnetic species. X-ray diffraction studies were performed on single crystals of the complexes as well. The series is shown in Figure 2.2, and a summary of bond lengths and angles describing the coordination environments is shown in Table 2.1. All complexes exhibited a pseudo-octahedral coordination environment around the ruthenium ion. The five pyridine donors form a square pyramidal coordination cap, leaving the sixth position available for chloride, acetonitrile, or water. Overall, the ruthenium cation fits well in the ligand pocket as judged by the very small distortion of the metal out of the plane generated by the four equatorial donors (0.0259(7)-0.0509(8) Å).

The C_s symmetry of **1** is reflected in the solid state by the *Pnma* space group in which it crystalizes, with the ruthenium atom positioned on a mirror plane of the unit cell. While one chloride ion is bound to ruthenium, the asymmetric unit also contains one outer sphere chloride counterion and three outer sphere methanol solvent molecules that exhibit a minor amount of rotational disorder in the methyl groups. Unlike the axial pyridine of **1**, which is perpendicular to the plane of the equatorial pyridine nitrogen atoms, the axial pyridines of **2** and **3** are slightly

tilted by 6° and 3°, respectively. For the structures of both **2** and **3**, the presence of two outer sphere trifluoromethanesulfonate anions is in agreement with an assignment of a Ru^{2+} oxidation state.

As stated previously, water oxidation by ruthenium complexes bearing polypyridyl ligands is well established, and a number of crystal structures for these complexes are known. With an average Ru–N_{pyr} bond length of 2.057(1) Å and a Ru–OH_2 bond length of 2.123(1) Å, compound **3** is in good agreement with the literature with respect to the ruthenium coordination sphere.[41–43] Interestingly, the hydrogen atoms of the bound water molecule could be identified from the electron density map because the two outer sphere trifluoromethanesulfonate anions were positioned above the complex, within hydrogen bonding distance (1.9 Å) of the aquo moiety. It should be noted that while another study has since published the isolation of **3**,[39] this is the first report of its crystal structure.

Electrochemical Characterization of Ruthenium Complexes. In order to probe the accessible oxidation states of **1**, a cyclic voltammetry experiment was performed in acetonitrile with tetrabutylammonium hexafluorophosphate as the electrolyte. At a scan rate of 100 mV/s, the complex exhibited one feature at 380 mV versus ferrocene that was assigned to the $Ru^{3+/2+}$ couple. The average difference between the forward and reverse peak potentials of this redox event over multiple scan rates was found to be 61 mV, which is nearly equal to the value of 59 mV for an ideally reversible one electron transfer, and the forward peak current ($i_{p,f}$) of this couple displays a linear dependence on the square root of the scan rate, signifying that the electron transfer is diffusion controlled.[44] However, the average value for the ratio of the reverse peak current to the forward peak current ($|i_{p,r}/i_{p,f}|$) for all scan rates was found to be 0.7 rather than the expected value of unity for a fully reversible electron transfer. This ratio suggested that a secondary chemical process may take place in response to the oxidation of **1**.[44]

The acetonitrile bound complex, **2,** was studied electrochemically in acetonitrile under the same conditions used for **1**. Sweeping in the anodic direction, the diffusion controlled $Ru^{3+/2+}$ couple appeared at 920 mV. It is unsurprising for the $Ru^{3+/2+}$ couple of **2** to appear at a higher potential that that of **1** since an anionic chloride ligand would better stabilize the higher-valent Ru^{3+} complex than a neutral acetonitrile ligand. Unlike **1**, the oxidation of **2** appeared to yield a chemically stable product, seeing as $|i_{p,r}/i_{p,f}|$ remained steadily near unity regardless of scan rate. While the anodic and cathodic peak potentials did begin to spread apart at higher scan rates (see Figure S2.3), the average separation of 66 mV did not stray far from that of an ideally reversibly feature. An irreversible wave at −2250 mV, which was observed near the edge of the solvent window when scanning in the cathodic direction, was assigned to the $Ru^{2+/1+}$ reduction.

Subsequently, **2** was also examined electrochemically in 0.1 M HNO_3 (pH 1) aqueous solution. The resulting cyclic voltammograms displayed two reversible waves at 890 and 1270 mV versus SHE. Though, when compared to the cyclic voltammogram of the aquo complex **3** under the same conditions, it became obvious that the feature at 890 mV corresponded to the $Ru^{3+/2+}$ couple of **3** while the feature at 1270 mV belonged to the $Ru^{3+/2+}$ couple of **2**. Thus, it was concluded that a portion of the coordinated acetonitrile had exchanged with the bulk water to generate **3** *in situ*, resulting in both species existing in solution simultaneously. Because **2** did not remain intact when dissolved in water nor completely convert to **3**, further electrochemical tests in aqueous solution were not pursued.

Ultimately, **3** was the most relevant complex to the study of water oxidation. In the literature, both $Ru^{4+/3+}$ and $Ru^{5+/4+}$ redox couples have been shown to induce catalytic water oxidation.[5] As a result, it was expected that redox events at potentials beyond that of $Ru^{3+/2+}$

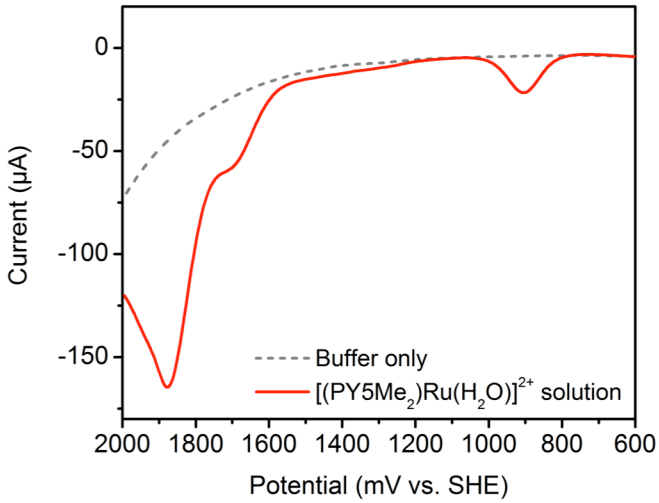


Figure 2.3. Square wave voltammogram of **3** in pH 1 aqueous solution. The concentration of **3** was 0.4 mM. Increment potential of each point, 4 mV; square wave amplitude, 25 mV; square wave frequency, 15 Hz.

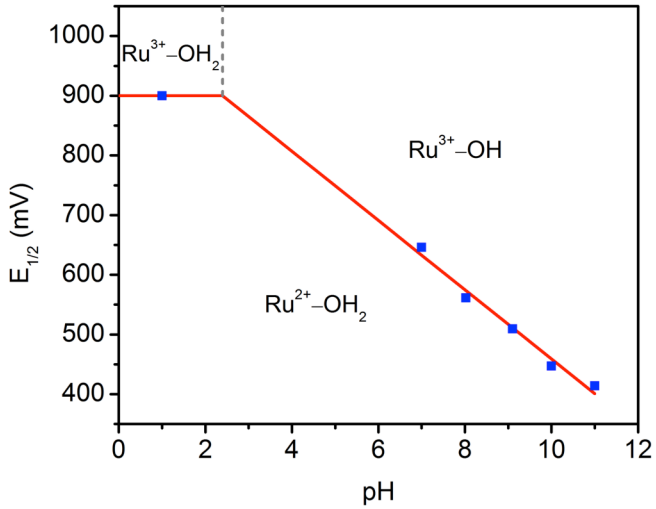


Figure 2.4. Pourbaix diagram of **3** at a scan rate of 100 mV/s in 0.1 M HNO_3 (pH 1) or 0.1 M phosphate (pH 7-11) buffer.

would be observed in the cyclic voltammograms of **3** prior to the onset of catalysis. Indeed, at pH 1 a second oxidation was observed at 1700 mV versus SHE prior to the rise of catalytic current. Because this feature was not clearly defined in the cyclic voltammograms, square wave voltammetry was performed in order to define the value of the oxidation potential of this feature. The square wave voltammogram shown in Figure 2.3 reveals a total of three oxidations at 900 mV, 1700 mV, and 1870 mV, which were assigned to the $Ru^{3+/2+}$, $Ru^{4+/3+}$, and $Ru^{5+/4+}$ oxidations, respectively. The $Ru^{5+/4+}$ feature had not been identified previously by cyclic voltammetry due to the fact that it was embedded as a shoulder in the catalytic current.

The incorporation of proton coupled electron transfer (PCET) into a water oxidation mechanism is beneficial in that shedding a proton with each electron loss prevents charge buildup in the transition state, thereby decreasing the activation barrier to the electron transfer.[45,46] Additionally, by increasing the pH of the electrolyte solution, the potential required to enact an oxidation decreases by 59 mV per decade for a species capable of PCET, making the

oxidized state more easily accessible. Returning to cyclic voltammetry, a partial Pourbaix diagram of the $Ru^{3+/2+}$ couple was compiled to determine if and in what pH range PCET occurs in the water oxidation mechanism of compound **3**. The features for the $Ru^{4+/3+}$ and $Ru^{5+/4+}$ couples could not be identified in the basic pH range, which prevented their inclusion into the Pourbaix diagram. Excluding the data point at pH 1 in Figure 2.4, the points for pH 7-11 generate a slope of approximately 58 mV per pH unit, which is indicative of a single PCET in this range.[47] The data point at pH 1 was excluded from the linear regression because such an acidic environment would be expected to prevent PCET from occurring. Although more data points should be collected, the traces obtained so far suggest a pK_a value of approximately 2.4 for the deprotonation of $[(PY5Me_2)Ru(H_2O)]^{3+}$ to $[(PY5Me_2)Ru(OH)]^{2+}$. It then follows that PCET for the $Ru^{3+/2+}$ couple is expected to occur from pH 2.4 to at least pH 11.

Ideally, an efficient catalyst would induce water oxidation at the thermodynamic potential for the conversion of water to O_2. Considering that this value is 1171 mV at pH 1, the potential required for the operation of **3** is rather high (1870 mV). Additionally, the potential necessary for **3** to initiate catalysis is high in comparison to other ruthenium-pyridyl complexes that have been evaluated for water oxidation under the same conditions, some of which have been found to have oxidation potentials as low as 1200 mV and 1600 mV for the $Ru^{4+/3+}$and $Ru^{5+/4+}$ couples, respectively.[43,48–50]

Despite these facts, the cyclic voltammogram of **3** did suggest that the complex was capable of water oxidation. Referring again to Figure 2.3, one can see that the current begins to take off after the $Ru^{4+/3+}$ couple. Because current is proportional to the rate of a reaction at a given potential, the dependence of the reaction rate on catalyst concentration was investigated by tracking the current at 1890 mV as a function of catalyst added. The resulting plot given in Figure S2.7 is linear, which suggests that the reaction possesses a first order rate dependence on the catalyst and that the mechanism for water oxidation utilizes only a single metal site as opposed to a bimolecular mechanism.[49]

To ensure that the irreversible feature at the anodic end of the solvent window for **3** was indeed a result of catalysis, chemical oxidation of the complex with excess equivalents of Ce^{4+} as the sacrificial oxidant was performed to verify the generation of O_2 and to evaluate the efficiency of the reaction. Manometry was used to quantify the amount of gas produced, and mass spectrometry was used to determine the composition of the gaseous products. As shown in

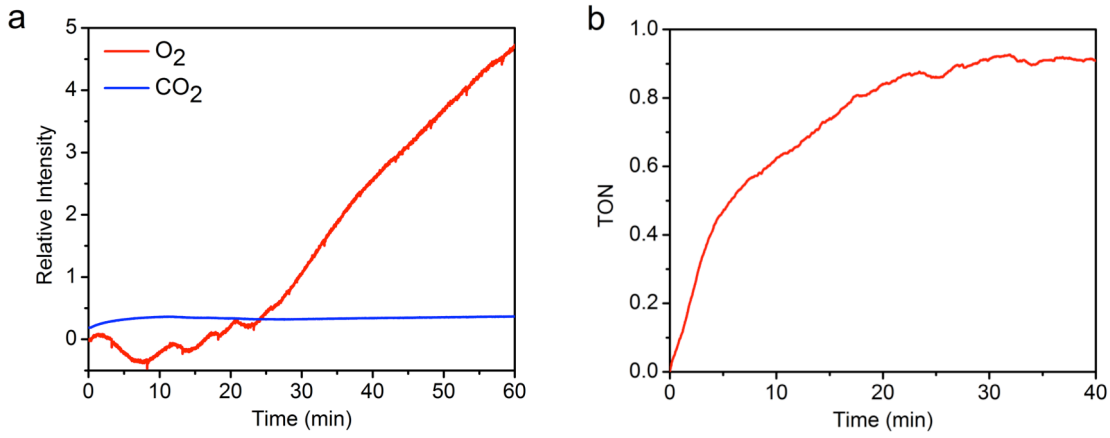


Figure 2.5. O_2 evolution experiments with **3**, using excess Ce^{4+} as the sacrificial oxidant. (a) Dynamic monitoring of gases formed by mass spectrometry. (b) Quantification of O_2 evolved over time via manometry.

Figure 2.5a, the amount of CO_2 eluted remains consistently negligible compared to the amount of O_2 formed during the course of the experiment, which supports the hypothesis that $PY5Me_2$ is chemically resistant to oxidative composition to CO_2. However, manometry showed that only one equivalent of O_2 was produced, despite the use of excess Ce^{4+} (Figure 2.5b). Consequently, it was concluded that **3** does not behave as a water oxidation catalyst and instead serves as a stoichiometric oxidant for this reaction. Although **3** did not prove to be a successful water oxidation catalyst, it has found use as an oxidant in a kinetic and reactivity study of electron transfer and hydrogen atom transfer reactions with organic substrates in water.[39]

Section 2.4 Results and Discussion of $PY5Me_2$ Complexes Containing Co^{2+} and Fe^{2+}

Synthesis and Structure of Co^{2+} and Fe^{2+} Complexes. Despite the lack of catalytic water oxidation ability found for **3**, evidence of O_2 evolution[26] by the structurally analogous cobalt system $[(PY5)Co(H_2O)]^{2+}$ inspired a subsequent investigation of the cobalt complex $[(PY5Me_2)Co(H_2O)]^{2+}$ (**5**). Furthermore, prior work by Sun and co-workers had established that tailoring the electronic properties of $PY5Me_2$ by adding electron donating ($–NMe_2$) or electron withdrawing ($–CF_3$) groups to the 4-position of the axial pyridine was able to shift the potential at which catalytic current was observed for water reduction to H_2.[20] In an attempt to determine if this effect could be replicated in the case of water oxidation, the series **5**, $[(NMe_2PY5Me_2)Co(H_2O)]^{2+}$ (**6**), and $[(CF_3PY5Me_2)Co(H_2O)]^{2+}$ (**7**) was synthesized as previously described.[20] Additionally, the iron complex $[(PY5Me_2)Fe(H_2O)]^{2+}$ (**4**) was generated through a two step synthesis starting from FeI_2. In the first step, FeI_2 reacted with $PY5Me_2$ in THF to form $[(PY5Me_2)FeI]I$, which precipitated from solution and was isolated in 96% yield as a yellow solid by filtration in a fashion analogous to that reported by Zadrozny et al.[18] Subsequently, $[(PY5Me_2)FeI]I$ was combined with two equivalents of $Ag(CF_3SO_3)$ in dichloromethane at room temperature followed by exposure to water in the same manner used to generate **3**, which gave **4**$(CF_3SO_3)_2$ as a brown solid in 42% yield. A simpler, one step route was later established in which $PY5Me_2$ was metalated directly with $Fe(CF_3SO_3)_2$ in a water and acetone mixture to give **4** in 52% yield.

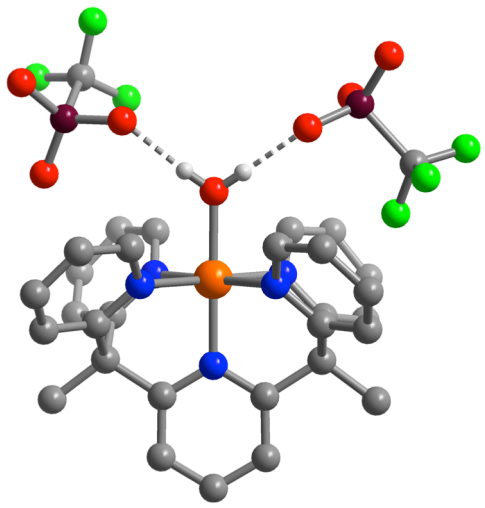


Figure 2.6. Single crystal X-ray structure of **4**. Orange, red, maroon, blue, gray, green, and light gray spheres represent Fe, O, S, N, C, F, and H atoms, respectively. Water H atoms were identified from the electron density map. All other H atoms were omitted for clarity. Hydrogen bonds are shown with dashed lines.

While single crystal X-ray structures of the high spin aquo complexes **5**, **6**, and **7** have been published elsewhere,[20] the crystal structure of **4** is shown here in Figure 2.6 for the first time. It reveals that the orientation of the trifluoromethanesulfonate anions is nearly identical to those found in the structure of **3**. The interatomic distances between the oxygen atoms of the counteranions and the hydrogen atoms of the metal-bound water molecule (1.8-1.9 Å) are within expected distances for hydrogen bonding as well. Previously, Goldsmith and co-workers published the crystal structure of the closely related ferrous-aquo complex $[(PY5)Fe(H_2O)]^{2+}$.[28] The average $Fe-N_{pyr}$ bond length for this complex was found to be 2.187(7) Å, which corresponded to a high spin iron center. Despite the striking similarities of the coordination environments of $[(PY5)Fe(H_2O)]^{2+}$ and **4**, the latter was ascertained to contain low spin Fe^{2+} due to its diamagnetic NMR spectrum in deuterium oxide (Figure S2.8) and its average $M-N_{pyr}$ bond length of 1.992(2) Å. This distance is approximately 0.2 Å shorter than that of $[(PY5)Fe(H_2O)]^{2+}$ and corroborates well with the structures of other low spin ferrous complexes found in Goldsmith's study and in literature.[28,51]

Electrochemical Characterization of Cobalt Complexes. As with the ruthenium $PY5Me_2$ complexes, the cobalt complexes were first evaluated by cyclic voltammetry. At pH 7 in aqueous phosphate buffer, **6**, **5**, and **7** exhibit quasireversible, diffusion-controlled $Co^{3+/2+}$ couples at 235 mV, 275 mV, and 323 mV versus SHE, respectively. The trend given by these complexes is to be expected, with **6** exhibiting the lowest $Co^{3+/2+}$ potential due to the electron donating characteristics of the $-NMe_2$ moiety and **7** exhibiting the highest $Co^{3+/2+}$ potential due to the electron withdrawing nature of its $-CF_3$ moiety. As shown by the Pourbaix diagram in Figure 2.7, this trend holds from pH 7 to pH 11. Additionally, PCET is apparent in this pH range due to the 52-58 mV per pH unit slopes calculated from the three datasets, which again are near to the expected value of 59 mV per pH unit for the transfer of a single electron-proton pair.

In order to better understand the structural transformation occurring during this first oxidation, the Co^{3+} hydroxide intermediate resulting from PCET was isolated via chemical oxidation of **5** in aqueous solution using O_2 from air. $[(PY5Me_2)Co(OH)]^{2+}$ (**5a**) was obtained as a purple solid in good yield (58%). The structure of this complex was verified by X-ray crystallography (Figure 2.8), elemental analysis, and electrospray ionization mass spectrometry. In addition to a conversion from high spin Co^{2+} to low spin Co^{3+} that was confirmed by the ^1H

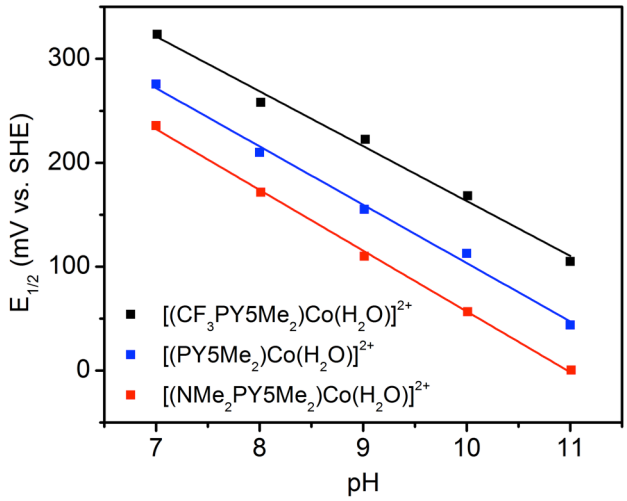


Figure 2.7. Pourbaix diagram of **5**, **6**, and **7** at a scan rate of 100 mV/s in 0.1 M phosphate buffer.

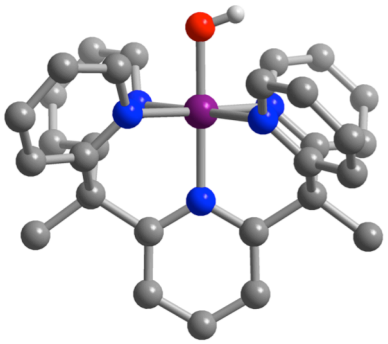


Figure 2.8. Single crystal X-ray structures of **5a**. Purple, red, blue, gray, and light gray spheres represent Co, O, N, C, and H atoms, respectively. H atoms other than the one corresponding to the hydroxide were omitted for clarity.

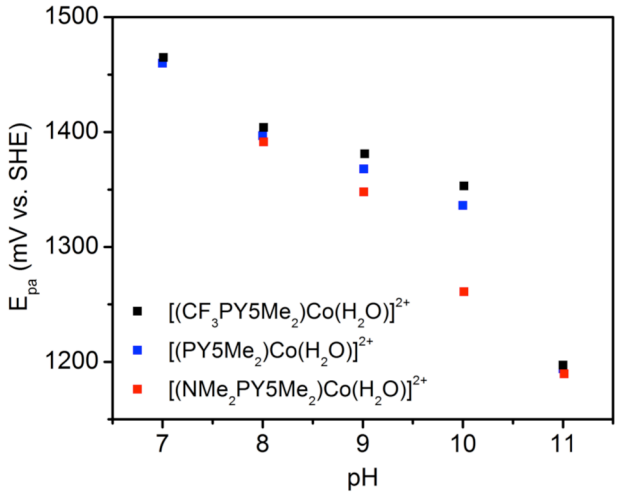


Figure 2.9. Anodic peak potentials (E_{pa}) observed for the second anodic features of **5**, **6**, and **7** at a scan rate of 100 mV/s at varying pH in 0.1 M phosphate.

NMR spectrum of **5a**, the Co–O and average Co–N_{pyr} bond lengths contract from 2.0549(15) Å to 1.8525(12) Å and from 2.1308(16) Å to 1.9724(15) Å, respectively, during this oxidation. The energy needed to perform these structural and electronic reorganizations may help to explain the quasireversible nature of the $Co^{3+/2+}$ couple (Figure S2.9).

Scanning to higher potentials at pH 7, an irreversible oxidation is observed at the onset of catalytic current. Figure 2.9 shows that the pH dependence of the anodic peak potential for this feature holds no reliable trend between the three Co^{2+} derivatives. At pH 7 and 8 the data points nearly overlap while in more basic media they begin to differentiate before collapsing again at pH 11. One explanation for the sudden collapse at pH 11 could be that these complexes are not stable at such basic conditions and consequently decompose, resulting in the same side product that in turn generates the observed feature. This proposal is not unprecedented as irregular electrochemical behavior was also observed for $[(PY5)Co(H_2O)]^{2+}$ at pH > 10.3, which was concluded to be a result of catalyst decomposition.[26]

Due to the erratic behavior of these irreversible oxidations, subsequent efforts focused specifically on compound **5** at pH 7 to better understand the behavior of this complex at high potentials. Initial results were promising; cyclic voltammetry exhibited what appeared to be catalytic current after the second anodic feature, and O_2 generation was confirmed with the aid of a fluorescence optical probe inserted into the reaction solution. Subsequently, controlled

potential electrolysis (CPE) was performed to determine the resistance of **4** to decomposition over time. During a 5 h experiment at pH 7 in phosphate buffer, the potential was held at 1500 mV versus SHE, and charge equivalent to 13 electrons per cobalt atom were passed. As shown in Figure 2.10, the charge versus time trace was not linear over the course of the experiment, suggesting that the reaction rate—and likely the concentration of catalyst in solution—was decreasing as the experiment progressed.

Additional evidence for catalyst decomposition came from cyclic voltammograms that were taken before and after the CPE experiment as shown in Figure 2.11a. Prior to CPE, the onset of catalytic current occurred at 1425 mV. Afterwards, the potential required to observe catalytic current had decreased to 1350 mV. Additionally, capacitive features, which had not been observed previously, had become apparent at 1015 mV on the anodic scan and at 940 mV on the cathodic scan. To further probe these features, a homogeneity test was performed, during which the working electrode was removed from the CPE solution, gently rinsed with fresh water, and transferred to a cell containing only fresh buffer. At this time, another cyclic voltammogram was

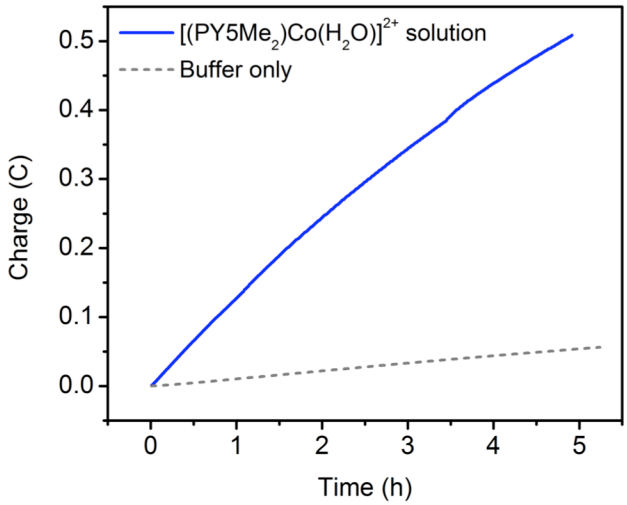


Figure 2.10. CPE experiment with **5** in pH 7 phosphate buffer. The potential was held at 1500 mV versus SHE for 5 h. The concentration of 5 was 70 uM.

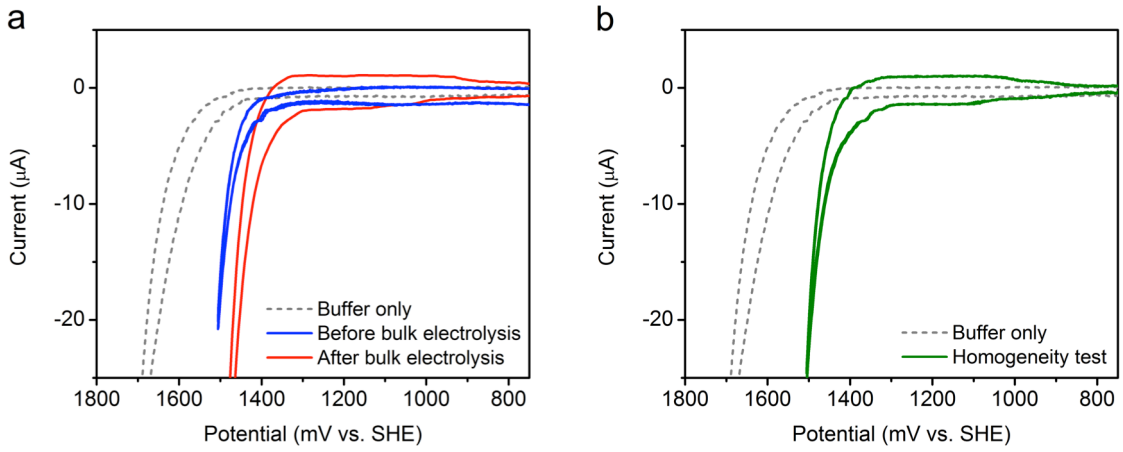


Figure 2.11. Cyclic voltammograms taken during the course of the CPE experiment with **5**. (a) The blue scan was taken prior to commencing CPE, and the red scan was taken immediately following CPE. (b) The green scan was obtained during the homogeneity test.

taken. Ideally, the trace obtained in the fresh buffer should be identical to that obtained from a buffer only solution. Yet in this case, the onset of catalytic current was observed at 1430 mV, and capacitive features at 1090 mV in the anodic direction and 995 mV in the cathodic direction remained (Figure 2.11b). The evidence provided by these cyclic voltammograms suggested that at the potentials required for catalysis, a decomposition product was deposited on the electrode surface and was contributing to the overall observed catalytic activity. Thus it was not trivial to distinguish how much of the observed catalytic activity was produced by **5** as opposed to that generated from the side product. Although the exact identity of the decomposition product was not determined, the capacitive features observed after CPE are extremely similar to those found in the heterogeneous Co-Pi catalyst published by Kanan and Nocera.[52]

Section 2.5 Conclusions and Outlook

During the course of this study, a series of ruthenium complexes bearing the $PY5Me_2$ ligand were synthesized and characterized both structurally and electrochemically. The aquo derivative, **3**, was of particular interest as a potential water oxidation catalyst due to its polypyridyl coordination environment, which is similar to other ruthenium complexes that have previously been shown to be catalytically active for O_2 evolution. Cyclic voltammetry suggested that **3** facilitated water oxidation, though chemical oxidation with concurrent evaluation by manometry and mass spectrometry established that **3** acts as only a stoichiometric oxidant for O_2 generation. Although the exact reason for its limitation as a stoichiometric oxidant was not explored, deactivation by oxidative decomposition of the ligand to CO_2 was ruled out since negligible amounts of CO_2 were detected by mass spectrometry during the experiments.

Motivated by the lower costs of first row transition metals compared to those of precious metals like ruthenium and by a report that demonstrated O_2 evolution from a molecular cobalt catalyst bearing a pentapyridyl ligand,[26] the family of cobalt complexes **5**, **6**, and **7** were also evaluated for catalytic activity. Cyclic voltammetry showed that changing the electronic properties of the $PY5Me_2$ ligand was able to shift the $Co^{3+/2+}$ couple in a systematic fashion, with the most electron donating ligand NMe_2PY5Me_2 producing the lowest potential oxidation and the most electron withdrawing derivative CF_3PY5Me_2 exhibiting the highest. This trend held for the pH range of 7-11, and the Pourbaix diagram generated for the $Co^{3+/2+}$ couple in this pH range indicated that PCET occurred as well. However, no clear trends were observed in regard to the second anodic feature, which occurred at the onset of catalytic current. To better understand this system, controlled potential electrolysis experiments were performed on the parent cobalt complex **5** to evaluate catalyst performance over an extended period of time. These experiments revealed that, at the potentials required to observe water oxidation, **5** decomposed and in the process generated a catalytically active deposit on the electrode surface. Due to the presence of this catalytically active side product, quantifying the efficiency and amount of O_2 generated specifically by **5** became impossible. Due in part to this development as well as to the conclusion that **5** was prone to decomposition under catalytically active conditions, the family of cobalt complexes bearing $PY5Me_2$ ligands was deemed unsuitable for water oxidation and no further studies were undertaken.

While the iron complex **7** has been synthesized and structurally characterized, electrochemical evaluation of any water oxidation ability has yet to be performed. While it is not fair to dismiss this complex based solely on the performance of its cobalt and ruthenium counterparts, the likelihood of this complex proving successful is called into question by recent

literature. To date, all molecular iron complexes capable of water oxidation possess either tetradentate ligands that allow for *cis* coordination sites for water or anionic ligand systems.[5] The single example of an iron complex possessing a neutral, pentadentate ligand (1-(di(pyridin-2-yl)methyl)-4,7-dimethyl-1,4,7-triazonane, $^{Me}PY_2CH$-tacn) that has been screened for water oxidation exhibited no catalytic activity.[53] Thus moving forward, rather than focusing on the $PY5Me_2$ systems, it would likely be more beneficial to test alternative ligand systems or develop new ones that can facilitate the formation of the high-valent metal centers that water oxidation demands, specifically scaffolds that remain resistant to oxidative decomposition and posses anionic donors. In addition to evaluating these new systems for water oxidation in aqueous media, they could also be screened for catalytic activity in regard to other oxidation reactions such as C–H activation of organic substrates.

Section 2.6 Acknowledgements

This research was supported by the National Science Foundation through Graduate Research Fellowship Grant No. DGE-1106400. The author thanks Dr. Antonio DiPasquale (supported by NIH Shared Instrumentation Grant S10-RR027172) for crystallographic assistance; Prof. Xavier Sala and Dr. Joan Aguiló for helpful discussion in regard to ruthenium water oxidation chemistry and for collecting the manometry and corresponding mass spectrometry data; Dr. Derek J. Wasylenko, Prof. Curtis P. Berlinguette, and Prof. Yogesh Surendranath for direction and helpful discussion in regard to the cobalt electrochemical experiments.

Section 2.7 References

(1) Conti, J. J. *International Energy Outlook 2016*; DOE/EIA-0484(2016); Energy Information Administration: Washington, DC, 2016.
(2) Lewis, N. S.; Nocera, D. G. *PNAS* **2006**, *103*, 15729–15735.
(3) Barber, J.; Tran, P. D. *J. R. Soc. Interface* **2013**, *10*, 20120984.
(4) Umena, Y.; Kawakami, K.; Shen, J.-R.; Kamiya, N. *Nature* **2011**, *473*, 55–60.
(5) Kärkäs, M. D.; Verho, O.; Johnston, E. V.; Åkermark, B. *Chem. Rev.* **2014**, *114*, 11863–12001.
(6) Berardi, S.; Drouet, S.; Francàs, L.; Gimbert-Suriñach, C.; Guttentag, M.; Richmond, C.; Stoll, T.; Llobet, A. *Chem. Soc. Rev.* **2014**, *43*, 7501–7519.
(7) Blakemore, J. D.; Crabtree, R. H.; Brudvig, G. W. *Chem. Rev.* **2015**, *115*, 12974–13005.
(8) Kim, J. H.; Nemson, J. A.; Melis, A. *Plant Physiol.* **1993**, *103*, 181–189.
(9) Melis, A. *Trends Plant Sci.* **1999**, *4*, 130–135.
(10) Liu, F.; Concepcion, J. J.; Jurss, J. W.; Cardolaccia, T.; Templeton, J. L.; Meyer, T. J. *Inorg. Chem.* **2008**, *47*, 1727–1752.
(11) Gersten, S. W.; Samuels, G. J.; Meyer, T. J. *J. Am. Chem. Soc.* **1982**, *104*, 4029–4030.
(12) Yin, Q.; Tan, J. M.; Besson, C.; Geletii, Y. V.; Musaev, D. G.; Kuznetsov, A. E.; Luo, Z.; Hardcastle, K. I.; Hill, C. L. *Science* **2010**, *328*, 342–345.
(13) Schley, N. D.; Blakemore, J. D.; Subbaiyan, N. K.; Incarvito, C. D.; D'Souza, F.; Crabtree, R. H.; Brudvig, G. W. *J. Am. Chem. Soc.* **2011**, *133*, 10473–10481.
(14) Duan, L.; Araujo, C. M.; Ahlquist, M. S. G.; Sun, L. *PNAS* **2012**, *109*, 15584–15588.
(15) Hong, D.; Mandal, S.; Yamada, Y.; Lee, Y.-M.; Nam, W.; Llobet, A.; Fukuzumi, S. *Inorg. Chem.* **2013**, *52*, 9522–9531.

(16) Freedman, D. E.; Jenkins, D. M.; Iavarone, A. T.; Long, J. R. *J. Am. Chem. Soc.* **2008**, *130*, 2884–2885.
(17) Bechlars, B.; D'Alessandro, D. M.; Jenkins, D. M.; Iavarone, A. T.; Glover, S. D.; Kubiak, C. P.; Long, J. R. *Nat. Chem.* **2010**, *2*, 362–368.
(18) Zadrozny, J. M.; Freedman, D. E.; Jenkins, D. M.; Harris, T. D.; Iavarone, A. T.; Mathonière, C.; Clérac, R.; Long, J. R. *Inorg. Chem.* **2010**, *49*, 8886–8896.
(19) Karunadasa, H. I.; Chang, C. J.; Long, J. R. *Nature* **2010**, *464*, 1329–1333.
(20) Sun, Y.; Bigi, J. P.; Piro, N. A.; Tang, M. L.; Long, J. R.; Chang, C. J. *J. Am. Chem. Soc.* **2011**, *133*, 9212–9215.
(21) Karunadasa, H. I.; Montalvo, E.; Sun, Y.; Majda, M.; Long, J. R.; Chang, C. J. *Science* **2012**, *335*, 698–702.
(22) Thoi, V. S.; Sun, Y.; Long, J. R.; Chang, C. J. *Chem. Soc. Rev.* **2013**, *42*, 2388–2400.
(23) Zee, D. Z.; Chantarojsiri, T.; Long, J. R.; Chang, C. J. *Acc. Chem. Res.* **2015**, *48*, 2027–2036.
(24) Metalprices.com. https://www.metalprices.com (accessed Jun 30, 2016).
(25) Pure Iron Price. Alibaba.com. https://www.alibaba.com (accessed Jun 26, 2016).
(26) Wasylenko, D. J.; Ganesamoorthy, C.; Borau-Garcia, J.; Berlinguette, C. P. *Chem. Commun.* **2011**, *47*, 4249–4251.
(27) Wasylenko, D. J.; Palmer, R. D.; Schott, E.; Berlinguette, C. P. *Chem. Commun.* **2012**, *48*, 2107–2109.
(28) Goldsmith, C. R.; Jonas, R. T.; Cole, A. P.; Stack, T. D. P. *Inorg. Chem.* **2002**, *41*, 4642–4652.
(29) Goldsmith, C. R.; Jonas, R. T.; Stack, T. D. P. *J. Am. Chem. Soc.* **2002**, *124*, 83–96.
(30) This project was undertaken in 2011-2012. In 2014, Zhang and co-workers (ref. 31) demonstrated O_2 evolution from a macrocyclic nickel complex that had previously been reported to generate H_2 from water.
(31) Zhang, M.; Zhang, M.-T.; Hou, C.; Ke, Z.-F.; Lu, T.-B. *Angew. Chem. Int. Ed.* **2014**, *53*, 13042–13048.
(32) Bruker. APEX2, Bruker AXS Inc., Madison, Wisconsin, USA, 2007.
(33) Sheldrick, G. M. *SADABS*, Bruker AXS Inc., University of Göttingen, Germany, 1996.
(34) Sheldrick, G. M. *Acta Crystallogr., Sect. A* **2008**, *64*, 112–122.
(35) Burla, M. C.; Caliandro, R.; Camalli, M.; Carrozzini, B.; Cascarano, G. L.; De Caro, L.; Giacovazzo, C.; Polidori, G.; Spagna, R. *J. Appl. Crystallogr.* **2005**, *38*, 381–388.
(36) van der Sluis, P.; Spek, A. L. *Acta Crystallogr., Sect. A* **1990**, *46*, 194–201.
(37) Dolomanov, O. V.; Bourhis, L. J.; Gildea, R. J.; Howard, J. A. K.; Puschmann, H. *J. Appl. Crystallogr.* **2009**, *42*, 339–341.
(38) Lee, J.; Chang, H.; Kim, S.; Bang, G. S.; Lee, H. *Angew. Chem. Int. Ed.* **2009**, *48*, 8501–8504.
(39) Ohzu, S.; Ishizuka, T.; Kotani, H.; Kojima, T. *Chem. Commun.* **2014**, *50*, 15018–15021.
(40) Gil-Sepulcre, M.; Axelson, J. C.; Aguiló, J.; Solà, L.; Francàs, L.; Gil-Moreno, S.; Poater, A.; Blancafort, L.; Benet-Buchholz, J.; Guirado, G.; Escriche, L.; Llobet, A.; Bofill, R.; Sala, X. Manuscript under review.
(41) Zong, R.; Thummel, R. P. *J. Am. Chem. Soc.* **2005**, *127*, 12802–12803.
(42) Duan, L.; Fischer, A.; Xu, Y.; Sun, L. *J. Am. Chem. Soc.* **2009**, *131*, 10397–10399.
(43) Yagi, M.; Tajima, S.; Komi, M.; Yamazaki, H. *Dalton Trans.* **2011**, *40*, 3802–3804.

(44) Bard, A. J.; Faulkner, L. R. *Electrochemical Methods: Fundamentals and Applications*, 2nd ed.; John Wiley & Sons, Inc.: New York, 2001.
(45) Gagliardi, C. J.; Westlake, B. C.; Kent, C. A.; Paul, J. J.; Papanikolas, J. M.; Meyer, T. J. *Coord. Chem. Rev.* **2010**, *254*, 2459–2471.
(46) Gagliardi, C. J.; Vannucci, A. K.; Concepcion, J. J.; Chen, Z.; Meyer, T. J. *Energy Environ. Sci.* **2012**, *5*, 7704–7717.
(47) Takeuchi, K. J.; Thompson, M. S.; Pipes, D. W.; Meyer, T. J. *Inorg. Chem.* **1984**, *23*, 1845–1851.
(48) Concepcion, J. J.; Jurss, J. W.; Norris, M. R.; Chen, Z.; Templeton, J. L.; Meyer, T. J. *Inorg. Chem.* **2010**, *49*, 1277–1279.
(49) Chen, Z.; Concepcion, J. J.; Meyer, T. J. *Dalton Trans.* **2011**, *40*, 3789–3792.
(50) Roeser, S.; Farràs, P.; Bozoglian, F.; Martínez-Belmonte, M.; Benet-Buchholz, J.; Llobet, A. *ChemSusChem* **2011**, *4*, 197–207.
(51) Jeon, I.-R.; Park, J. G.; Haney, C. R.; Harris, T. D. *Chem. Sci.* **2014**, *5*, 2461–2465.
(52) Kanan, M. W.; Nocera, D. G. *Science* **2008**, *321*, 1072–1075.
(53) Fillol, J. L.; Codolà, Z.; Garcia-Bosch, I.; Gómez, L.; Pla, J. J.; Costas, M. *Nat. Chem.* **2011**, *3*, 807–813.

Section 2.8 Supporting Information

Table S2.1. Unit cell data and select bond lengths (Å) and angles (deg) for crystal structures of **1**, **2**, **3**, **4**, and **5a**.

Complex	**1**Cl	**2**$(CF_3SO_3)_2$	**3**$(CF_3SO_3)_2$	**4**$(CF_3SO_3)_2$	**5a**$(CF_3SO_3)_2$
Empirical Formula[a]	$C_{33}H_{41}Cl_2N_5O_4Ru$	$C_{37}H_{34}F_6N_8O_6RuS_2$	$C_{31}H_{27}F_6N_5O_7RuS_2$	$C_{31}H_{27}F_6FeN_5O_7S_2$	$C_{31}H_{26}CoF_6N_5O_7S_2$
Molecular Weight	743.68	965.91	860.77	815.55	817.62
Crystal System	Orthorhombic	Monoclinic	Triclinic	Triclinic	Triclinic
Space Group	*Pnma*	$P2_1/n$	$P\bar{1}$	$P\bar{1}$	$P\bar{1}$
a, Å	15.790(4)	12.4865(13)	11.0219(3)	11.0082(4)	8.7447(7)
b, Å	13.929(4)	15.8119(17)	12.5423(4)	12.4193(4)	14.1512(11)
c, Å	14.981(4)	20.111(2)	13.0793(4)	13.0650(4)	16.3199(13)
α, deg	90	90	82.2640(10)	82.5050(10)	102.2360(10)
β, deg	90	90.770(5)	88.6300(10)	88.4860(10)	102.0880(10)
γ, deg	90	90	66.3630(10)	66.2820(10)	104.9800(10)
Volume, Å^3	3294.8(15)	3970.2(7)	1640.42(9)	1620.66(9)	1830.4(3)
Z	4	4	2	2	2
M–N_1[b]	2.070(3)	2.0794(17)	2.0846(14)	1.9908(19)	1.9777(15)
M–N_2	2.070(3)	2.0803(17)	2.0624(14)	2.0159(18)	1.9747(15)
M–$N_{3,ax}$	2.018(5)	2.0271(16)	2.0008(14)	1.9538(18)	1.9795(15)
M–N_4	2.074(3)	2.0862(16)	2.0688(14)	1.9962(19)	1.9634(15)
M–N_5	2.074(3)	2.0704(17)	2.0699(14)	2.0038(18)	1.9665(15)
M–N_{avg}	2.0612(3)	2.06868(17)	2.0573(14)	1.9921(18)	1.97236(15)
M–X[c]	2.4082(15)	2.0391(18)	2.1228(13)	1.9916(17)	1.8525(12)
N_1–M–N_4	177.52(13)	177.18(7)	177.80(6)	178.38(7)	176.95(6)
N_2–M–N_5	177.52(13)	176.64(7)	177.94(6)	178.55(8)	177.38(6)
X–M–$N_{3,ax}$	179.86(14)	177.56(7)	178.13(5)	179.01(8)	179.48(6)
PY-tilt[d]	90.000(6)	96.483(8)	92.957(1)	93.330(1)	90.698(2)
OOP[e]	0.0462(1)	0.0509(8)	0.0259(7)	0.0022(10)	0.0086(1)

[a] Empirical formulas include outer sphere solvent molecules, with the exception of **5a**, in which case the solvent molecules were disordered to the extent that they could not be modeled and so were removed using SQUEEZE. [b] Numbering schemes can be found in Figure S2.1. [c] X represents the exogenous ligand: Cl in **1**, MeCN in **2**, H_2O in **3** and **4,** and OH in **5a**. [d] The PY-tilt is defined as the angle between the least squares planes generated by the four equatorial pyridine donors and the atoms of the axial pyridine ring and was calculated using Olex. [e] The out-of-plane (OOP) distortion is defined as the displacement of the metal center from the least-squares plane generated by the four equatorial pyridine atoms and was calculated using Olex.

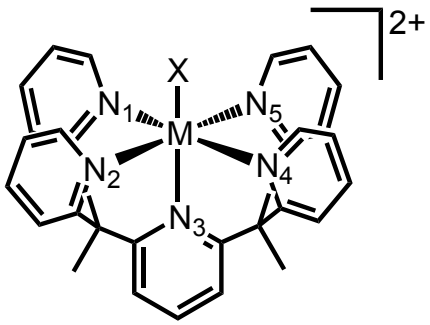


Figure S2.1. Numbering scheme used to describe the single crystal X-ray structures of the $PY5Me_2$ complexes.

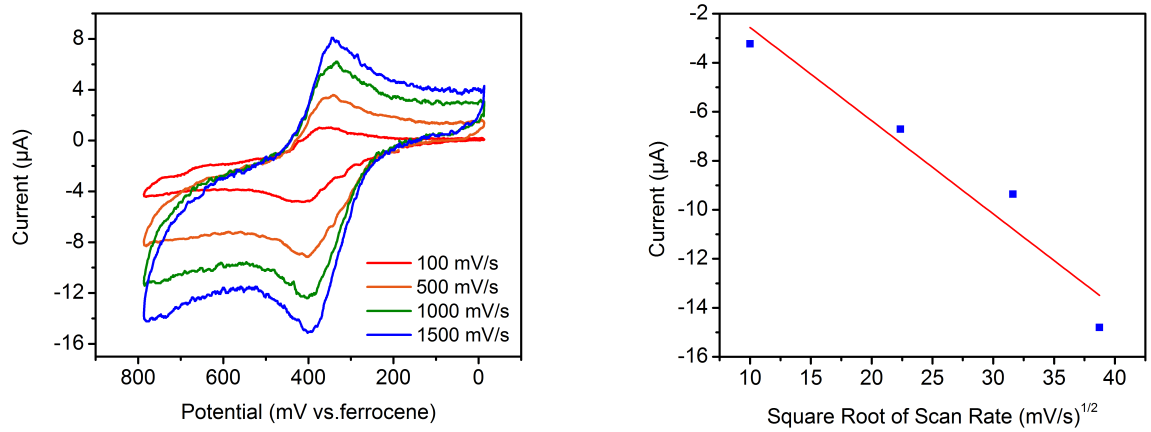


Figure S2.2. $Ru^{3+/2+}$ couple of **1** at different scan rates in acetonitrile (left). Concentration of **1**, 1.6 mM; electrode, platinum; electrolyte, 0.1 M tetrabutylammonium hexafluorophosphate. Dependence of $i_{f,p}$ on the square root of the scan rate (right).

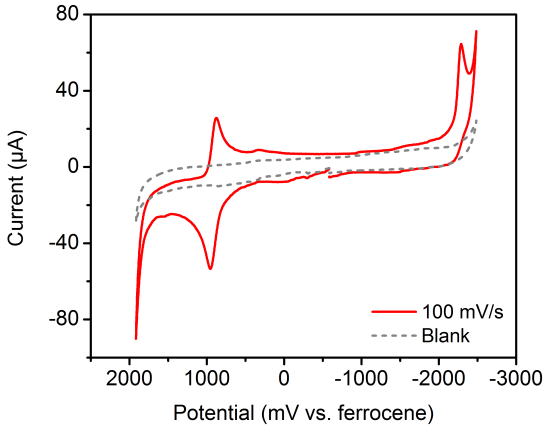


Figure S2.3. Cyclic voltammogram of **2** in acetonitrile at 100 mV/s. Concentration of **2**, 1.7 mM; electrode, glassy carbon; electrolyte, 0.1 M tetrabutylammonium hexafluorophosphate.

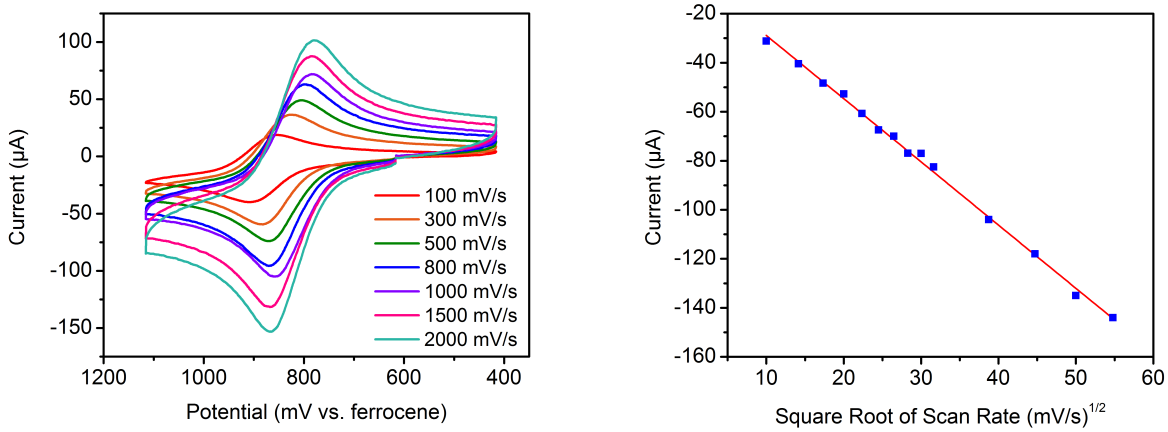


Figure S2.4. $Ru^{3+/2+}$ couple of **2** at different scan rates in acetonitrile (left). Concentration of **2**, 1.7 mM; electrode, glassy carbon; electrolyte, 0.1 M tetrabutylammonium hexafluorophosphate. Dependence of $i_{f,p}$ on the square root of the scan rate (right).

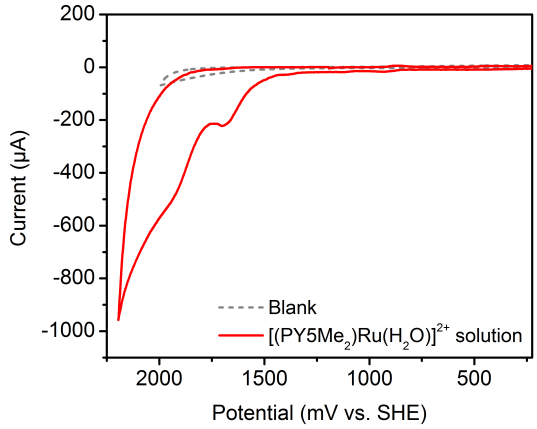


Figure S2.5. Cyclic voltammogram of **3** in pH 1 aqueous solution at 100 mV/s. Concentration of **3**, 0.4 mM; electrode, glassy carbon; electrolyte, 0.1 M HNO_3.

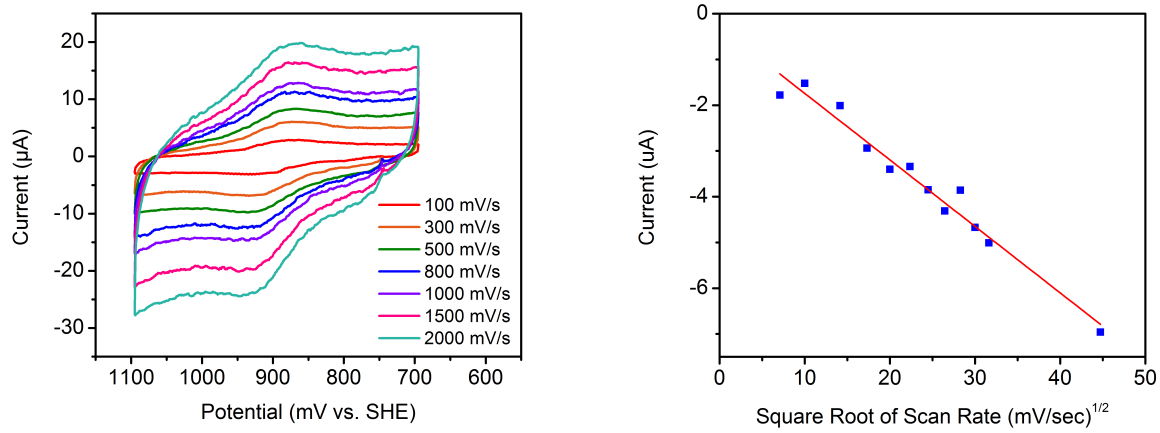


Figure S2.6. $Ru^{3+/2+}$ couple of **3** at different scan rates in pH 1 aqueous solution at 100 mV/s (left). Concentration of **3**, 0.4 mM; electrode, glassy carbon; electrolyte, 0.1 M HNO_3. Dependence of $i_{f,p}$ on the square root of the scan rate (right).

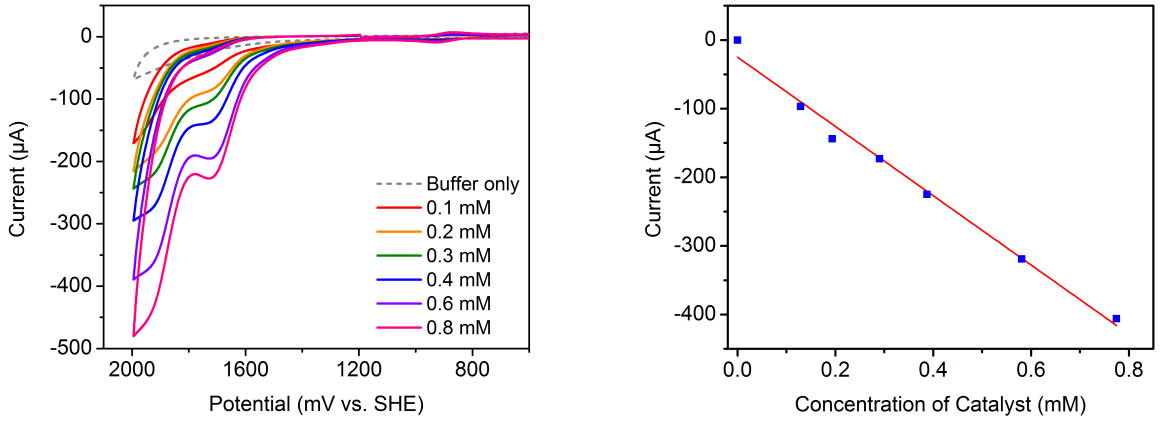


Figure S2.7. Current dependence on the concentration of **3** in solution at a scan rate of 100 mV/s. Electrode, glassy carbon; electrolyte, 0.1 M HNO_3.

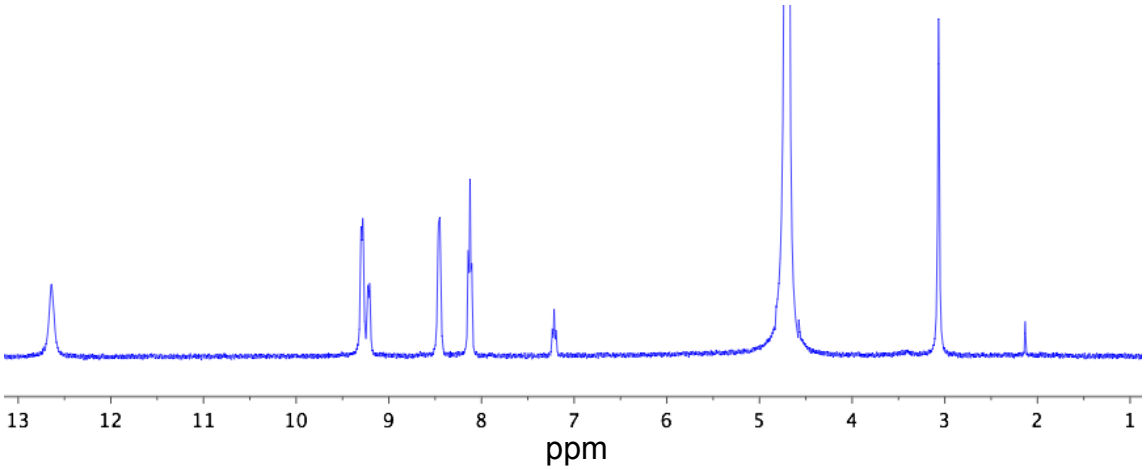


Figure S2.8. ^{1}H NMR spectrum of **6** at room temperature in deuterium oxide.

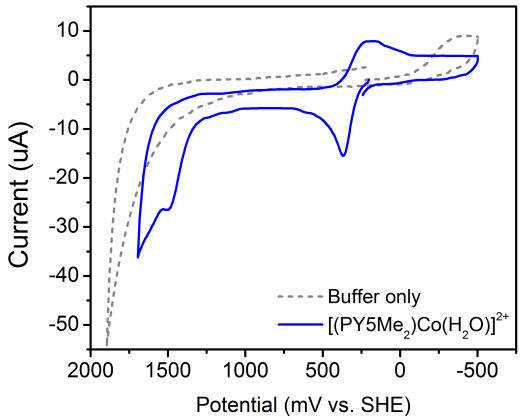


Figure S2.9. Cyclic voltammogram of **5** in pH 7 aqueous solution at 100 mV/s. Concentration of **5**, 1 mM; electrode, glassy carbon; electrolyte, 0.1 M phosphate buffer.

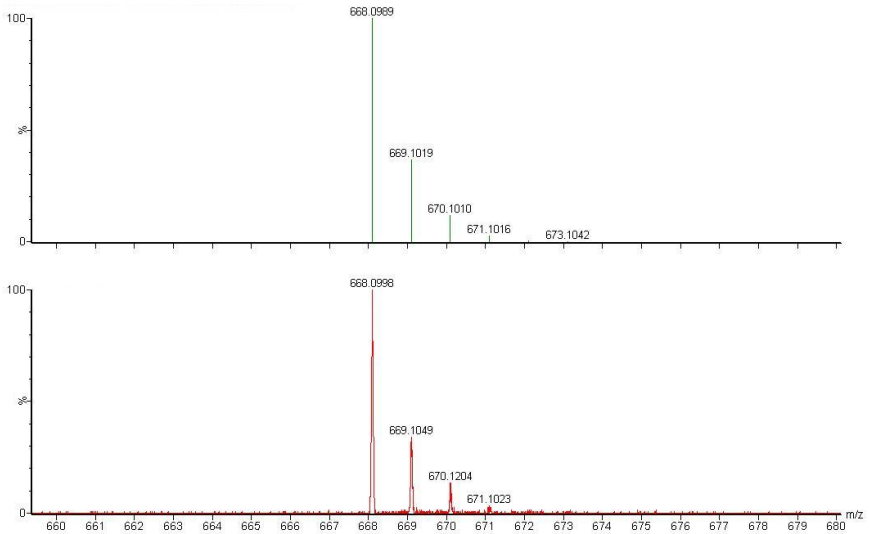


Figure S2.10. Mass spectrum of **5a** (red) with the isotope model for $C_{30}H_{26}N_5CoO_4SF_3$ (green), which corresponds to $\{[(PY5Me_2)Co(OH)](O_3SCF_3)\}^+$, 668.1.

Chapter Three

Synthesis and Characterization of a Tetrapodal NO_4^{4-} Ligand and Its Transition Metal Complexes and Synthetic Efforts toward a N_4C^- Tetrapodal Ligand

"The chemists are a strange class of mortals, impelled by an almost insane impulse to seek their pleasures amid smoke and vapor, soot and flame, poisons and poverty; yet among all these evils I seem to live so sweetly that may I die if I were to change places with the Persian king."

- Johann Joachim Becher

Section 3.1 Introduction

Tetrapodal pentadentate ligands are chelators that form square pyramidal coordination caps when bound to a single metal ion.[1] Complexes incorporating these ligands have been studied in a wide variety of applications, for example as hydrogen evolution catalysts,[2] water oxidation catalysts,[3] enzyme mimics,[4,5] redox mediators in dye-sensitized solar cells,[6] and metal cluster systems exhibiting slow magnetic relaxation.[7] In addition to their unique versatility, tetrapodal ligands are advantageous due to their ability to restrict substrate access to a single open coordination site on the metal center and to form discrete, mononuclear complexes with well-defined coordination environments. Moreover, these ligands can afford enhanced stability through the chelate effect compared to their analogous mono- or bidentate counterparts, which is a desirable trait particularly for systems incorporating labile first-row transition metals.[8]

Recently, complexes of the neutral pentadentate ligand 2,6-bis[1,1-bis(2-pyridyl)ethyl]pyridine ($PY5Me_2$) and its derivatives have been extensively investigated in the areas of water reduction catalysis[2] and molecular magnetism.[7a,7c] The $PY5Me_2$ ligand exclusively contains pyridine donors, and indeed the vast majority of tetrapodal ligands in the literature contain neutral aliphatic or aromatic nitrogen donating groups. In contrast, very few tetrapodal scaffolds incorporate carbon-, phosphorus-, oxygen-, or sulfur-based donors, and scaffolds with anionic donors are especially uncommon.[1,9] Given that anionic donors have been shown to facilitate access to high-valent metal complexes,[5,10] a suitable anionic tetrapodal ligand could present an advantageous platform for generating and studying such reactive species. In particular, a primarily anionic oxygen-based environment could engender unique electronic configurations and interesting chemical reactivity due to the different donating capabilities of nitrogen and oxygen.[5,11]

Prior to this work, the only reported tetrapodal ligands exhibiting predominantly oxygen-based environments were the polyalcohols 2,2′-(pyridine-2,6-diyl)bis(2-methylpropane-1,3-diol) (PYO_4) and 2-(bis(hydroxymethyl)amino)-2-(hydroxymethyl)propane-1,3-diol (bis-tris). The crystal structures of PYO_4 found in the literature reveal that the ligand is fully protonated and bridges multiple Li^+ and Ba^{2+} perchlorate salts instead of binding to the cation in a κ^5 fashion.[12] While bis-tris has been shown to coordinate to transition metals as a pentadentate ligand, it only forms mononuclear complexes as a neutral or 2− ligand[13] and forms clusters when further deprotonated to bear a 3− or 4− charge.[14] We therefore sought to expand this small and unconventional contingent of tetrapodal ligand scaffolds by exploring an all-anionic equatorial oxygen environment.

Tetrapodal ligands containing carbon donors are also few in number. To date, the only scaffold in this category known to bind in a κ^5 fashion, 1,3-bis[bis(2-pyridyl)methyl]imidazole-2-ylidene (PY4Im), was synthesized by Smith and Long in 2010.[15] As an analogue of $PY5Me_2$, Figure 3.1 shows that PY4Im retains the equatorial ligand set but the axial pyridine is exchanged for an *N*-heterocyclic carbene (NHC) donor. Due to the addition of the strongly donating NHC component, PY4Im provides a strong ligand field that encourages low-spin electron configurations on the metal center and lowers the $M^{3+/2+}$ redox couples for the iron, cobalt, and nickel complexes by ~0.25 V compared to those of the corresponding $PY5Me_2$ complexes. Previously, the Long Group synthesized 2,6-bis[1,1-bis(2-pyridyl)ethyl]benzene ($PY4PhMe_2$), in which the axial pyridine of $PY5Me_2$ is replaced by a benzene ring, with the intention of generating a N_4C^- coordination environment via activation of the central C_{aryl}–H bond.[16] Despite attempting a variety of deprotonation conditions (NaH, potassium *tert*-butoxide, *n*-butyllithium,

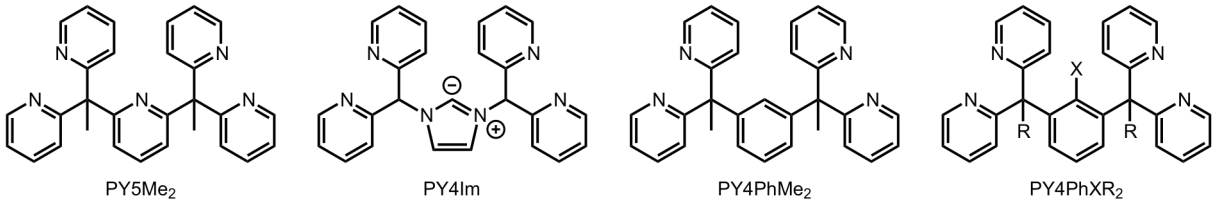


Figure 3.1. Evolution of tetrapodal synthetic targets from $PY5Me_2$ to ligands possessing carbon donor atoms. $PY5Me_2$ (left), PY4Im, $PY4PhMe_2$, and $PY4PhXR_2$ (right).

$KN(SiMe_3)_2$, and $PhCH_2K$), the proton could not be removed, and no species were found bound in a κ^5 fashion. In order to continue the pursuit of a new N_4C^- ligand and isolate the pentadendate target, alternative synthetic routes and targets must be explored.

Herein, we report the synthesis of the tetraanionic NO_4 ligand 2,2′-(pyridine-2,6-diyl)bis(2-methylmalonate) ($[PY(CO_2)_4]^{4-}$) via deprotection of the neutral ligand tetraethyl 2,2′-(pyridine-2,6-diyl)bis(2-methylmalonate) ($PY(CO_2Et)_4$). The reaction of $K_4[PY(CO_2)_4]$ with divalent first-row transition metals further affords the complexes $[(PY(CO_2)_4)M(H_2O)]^{2-}$ (M = Mn^{2+}, Fe^{2+}, Co^{2+}, Ni^{2+}, Zn^{2+}). Both $[PY(CO_2)_4]^{4-}$ and $PY(CO_2Et)_4$ represent novel additions to the tetrapodal ligand family, and to our knowledge $[PY(CO_2)_4]^{4-}$ is the first tetraanionic, tetrapodal ligand with an NO_4 donor set to successfully form mononuclear complexes with transition metals. We present the synthesis and characterization of the new ligands and comprehensive synthetic, structural, spectroscopic, and electrochemical characterization data for the metal complexes. In addition, multiple routes that have been attempted in order to access the new N_4C^- target $PY4PhXR_2$ will be described and the most promising directions for the project moving forward will be outlined.

Section 3.2 Experimental Section

General Information. Unless specified otherwise, all reactions and manipulations were performed under an inert atmosphere using a glovebox, glovebag, or Schlenk techniques. Dimethylformamide (DMF) and tetrahydrofuran (THF) were dried by passage over activated molecular sieves using a custom-built solvent purification system designed by JC Meyer Solvent Systems. Diethyl malonate, anhydrous 1,4-dioxane (Sigma-Aldrich), and other degassed solvents were purged with N_2 for 30-60 min prior to use. All other solvents and reagents were obtained from commercial vendors and utilized without further purification. Because determination of an effective route to $PY4PhXR_2$ is still underway, details for syntheses that have been attempted are reviewed in the Supporting Information rather than reported here.

Synthesis of Tetraethyl 2,2′-(Pyridine-2,6-diyl)bis(2-methylmalonate) ($PY(CO_2Et)_4$). An oven-dried Schlenk flask was charged with 2,6-dibromopyridine (14.6 g, 61.5 mmol), CuI (2.34 g, 12.3 mmol), picolinic acid (3.03 g, 24.6 mmol), Cs_2CO_3 (120 g, 270 mmol), diethyl malonate (40.0 mL, 262 mmol), and 300 mL of anhydrous 1,4-dioxane. The reaction was heated to 80 °C for 14 h. Once cooled, the reaction was quenched with 200 mL of water and extracted four times with 200 mL of ethyl acetate. The organic portions were combined, washed with brine, dried with $MgSO_4$, and concentrated via rotary evaporation to give a yellow oil. The crude product was purified by flash chromatography on silica (3:1 hexanes/ethyl acetate), after which a small amount of side product still remained that could not be removed through additional purification efforts. A ^1H NMR spectrum suggested the mixture to be approximately 5:1

tetraethyl 2,2′-(pyridine-2,6-diyl)dimalonate to impurity (Figure S3.6). Because this impurity did not substantially impede the synthesis or yield of the desired ligand (see below), the yellow oil obtained from chromatography was dried under reduced pressure and used without further purification in subsequent manipulations. R_f 0.31 (3:1 hexanes/ethyl acetate, UV). ^{1}H NMR ($CDCl_3$, 400 MHz): δ 7.74 (t, J = 7.8 Hz, 1H), 7.48 (d, J = 7.8 Hz, 2H), 4.91 (s, 2H), 4.23 (m, 8H), 1.26 (t, J = 7.1, 12H).

An oven-dried Schlenk flask was charged with the yellow oil containing tetraethyl 2,2′-(pyridine-2,6-diyl)dimalonate (19.1 g), K_2CO_3 (33.3 g, 241 mmol), methyl iodide (19.5 mL, 313 mmol), and 250 mL of anhydrous DMF, and the mixture was left to stir at room temperature under N_2 for 24 h. Subsequently, the flask was cooled to 0 °C in an ice bath, and the reaction was quenched with 200 mL of water followed by 200 mL of Et_2O. The organic layer was isolated, and the aqueous layer was extracted three times with 100 mL of Et_2O. The organic portions were combined and washed with 150 mL of concentrated Na_2SO_3 followed by 150 mL of brine. After drying with $MgSO_4$, the solution was concentrated to an oily, yellow solid. The crude product was dissolved in a minimal amount of dichloromethane, layered with hexanes, and stored overnight in a −20 °C freezer. Colorless crystals of $PY(CO_2Et)_4$ were isolated by vacuum filtration in a 62% yield (16.1 g) with respect to 2,6-dibromopyridine. ^{1}H NMR ($CDCl_3$, 400 MHz): δ 7.63 (t, J = 7.9 Hz, 1H), 7.35 (d, J = 7.9 Hz, 2H), 4.24−4.12 (m, 8H), 1.78 (s, 6H), 1.19 (t, J = 7.1 Hz, 12H). ^{13}C NMR ($CDCl_3$, 400 MHz): δ 170.7, 156.9, 136.5, 121.4, 61.7, 61.6, 22.3, 14.0. IR (neat, cm^{-1}): 2979w, 2937w, 2904w, 2870w, 1758w, 1729s, 1585w, 1576w, 1460m, 1450m, 1387w, 1372m, 1282m, 1244s, 1223s, 1175m, 1161m, 1102s, 1020s, 997m, 953w, 927w, 861m, 823m, 759m, 740w, 713w, 647w, 611m, 515m, 471w. Anal. Calcd. for $C_{21}H_{29}NO_8$: C, 59.56; H, 6.90; N, 3.31%. Found: C, 59.42; H, 6.78; N, 3.55%.

Synthesis of [(PY(CO$_2$Et)$_4$)Cu(THF)](CF$_3$SO$_3$)$_2$. Solid portions of $Cu(CF_3SO_3)_2$ (71.0 mg, 0.196 mmol) and $PY(CO_2Et)_4$ (82.7 mg, 0.195 mmol) were weighed into separate 20-mL vials, and 1.5 mL of THF were added to each vial. Once the $PY(CO_2Et)_4$ had dissolved, the two solutions were combined and heated to 60 °C for 2 h in order to dissolve all reagents. The vial was then left to stir at ambient temperature overnight. Any remaining particulate was removed by vacuum filtration, and the filtrate was concentrated. Blue crystals (96.0 mg, 57% yield) suitable for X-ray analysis were obtained by slow diffusion of ether into the concentrated THF solution at room temperature over 2 d. IR (neat, cm^{-1}): 2984w, 2941w, 2903w, 1692s, 1640m, 1598w, 1460w, 1414w, 1372m, 1325m, 1262s, 1222s, 1182w, 1149s, 1112m, 1091w, 1067w, 1031s, 1010s, 932m, 912m, 864s, 819w, 790w, 753w, 637s, 570s, 516s, 478w, 469w, 461w, 455w. Anal. Calcd. for $C_{27}H_{37}CuF_6NO_{15}S_2$: C, 37.83; H, 4.35; N, 1.63%. Found: C, 37.61; H, 4.34; N, 1.90%.

Synthesis of 2,2′-(Pyridine-2,6-diyl)bis(2-methylmalonate) salts (A$_4$[PY(CO$_2$)$_4$], A = Li$^+$, Na$^+$, K$^+$, Cs$^+$). In air, $PY(CO_2Et)_4$ (120 mg, 0.28 mmol) was dissolved in 13 mL of methanol and cooled to 0 °C. Five equivalents of AOH (A = Li$^+$, Na$^+$, K$^+$, Cs$^+$) in deionized water (1.5 mL of a 0.95 M stock solution) were subsequently added dropwise to the methanol solution. After stirring for 6 h, the reaction solution was purged with N_2 to evaporate the solvent, all the while ensuring that the temperature remained at or below 0 °C. Although a small amount of side product was observed via ^{1}H NMR spectroscopy (Figure S3.7), the crude product was used without further purification in the synthesis of the metal complexes. Due to the extra equivalent of unreacted AOH, the isolated white solid was treated as $A_4[PY(CO_2)_4]\cdot AOH$ for stoichiometric purposes in the synthesis of the complexes. ^{1}H NMR (D_2O, 400 MHz): δ 7.62 (t, J = 7.9 Hz, 1H), 7.26 (d, J = 7.9 Hz, 2H), 1.72 (s, 6H). ^{13}C NMR (D_2O, 400 MHz): δ 181.4, 161.2, 136.7, 120.4, 66.8, 23.2.

IR (neat, cm^{-1}): 3349m, 3283m, 2977w, 2945w, 1677w, 1560s, 1451m, 1414m, 1392m, 1326s, 1171w, 1135w, 1100w, 1081w, 994w, 986w, 932w, 901w, 821m, 792w, 762w, 749m, 691m, 641m, 618s, 532s.

General Synthesis of $K_2[(PY(CO_2)_4)M(H_2O)]$ Complexes. In air, a 20-mL vial was charged with the crude $K_4[PY(CO_2)_4]\cdot KOH$ (200-400 mg) and one equivalent of divalent metal chloride ($ZnCl_2$) or divalent metal chloride hydrate ($MnCl_2\cdot 4H_2O$, $FeCl_2\cdot 4H_2O$, $CoCl_2\cdot 6H_2O$, $NiCl_2\cdot 6H_2O$,). The vial was topped with a rubber septum and purged with N_2 for 30 min before 5-10 mL of degassed, deionized water were added to the vial via syringe. After the solution had stirred at room temperature for 30 min, the vial was transferred to an N_2-filled glovebag, and the solution was vacuum filtered. Subsequently, 40-80 mL of degassed acetone were added to the filtrate in order to precipitate the product. The solids were isolated by vacuum filtration, dissolved in a minimal amount of water, and recrystallized by diffusion of acetone into the aqueous solution, which produced block crystals suitable for X-ray analysis. Note that the synthesis and handling of the Ni^{2+} and Zn^{2+} complexes can be performed entirely in air. Lower yields for the Mn^{2+} and Fe^{2+} complexes were attributed to their air sensitivity. Yields given below were calculated based on the initial amount of metal chloride salt employed. Special considerations for each complex are noted in their respective sections.

$K_2[(PY(CO_2)_4)Mn(H_2O)]$. Pale yellow solids (124 mg) were obtained in 42% yield. IR (neat, cm^{-1}): 3246w, 3017w, 2992w, 2950w, 1670w, 1612s, 1577s, 1568s, 1455m, 1435w, 1413m, 1390s, 1358s, 1299s, 1236m, 1221w, 1182w, 1157w, 1110w, 1078w, 1016w, 987w, 919w, 887s, 846m, 825m, 803w, 768s, 653s, 622s, 608s, 592m, 562m, 455w. μ_{eff}(Evans) = 5.6(2)μ_B. Anal. Calcd. for $C_{13}H_{11}K_2MnNO_9\cdot H_2O$: C, 32.78; H, 2.75; N, 2.94%. Found: C, 32.42; H, 2.54; N, 3.06%.

$K_2[(PY(CO_2)_4)Fe(H_2O)]$. All synthetic manipulations, including the recrystallization, were carried out using Schlenk line techniques. Cannula filtrations were performed instead of vacuum filtrations to obtain 85 mg of the yellow product in 30% yield. IR (neat, cm^{-1}): 3316w, 3016w, 2989w, 2948w, 1670w, 1615s, 1570s, 1456m, 1432m, 1388s, 1357s, 1296s, 1240m, 1227m, 1182m, 1159m, 1111w, 1078w, 1020w, 987w, 919m, 888s, 847m, 826m, 768s, 707m, 653m, 624s, 604s, 596s, 581s, 553s, 532m, 458m. μ_{eff}(Evans) = 4.9(1)μ_B. UV-vis-NIR (H_2O): λ_{max} (ε_M, M^{-1} cm^{-1}) 427 (170), 958 (4) nm. Anal. Calcd. for $C_{13}FeH_{11}K_2NO_9\cdot H_2O$: C, 32.71; H, 2.75; N, 2.93%. Found: C, 32.51; H, 2.52; N, 2.69%.

$K_2[(PY(CO_2)_4)Co(H_2O)]$. The pink solids were isolated prior to recrystallization and sonicated with 1-2 mL of methanol. Recrystallization afforded 131 mg of product in 59% yield. IR (neat, cm^{-1}): 3326m, 3016w, 2988w, 2948w, 1673w, 1616s, 1572s, 1458m, 1432m, 1419m, 1390s, 1359s, 1299s, 1244m, 1226m, 1185m, 1162m, 1111w, 1079w, 1026w, 988w, 920w, 887s, 849m, 824w, 769s, 713w, 654s, 629s, 608s, 552s, 466m, 457m. μ_{eff}(Evans) = 4.2(2)μ_B. UV-vis-NIR (H_2O): λ_{max} (ε_M, M^{-1} cm^{-1}) 465 (10), 495 (sh) (9), 525 (sh) (7), 1049 (8) nm. Anal. Calcd. for $C_{13}CoH_{11}K_2NO_9\cdot 0.5H_2O$: C, 33.13; H, 2.57; N, 2.97%. Found: C, 33.03; H, 2.35; N, 2.99%.

$Li_2[(PY(CO_2)_4)Ni(H_2O)]$. Purple solids (68 mg) were obtained in 23% yield. The low yield for this complex was attributed to poor conversion to the $Li_4[(PY(CO_2)_4]$ ligand based on the qualitative observation that more insoluble side products were removed during the first filtration step compared to the other analogues. IR (neat, cm^{-1}): 3601w, 3228w, 3025w, 3007w, 2960w, 1978w, 1638m, 1628m, 1571s, 1458m, 1429s, 1397s, 1364m, 1316s, 1248m, 1226w, 1187w, 1167w, 1081w, 1030w, 927w, 901m, 859m, 805w, 780m, 680m, 625m, 601s, 486s. UV-vis-NIR

(H_2O): λ_{max} (ε_M, M^{-1} cm^{-1}) 575 (4), 751 (3), 940 (19) nm. Anal. Calcd. for $C_{13}H_{11}Li_2NNiO_9 \cdot 2.5$ $H_2O \cdot 0.5$ LiCl: C, 33.65; H, 3.48; N, 3.02%. Found: C, 33.41; H, 3.17; N, 3.02%.

$Na_2[(PY(CO_2)_4)Ni(H_2O)]$. In order to remove residual NaCl, the purple solids were recrystallized a second time by slow evaporation of a concentrated aqueous solution of the complex over 2 d, resulting in 274 mg of purple crystals in 70% yield. IR (ATR, cm^{-1}) 3581w, 3418m, 3289m, 3097m, 3003m, 2961m, 2467w, 1591s, 1572s, 1459s, 1437s, 1383s, 1352s, 1312s, 1272s, 1247m, 1189m, 1167m, 1114w, 1079m, 1032m, 994w, 922m, 893s, 866s, 853s, 829s, 801m, 774s, 738m, 662s, 632s, 596s, 540s, 522s, 467s, 458s. UV-vis-NIR (H_2O): λ_{max} (ε_M, M^{-1} cm^{-1}) 575 (4), 751 (3), 940 (20) nm. Anal. Calcd. for $C_{13}H_{11}NNa_2NiO_9 \cdot 5.5H_2O$: C, 29.52; H, 4.19; 2.65%. Found: C, 29.69; H, 4.05; N, 2.56%.

$K_2[(PY(CO_2)_4)Ni(H_2O)]$. Purple solids were isolated prior to recrystallization and sonicated with 1-2 mL of methanol. Recrystallization afforded 170 mg of product in 63% yield. IR (neat, cm^{-1}): 3568w, 3099w, 2982w, 2948w, 2887w, 1618s, 1610s, 1589s, 1577s, 1571s, 1560s, 1535m, 1459m, 1425m, 1383s, 1362s, 1294s, 1281s, 1246s, 1187m, 1166m, 1118w, 1080m, 1030w, 987w, 923m, 892s, 847m, 834m, 809m, 770s, 739m, 716m, 669s, 633s, 601s, 530m, 517m, 470s. μ_{eff}(Evans) = 3.0(1)μ_B. UV-vis-NIR (H_2O): λ_{max} (ε_M, M^{-1} cm^{-1}) 577 (5), 751 (4), 940 (21) nm. Anal. Calcd. for $C_{13}H_{11}K_2NNiO_9 \cdot H_2O$: C, 32.52; H, 2.73; N, 2.92%. Found: C, 32.82; H, 2.46; N, 2.88%.

$Cs_2[(PY(CO_2)_4)Ni(H_2O)]$. The blue solids were isolated prior to recrystallization and sonicated with 1-2 mL of methanol. Recrystallization afforded 191 mg of product in 60% yield. IR (neat, cm^{-1}): 3142w, 3000w, 2991w, 2942w, 1619s, 1586s, 1575s, 1457m, 1446m, 1421m, 1348s, 1360s, 1290s, 1277s, 1246s, 1187m, 1165m, 1121w, 1079m, 1031w, 988w, 924m, 890s, 847m, 830m, 808w, 766s, 723m, 706m, 689m, 665s, 633s, 600s, 548w, 521w, 476w, 467w, 457w. UV-vis-NIR (H_2O): λ_{max} (ε_M, M^{-1} cm^{-1}) 575 (4), 751 (4), 939 (21) nm. Anal. Calcd. for $C_{13}H_{11}Cs_2NNiO_9$: C, 24.03; H, 1.71; N, 2.16%. Found: C, 23.94; H, 1.39; N, 2.04%.

$K_2[(PY(CO_2)_4)Zn(H_2O)]$. White solids were isolated prior to recrystallization and sonicated with 1-2 mL of methanol. Recrystallization afforded 43 mg of product in 32% yield. ^{1}H NMR (D_2O, 600 MHz): δ 7.91 (t, J = 8.1 Hz, 1H), 7.57 (d, J = 8.1 Hz, 2H), 1.82 (s, 6H). IR (neat, cm^{-1}): 3012w, 2983w, 2947w, 1636s, 1624s, 1617s, 1610s, 1577s, 1571s, 1560s, 1458m, 1430m, 1382s, 1355m, 1289s, 1258s, 1242s, 1185m, 1164m, 1117w, 1077m, 1023w, 988w, 921m, 892s, 844m, 830m, 803m, 768s, 738m, 674m, 664m, 627s, 599s, 591s, 526m, 510m, 481m, 465m. Anal. Calcd. for $C_{13}H_{11}K_2NO_9Zn \cdot 1.5H_2O$: C, 31.49; H, 2.85; N, 2.82%. Found: C, 31.34; H, 2.57; N, 2.73%.

Synthesis of $K_2[(PY(CO_2)_4)Co(OH)]$. In air, $K_2[(PY(CO_2)_4)Co(H_2O)]$ (54.0 mg, 0.115 mmol) was dissolved in 4.5 mL of deionized water and filtered to remove any remaining particulate. While stirring the solution at ambient temperature in a 20-mL vial, 0.3 mL of hydrogen peroxide (34-37% by mass) was slowly added dropwise over 1.5 min. The vial was left to stir uncapped for 24 h and the solution was then concentrated to 3 mL. Dark purple needles suitable for X-ray analysis were obtained by slow diffusion of acetone into the aqueous solution at room temperature over 3 d. The final product (46.9 mg, 85% yield) was collected by vacuum filtration, and the solids were washed three times with 1.5 mL of methanol. ^{1}H NMR (D_2O, 400 MHz) δ 8.30 (t, J = 8.1 Hz, 1H), 7.78 (d, J = 8.1 Hz, 2H), 1.83 (s, 6H). IR (neat, cm^{-1}): 3587w, 3094w, 2999w, 2952w, 1705m, 1666s, 1637s, 1589s, 1571s, 1465m, 1428w, 1386s, 1338m, 1312m, 1255m, 1198m, 1171m, 1115w, 1079w, 1044w, 992w, 923m, 897s, 804w, 783s, 741m, 717w, 705w, 675m, 655s, 608s, 568w, 549w, 540w, 521w, 503w, 486s, 455m. UV-vis-NIR

(H_2O): λ_{max} (ε_M, M^{-1} cm^{-1}) 374 (130), 541 (170) nm. Anal. Calcd. for $C_{13}H_{10}CoK_2NO_9 \cdot H_2O$: C, 32.57; H, 2.52; N, 2.92%. Found: C, 32.50; H, 2.50; N, 2.89%.

Physical Measurements. ^1H and ^{13}C NMR spectra were collected at room temperature (22-25 °C) on Bruker AV-600 MHz, AVB-400 MHz, or AVQ-400 MHz instruments and analyzed with MestReNova software (v8.0.2-11021, Mestrelab Research S.L.). All resonances were referenced to the residual solvent signals of $CDCl_3$ (^1H, 7.26 ppm; ^{13}C, 77.16 ppm) or D_2O (^1H, 4.80 ppm). The ^{13}C NMR spectrum of $[PY(CO_2)_4]^{4-}$ was referenced to $CDCl_3$ by dissolving $[PY(CO_2)_4]^{4-}$ in D_2O and inserting a 2-mm coaxial tube filled with $CDCl_3$ into the NMR tube. Evans method magnetic measurements[17] were performed using a solvent-standard mixture of 2% acetone in D_2O (v/v) at room temperature (22-25 °C). The μ_{eff} values were calculated by the simplified form recommended by Grant,[18] which excludes solvent correction, and are reported as the average of three samples measured. Diamagnetic contributions were accounted for using Pascal's constants.[19] A Cary 5000 UV-Vis-NIR spectrophotometer and Cary WinUV v3.0 software were used to obtain spectra of solution samples in water and diffuse reflectance spectra of solid samples mixed with poly(vinylidene fluoride). A Kubelka-Munk conversion was applied to the diffuse reflectance spectra. Infrared spectra were collected on a Perkin-Elmer Spectrum 400 FT-IR spectrometer using the attenuated total reflectance mode. C, H, and N elemental analyses were performed in the Microanalytical Laboratory of the University of California, Berkeley.

Electrochemical Measurements. Electrochemical measurements were made with a BioLogic SP-200 potentiostat using the EC-Lab® v10.37 software. Experiments were performed under an argon atmosphere in a single compartment cell using a glassy carbon working electrode, Ag/AgCl (3.0 M NaCl) reference electrode, and platinum wire counter electrode. An aqueous solution of 0.1 M $KClO_4$ was used as the electrolyte. The pH of the electrolyte solutions was adjusted using KOH and HCl. Between each scan, the working electrode was removed from solution and polished with 0.05 micron MicroPolish (CH Instruments, Inc.).

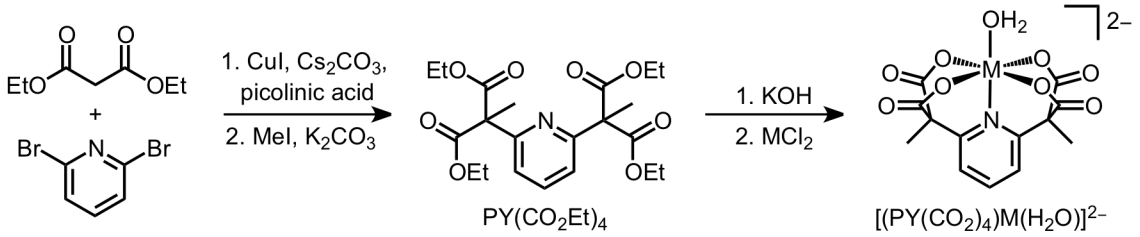
Crystallography. Crystallography was performed at the Small Molecule X-ray Crystallography Facility at the University of California, Berkeley, and the Advanced Light Source at Lawrence Berkeley National Laboratory. X-ray data was collected on single crystals coated with paratone oil and mounted on Kapton or MiTeGen loops. All data collections were performed at 100 K using a Bruker QUAZAR diffractometer equipped with a microfocus sealed X-ray source of Mo Kα (λ = 0.71073 Å) radiation and a Bruker APEX-II detector; a Bruker APEX diffractometer equipped with a fine-focus sealed X-ray source of Mo Kα (λ = 0.71073 Å) radiation and a Bruker APEX-I detector; or at Beamline 11.3.1 at the Advanced Light Source using synchrotron radiation with either a Bruker AXS APEX II CCD detector or a Bruker PHOTON100 CMOS detector on a Bruker D8 Diffractometer. Raw data were integrated and corrected for Lorentz and polarization effects using Bruker APEX2 V. 2011.4 software.[20] Absorption corrections were applied using SADABS [21] or TWINABS. [22] Space group assignments were determined by examination of systematic absences, E-statistics, and successive refinement of the structures. All structures were solved by direct methods using SHELXT.[23] Additional refinement was performed with SHELXL-2014/7[24] operated through the WinGX[25] and OLEX2[26] interfaces. Molecular graphics were generated with DIAMOND.[27] None of the crystals showed significant decay during data collection. Specific details concerning each data set can be found in the Supporting Information.

Section 3.3. Results and Discussion of $[PY(CO_2)_4]^{4-}$ and Its Complexes

In our design of a tetraanionic pentadentate scaffold, we targeted functional groups resistant to oxidative decomposition such as carboxylates and phenolates, as both could withstand the conditions required for the formation of high-valent metal complexes. Ultimately, we chose to focus on a carboxylate-based ligand, as it could be readily designed to retain a binding pocket analogous to that of $PY5Me_2$. However, while the addition of the peripheral pyridine rings during the synthesis of $PY5Me_2$ is well established and proceeds though a simple S_NAr reaction,[7c,28] the installation of equatorial carboxylate moieties is less straightforward.

Retrosynthetically, the most direct way to achieve oxygen donors at positions matching those of the pyridine nitrogen atoms in $PY5Me_2$ is to connect two malonate functional groups to the central pyridine. A review of potential routes revealed three methods most amenable to this aim: (i) activation of pyridine-N-oxide with the phosphonium salt PyBroP,[29] (ii) synthesis of a linear 1,5-dicarbonyl precursor with subsequent oxidation to a pyridine ring,[30] or (iii) a copper-catalyzed Ullman-type reaction with 2,6-dibromopyridine.[31] Although we were able to add a single malonate unit to pyridine-N-oxide with PyBroP, a second addition was not observed upon further reaction of the monosubstituted pyridine-N-oxide intermediate under the same conditions. Additionally, while we were able to isolate the linear precursor tetraethyl 2,6-dioxoheptane-1,1,7,7-tetracarboxylate, exposure of this molecule to the amine sources needed to close the ring (NH_3, NH_4OH, NH_4OAc, or NH_2OH) only resulted in decarboxylation of the diethyl malonate components, even at room temperature. Ultimately, we found the Ullman-type reaction to be the most successful, and requiring shorter reaction times than originally reported.[29]

Scheme 3.1. Synthesis of divalent transition metal complexes $[(PY(CO_2)_4)M(H_2O)]^{2-}$ (M = Mn^{2+}, Fe^{2+}, Co^{2+}, Ni^{2+}, Zn^{2+}).



Utilizing this latter strategy, the tetraester ligand $PY(CO_2Et)_4$ was generated via a two-step synthesis from 2,6-dibromopyridine (Scheme 1). In the first step, a copper catalyzed Ullman-type reaction substituted both bromine atoms on the pyridine with diethyl malonate units. Attempts were also made with diethyl methylmalonate, however no reaction was observed. The majority of unwanted side products were then removed from the crude oil via column chromatography. One impurity that could not be completely eliminated, however, was likely the asymmetric decomposition product formed by the loss of a single ester group (see the ^1H NMR spectrum of the chromatographed oil, Figure S3.6). In spite of this impurity, methylation at the tertiary carbon was performed successfully with methyl iodide and K_2CO_3 at room temperature under N_2 in anhydrous DMF. Pure $PY(CO_2Et)_4$ was isolated as a white solid in 62% yield (based on 2,6-dibromopyridine) after recrystallization from a dichloromethane solution layered with hexanes and stored at −20 °C overnight. The ester ligand is soluble in ethereal, halogenated, and polar organic solvents such as acetone and methanol, and can be stored indefinitely at room temperature.

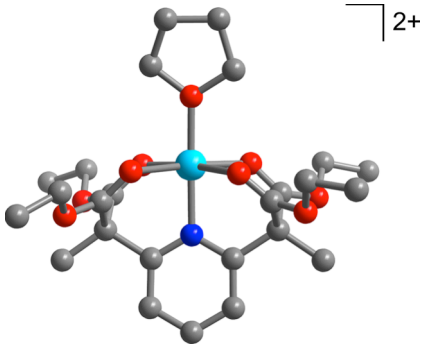


Figure 3.2. X-ray crystal structure of $[(PY(CO_2Et)_4)Cu(THF)]^{2+}$. Cyan, red, blue, and gray spheres represent Cu, O, N, and C, respectively; H atoms and counter ions were omitted for clarity.

Although not our final tetraanionic ligand target, we were interested in the possibility of isolating metal complexes based on the weakly-donating environment of $PY(CO_2Et)_4$. While air-free reactions of $PY(CO_2Et)_4$ with halide and triflate salts of Mn^{2+}, Fe^{2+}, Fe^{3+}, and Co^{2+} showed no reaction, the combination of $PY(CO_2Et)_4$ with one equivalent of $Cu(CF_3SO_3)_2$ under N_2 in anhydrous THF resulted in the formation of a blue solution. Diffusion of diethyl either into this solution at room temperature yielded pale blue crystals of $[(PY(CO_2Et)_4)Cu(THF)](CF_3SO_3)_2$. More coordinating solvents such as acetonitrile could not be used in recrystallization as they displaced the tetrapodal ligand from the metal center. A crystal structure determination confirmed that the ligand binds in a κ^5 fashion through the axial pyridine and the four carbonyls of the ester groups (Figure 3.2). A molecule of THF fills the open coordination site to yield a distorted octahedral coordination geometry, while two outer-sphere trifluoromethanesulfonate counteranions confirm the presence of divalent copper. Unlike most octahedral Cu^{2+} complexes, the distortion akin to a Jahn-Teller effect manifests as a compression along the z-axis of the molecule: the average bond length of the equatorial esters is 2.1137(15) Å while the $Cu–O_{THF}$ and $Cu–N_{PY}$ bond lengths are 1.9432(15) Å and 1.9895(16) Å, respectively. This axial compression and resultant destabilization of the d_z^2, d_{xz}, and d_{yz} orbitals is attributed to the stronger donor properties of the pyridyl nitrogen as compared to the weaker carbonyl oxygens of the esters.

Salts of the tetracarboxylate ligand $A_4[PY(CO_2)_4]$ ($A = Li^+$, Na^+, K^+, Cs^+) were synthesized via deprotection of the $PY(CO_2Et)_4$ ester groups with hydroxide in a mixture of 9:1 methanol to water at 0 °C. Compounds of the type $A_4[PY(CO_2)_4]$ could be obtained from reactions with LiOH, NaOH, KOH, or CsOH, while conversion attempts with $(NBu_4)OH$ were unsuccessful. A ^1H NMR spectrum of the product obtained via conversion with $(NBu_4)OH$ revealed the loss of two carboxylate moieties, thus suggesting that the alkali metal hydroxides are necessary for preservation of the ligand. The alkali metal salts of $[PY(CO_2)_4]^{4-}$ appear to be quite temperature sensitive, and significant decomposition could be observed in the ^1H NMR spectrum when the reaction was performed even at room temperature. This sensitivity is likely due to the propensity of malonate functional groups toward decarboxylation. However, it was found that $A_4[PY(CO_2)_4]$ salts could be reproducibly synthesized by maintaining a temperature at or below 0 °C throughout the reaction and during subsequent solvent removal. The purification of $A_4[PY(CO_2)_4]$ salts also proved challenging due to this temperature sensitivity. Consequently the as-synthesized material was combined immediately with one equivalent of divalent metal chloride in water to obtain the complex salts $K_2[(PY(CO_2)_4)M(H_2O)]$ ($M = Mn^{2+}$, Fe^{2+}, Co^{2+}, Ni^{2+}, Zn^{2+}).[32] Any impurities carried over from the ligand synthesis were subsequently removed

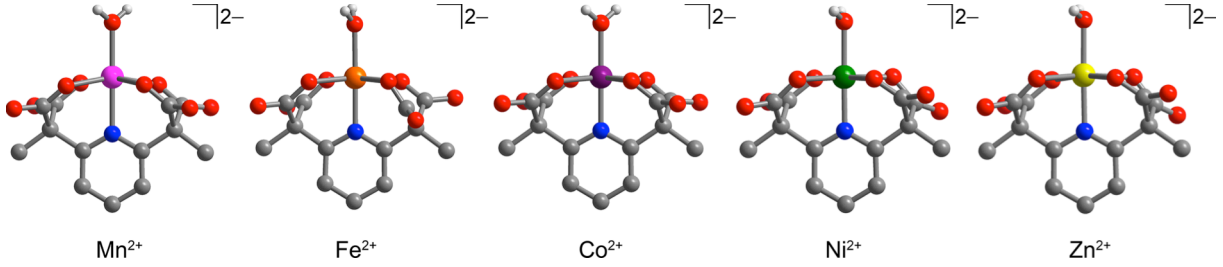


Figure 3.3. X-ray crystal structures of $[(PY(CO_2)_4)M(H_2O)]^{2-}$ complexes. Magenta, orange, purple, green, yellow, red, blue, gray, and light gray spheres represent Mn, Fe, Co, Ni, Zn, O, N, C, and H atoms, respectively. Water H atoms were identified from the electron density map. All other H atoms and counterions were omitted for clarity.

Table 3.1. Crystallographic data for $K_2[(PY(CO_2)_4)M(H_2O)]$ complexes with selected bond lengths (Å) and angles (deg).

M	Mn^{2+}	Fe^{2+}	Co^{2+}	Ni^{2+}	Zn^{2+}
Formula	$C_{13}H_{13}K_2MnNO_{10}$	$C_{13}H_{15}FeK_2NO_{11}$[a]	$C_{13}H_{13}CoK_2NO_{10}$	$C_{13}H_{15}K_2NNiO_{11}$[a]	$C_{13}H_{15}K_2NO_{11}Zn$[a]
Crystal System	Orthorhombic	Triclinic	Orthorhombic	Triclinic	Triclinic
Space Group	*Pnna*	$P\bar{1}$	*Pnna*	$P\bar{1}$	$P\bar{1}$
$M–O_{eq}$, Å[b]	2.1405(16)	2.0945(1)	2.0678(17)	2.0321(18)	2.0790(3)
$M–O_{water}$, Å	2.125(3)	2.1041(1)	2.070(3)	2.0645(18)	2.063(2)
$M–N_{PY}$, Å	2.210(3)	2.1247(1)	2.067(3)	2.011(2)	2.092(3)
$O_{ax}–M–N_{PY}$, deg	180	178.37(17)	180	178.89(8)	178.83(4)
PY-tilt, deg[c]	90	89.730(157)	90	88.195(68)	89.147(107)
OOP distortion, Å[d]	0.2924(12)	0.1377(16)	0.1330(12)	0.0515(9)	0.1195(11)

[a]Protons belonging to all water molecules are included in the chemical formula here, though they were omitted from the refinement of the data set. [b]Average of the four equatorial M–O distances. [c]The PY-tilt is defined as the angle between the least squares planes generated by the four equatorial oxygen donors and the atoms of the pyridine ring. [d]The out-of-plane (OOP) distortion is defined as the displacement of the metal center from the least-squares plane generated by the four equatorial oxygen atoms.

by filtration and recrystallization to give the pure metal complex. In the case of Ni^{2+} and Zn^{2+}, the metalation could be carried out at room temperature in air, and the resulting compounds are quite robust and can be stored indefinitely in air at room temperature. For Mn^{2+}, Fe^{2+}, and Co^{2+}, it was necessary to perform all reactions and subsequent manipulations under an inert atmosphere. The potassium salts of these complexes are soluble in water and completely insoluble in the organic solvents methanol, acetonitrile, and acetone. Aqueous UV-visible-NIR spectra for all the complexes exhibit low-ε intensity absorption bands consistent with Laporte-forbidden d-d transitions (Figure S3.9).

Diffusion of acetone into concentrated aqueous solutions of all the complexes resulted in block-shaped X-ray quality crystals, and the metrical data from diffraction studies are given in Table 3.1.[33] All of the complexes are isostructural and exhibit a distorted octahedral geometry arising from pentadentate coordination of $[PY(CO_2)_4]^{4-}$ and an axially-bound water molecule (Figure 3.3). For the paramagnetic ions, all metal-ligand bond distances are within the expected ranges for octahedral, high-spin complexes,[5,34] while magnetic moments determined using the Evans method[15-17] further support the high-spin assignments.[35] The metal-ligand distances decrease across the series from Mn^{2+} to Ni^{2+}, in accordance with the expected trend based on ionic radii, as does the extent to which the metal cation distorts out of the equatorial ligand plane. For example, the Mn^{2+} cation projects nearly 0.3 Å out of the binding pocket while the same

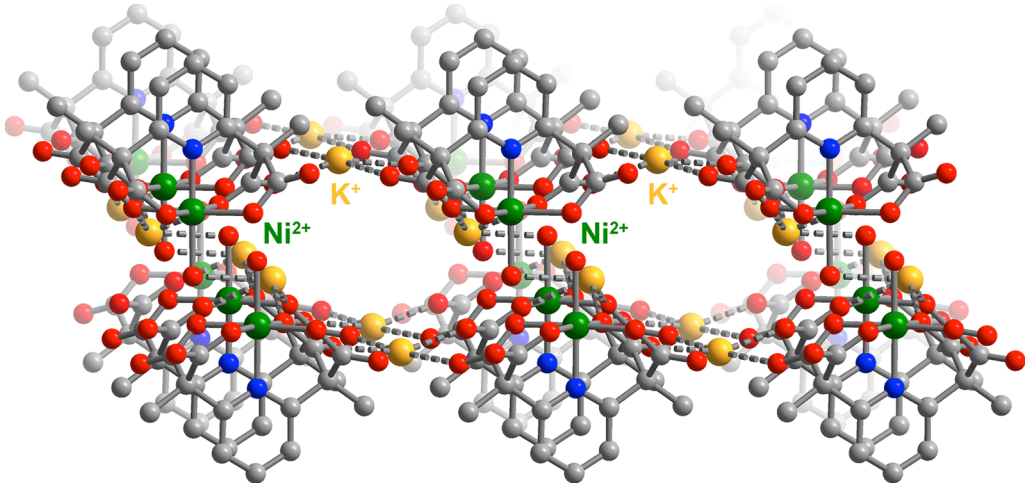


Figure 3.4. Extended structure of $K_2[(PY(CO_2)_4)Ni(H_2O)]$ viewed along the *a*-axis. Green, light yellow, red, blue, and gray spheres represent Ni, K, O, N, and C atoms, respectively. Water molecules coordinated to K^+ have been removed to accentuate the channels. All H atoms were omitted for clarity.

distortion for Ni^{2+} is only 0.05 Å, suggesting that smaller transition metal ions are better accommodated by $[PY(CO_2)_4]^{4-}$.

Crystal structure determinations also revealed some intriguing extended structures for these carboxylate-rich complexes. Indeed, pyridyl π–π stacking and potassium bridging between adjacent complexes generates a three-dimensional network with channels extending along the crystallographic *a*-axis that are filled with water molecules bound to the bridging cations (see Figure 3.4). Synthesis and solid-state characterization of the series $A_2[(PY(CO_2)_4)Ni(H_2O)]$ (A = Li^+, Na^+, and Cs^+), in the manner described above for A = K^+, revealed that the identity of the counter cation has a substantial influence on the molecular packing.[36] Indeed, although the immediate coordination environment of the Ni^{2+} centers varies only slightly (Table S3.8), the mode of alkali metal ion coordination influences the resultant channel formation, size, and solvent occupancy. For example, the height of the channels in the K^+ compound ($K^+\cdots K^+$) is 6.935(3) Å ($Ni^{2+}\cdots Ni^{2+}$ = 10.3400(5) Å)[37] with two water molecules per formula unit. In comparison, though it contains more water molecules (2.5 per formula unit, Figure S3.23), the channel height in the Li^+ structure ($Li^+\cdots Li^+$) is only 4.5691(9) Å ($Ni^{2+}\cdots Ni^{2+}$ = 7.356(2) Å). The channel of the Na^+ analogue is the largest in size, with a $Na^+\cdots Na^+$ separation of 11.044(2) Å ($Ni^{2+}\cdots Ni^{2+}$ = 13.371(3) Å). Six extra solvent molecules occupy each formula unit in this expanded volume, and one Na^+ ion is completely solvated by water (Figure S3.24). In contrast to the other three structures, $Cs_2[(PY(CO_2)_4)Ni(H_2O)]$ does not exhibit channels and packing does not accommodate water outside of the Ni^{2+} coordination sphere (Figure S3.26).

Encouraged by the successful metalation of $[(PY(CO_2)_4)]^{4-}$, we further sought to enhance the solubility of the $[(PY(CO_2)_4)M(H_2O)]^{2-}$ complexes in organic solvents by exchanging K^+ with aliphatic cations. Indeed, if this ligand scaffold were capable of supporting a high-valent metal center, the ability to utilize a more inert solvent system with a wider electrochemical window would aid in the isolation and reactivity studies of such a species. Due to their ease of handling in air, we first carried out salt metathesis with $K_2[(PY(CO_2)_4)Ni(H_2O)]$ and $K_2[(PY(CO_2)_4)Zn(H_2O)]$ via reaction with one equivalent of bis(triphenylphosphoranylidene)ammonium (PPN^+) chloride in a 3:1 mixture of water:ethanol. The transparent mixtures were then left to stand open to air, and over the course of 2-3 d the

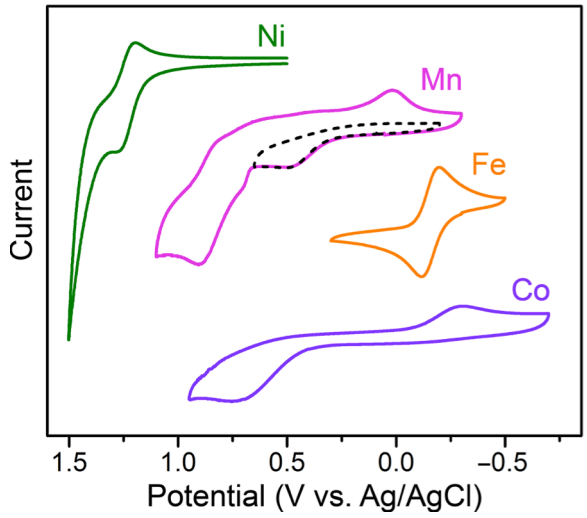


Figure 3.5. Cyclic voltammograms of $K_2[(PY(CO_2)_4)M(H_2O)]$ complexes in pH 7 aqueous solution with 0.1 M $KClO_4$ electrolyte. All scans were performed at 100 mV sec^{-1}. M = Mn^{2+} (magenta), Fe^{2+} (orange), Co^{2+} (purple), and Ni^{2+} (green).

ethanol evaporated to yield colorless (Zn^{2+}) and pale purple (Ni^{2+}) needles. Elemental analysis of both the Ni^{2+} and Zn^{2+} products and single-crystal X-ray characterization of the Zn^{2+} complex (Figure S3.22) confirmed successful cation exchange. The resulting PPN^+ salts are indeed soluble in a number of organic solvents (e.g., methanol, acetonitrile, acetone, and dichloromethane); however, the complexes decompose rapidly in solution at room temperature, precluding further study under these conditions (see the Supporting Information for details).

Consequently, aqueous cyclic voltammetry was performed on the series of $[PY(CO_2)_4]^{4-}$ metal complexes at pH 7 in 0.1 M $KClO_4$ electrolyte solution to examine the impact of the tetraanionic donor on the redox potentials. The Zn^{2+} complex exhibited no redox activity from −1.5 to 1.5 V versus Ag/AgCl, confirming that $[PY(CO_2)_4]^{4-}$ is not electrochemically active within this range. As shown in Figure 3.5, quasireversible 3+/2+ redox couples were observed for the Fe^{2+} and Ni^{2+} complexes with $E_{1/2}$ values of −0.16 and 1.24 V, respectively, though neither of these redox events exhibited pH dependence from pH = 7–10. In the case of the Co^{2+} complex, an irreversible oxidation occurred at 0.74 V and was followed by an irreversible reduction at −0.30 V on the return scan. This cathodic feature was only observed after initial oxidation of $[(PY(CO_2)_4)Co(H_2O)]^{2-}$. In an effort to identify the oxidized species, we also carried out cyclic voltammetry on the low-spin complex $[(PY(CO_2)_4)Co(OH)]^{2-}$, which is formed cleanly via chemical oxidation of $[(PY(CO_2)_4)Co(H_2O)]^{2-}$ with H_2O_2.[38] This experiment revealed a cathodic trace identical to that of $[(PY(CO_2)_4)Co(H_2O)]^{2-}$, which suggests that the oxidation of $[(PY(CO_2)_4)Co(H_2O)]^{2-}$ at 0.74 V is accompanied by deprotonation of the aquo ligand. The separation of the anodic and cathodic peak potentials by more than 1 V is likely due to stabilization of Co^{3+} by the resultant hydroxide moiety as well as to the low to high-spin conversion mediated by the reduction.

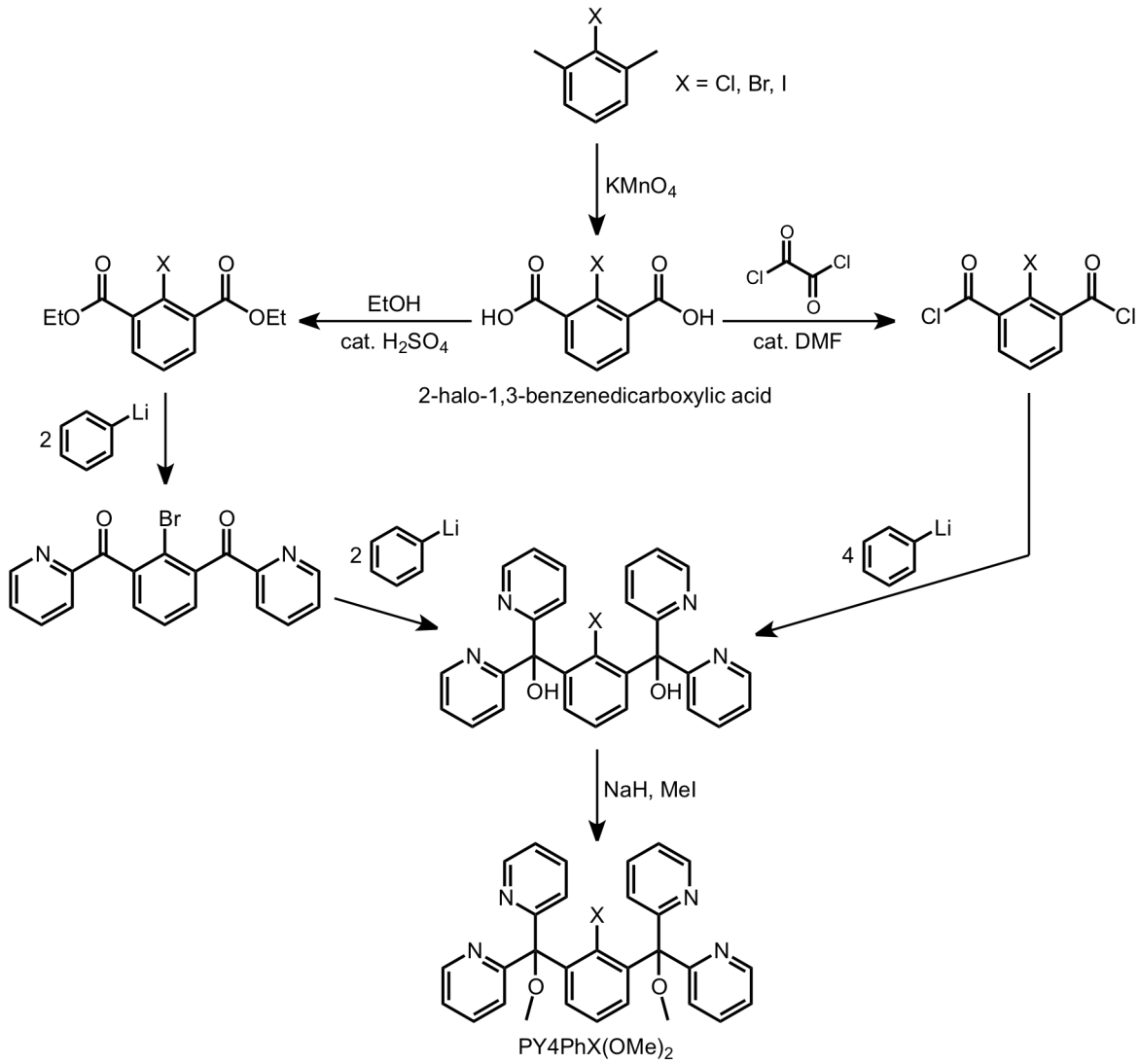
Cyclic voltammograms of the Mn^{2+} complex were more complex than the other compounds. An initial irreversible anodic feature was present with E_{pa} = 0.50 V and was assigned as the oxidation of the Mn^{2+} complex to a Mn^{3+} species. Upon scanning to higher potentials, another anodic feature appeared at 0.90 V with a peak current more than twice that of the oxidation occurring at 0.50 V. A subtle shoulder in this second feature suggested at least two overlapping oxidations in this region. These oxidations were not electrochemically reversible and higher-

valent manganese species could not be isolated via chemical oxidation; thus, it was not possible to definitively identify the oxidized products. After the oxidation at 0.90 V, a further reduction at 0.02 V, not associated with the initial feature at 0.50 V, appeared on the return cathodic scan.

Section 3.4. Results and Discussion of $PY4PhXR_2$

Previously, efforts to generate a $PY5Me_2$ analogue with an axial phenyl carbene donor had focused on $PY4PhMe_2$ as a synthetic target, and indeed, this ligand was successfully generated in two steps. First, 1,3-dibromobenzene was exposed to cesium hydroxide and two equivalents of bis(2-pyridyl)methane in a palladium catalyzed cross-coupling reaction, which produced the intermediate 2,6-bis[bis(2-pyridyl)methyl]benzene. In the second step, deprotonation of the tertiary carbons with *n*-butyllithium followed by addition of MeI produced $PY4PhMe_2$ in good yield (91%).[16] However, the inability to deprotonate the proton at the 2-position of the axial benzene ring prevented the ligand from binding metals in a pentadentate fashion. As a result, a

Scheme 3.2. Proposed synthetic routes for $PY4PhX(OMe)_2$ starting from 2-halo-1,3-benzenedicarboxylic acids.



new synthetic target was chosen, $PY4PhXR_2$, in which the unwanted hydrogen atom is replaced with a halogen that would allow for subsequent metalation to be performed via a metal halogen exchange.

A number of different routes were attempted in order to obtain $PY4PhXR_2$. Scheme 3.2 depicts the first target, 1,3-(bis(bis-2-pyridyl)methoxymethane)-2-halobenzene ($PY4PhX(OMe)_2$), produced through syntheses similar to those used by Stack and co-workers to make 2,6-(bis(bis-2-pyridyl)methoxymethane)pyridine (PY5).[39,40] The *meta*-2-haloxylenes were commercially available and were converted to the corresponding 2-halo-1,3-benzenedicarboxylic acids via oxidation with $KMnO_4$ in water as directed by Gilman and Stuckwisch.[41] Excellent yields for the 2-bromo- (98%) and 2-chloro-1,3-benzenedicarboxylic acids (70%) were obtained using 6 and 8 equivalents of $KMnO_4$, respectively. However, the yield for 2-iodo-1,3-benzenedicarboxylic acid (3 equivalents of $KMnO_4$) was only 32%. This lower yield was in part due to the presence of a hypervalent iodosodilacton side product,[42] which necessitated additional purification by recrystallization from water in order to obtain the pure product.

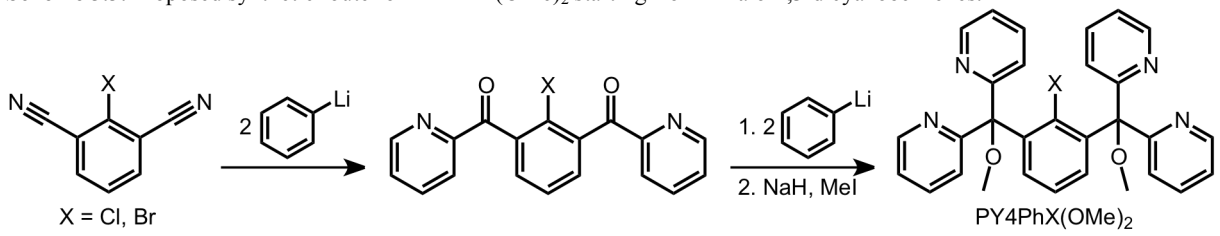
Due to the report that two sequential additions of 2-lithiopyridine to diethyl pyridine-2,6-dicarboxylate resulted in easier purification of the intermediates in the synthesis of PY5, the route through the ester was attempted first. The diethyl 2-halo-1,3-benzenedicarboxylates were generated in 40-50% yield through Fisher esterification in ethanol with catalytic H_2SO_4 at reflux over the course of 5 d. Due to the long reaction time for this synthesis, an alternate method for this step was tested as well. It involved subjecting the 2-halo-1,3-benzenedicarboxylic acids to oxalyl chloride with catalytic DMF in dichloromethane followed by addition of ethanol. Although this route formed the desired product more quickly, ^{1}H NMR revealed the presence of an unidentified impurity that was difficult to remove. Thus, Fischer esterification was preferred. Having obtained the ester intermediate, the first addition of two equivalents of 2-lithiopyridine was attempted following the method published by Goldsmith and Stack.[40] Unfortunately, this reaction resulted in intractable mixtures despite attempts to optimize the reaction time and temperature.

The second route presented in Scheme 3.2 was tried as well. Whereas Jonas and Stack utilized thionyl chloride at reflux to generate the acid dichloride corresponding to 2,6-pyridinedicarboxylic acid, ^{1}H NMR[43] indicated that neat oxalyl chloride with catalytic DMF at room temperature was sufficient to perform the reaction with the 2-halo-1,3-dicarboxylic acids in less than 1 h. After removing excess oxalyl chloride under reduced pressure, the white residue was immediately combined with four equivalents of 2-lithiopyridine. However, this reaction also resulted in intractable mixtures.

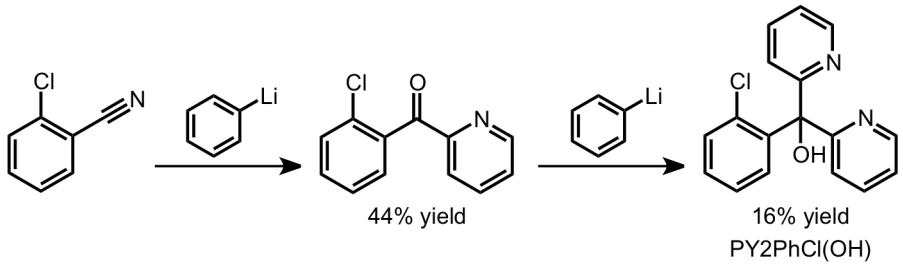
Scheme 3.3 shows a third option to obtain $PY4PhX(OMe)_2$, in which 2-halo-1,3-dicyanobenzenes are used as starting materials. As an initial evaluation of this route, 2-chlorobenzonitrile, an inexpensive and commercially available reagent, was added to 2-lithiopyridine at −78 °C in ether, similar to the method used by Ghorai and co-workers.[44] Upon sequential acidic and basic work-ups and purification by column chromatography, the intermediate (2-chlorophenyl)(pyridin-2-yl)methanone was obtained in 44% yield as a yellow oil. A second addition of 2-lithiopyridine followed by aqueous work-up and recrystallization gave (2-chlorophenyl)di(pyridin-2-yl)methanol (PY2PhCl(OH)) in 16% yield as a tan solid (Scheme 3.4).

Encouraged by this result, 2-bromo-1,3-dicyanobenzene was synthesized from 1,3-dicyanobenzene, lithium diisopropylamide, and 1,2-dibromo-1,1,2,2-tetrachloroethane.[45] Despite attempts to purify the crude product by column chromatography, the isolated material was

Scheme 3.3. Proposed synthetic route for PY4PhX(OMe)$_2$ starting from 2-halo-1,3-dicyanobenzenes.



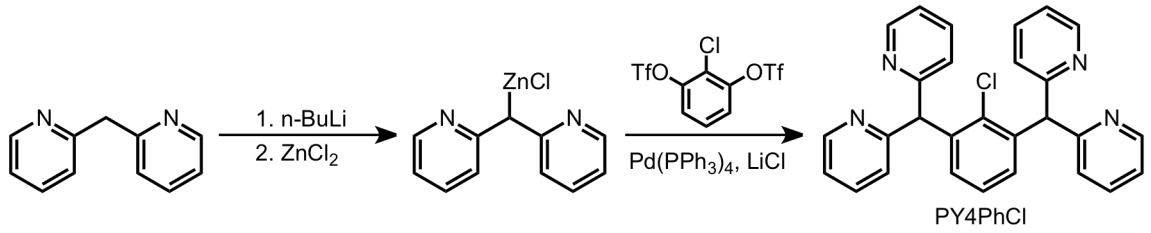
Scheme 3.4. Synthetic route for PY2PhCl(OH) starting from 2-chlorobenzonitrile.



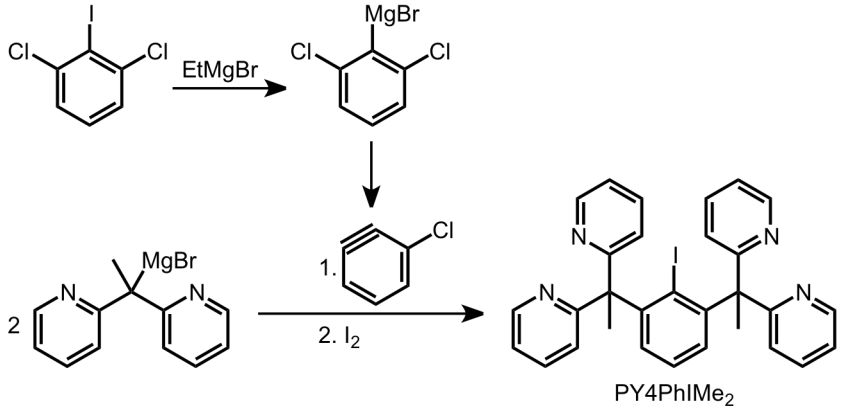
composed of a mixture of 2-bromo- and 2-chloro-1,3-dicyanobenzene in a 7 to 1 ratio. When exposed to 2-lithiopyridine, this mixture returned predominantly 1,3-dicyanobenzene, suggesting that lithium halogen exchange with bromine was favored over nucleophilic attack on the nitriles. However, ESI-MS revealed the presence of trace amounts of the desired dicarbonyl product with chlorine at the 2-position due to the small amount of 2-chloro-1,3-dicyanobenzene that had not been removed from the starting material. In order to capitalize on this finding, pure 2-chloro-1,3-dicyanobenzene was synthesized[46] and subsequently exposed to 2-lithiopyridine at −78 °C. Regrettably upon aqueous work-up and purification by flash chromatography, ESI-MS indicated that, though nucleophilic addition did occur, the halogen had been lost yet again and that only 1,3-phenylenebis(pyridin-2-ylmethanone) had been isolated. This reaction was also performed at −104 °C in a liquid N_2 and cyclohexane bath, but formation of the desired product was not observed. Thus it was concluded that including two electron withdrawing substituents on the ring, whether they be carbonyls or nitriles, is sufficient to promote lithium halogen exchange over nucleophilic addition, which likely helps to explain the intractable mixtures formed during the routes starting from the dicarboxylic acids.

Scheme 3.5 shows an entirely different path toward PY4PhXR$_2$ in which 1,3-bis[bis(2-pyridyl)methyl]-2-halobenzene (PY4PhCl) was the intended target. A report by Woo and co-works described the palladium catalyzed Negishi coupling of a 1-cyclopentenyl trifluoromethanesulfonate reagent with 2-picoline.[47] Using a similar method, di(pyridin-2-yl)methane was deprotonated with *n*-butyllithium and exposed to $ZnCl_2$ to generate the organozinc intermediate, which was immediately added to a THF solution of tetrakis(triphenylphosphine)palladium(0), lithium chloride, and 2-chloro-1,3-phenylene bis(trifluoromethanesulfonate).[48] After holding at reflux for 15 hours, the reaction was allowed to cool and quenched with aqueous $NaHCO_3$. Extraction with dichloromethane produced a peach solid. The only identifiable signals in the ^{1}H NMR of this crude material belonged to the di(pyridin-2-yl)methane starting material, though ESI-MS also suggested the presence of 1,1,2,2-tetra(pyridin-2-yl)ethane, the result of homocoupling of two di(pyridin-2-yl)methane units. Due to this result, it was thought that the di(pyridin-2-yl)methane anion might not be sufficiently reactive to promote coupling to the trifluoromethanesulfonate reagent. To better evaluate the

Scheme 3.5. Proposed synthetic route for PY4PhCl via a palladium catalyzed Negishi coupling.



Scheme 3.6. Synthetic route for $PY4PhIMe_2$ starting from 1,3-dichloro-2-iodobenzene.



potential of this route and determine if di(pyridin-2-yl)methane could indeed serve as a coupling partner, the same reaction conditions were performed using the simpler reagent phenyl trifluoromethanesulfonate and one of two second generation palladium catalysts, SPhos Pd or XPhos Pd. Regardless which catalyst was used, only the phenyl trifluoromethanesulfonate starting material was identified in the ^{1}H NMR of the crude, and no evidenced was obtained for the formation of PY4PhCl. Consequently, it was determined that this route was not promising and no further investigations were performed.

The final method attempted is shown in Scheme 3.6. Here, 1,3-dichloro-2-iodobenzene is subjected to EtMgBr, inducing preferential metal-halogen exchange at iodine to generate a phenyl Grignard reagent. Displacement of one of the chlorides produces a benzyne intermediate, which is attacked by 1,1-bis(2-pyridyl)ethylmagnesium bromide. Due the electron withdrawing character of the remaining chloride, attack at the position *meta* to the remaining chloride is more favorable as the resulting anion will be better stabilized at the 2-position. After installation of the first substituent, steric factors should encourage replacement of the second chloride with another equivalent of 1,1-bis(2-pyridyl)ethylmagnesium bromide. Moreover, the first set of appended pyridine rings should help to establish the binding pocket at the 2-position of the benzene ring. Following the attachment of both substituents, the final product can be trapped with addition of I_2, reinstalling the halogen at the 2-position. Du and co-workers used this method to generate *meta*-terphenyls in good yields,[49] and indeed evidence for the production of the desired product, 1,3-bis[1,1-bis(2-pyridyl)ethyl]-2-iodobenzene ($PY4PhIMe_2$), was obtained. Single crystal X-ray diffraction revealed that the ligand was doubly protonated, with the H atoms identified from the electron difference map due to hydrogen bonding to the pyridines, and accompanied by iodide and triiodide counterions (Figure 3.6). Likely as a result of this protonation, solubility of this compound in organic solvents was inconsistent. In fact, the X-ray quality crystals were obtained by spontaneous crystallization of an NMR sample of the crude mixture. By washing the crude

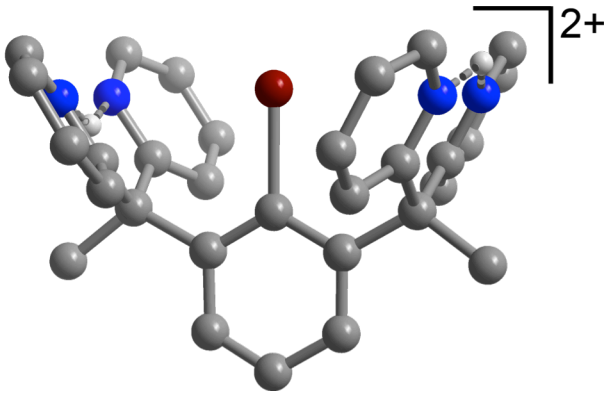


Figure 3.6. Single crystal X-ray structure of $PY4PhIMe_2$. Maroon, blue, gray, and light gray spheres represent I, N, C, and H, respectively. H atoms bound to C and counter ions were omitted for clarity.

mixture with NaOH and passing it through a basic alumina plug, an NMR spectrum was obtained and ESI-MS confirmed the identity of the product. However, in part due to the solubility issues, yields for $PY4PhIMe_2$ were low. Quenching the reaction with water instead of I_2 showed that even in the presence of excess 1,1-bis(2-pyridyl)ethylmagnesium bromide, conversion was less than 28%.

Section 3.5. Conclusions and Outlook

As demonstrated by the preceding section, obtaining $PY4PhXR_2$ is not a trivial pursuit, and further work will need to be performed in order to generate it in good and reliable yield. Based on the routes attempted thus far, the method utilizing the benzyne intermediate to form $PY4PhIMe_2$ seems most promising. Because 1,1-bis(2-pyridyl)ethylmagnesium bromide is likely a weaker nucleophile than the phenyl magnesium bromides used by Du and co-workers, switching to a higher boiling point solvent, such as 1,4-dixoane, and increasing the reaction temperature may allow for better conversion to the desired product. Additionally, a turbo-Grignard could also be used instead of the standard EtMgBr to increase nucleophilicity. As an alternative method for isolating the final ligand, I_2 could be replaced with divalent metal salts, which should preferentially replace lithium in the binding pocket. Once the metal is in place, protonation of the pyridine rings would likely not occur, which might also improve the solubility of the product and facilitate successful isolation.

In regard to the development of NO_4 ligands, two new tetrapodal ligands, $PY(CO_2Et)_4$ and $[PY(CO_2)_4]^{4-}$, were synthesized and metalated with first-row transition metals to generate the octahedral complexes $[(PY(CO_2Et)_4)Cu(THF)]^{2+}$ and $[(PY(CO_2)_4)M(H_2O)]^{2-}$ ($M = Mn^{2+}$, Fe^{2+}, Co^{2+}, Ni^{2+}, Zn^{2+}). In particular, $[PY(CO_2)_4]^{4-}$ provides the first example of a tetraanionic, tetrapodal framework capable of forming mononuclear complexes, and although it is moderately temperature sensitive as an alkali metal salt, its stability is significantly enhanced when bound to divalent transition metal cations. X-ray structural characterization of the complex salts $K_2[(PY(CO_2)_4)M(H_2O)]$ verified that the ligand chelates in a κ^5 fashion and that the binding pocket is best suited for smaller divalent cations such as Ni^{2+}. The packing of the transition metal complexes in the solid-state further revealed a unique three-dimensional network that is dependent on the nature of the charge balancing alkali metal cation. Aqueous cyclic voltammetry experiments further established accessible trivalent oxidation states for the Fe, Co, and Ni complexes. Though, in our hands only the Co^{3+} species $[(PY(CO_2)_4)Co(OH)]^{2-}$ was isolated and

structurally characterized. While it was not possible to solubilize $[(PY(CO_2)_4)M(H_2O)]^{2-}$ in organic solvents and probe even higher oxidation states, this work importantly highlights the tunability of the tetrapodal ligand framework and suggests that even more exotic ligand variations capable of generating new reactive metal complexes are within reach.

Section 3.6 Acknowledgements

This research was supported by the National Science Foundation through Grant CHE-1464841 to Jeffrey R. Long and Graduate Research Fellowship Grant No. DGE-1106400 to the author. Contributions of Prof. Christopher J. Chang were supported by U.S. Department of Energy/Lawrence Berkeley National Laboratory Grant 101528-002. C. J. Chang is an Investigator with the Howard Hughes Medical Institute. The author thanks Dr. Antonio DiPasquale (supported by NIH Shared Instrumentation Grant S10-RR027172) and Dr. Simon J. Teat for crystallographic assistance, Prof. Michael Nippe for helpful discussions, and Dr. Katie R. Meihaus for editorial assistance. Support in screening reaction conditions for $PY4PhXR_2$ was provided by Brittany "Nova" Gomez and Prof. Robert G. Bergman's Spring 2015 CHEM 115 class (Youn Jue Bae, Steven Lai, and Juwita Wijaya). Crystal structures of the Ni^{2+} and Co^{3+} complexes were collected by Miguel I. Gonzalez and carried out at the Advanced Light Source at Lawrence Berkeley National Lab, a user facility supported by the Director, Office of Science, Office of Basic Energy Sciences, of the U.S. Department of Energy under Contract No. DE-AC02-05CH11231. The portion of this chapter pertaining to $[PY(CO_2)_4]^{4-}$ has previously been published as "Synthesis and Characterization of a Tetrapodal NO_4^{4-} Ligand and Its Transition Metal Complexes" in *Inorganic Chemistry* (DOI: 10.1021/acs.inorgchem.6b00908).

Section 3.7 References

(1) Grohmann, A. *J. Chem. Soc., Dalton Trans.* **2010**, *39*, 1432−1440.

(2) (a) Karunadasa, H. I.; Chang, C. J.; Long, J. R. *Nature* **2010**, *464*, 1329–1333. (b) Sun, Y.; Bigi, J. P.; Piro, N. A.; Tang, M. L.; Long, J. R.; Chang, C. J. *J. Am. Chem. Soc*. **2011**, *133*, 9212−9215. (c) Karunadasa, H. I.; Montalvo, E.; Sun, Y.; Majda, M.; Long, J. R.; Chang, C. J. *Science* **2012**, *335*, 698−702. (d) Thoi, V. S.; Karunadasa, H. I.; Surendranath, Y.; Long, J. R.; Chang, C. J. *Energy Environ. Sci.* **2012**, *5*, 7762-7770. (e) Sun, Y.; Sun, J.; Long, J. R.; Yang, P.; Chang, C. J. *Chem. Sci.* **2013**, *4*, 118-124. (f) Thoi, V. S.; Sun, Y.; Long, J. R.; Chang, C. J. *Chem. Soc. Rev.* **2013**, *42*, 2388–2400. (g) King, A. E.; Surendranath, Y.; Piro, N. A.; Bigi, J. P.; Long, J. R.; Chang, C. J. *Chem. Sci.* **2013**, *4*, 1578-1587. (h) Zee, D. Z.; Chantarojsiri, T.; Long, J. R.; Chang, C. J. *Acc. Chem. Res.* **2015**, *48*, 2027–2036.

(3) (a) Wasylenko, D. J.; Ganesamoorthy, C.; Borau-Garcia, J.; Berlinguette, C. P. *Chem. Commun.* **2011**, *47*, 4249−4251. (b) Wasylenko, D. J.; Palmer, R. D.; Schott, E.; Berlinguette, C. P. *Chem. Commun.* **2012**, *48*, 2107−2109. (c) Wang, L., Duan, L.; Ambre, R. B.; Daniel, Q.; Chen, H.; Sun, J.; Das, B.; Thapper, A.; Uhlig, J.; Dinér, P.; Sun, S. *J. Catal.* **2016**, *335*, 72-78.

(4) (a) Goldsmith, C. R.; Jonas, R. T.; Stack, T. D. P. *J. Am. Chem. Soc.* **2002**, *124*, 83–96. (b) Que, L. *Acc. Chem. Res.* **2007**, *40*, 493−500. (c) McQuilken, A. C.; Ha, Y.; Sutherlin, K. D.; Siegler, M. A.; Hodgson, K. O.; Hedman, B.; Solomon, E. I.; Jameson, G. N. L.; Goldberg, D. P. *J. Am. Chem. Soc.* **2013**, *135*, 14024–14027.

(5) McDonald, A. R.; Guo, Y.; Vu, V. V.; Bominaar, E. L.; Münck, E.; Que, L. *Chem. Sci.* **2012**, *3*, 1680–1693.
(6) Kashif, M. K.; Axelson, J. C.; Duffy, N. W.; Forsyth, C. M.; Chang, C. J.; Long, J. R.; Spiccia, L.; Bach, U. *J. Am. Chem. Soc.* **2012**, *134*, 16646–16653.
(7) (a) Freedman, D. E.; Jenkins, D. M.; Iavarone, A. T.; Long, J. R. *J. Am. Chem. Soc.* **2008**, *130*, 2884–2885. (b) Atanasov, M.; Busche, C.; Comba, P.; Hallak, F. El; Martin, B.; Rajaraman, G.; van Slageren, J.; Wadepohl, H. *Inorg. Chem.* **2008**, *47*, 8112–8125. (c) Bechlars, B.; D'Alessandro, D. M.; Jenkins, D. M.; Iavarone, A. T.; Glover, S. D.; Kubiak, C. P.; Long, J. R. *Nat. Chem.* **2010**, *2*, 362–368.
(8) Grohmann, A. Tetrapodal Pentadentate Nitrogen Ligands: Aspects of Complex Structure and Reactivity. In *Advances in Inorganic Chemistry*; van Eldik, R., Olabe, J. A., Eds.; Academic Press: 2004; Vol. 56, pp 179–210.
(9) See Figures 1.4 and 1.5 for a distribution of coordination environments and net formal charges of donor atoms found in tetrapodal ligands that have been deposited in the Cambridge Crystallographic database.
(10) (a) Lomoth, R.; Huang, P.; Zheng, J.; Sun, L.; Hammarström, L.; Åkermark, B.; Styring, S. *Eur. J. Inorg. Chem.* **2002**, *2002*, 2965–2974. (b) Xu, Y.; Åkermark, T.; Gyollai, V.; Zou, D.; Eriksson, L.; Duan, L.; Zhang, R.; Åkermark, B.; Sun, L. *Inorg. Chem.* **2009**, *48*, 2717–2719. (c) Duan, L.; Fischer, A.; Xu, Y.; Sun, L. *J. Am. Chem. Soc.* **2009**, *131*, 10397–10399. (d) Chantarojsiri, T.; Sun, Y.; Long, J. R.; Chang, C. J. *Inorg. Chem.* **2015**, *54*, 5879–5887.
(11) (a) Pestovsky, O.; Stoian, S.; Bominaar, E. L.; Shan, X.; Münck, E.; Que, L.; Bakac, A. *Angew. Chem.* **2005**, *117*, 7031–7034. (b) Xiao, D. J.; Bloch, E. D.; Mason, J. A.; Queen, W. L.; Hudson, M. R.; Planas, N.; Borycz, J.; Dzubak, A. L.; Verma, P.; Lee, K.; Bonino, F.; Crocellà, V.; Yano, J.; Bordiga, S.; Truhlar, D. G.; Gagliardi, L.; Brown, C. M.; Long. J. R. *Nat. Chem.* **2014**, *6*, 590–595.
(12) (a) Schmidt, S.; Omnes, L.; Heinemann, F. W.; Kuhnigk, J.; Krüger, C.; Grohmann, A. *Z. Naturforsch., B: Chem. Sci.* **1998**, *53*, 946–954. (b) Zimmermann, C.; Bauer, W.; Heinemann, F. W.; Grohmann, A. *Z. Naturforsch., B: Chem. Sci.* **2002**, *57*, 1256–1264.
(13) (a) Inomata, Y.; Gochou, Y.; Nogami, M.; Howell, F. S.; Takeuchi, T. *J. Mol. Struct.* **2004**, *702*, 61–70. (b) Stamatatos, T. C.; Abboud, K. A.; Christou, G. *J. Chem. Soc., Dalton Trans.* **2009**, 41–50. (c) Graham, K.; Sharp, L. E.; Thomas, L. H.; Murrie, M. *Inorg. Chem. Commun.* **2012**, *25*, 89–91.
(14) (a) Ferguson, A.; Parkin, A.; Murrie, M. *J. Chem. Soc., Dalton Trans.* **2006**, 3627–3628. (b) Ferguson, A.; McGregor, J.; Parkin, A.; Murrie, M. *J. Chem. Soc., Dalton Trans.* **2008**, 731–733.
(15) Smith, J. M.; Long, J. R. *Inorg. Chem.* **2010**, *49*, 11223–11230.
(16) Karunadasa, H. I. Heavy Atom Building Units for Magnetic Clusters and Molecular Catalysts for Generating Hydrogen from Water. Ph.D. Dissertation, University of California, Berkeley, Berkeley, CA, 2009.
(17) (a) Evans, D. F. *J. Chem. Soc.* **1959**, 2003–2005. (b) Schubert, E. M. *J. Chem. Educ.* **1992**, *69*, 62. (c) Girolami, G. S.; Rauchfuss, T. B.; Angelici, R. J. *Synthesis and Technique in Inorganic Chemistry: A Laboratory Manual,* 3rd ed.; University Science Books: Sausalito, California, 1999.
(18) Grant, D. H. *J. Chem Educ*. **1995**, *72*, 39–40.

(19) Bain, G. A.; Berry, J. F. *J. Chem. Educ.* **2008**, *85*, 532-536.
(20) Bruker. APEX2, Bruker AXS Inc., Madison, Wisconsin, USA, 2007.
(21) Sheldrick, G. M. SADABS, Bruker AXS Inc., University of Göttingen, Germany, 1996.
(22) Sheldrick, G. M. TWINABS, University of Göttingen, Germany, 1996.
(23) Sheldrick, G. M. *Acta Crystallogr., Sect. A* **2015**, *71*, 3–8.
(24) Sheldrick, G. M. *Acta Crystallogr., Sect. A* **2008**, *64*, 112–122.
(25) Farrugia, L. J. *J. Appl. Crystallogr.* **2012**, *45*, 849–854.
(26) Dolomanov, O. V.; Bourhis, L. J.; Gildea, R. J.; Howard, J. A. K.; Puschmann, H. *J. Appl. Crystallogr.* **2009**, *42*, 339–341.
(27) Brandenburg, K. DIAMOND, Crystal Impact GbR, Bonn, Germany, 1999.
(28) (a) Canty, A. J.; Minchin, N. J.; Skelton, B. W.; White, A. H. *J. Chem. Soc., Dalton Trans.* **1986**, 2205–2210. (b) Ünal, E. A.; Wiedemann, D.; Seiffert, J.; Boyd, J. P.; Grohmann, A. *Tetrahedron Lett.* **2012**, *53*, 54–55.
(29) Londregan, A. T.; Jennings, S.; Wei, L. *Org. Lett.* **2011**, *13*, 1840–1843.
(30) Boivin, J.; Carpentier, F.; Jrad, R. *Synthesis* **2006**, *2006*, 1664–1672.
(31) Yip, S. F.; Cheung, H. Y.; Zhou, Z.; Kwong, F. Y. *Org. Lett.* **2007**, *9*, 3469–3472.
(32) If needed, the $A^4[PY(CO^2)^4]$ salts can be stored overnight in a −20 °C freezer before metalation.
(33) Detailed crystallographic information for all $[PY(CO_2)_4]^{4-}$ complexes can be found in Table S3.5.
(34) Mn: (a) Baca, S. G.; Malaestean, I. L.; Keene, T. D.; Adams, H.; Ward, M. D.; Hauser, J.; Neels, A.; Decurtins, S. *Inorg. Chem.* **2008**, *47*, 11108–11119. (b) Déniz, M.; Hernández-Rodríguez, I.; Pasán, J.; Fabelo, O.; Cañadillas-Delgado, L.; Yuste, C.; Julve, M.; Lloret, F.; Ruiz-Pérez, C. *Cryst. Growth Des.* **2012**, *12*, 4505–4518. (c) Chen, S.; Cheng, M.; Ren, Y.; Tang, L.; Liu, X.; Zai, C.; Liu, Q. *Z. Anorg. Allg. Chem.* **2015**, *641*, 610–616. Fe: (d) Laine, P.; Gourdon, A.; Launay, J.-P. *Inorg. Chem.* **1995**, *34*, 5129–5137. (e) Yoon, S.; Lippard, S. J. *J. Am. Chem. Soc.* **2005**, *127*, 8386–8397. Co: (f) Stamatatos, T. C.; Dionyssopoulou, S.; Efthymiou, G.; Kyritsis, P.; Raptopoulou, C. P.; Terzis, A.; Vicente, R.; Escuer, A.; Perlepes, S. P. *Inorg. Chem.* **2005**, *44*, 3374–3376. (g) Grirrane, A.; Pastor, A.; Álvarez, E.; Mealli, C.; Ienco, A.; Rosa, P.; Galindo, A. *Eur. J. Inorg. Chem.* **2007**, *2007*, 3543–3552. (h) Lian, Z.; Zhao, N.; Liu, P. *Z. Kristallogr. - New Cryst. Struct.* **2010**, *225*, 371–373. Ni: (i) Alexiou, M.; Dendrinou-Samara, C.; Raptopoulou, C. P.; Terzis, A.; Tangoulis, V.; Kessissoglou, D. P. *Eur. J. Inorg. Chem.* **2004**, *2004*, 3822–3827. (j) Yang, A.-H.; Zhang, H.; Gao, H.-L.; Zhang, W.-Q.; He, L.; Cui, J.-Z. *Cryst. Growth Des.* **2008**, *8*, 3354–3359. (k) Zhang, Y.-J.; Wang, J.-J.; Chen, J. Z. *Anorg. Allg. Chem.* **2012**, *638*, 1849–1854. Zn: (l) Chen, Z.; Gao, D.-L.; Diao, C.-H.; Liu, Y.; Ren, J.; Chen, J.; Zhao, B.; Shi, W.; Cheng, P. *Cryst. Growth Des.* **2012**, *12*, 1201–1211. (m) Faure, R.; Loiseleur, H. *Acta Crystallogr., Sect. B: Struct. Sci.* **1972**, *28*, 811–815. (n) Zhang, L.; Lin, Q.-P.; Li, Z.-J.; Zhang, J.; Qin, Y.-Y.; Cheng, J.-K.; Yao, Y.-G. *CrystEngComm* **2009**, *11*, 1201–1203.
(35) (a) Figgis, B. N.; Lewis, J. The Magnetic Properties of Transition Metal Complexes. In *Progress in Inorganic Chemistry*; Cotton, F. A., Ed.; Wiley: Chichester, U.K., 1964; pp 37–239. (b) *Encyclopedia of Inorganic Chemistry,* 2nd ed.; King, R. B., Ed.; Wiley: Chichester, U.K., 2005.
(36) Subtle changes in the color of solid samples of the complexes were also observed—from purple (Na^+) to purple-blue (Li^+ and K^+) to blue (Cs^+)—and were confirmed by minor

changes in the diffuse reflectance spectra of these compounds in the solid state. In particular, the two maxima at 573 and 915 nm in the Na^+ spectrum were noticeably blueshifted in comparison to the maxima of the other three (Figure S3.12). Yet, the complexes exhibit identical solution UV-vis/NIR spectra (Figure S3.13). Thus, the minor differences in coloration of the solid samples likely arises from packing effects.

(37) Channel dimensions were calculated using Diamond.

(38) Further discussion of $[(PY(CO_2)_4)Co(OH)]^{2-}$ can be found in the Supporting Information.

(39) Jonas, R. T.; Stack, T. D. P. *J. Am. Chem. Soc.* **1997**, *119*, 8566–8567.

(40) Goldsmith, C. R.; Stack, T. D. P. *Inorg. Chem.* **2006**, *45*, 6048–6055.

(41) Gilman, H.; Stuckwisch, C. G. *J. Am. Chem. Soc.* **1943**, *65*, 1729–1733.

(42) Tian, J.; Gao, W.-C.; Zhou, D.-M.; Zhang, C. *Org. Lett.* **2012**, *14*, 3020–3023.

(43) Denmark, S. E.; Stavenger, R. A.; Faucher, A.-M.; Edwards, J. P. *J. Org. Chem.* **1997**, *62*, 3375–3389.

(44) Ghorai, P.; Kraus, A.; Keller, M.; Götte, C.; Igel, P.; Schneider, E.; Schnell, D.; Bernhardt, G.; Dove, S.; Zabel, M.; Elz, S.; Seifert, R.; Buschauer, A. *J. Med. Chem.* **2008**, *51*, 7193–7204.

(45) Krizan, T. D.; Martin, J. C. *J. Org. Chem.* **1982**, *47*, 2681–2682.

(46) Betson, M. S.; Clayden, J.; Worrall, C. P.; Peace, S. *Angew. Chem. Int. Ed.* **2006**, *45*, 5803–5807.

(47) Woo, L. W. L.; Bubert, C.; Sutcliffe, O. B.; Smith, A.; Chander, S. K.; Mahon, M. F.; Purohit, A.; Reed, M. J.; Potter, B. V. L. *J. Med. Chem.* **2007**, *50*, 3540–3560.

(48) Dolle, R. E.; Schmidt, S. J.; Kruse, L. I. *J. Chem. Soc. Chem. Commun.* **1987**, 904–905.

(49) Du, C. J. F.; Hart, H.; Ng, K. K. D. *J. Org. Chem.* **1986**, *51*, 3162–3165.

(50) van der Sluis, P.; Spek, A. L. *Acta Crystallogr., Sect. A* **1990**, *46*, 194–201.

(51) Spek, A. L. *J. Appl. Crystallogr.* **2003**, *36*, 7–13.

(52) Chavez, F. A.; Briones, J. A.; Olmstead, M. M.; Mascharak, P. K. *Inorg. Chem.* **1999**, *38*, 1603–1608.

(53) Kucharski, E. S.; Skelton, B. W.; White, A. H. *Aust. J. Chem.* **1978**, *31*, 47–51.

(54) Poth, T.; Paulus, H.; Elias, H.; van Eldik, R.; Grohmann, A. *Eur. J. Inorg. Chem.* **1999**, *1999*, 643–650.

(55) Bernhardt, P. V.; Hayes, E. J. *Inorg. Chem.* **2002**, *41*, 2892–2902.

(56) Bernhardt, P. V.; Macpherson, B. P. *Acta Crystallogr., Sect. C* **2003**, *59*, m533–m536.

(57) Kon, H.; Nagata, T. *Inorg. Chem.* **2009**, *48*, 8593–8602.

(58) Attia, M. W.; Zangrando, E.; Randaccio, L.; Lopez, C. *Acta Crystallogr., Sect. C* **1987**, *C43*, 1521–1524.

(59) Brasch, N. E.; Buckingham, D. A.; Clark, C. R.; Simpson, J. *Inorg. Chem.* **1996**, *35*, 7728–7734.

(60) Cu-OH_2 bond length: 2.452 Å. Hong, L.; Li, X.-M.; Wang, Q.-W.; Xu, Z.-L.; Liu, B.; Xuaxue, J. *Chin. J. Struct. Chem.* **2010**, *29*, 801.

(61) Cu-OH_2 bond length: 2.680 Å. Caballero, A. B.; Rodríguez-Diéguez, A.; Lezama, L.; Salas, J. M. *Cryst. Growth Des.* **2012**, *12*, 3583–3593.

(61) Vedernikov, A. N.; Fettinger, J. C.; Mohr, F. *J. Am. Chem. Soc.* **2004**, *126*, 11160–11161.

(62) Bolton, R.; Sandall, J. P. B. *J. Chem. Soc. Perkin Trans. 2* **1977**, 278.

(63) Coe, J. W.; Wirtz, M. C.; Bashore, C. G.; Candler, J. *Org. Lett.* **2004**, *6*, 1589–1592.

Section 3.8 Supporting Information

Additional Experimental Details for $PY(CO_2)_4^{4-}$ and Its Complexes

Physical Measurements. ^1H and ^{13}C NMR spectra were collected at room temperature (22-25 °C) on Bruker AV-600, Bruker AVB-400 MHz, or AVQ-400 MHz instruments and analyzed with MestReNova software (v8.0.2-11021, Mestrelab Research S.L.). All resonances are referenced to the residual solvent signals of $CDCl_3$ (^1H, 7.26 ppm; ^{13}C, 77.16 ppm), D_2O (^1H, 4.80 ppm), methanol-d_4 (^1H, 3.31 ppm), and acetonitrile-d_3 (^1H, 1.94 ppm). The ^{13}C NMR of L_1 was referenced to $CDCl_3$ by dissolving L_1 in D_2O and inserting a 2 mm coaxial tube filled with $CDCl_3$ into the NMR tube. A Cary 5000 UV-Vis-NIR Spectrophotometer and Cary WinUV v3.0 software were used to obtain spectra of solution samples in water and diffuse reflectance spectra of solid samples mixed with poly(vinylidene fluoride) at room temperature (22 °C). A Kubelka–Munk conversion was applied to the diffuse reflectance spectra. Infrared spectra were collected on a Perkin-Elmer Spectrum 400 FT-IR Spectrometer using attenuated total reflectance (ATR) mode. Mass spectrometry was performed at the QB3/Chemistry Mass Spectrometry Facility at the University of California, Berkeley using an orthogonal acceleration quadrupole time-of-flight (Q-tof) mass spectrometer with an electrospray ionization (ESI) source operated in positive ion mode (Q-tof Premier, Waters, Milford, MA). CHN elemental analyses were performed at the Microanalytical Laboratory of the University of California, Berkeley.

Electrochemical Measurements. Electrochemical measurements were performed with a BioLogic SP-200 potentiostat and EC-Lab® v10.37 software. Experiments involving all $[PY(CO_2)_4]^{4-}$ complexes were performed under an argon atmosphere in a single compartment cell. The electrodes used included a glassy carbon working electrode, a Ag/AgCl (3.0 M NaCl) reference electrode for aqueous solutions, a silver wire pseudoreference electrode for acetonitrile solutions that was subsequently referenced to ferrocene, and a platinum wire counter electrode. The supporting electrolytes used in aqueous and acetonitrile solutions were 0.1 M $KClO_4$ or 0.1 M tetrabutylammonium hexafluorophosphate, respectively. The pH of the aqueous solutions was adjusted using KOH or HCl. Between each scan in aqueous solutions, the working electrode was removed from solution and polished with 0.05 micron MicroPolish (CH Instruments, Inc.).

Single Crystal X-ray Diffraction Methods. Crystallography was performed at the Small Molecule X-ray Crystallography Facility at the University of California, Berkeley, and the Advanced Light Source at Lawrence Berkeley National Laboratory. X-ray data was collected on single crystals coated with paratone oil and mounted on Kapton or MiTeGen loops. Data collections were performed at 100 K using a Bruker QUAZAR diffractometer equipped with a microfocus sealed X-ray source of Mo Kα (λ = 0.71073 Å) radiation and a Bruker APEX-II detector (Fe^{2+}, $Ni^{2+}(K^+)$, $[(L_1)Cu(H_2O)]$, $[(L_1)CuCl(H_2O)_2]^-$, PY4PhIMe$_2$); a Bruker APEX diffractometer equipped with a fine-focus sealed X-ray source of Mo Kα (λ = 0.71073 Å) radiation and a Bruker APEX-I detector (Mn^{2+}, Co^{2+}, $Zn^{2+}(K^+)$, $[(PY(CO_2Et)_4)Cu(THF)]^{2+}$); or at Beamline 11.3.1 at the Advanced Light Source using synchrotron radiation with either a Bruker AXS APEX II CCD detector or a Bruker PHOTON100 CMOS detector on a Bruker D8 Diffractometer (λ = 0.6888 Å for $Co^{3+}(OH^-/H_2O)$; λ = 0.7749 Å for $Ni^{2+}(Na^+)$, $Ni^{2+}(Cs^+)$, and $Co^{3+}(OH^-/MeO^-)$; λ = 0.8856 Å for $Ni^{2+}(Li^+)$ and Zn^{2+}(PPN)). Raw data were integrated and corrected for Lorentz and polarization effects using Bruker APEX2 V. 2011.4.[20] Absorption corrections were applied using SADABS[21] or TWINABS.[22] Space group assignments were determined by examination of systematic absences, E-statistics, and successive refinement of the

structures. All structures were solved by direct methods using SHELXT.[23] Additional refinement was performed with SHELXL-2014/7[24] operated through the WinGX[25] or OLEX2[26] interfaces. Molecular graphics were generated with DIAMOND.[27] None of the crystals showed significant decay during data collection.

Thermal parameters were refined anisotropically for all non-hydrogen atoms, with the exception of $K_2[(PY(CO_2)_4)Fe(H_2O)]$ and $[(L_1)Cu(H_2O)]$ data sets. For the Fe^{2+} structure, anisotropic refinement resulted in all carbon atoms (C1-C13) and two oxygen atoms from water molecules (O10/O11A) becoming non-positive definite as well as in a severely oblate ellipsoid for one of the carboxylate oxygen atoms (O7). As a consequence of the quality of this dataset, these atoms were refined isotropically only. In the case of $[(L_1)Cu(H_2O)]$, one molecule of water (O10/O10A) was found to be disordered over two positions. The disorder was modeled using the PART instruction, but as a result the two positions identified were too close for the atoms to be successfully anisotropically refined, and thus were refined isotropically only.

For the structures containing Fe^{2+}, $Ni^{2+}(K^+)$, and $Zn^{2+}(K^+)$ one molecule of water and one potassium atom were found to be disordered over two positions. The disorder was modeled using the PART instruction. Solvent water disordered over two positions was found in the $Co^{3+}(OH^-/MeO^-)$ structure as well. The relative occupancies of water in these two positions were refined against each other and then fixed. Additionally, the methoxide bound to the cobalt center was found to have only half occupancy. In the absence of the methoxide, the cobalt center was coordinated by hydroxide. Thus the oxygen coordinated to the cobalt center was assigned full occupancy, but the carbon of methoxide was assigned only half occupancy. In the $Ni^{2+}(Cs^+)$ structure, hydrogen atoms on two water molecules were found to be disordered over two orientations, thus their occupancies were fixed to 50%.

Whenever possible, hydrogen atoms of water molecules were identified from the electron density map and either refined using a riding model or fixed at 0.84 angstroms. In cases for which they could not be identified in this manner, datasets were refined without them, though they are acknowledged in the chemical formulas of the compounds given in the Supplementary Information. All other hydrogen atoms were placed in ideal positions and refined using a riding model.

The Fe^{2+}, $Co^{3+}(OH^-/MeO^-)$, $Ni^{2+}(Li^+)$, and $Zn^{2+}(K^+)$ structures were modeled as two-component non-merohedral twins based on the diffraction pattern. CELL_NOW was used to determine the orientation matrices, and the integration was preformed with both matrices. TWINABS was used to produce a merged HKLF4 file for structure solution and initial refinement and a HKLF5 file for final structure refinement. The HKLF5 file contained all reflections that involved domain 1. These structures were solved using the HKLF4 file, but the HKLF5 file gave the best refinement.

The structure of $Zn^{2+}(PPN)$ features dianionic Zn complexes with charge-balancing bis(triphenylphosphine)iminium cations. The bis(triphenylphosphine)iminium cations form sheets that are interspersed with layers that contain the dianionic Zn complexes surrounded by numerous water molecules. Examination of the diffraction pattern revealed diffuse scattering perpendicular to the layers in the crystal structure. This is likely due to imperfect stacking of the layers in the crystal, which would result in disorder between sheets. The crystal also diffracted very poorly beyond 1.00 angstrom resolution, so a resolution of 0.83 angstroms could not be achieved. The data used for refinement was integrated to a resolution limit where I/sigma > 3 and $R_{int} < 0.25$. The diffuse scattering and weak diffraction of the crystal lead to a structure that is of

inadequate quality for accurate determination of bond distances and angles. Thus, only the overall connectivity and arrangement of molecules should be interpreted from the structure.

In the structure of $[(PY(CO_2Et)_4)Cu(THF)]^{2+}$, residual electron density due to a disordered diethyl ether solvent molecule could not be modeled. Thus, it was removed using SQUEEZE.[50,51]

The structures for $Ni^{2+}(Na^+)$, $Ni^{2+}(K^+)$, Co^{2+}, $Co^{3+}(OH^-/MeO^-)$, $Co^{3+}(OH^-/H_2O)$, $[(PY(CO_2Et)_4)Cu(THF)]^{2+}$, $[(L_1)Cu(H_2O)]$, $[(L_1)CuCl(H_2O)_2]^-$, Fe^{2+}, $Zn^{2+}(K^+)$, and $Zn^{2+}(PPN)$ gave rise to A and B level alerts from checkCIF. Responses addressing these alerts have been included in the CIFs and can be read in reports generated by checkCIF.

Discussion of $K_2[(PY(CO_2)_4)Co(OH)]$

The trivalent cobalt complex $K_2[(PY(CO_2)_4)Co(OH)]$ was first obtained by combining equimolar portions of $CoCl_2 \cdot 6H_2O$ and $K_4[PY(CO_2)_4]$ in methanol in air, utilizing O_2 as an oxidant. This complex is insoluble in methanol and consequently was isolated as a dark purple powder by filtration of the crude reaction mixture. However, structural characterization by X-ray crystallography showed that the crystals grown by diffusion of acetone into aqueous solutions of $K_2[(PY(CO_2)_4)Co(OH)]$ displayed only half occupancy of the axial hydroxide, with the remaining occupancy being filled by methoxide (Figure S3.21).

Thus, a cleaner and more efficient route was established via oxidation of $K_2[(PY(CO_2)_4)Co(H_2O)]$ with H_2O_2 in water. In addition to a color change from pink to purple that was observed during the reaction, the assignment of a Co^{3+} oxidation state was supported by the X-ray crystal structure due to the anticipated contraction of metal-ligand bond lengths (Table S3.6). The $Co–N_{PY}$ and average $Co–O_{eq}$ distances for the two nearly identical complexes in the crystal were found to be 1.882(1)-1.886(1) Å and 1.885(1)-1.887(1) Å, respectively, which are similar to those found in a series of low-spin Co^{3+} acetylacetonate complexes.[52] Indeed, the ^1H NMR spectrum was consistent with the presence of a diamagnetic, low-spin Co^{3+} center.

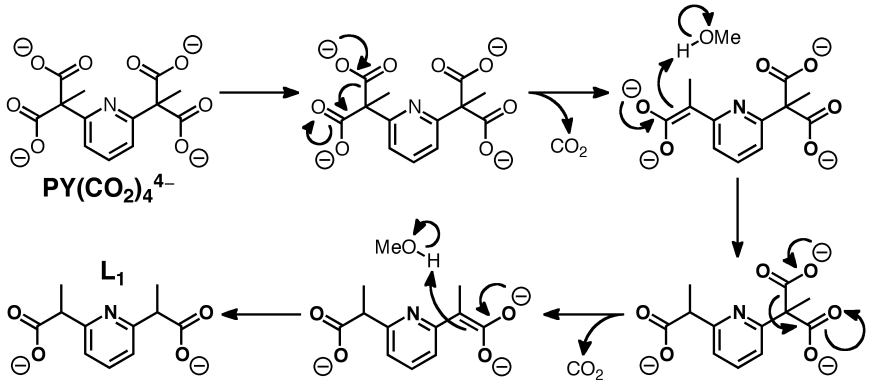
Although elemental analysis was in agreement with the expected molecular formula for $K_2[(PY(CO_2)_4)Co(OH)]$, the crystal used in the X-ray diffraction study exhibited only $1.5K^+$ per cobalt center instead of the expected $2K^+$. Upon further inspection, hydrogen atoms identified from the electron difference map explained this discrepancy by revealing that one cobalt center was in fact bound to a hydroxide moiety while the other was instead bound to a water molecule. Indeed, the $Co–O_{OH}$ distance (1.899(1) Å) was in good agreement with other Co^{3+}–OH distances previously reported in the literature,[53-57] and though the $Co–O_{water}$ distance (1.912(1) Å) was found to be shorter than most, it is not unprecedented as shown by other published systems.[58,59]

The aqueous UV-visible-NIR spectrum of this complex exhibited maxima at 374 and 541 nm, which matched well with the $^1T_{2g} \longleftarrow {}^1A_{1g}$ and $^1T_{1g} \longleftarrow {}^1A_{1g}$ transitions found in other octahedral Co^{3+} complexes.[54] These absorption bands are redshifted compared to the λ_{max} of 343 and 480 nm found for the related complex $[(PYN_4)Co(OH)]^{2+}$ (PYN_4 = 2,2'-(pyridine-2,6-diyl)bis(2-methylpropane-1,3-diamine)), in which the four equatorial carboxylates of $[PY(CO_2)_4]^{4-}$ are replaced with neutral primary amines. Considering the positions of carboxylates and amines in the spectrochemical series, a weaker ligand field for $[PY(CO_2)_4]^{4-}$ is to be expected.

Isolation of the Decomposition Product $K_2(L_1)$ (L_1 = 2,2'-(pyridine-2,6-diyl)dipropanoate)

$K_4[PY(CO_2)_4]$ was suspended in MeOH to give a cloudy solution and stirred at room temperature overnight. The solution was vacuum filtered, and the filtrate was concentrated. The product was obtained by diffusion of acetone into the methanolic solution. The resulting white powder was isolated by vacuum filtration. 68% yield. ^{1}H NMR (D_2O, 400 MHz): δ 7.75 (t, J = 7.8 Hz, 1H), 7.21 (d, J = 7.8 Hz, 2H), 3.75 (m, 2H), 1.42 (dd, J = 7.3, 2.6 Hz, 6H). ^{13}C NMR (D_2O, 400 MHz): δ 182.4, 161.6, 160.4, 138.8, 138.7, 119.8, 119.7, 50.6, 17.9, 17.8 IR (neat, cm^{-1}): 3008w, 2991w, 2961m, 2844w, 1663s, 1656s, 1473m, 1458m, 1434s, 1391s, 1355s, 1294s, 1183s, 1161m, 1071s, 1008m, 890s, 824s, 796m, 776w, 748m, 725m, 705m, 684m, 662w, 628m, 583s, 555m, 518m, 475w. ESI-MS (m/z): $\{C_{11}H_{11}K_3NO_4\}^+$, 338; $\{C_{11}H_{12}K_2NO_4\}^+$, 300; $\{C_{11}H_{13}KNO_4\}^+$, 262; $\{C_{11}H_{11}KNO_4\}^-$, 260. Anal. Calcd. for $C_{11}H_{11}K_2NO_4 \cdot 5KOH \cdot 0.5H_2O$: C, 22.43; H, 2.91; N, 2.38%. Found: C, 22.89; H, 2.37; N, 1.65%.

Scheme S3.1. Proposed decomposition pathway of $[PY(CO_2)_4]^{4-}$ to generate a racemic mixture of L_1.



Synthesis of $(PPN)_2[(PY(CO_2)_4)M(H_2O)]$ ($M = Ni^{2+}, Zn^{2+}$) Complexes

$K_2[(PY(CO_2)_4)Zn(H_2O)] \cdot 1.5\ H_2O$ (29 mg, 0.062 mmol) was suspended in 1.5 mL deionized water and sonicated until the solids dissolved. Separately, bis(triphenylphosphoranylidene)ammonium (PPN) chloride (97% pure, 35 mg, 0.059 mmol) was dissolved in 0.5 mL of ethanol. The two solutions were mixed and then filtered to remove any remaining particulate. The filtrate was place in a vial, which was left open to air. After two to three d, colorless crystals formed. The product was collected by vacuum filtration and then left to dry in air for 6 h to yield 38 mg (37% yield) of white solid. ^{1}H NMR (methanol-d_4, 400 MHz,) δ 7.80 (t, J = 8.1 Hz, 1H), 7.46 (d, J = 8.1 Hz, 2H), 1.83 (s, 6H). IR (neat, cm^{-1}): 3406m, 3054w, 1607s, 1583s, 1480m, 1458m, 1434m, 1386m, 1362m, 1283s, 1246s, 1184m, 1160w, 1110s, 1024m, 996m, 921w, 888s, 840w, 829m, 792w, 750s, 720s, 689s, 630s, 614s, 592s, 544s, 529s, 498s, 446s, 428s, 410s. Anal. Calcd. for $C_{85}H_{71}N_3O_9P_4Zn \cdot 11H_2O$: C, 61.28; H, 5.63; N, 2.52%. Found: C, 61.58; H, 5.61; N, 2.51%.

$(PPN)_2[(PY(CO_2)_4)Ni(H_2O)]$ was synthesized in the same manner from $K_2[(PY(CO_2)_4)Ni(H_2O)] \cdot H_2O$ to yield 41 mg (40% yield) of purple solid. IR (neat, cm^{-1}): 3389m, 3050w, 1607s, 1576s, 1480m, 1456m, 1434s, 1384s, 1357m, 1281s, 1241s, 1184m, 1162w, 1110s, 1072w, 1024w, 996s, 886s, 827w, 809w, 790w, 750s, 722s, 689s, 627w, 614m, 590m, 544s, 529s, 500s, 483m, 476m, 454m, 417s, 408s. Anal. Calcd. for $C_{85}H_{71}N_3NiO_9P_4 \cdot 10\ H_2O$: C, 62.20; H, 5.59; N, 2.56%. Found: C, 62.10; H, 5.63; N, 2.55%.

NMR Study of $(PPN)_2[(PY(CO_2)_4)Zn(H_2O)]$ in Methanol-d_4 and Acetonitrile-d_3

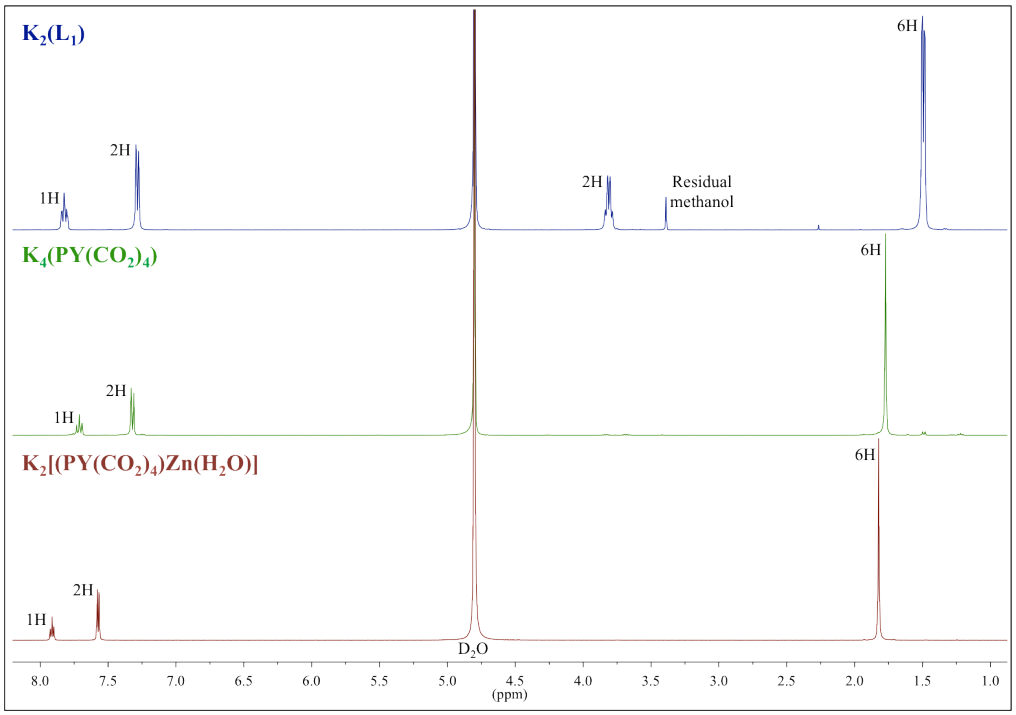


Figure S3.1. ^{1}H NMR spectra at room temperature in D_2O of $K_2[(PY(CO_2)_4)Zn(H_2O)]$, free $K_4[PY(CO_2)_4]$, and $K_2(L_1)$.

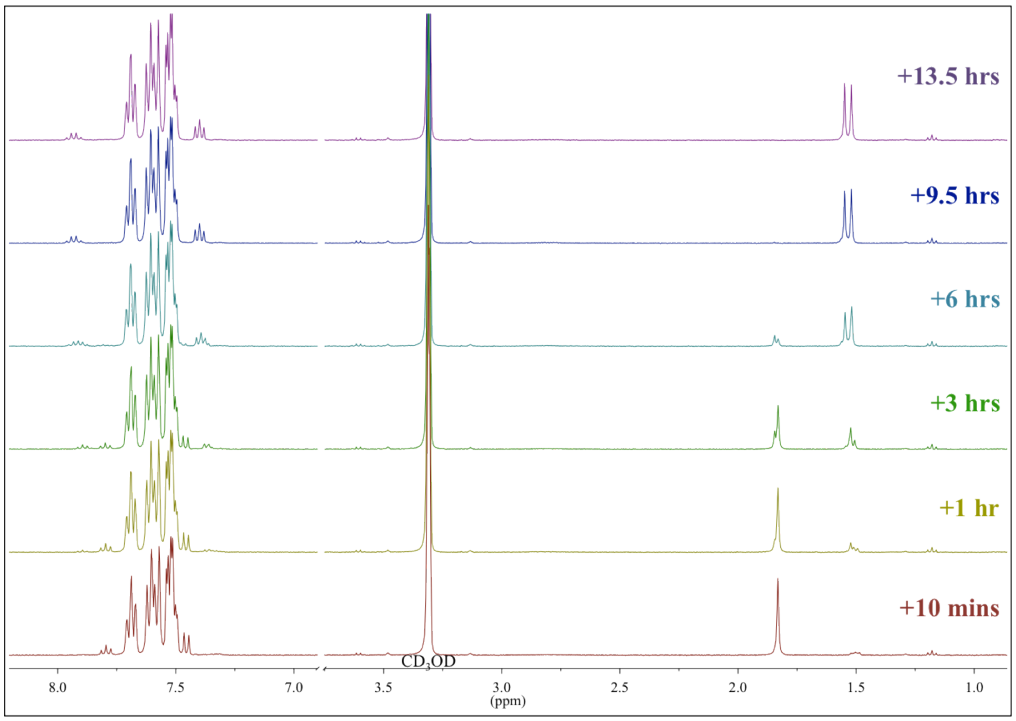


Figure S3.2. The ^{1}H NMR spectra of $(PPN)_2[(PY(CO_2)_4)Zn(H_2O)]$ in methanol-d_4 at room temperature shows that the complex decomposes in less than 9.5 hours.

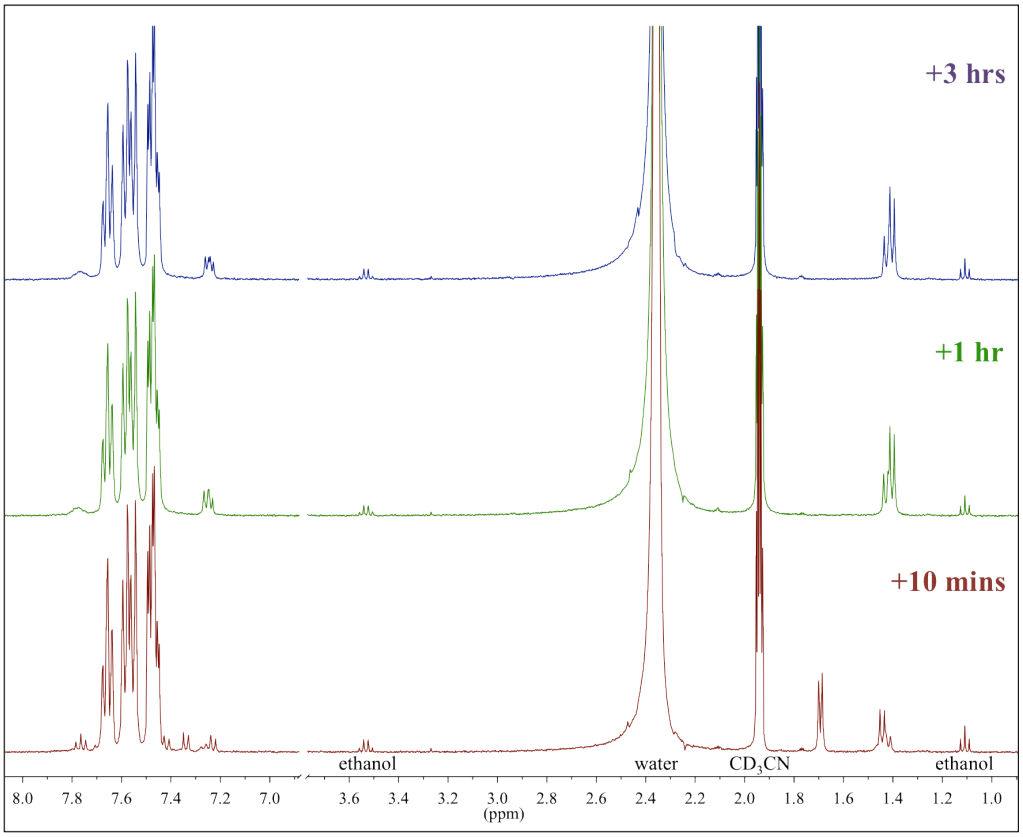


Figure S3.3. The ^{1}H NMR spectra of $(PPN)_2[(PY(CO_2)_4)Zn(H_2O)]$ in acetonitrile-d_3 at room temperature shows that the complex completely decomposes in less than 1 hour.

The NMR spectra in D_2O of $K_2[(PY(CO_2)_4)Zn(H_2O)]$, $K_4[PY(CO_2)_4]$, and the decomposition product $K_2(L_1)$ (L_1 = 2,2'-(pyridine-2,6-diyl)dipropanoate) are shown for reference in Figure S3.1. The decomposition of $[(PY(CO_2)_4)Zn(H_2O)]^{2-}$ in organic solvents was tracked via ^{1}H NMR spectroscopy in both methanol-d_4 (Figure S3.2) and acetonitrile-d_3 (Figure S3.3). The prominent signals in the ranges of 7.48-7.73 ppm in methanol-d_4 and 7.44-7.70 ppm in acetonitrile-d_3 correspond to the aromatic rings of PPN^+ and do not change over the course of the experiments, as ^{31}P NMR spectra collected at every time point showed no change. Thus, it was concluded that the PPN^+ cations remained fully intact.

The initial NMR spectrum of $(PPN)_2[(PY(CO_2)_4)Zn(H_2O)]$ in methanol-d_4 appeared similar to that of the potassium salt in D_2O, in particular the signals of the methyl groups were 1.83 ppm and 1.82 ppm, respectively. After 9 h the signal of the intact complex at 1.83 ppm had completely disappeared and had been replaced by a doublet upfield at 1.53 ppm, imitating the shift to 1.42 ppm observed for the methyl signal of the $[PY(CO_2)_4]^{4-}$ decomposition product L_1. Unlike the ^{1}H NMR spectrum of L_1, the spectrum in Figure S3.2 taken after 9 h did not exhibit the expected quartet corresponding to the new proton alpha to the remaining carboxylate. Its absence was attributed to the experiment being performed in a deuterated solvent, since this signal was also missing when the decomposition of $K_4[PY(CO_2)_4]$ was followed in D_2O. Only when the decomposition took place in a protonated solvent was the quartet observed in the NMR spectrum of the resulting L_1 product.

Decomposition in acetonitrile-d_3 was significantly faster than that observed in methanol-d_4. After the 10 min required to prepare the sample and to obtain the NMR spectrum, the signal at

1.69 ppm, which was attributed to the intact complex, had already begun to split into two features. Additionally, three doublets—opposed to the expected one—were observed in the aromatic region, further supporting the conclusion that the intact complex was no longer the only species in solution. After only 1 h, the signal at 1.69 ppm had completely disappeared, leaving a new signal at 1.41 ppm, while the series of doublets in the aromatic region had coalesced into a single feature at 7.25 ppm.

The explanation that the complex decomposed due to the removal of the potassium cations was disregarded seeing as $(PPN)_2[(PY(CO_2)_4)Zn(H_2O)]$ and $(PPN)_2[(PY(CO_2)_4)Ni(H_2O)]$ could be isolated as crystals from a mixture of water and ethanol and that these products passed elemental analysis successfully. Furthermore, once collected by vacuum filtration, these crystals were stable at room temperature for at least 2 months at ambient temperature. As shown in the crystal structure in Figure S3.22, the Zn^{2+} complexes and the PPN cations organize into alternating layers, leaving large spaces between the complexes that are filled with disordered water molecules. This observation suggests that water might provide a stabilizing environment for the complex. Conversely, dissolving the salt in an organic solvent would effectively eliminate the aqueous environment and corresponding hydrogen-bonding network around the complexes, resulting in its decomposition. The necessity of a hydrogen-bonding network is further supported by the fact that $[(PY(CO_2)_4)Zn(H_2O)]^{2-}$ persisted longer in methanol than in that of the aprotic acetonitrile. A second explanation for the faster decomposition of the Zn^{2+} complex in acetonitrile could be due to acetonitrile being a stronger ligand compared to either methanol or water. Consequently, it might compete with $[PY(CO_2)_4]^{4-}$ to the extent that the resulting displacement of the equatorial carboxylates from the metal center is long enough to promote decomposition.

Because of the clean conversion to a single decomposition product and the notable upfield shift of the methyl signals in these two experiments, which mirrored the shift of the methyl signals resulting from the decarboxylation of the $[PY(CO_2)_4]^{4-}$ ligand to form L_1, it was concluded that the complex was not stable in these solvents and that the ligand was likely decarboxylating to form L_1. Although an X-ray crystal structure of the Zn^{2+} decomposition product could not be obtained, crystal structures of Cu^{2+} bound to L_1 were isolated (Figures S3.18 and S3.19) and provide additional evidence that L_1 or a complex of the metal and L_1 were indeed formed.

Evaluation of $(PPN)_2[(PY(CO_2)_4)Ni(H_2O)]$ in Organic Solvents

Table S3.1. Color changes of methanol and acetonitrile solutions of $(PPN)_2[(PY(CO_2)_4)Ni(H_2O)]$ over time at room temperature.

Time after dissolution of $(PPN)_2[(PY(CO_2)_4)Ni(H_2O)]$	Methanol	Acetonitrile
0 hours	Purple	Purple
6 hours	Purple	Blue
1 day	Purple	Green
2 days	Purple-blue	Pink
3 days	Blue-green	Red

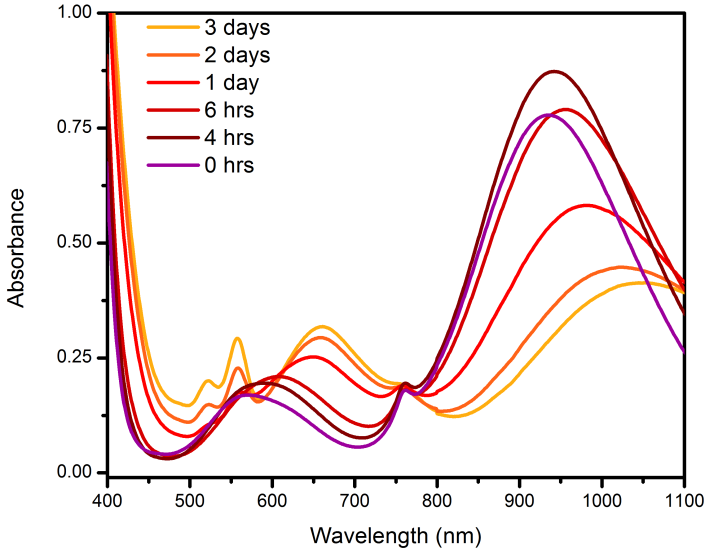


Figure S3.4. UV-visible spectrum of $(PPN)_2[(PY(CO_2)_4)Ni(H_2O)]$ in acetonitrile over 3 d at room temperature.

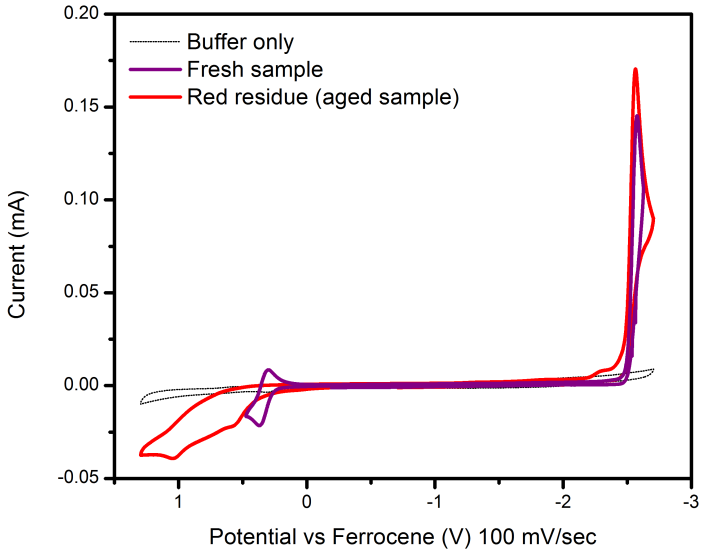


Figure S3.5. Cyclic voltammograms at 100 mV sec^{-1} of freshly made and aged samples of $(PPN)_2[(PY(CO_2)_4)Ni(H_2O)]$ in acetonitrile. Glassy carbon working electrode, silver wire pseudo-reference electrode, platinum wire counter electrode. A 0.1 M solution of tetrabutylammonium hexafluorophosphate was used as the supporting electrolyte.

Color changes were observed in solutions of $(PPN)_2[(PY(CO_2)_4)Ni(H_2O)]$ in organic solvents as reported by Table S3.1. In particular, the color change in acetonitrile was tracked via UV-visible-NIR spectroscopy (Figure S3.4). Initially, the complex exhibited maxima at 571, 762, and 935 nm, which matched well with the λ_{max} values for $[(PY(CO_2)_4)Ni(H_2O)]^{2-}$ in aqueous solution. Yet, after 3 d the peaks at 571 and 935 nm had shifted to 661 and 1053 nm, respectively, and two new features had appeared at 522 and 558 nm. Cyclic voltammetry was used to further investigate this transformation. As shown in Figure S3.5, a fresh solution of $(PPN)_2[(PY(CO_2)_4)Ni(H_2O)]$ dissolved in acetonitrile exhibited a reversible oxidation at 0.36 V versus ferrocene, whereas a solution prepared with the red product obtained from the UV-visible experiment no longer possessed this feature and instead exhibited two irreversible oxidations at 0.59 and 1.05 V. These data suggested that, like $[(PY(CO_2)_4)Zn(H_2O)]^{2-}$, the Ni^{2+} complex was not stable in organic solvents and consequently decomposed.

Attempts to Isolate $K_2[(PY(CO_2)_4)Cu(H_2O)]$

Despite attempts to metalate $[PY(CO_2)_4]^{4-}$ with copper using the same methods as for the other divalent metal compounds, formation of the desired Cu^{2+} complex could not be validated by elemental analysis or mass spectrometry. Additionally, recrystallization of the blue solids that were obtained from these reactions by slow diffusion of acetone into aqueous solution produced only powders. Consequently, other reaction and recrystallization conditions were explored.

In one attempt, the synthesis of the copper complex was performed in the same manner as for the other $[PY(CO_2)_4]^{4-}$ complexes, but the isolated blue solids were recrystallized via slow evaporation in air from a concentrated aqueous KCl solution. An X-ray diffraction study indicated that the resulting crystals contained $K[(L_1)CuCl(H_2O)_2]$ rather than the desired $[PY(CO_2)_4]^{4-}$ complex. As shown in Figure S3.18, L_1 chelated as a tridentate ligand, a chloride atom coordinated trans to the nitrogen of the pyridine ring, and two trans water molecules completed the distorted octahedral environment. This complex exhibits an axial elongation along the axis of the water molecules with a Cu–O bond length of 2.6556(11) Å. Although this distance is toward the longer end of Cu–OH_2 bond lengths it is not unprecedented, as other complexes have contained comparable lengths in cases where the water ligand bridges two metal cations.[60.61] As shown in Figure S3.18, these water molecules are also bound to the potassium countercations.

In another attempt, the synthesis of a copper complex was performed using the same synthetic methods as for the other $[PY(CO_2)_4]^{4-}$ complexes but with $Cu(OAc)_2$ as the metal salt instead of $CuCl_2$. Once the blue powder had been isolated, a small amount was dissolved in a minimal amount of a 0.1 M solution of aqueous KOAc. The solution was stored in a vial for three days, after which time blue crystals had formed. Single crystal X-ray diffraction revealed the identity of the isolated species to be $[(L_1)Cu(H_2O)]$, which is depicted in Figure S3.19. One carboxylate oxygen (O_7) on each ligand bridges to a copper atom on the adjacent complex to form chains in the solid state. A single water molecule bound to each copper atom completes the distorted trigonal bipyramidal coordination environment.

Supplemental NMR Spectra

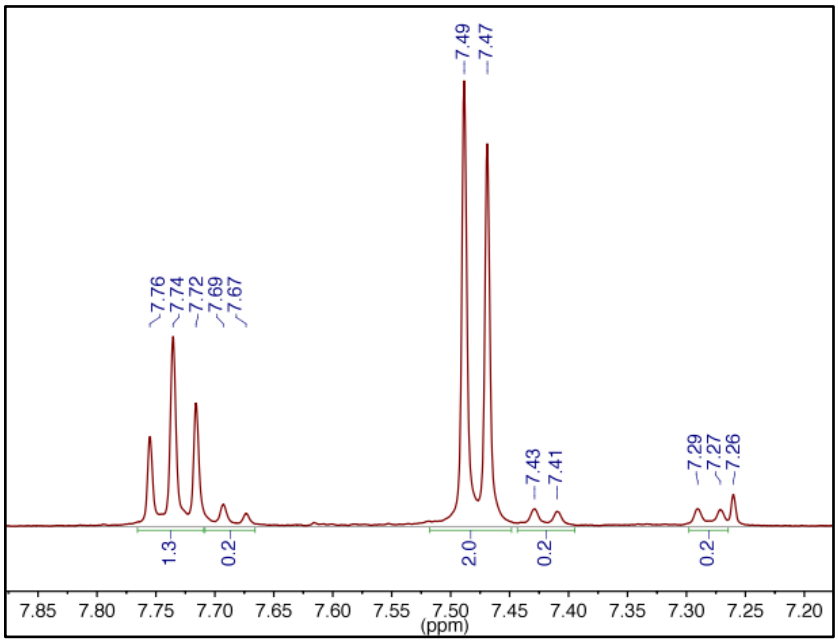


Figure S3.6. The ^{1}H NMR spectrum at room temperature in $CDCl_3$ of the aromatic region of tetraethyl 2,2′-(pyridine-2,6-diyl)dimalonate, the precursor to $PY(CO_2Et)_4$, and the impurity that could not be completely removed by column chromatography. The assignment of the impurity peaks in the upfield region was difficult due to overlap with the signals of the precursor, thus only the aromatic signals are reported here. Impurity: ^{1}H NMR ($CDCl_3$, 400 MHz): δ 7.69 (t, J = 7.7 Hz, 1H), 7.42 (d, J = 7.8 Hz, 1H), 7.28 (d, J = 7.7 Hz, 1H).

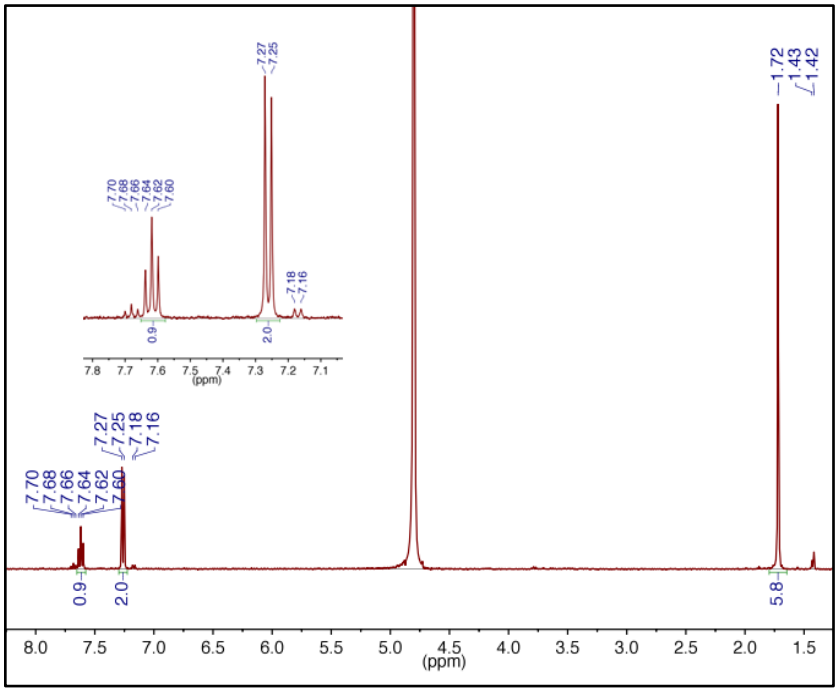


Figure S3.7. A typical ^{1}H NMR spectrum of crude $[PY(CO_2)_4]^{4-}$ in D_2O at room temperature and a small amount of side product, the latter of which corresponds well with the NMR spectrum of L_1 shown in Figure S10. Side product: ^{1}H NMR (D_2O, 400 MHz): δ 7.68 (t, J = 7.8 Hz, 1H), 7.17 (d, J = 8.0 Hz, 2H), 1.43 (d, J = 6.9 Hz, 6H).

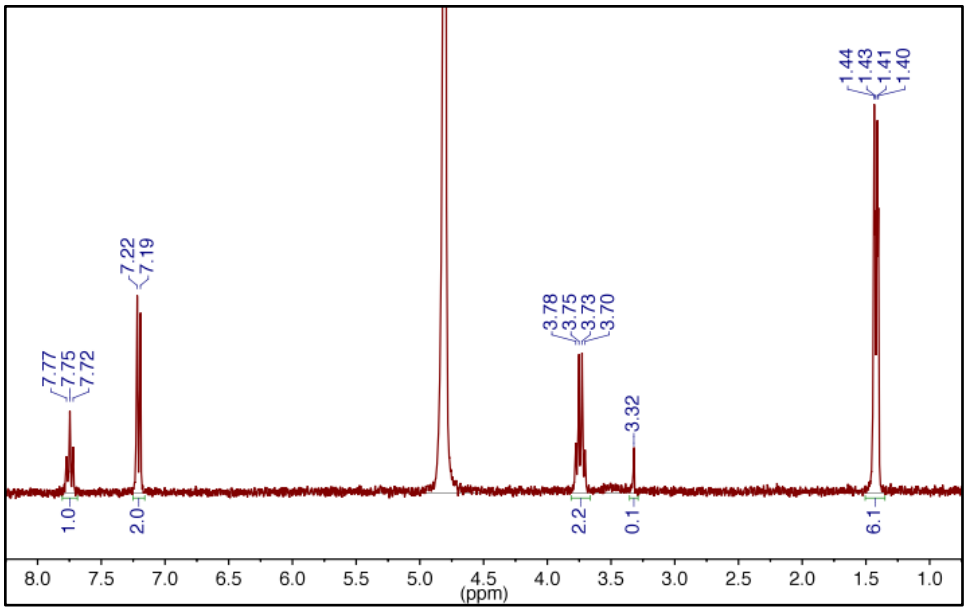


Figure S3.8. ^{1}H NMR spectrum of L_1 in D_2O at room temperature. The signal at 3.32 ppm is due to residual methanol.

Electrochemical and UV-visible Absorption Spectra for the $[PY(CO_2)_4]^{4-}$ Complexes

Table S3.2. Electrochemistry of metal complexes $K_2[(PY(CO_2)_4)M(H_2O)]$.

M	Mn^{2+}	Fe^{2+}	Co^{2+}	Ni^{2+}	Zn^{2+}
Potential, V vs. Ag/AgCl[a]	$E_{pa} = 0.90$ $E_{pa} = 0.30$	$E_{1/2} = -0.16$	$E_{pa} = 0.74$ $E_{pc} = -0.30$	$E_{1/2} = 1.24$	$E_{pa} = 1.75$

[a] 100 mV sec^{-1} in 0.1 M $KClO_4$ buffer at pH 7. Glassy carbon working electrode, Ag/AgCl reference electrode, platinum wire auxiliary electrode.

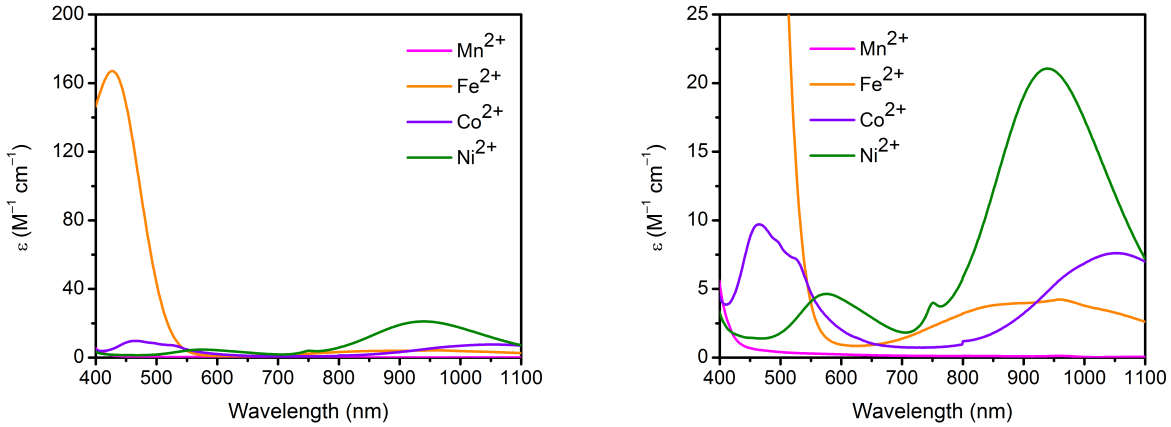


Figure S3.9. UV-Visible absorption spectra of $K_2[(PY(CO_2)_4)M(H_2O)]$ complexes (M = Mn^{2+}, Fe^{2+}, Co^{2+}, Ni^{2+}) in water. The Mn^{2+} (53 mM), Fe^{2+} (10 mM), and Co^{2+} (23 mM) samples were prepared under N_2 in a glovebag. The Ni^{2+} (72 mM) sample was prepared in air. All spectra were obtained at room temperature (22 °C).

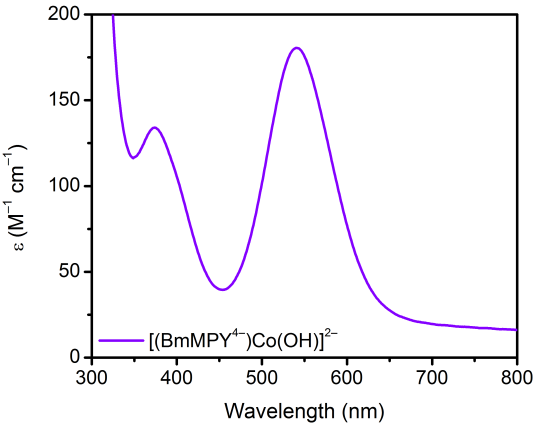


Figure S3.10. UV-Visible absorption spectrum of $K_2[(PY(CO_2)_4)Co(OH)]$ (2 mM) in water at room temperature (22 °C). The sample was prepared in air.

UV-visible and Diffuse Reflectance Spectra of $A_2[(PY(CO_2)_4)Ni(H_2O)]$ Complexes ($A = Li^+$, Na^+, K^+, Cs^+)

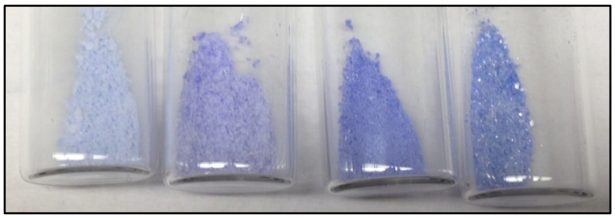


Figure S3.11. Crystals of $Li_2[(PY(CO_2)_4)Ni(H_2O)]$ (far left), $Na_2[(PY(CO_2)_4)Ni(H_2O)]$, $K_2[(PY(CO_2)_4)Ni(H_2O)]$, and $Cs_2[(PY(CO_2)_4)Ni(H_2O)]$ (far right).

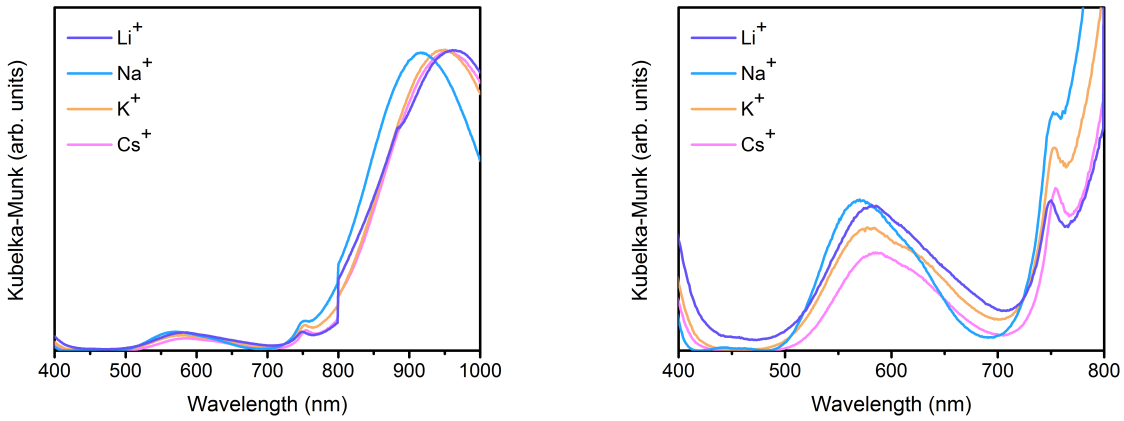


Figure S3.12. Diffuse reflectance spectra of $A_2[(PY(CO_2)_4)Ni(H_2O)]$ ($A = Li^+$, Na^+, K^+, Cs^+) after Kubelka-Munch treatment.The sudden step at 800 nm is an artifact due to an adjustment of the spectrometer grating.

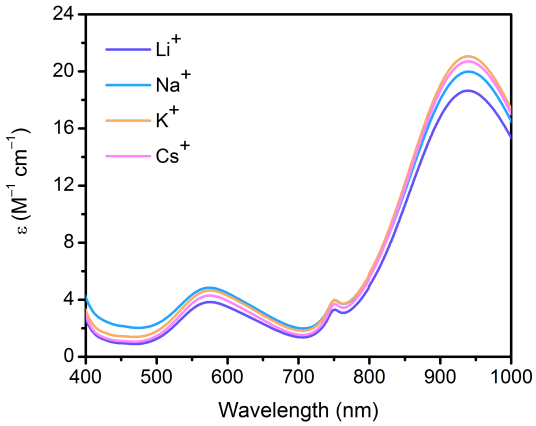


Figure S3.13. UV-visible spectra of $A_2[(PY(CO_2)_4)Ni(H_2O)]$ ($A = Li^+$, Na^+, K^+, Cs^+) complexes in water. The Li^+ (70 mM), Na^+ (72 mM), K^+ (72 mM) and Cs^+ (71 mM) samples were prepared in air. All spectra were obtained at room temperature (22 °C).

IR Spectra for the $[PY(CO_2)_4]^{4-}$ Complexes

Table S3.3. Carbonyl stretches of $[PY(CO_2)_4]^{4-}$ complexes.

Compound	ν(CO) cm^{-1}
$K_4[PY(CO_2)_4]$	1560
$K_2[(PY(CO_2)_4)Mn(H_2O)]$	1612, 1577, 1568
$K_2[(PY(CO_2)_4)Fe(H_2O)]$	1615, 1570
$K_2[(PY(CO_2)_4)Co(H_2O)]$	1616, 1572
$K_2[(PY(CO_2)_4)Co(OH)]$	1666, 1637, 1589, 1571
$Li_2[(PY(CO_2)_4)Ni(H_2O)]$	1638, 1628, 1571
$Na_2[(PY(CO_2)_4)Ni(H_2O)]$	1591, 1572
$K_2[(PY(CO_2)_4)Ni(H_2O)]$	1618, 1610, 1589, 1577, 1571, 1560
$Cs_2[(PY(CO_2)_4)Ni(H_2O)]$	1619, 1586, 1575
$K_2[(PY(CO_2)_4)Zn(H_2O)]$	1636, 1624, 1617, 1610, 1577, 1571, 1560
$(PPN)_2[(PY(CO_2)_4)Ni(H_2O)]$	1607, 1583
$(PPN)_2[(PY(CO_2)_4)Zn(H_2O)]$	1607, 1576

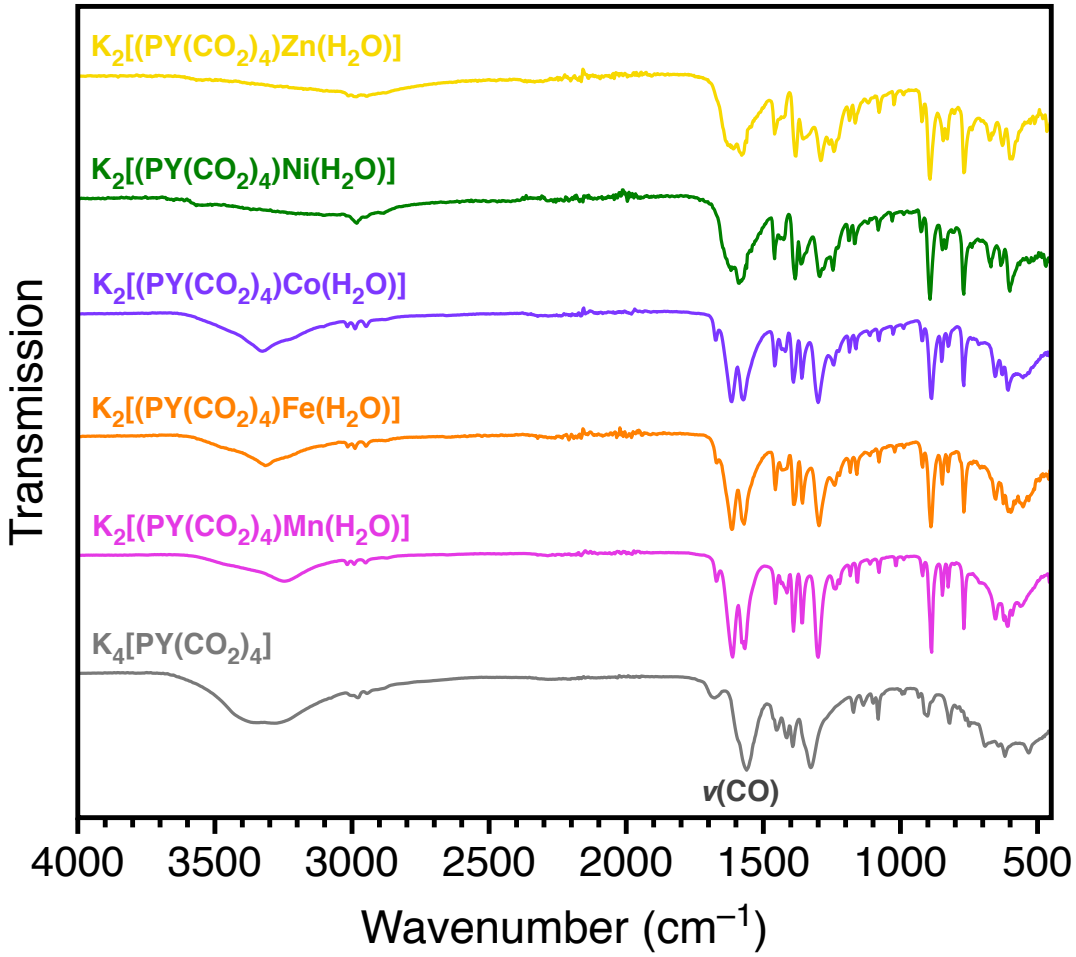


Figure S3.14. IR spectra at room temperature of the $K_2[(PY(CO_2)_4)M(H_2O)]$ complexes (M = Mn^{2+}, Fe^{2+}, Co^{2+}, Ni^{2+}, Zn^{2+}) and the $K_4[PY(CO_2)_4]$ ligand.

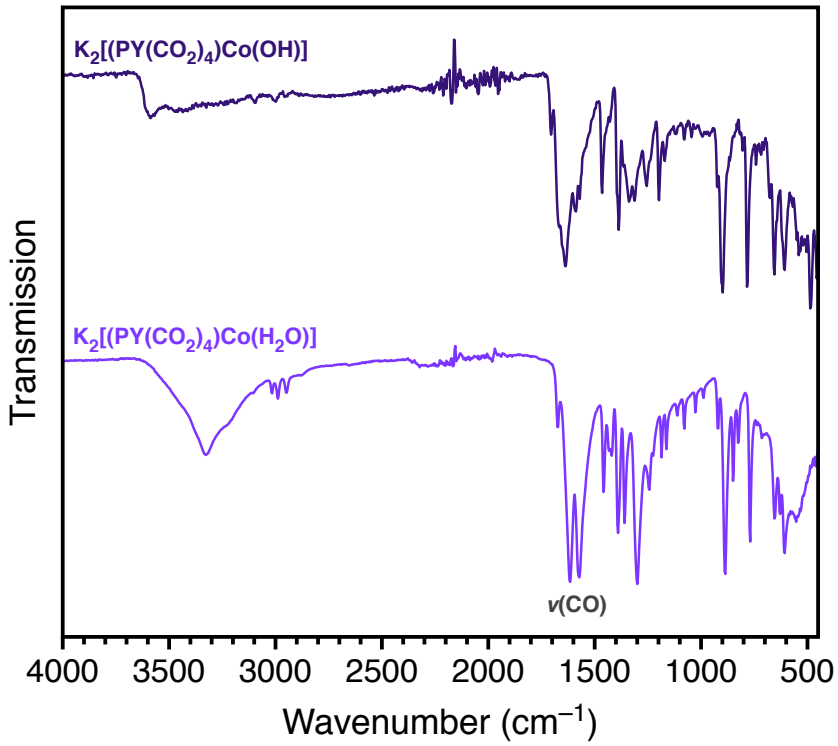


Figure S3.15. IR spectra at room temperature of $K_2[(PY(CO_2)_4)Co(H_2O)]$ and of $K_2[(PY(CO_2)_4)Co(OH)]$.

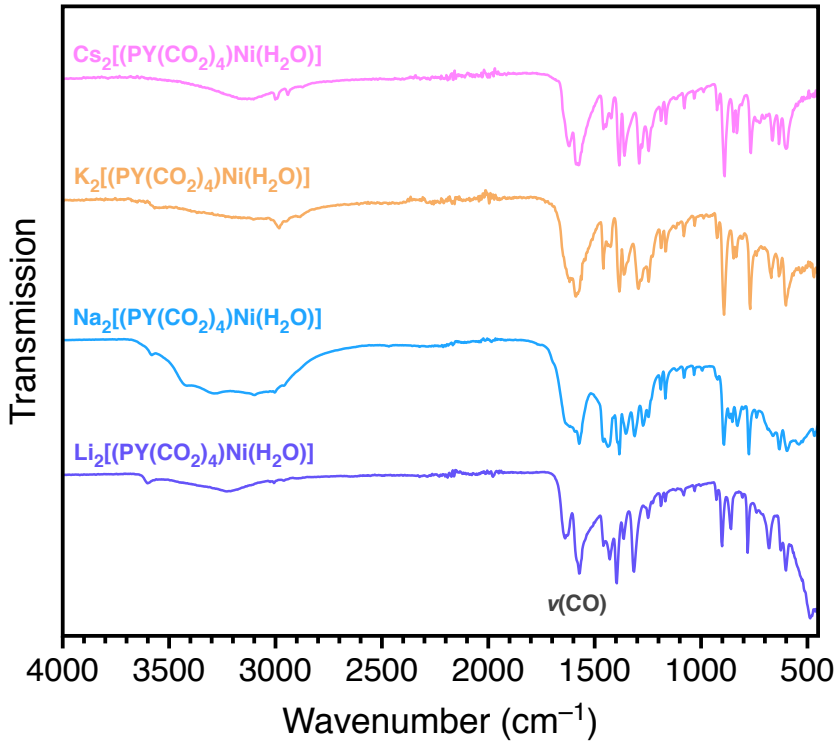


Figure S3.16. IR spectra at room temperature of the $A_2[(PY(CO_2)_4)Ni(H_2O)]$ complexes ($A = Li^+$, Na^+, K^+, Cs^+).

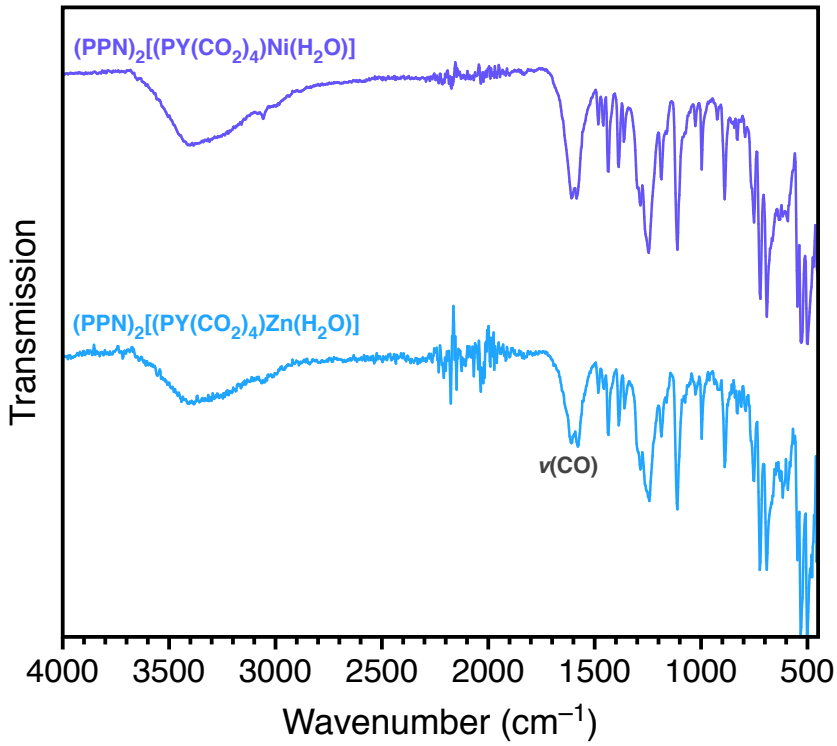


Figure S3.17. IR spectra at room temperature of $(PPN)_2[(PY(CO_2)_4)Zn(H_2O)]$ and $(PPN)_2[(PY(CO_2)_4)Ni(H_2O)]$.

Single-crystal X-ray Diffraction Studies

Single Crystal X-ray Structures of Cu^{2+} Complexes

Table S3.4. Crystallographic data for Cu^{2+} complexes $[(PY(CO_2Et)_4)Cu(THF)]^{2+}$, $[(L_1)Cu(H_2O)]$, and $[(L_1)CuCl(H_2O)_2]^-$ with selected bond lengths (Å) and angles (deg).

Compound	$[(PY(CO_2Et)_4)Cu(THF)]^{2+}$		$[(L_1)Cu(H_2O)]$	$[(L_1)CuCl(H_2O)_2]^-$
Formula	$C_{27}H_{37}CuF_6NO_{15}S_2$		$C_{11}H_{15}CuNO_6$[a]	$C_{11}H_{15}ClCuKNO_6$
FW	857.23		320.79	395.33
Crystal system	Monoclinic		Monoclinic	Monoclinic
Space Group	*P 2₁/n*		*P 2₁/n*	*C 2/c*
Z	4		4	4
a, Å	9.1417(8)		8.3978(6)	11.1219(6)
b, Å	26.613(2)		7.3031(5)	21.1832(13)
c, Å	17.0582(14)		19.9835(14)	6.8152(3)
α, deg	90		90	90
β, deg	95.3160(10)		90.631(3)	118.754(2)
γ, deg	90		90	90
V, Å^3	4132.2(6)		1225.51(15)	1407.66(13)
Temperature, K	100(2)		100(2)	100(2)
Wavelength, Å	0.71073		0.71073	0.71073
Reflections collected	125863		17809	26759
Independent reflections	7574		2250	1299
R(int), %	3.43		6.11	2.41
Completeness to theta = 25.000°, %	100.0		100.0	100.0
Goodness-of-fit on F^2	1.033		1.055	1.098
R1(wR2), %	3.30(7.95)		3.81(8.68)	1.80(4.41)
M–O_1, Å	2.2078(15)	M–O_1, Å	1.933(2)	1.9383(12)
M–O_2, Å	2.0196(14)	M–O_3, Å	1.950(2)	1.9383(12)
M–O_3, Å	2.1723(14)	M–N_{Py}, Å	2.009(3)	2.0135(19)
M–O_4, Å	2.0550(15)	M–O_{water}, Å	2.162(2)	2.6556(11)
M–O_{THF}, Å	1.9432(15)	M–O_7, Å	2.019(2)	--
M–N_{Py}, Å	1.9895(16)	M–Cl, Å	--	2.2852(6)
O_{axial}–M–N_{py}	178.17(7)	Cl–M–N_{py}, deg	--	180
O_1–M–O_3, deg	173.32(6)	O_1–M–O_3, deg	178.01(10)	179.29(7)
O_2–M–O_4, deg	174.92(6)			

[a]Hydrogen atoms on water molecules were placed when identified in the electron difference map; however, not all could be located. Two missing hydrogen atoms from this dataset were omitted from the refinement but included in the given formula.

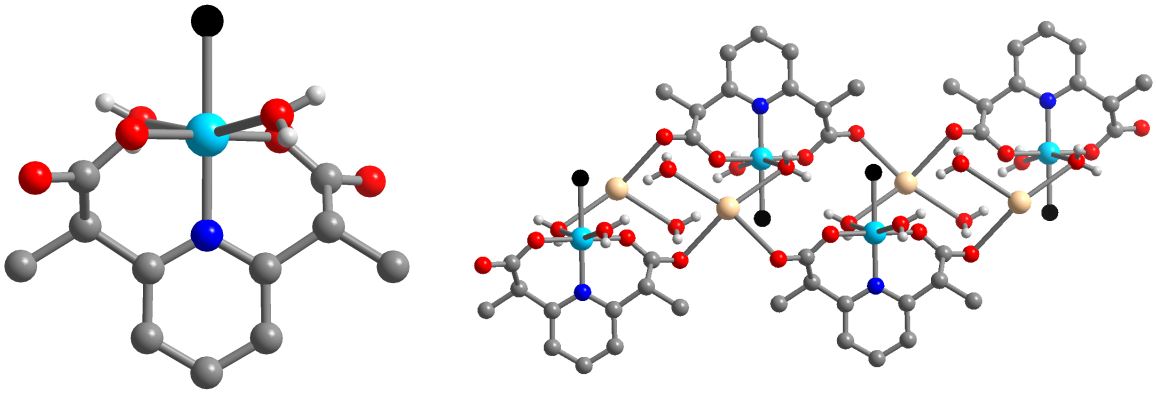


Figure S3.18. X-ray crystal structure of $K[(L_1)CuCl(H_2O)_2]$. Cyan, red, blue, black, pale yellow, gray, and small gray spheres represent Cu, O, N, Cl, K, C, and H atoms/ions, respectively. H atoms of water were identified from the electron density map. All other H atoms have been omitted for clarity.

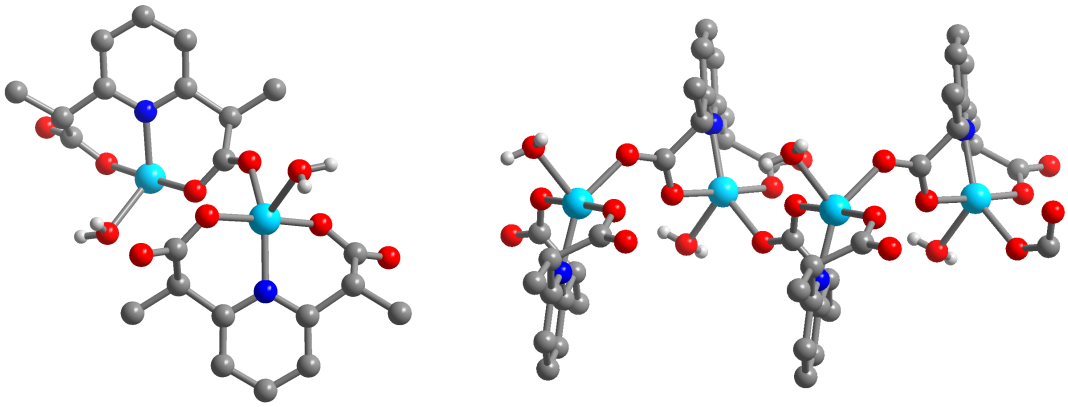


Figure S3.19. X-ray crystal structure of $[(L_1)Cu(H_2O)]$. Cyan, red, blue, gray, and small gray spheres represent Cu, O, N, C, and H atoms/ions, respectively. H atoms of water were identified from the electron density map. All other H atoms have been omitted for clarity.

Single Crystal X-ray Structures of $K_2[(PY(CO_2)_4)M(H_2O)]$ Complexes

Table S3.5. Crystallographic data for metal complexes $K_2[(PY(CO_2)_4)M(H_2O)]$ with selected bond lengths (Å) and angles (deg).

M	Mn^{2+}	Fe^{2+}	Co^{2+}	Ni^{2+}	Zn^{2+}
Formula	$C_{13}H_{13}K_2MnNO_{10}$	$C_{13}H_{15}FeK_2NO_{11}$[a]	$C_{13}H_{13}CoK_2NO_{10}$	$C_{13}H_{15}K_2NNiO_{11}$[a]	$C_{13}H_{15}K_2NO_{11}Zn$[a]
FW	476.38	495.30	480.37	498.15	504.84
Crystal system	Orthorhombic	Triclinic	Orthorhombic	Triclinic	Triclinic
Space Group	*Pnna*	*P*−1	*Pnna*	*P*−1	*P*−1
Z	4	2	4	2	2
a, Å	7.3220(2)	7.5937(4)	7.320(2)	7.5800(2)	7.5984(16)
b, Å	10.9900(3)	10.3520(4)	10.894(3)	10.3400(3)	10.346(2)
c, Å	20.2140(6)	10.9128(5)	20.194(6)	10.7590(3)	10.831(7)
α, deg	90	81.500(2)	90	82.2410(10)	81.810(3)
β, deg	90	88.018(2)	90	88.3690(10)	88.158(4)
γ, deg	90	86.820(2)	90	87.1540(10)	86.912(3)
V, $Å^3$	1626.60(8)	846.82(7)	1610.3(8)	834.31(4)	841.3(6)
Temperature, K	100(2)	100(2)	100(2)	100(2)	100(2)
Wavelength, Å	0.71073	0.71073	0.71073	0.71073	0.71073
Reflections collected	28805	14312	10843	11121	21088
Independent reflections	1487	9131	1458	3043	12504
R(int), %	3.61	4.81	4.62	2.17	2.62
Completeness to theta = 25.000°, %	100.0	98.9	99.9	99.8	99.7
Goodness-of-fit on F^2	1.130	1.042	1.049	1.089	1.073
R1(wR2), %	3.01(7.86)	4.18(10.27)	2.89(7.31)	2.90(7.45)	3.07(7.88)
$M–O_1$, Å	2.1337(16)	2.0512(1)	2.0771(17)	2.0315(18)	2.067(3)
$M–O_2$, Å	2.1472(16)	2.1157(1)	2.0584(17)	2.0122(18)	2.111(2)
$M–O_3$, Å	2.1337(16)	2.0803(1)	2.0771(17)	2.0598(18)	2.039(3)
$M–O_4$, Å	2.1472(16)	2.1307(1)	2.0584(17)	2.0250(18)	2.079(2)
$M–O_{eq}$, Å[b]	2.1405(16)	2.0945(1)	2.0678(17)	2.0321(18)	2.0790(3)
$M–O_{axial}$, Å	2.125(3)	2.1041(1)	2.070(3)	2.0645(18)	2.063(2)
$M–N_{PY}$, Å	2.210(3)	2.1247(1)	2.067(3)	2.011(2)	2.092(3)
$O_{axial}–M–N_{py}$	180	178.37(17)	180	178.89(8)	178.83(4)
$O_1–M–O_3$, deg	165.92(8)	171.022(3)	172.03(9)	176.12(7)	172.36(8)
$O_2–M–O_4$, deg	162.68(8)	171.466(3)	173.23(9)	176.68(7)	172.63(10)
Py-tilt, deg[c]	90.000(2)	89.730(157)	90.000(18)	88.195(68)	89.147(107)
OOP distortion, Å[d]	0.2924(12)	0.1377(16)	0.1330(12)	0.0515(9)	0.1195(11)

[a]Hydrogen atoms on water molecules were placed when identified in the electron difference map; however, not all could be located. Four missing hydrogen atoms from this dataset were omitted from the refinement but included in the given formula. [b]Average of the four equatorial M–O distances. [c]The PY-tilt is defined here as the angle between the least squares planes generated by the four equatorial oxygen donors and the atoms of the pyridine ring. [d]The out of plane (OOP) distortion is defined as the displacement of the metal center from the least-squares plane generated by the four equatorial oxygen atoms.

Single Crystal X-ray Structures of Co^{2+} and Co^{3+} Complexes

Table S3.6. Crystallographic data for metal complexes $K_2[(PY(CO_2)_4)Co(H_2O)]$, $K_2[(PY(CO_2)_4)Co(OH)]$, $K_2[(PY(CO_2)_4)Co(OH)_{0.5}(OMe)_{0.5}]$ with selected bond lengths (Å) and angles (deg).

Compound	$K_2[(PY(CO_2)_4)Co(H_2O)]$	$K_2[(PY(CO_2)_4)Co(OH)]$	$K_2[(PY(CO_2)_4)Co(OH)_{0.5}(OMe)_{0.5}]$
Formula	$C_{13}H_{13}CoK_2NO_{10}$	$C_{26}H_{29}Co_2K_3N_2O_{22}$[a]	$C_{13.50}H_{20.04}CoK_2NO_{13.52}$[a]
FW	480.37	956.67	549.79
Crystal system	Orthorhombic	Triclinic	Monoclinic
Space Group	*Pnna*	*P*−1	*C* 1 2/*m* 1
Z	4	2	4
a, Å	7.320(2)	11.7659(5)	21.901(5)
b, Å	10.894(3)	12.2288(5)	7.4450(17)
c, Å	20.194(6)	12.3782(5)	13.408(3)
α, deg	90	106.112(2)	90
β, deg	90	110.326(2)	115.296(3)
γ, deg	90	92.152(2)	90
V, $Å^3$	1610.3(8)	1586.67(12)	1976.7(8)
Temperature, K	100(2)	100(2)	100(2)
Wavelength, Å	0.71073	0.6888	0.7749
Reflections collected	10843	47289	24859
Independent reflections	1458	19702	3260
R(int), %	4.62	5.09	5.87
Completeness to theta = 25.000°, %	99.9	99.7	98.3
Goodness-of-fit on F^2	1.049	1.017	1.181
R1(wR2), %	2.89(7.31)	5.51(12.08)	6.28 (16.26)
M–O_1, Å	2.0771(17)	1.8932(13), 1.8933(14)[e]	1.898(3)
M–O_2, Å	2.0584(17)	1.8871(13), 1.8841(12)	1.898(3)
M–O_3, Å	2.0771(17)	1.8846(13), 1.8791(14)	1.913(3)
M–O_4, Å	2.0584(17)	1.8833(13), 1.8834(12)	1.913(2)
M–O_{eq}, Å[b]	2.0678(17)	1.8871(13), 1.8850(13)	1.906(3)
M–O_{axial}, Å	2.070(3)	1.9120(13), 1.8988(14)	1.897(4)
M–N_{PY}, Å	2.067(3)	1.8817(13), 1.8856(13)	1.926(4)
O_{axial}–M–N_{py}	180	175.86(6), 178.07(6)	179.81(17)
O_1–M–O_3, deg	172.03(9)	179.09(6), 179.65(6)	179.24(11)
O_2–M–O_4, deg	173.23(9)	178.20(5), 178.57(5)	179.23(11)
Py-tilt, deg[c]	90.000(18)	87.58(4), 89.41(5)	90.000(13)
OOP distortion, Å[d]	0.1330(12)	0.0159(6), 0.0127(7)	0.0080(18)

[a]Hydrogen atoms on water molecules and hydroxide were placed when identified in the electron difference map; however, not all could be located. Missing hydrogen atoms were omitted from the refinement but included in the given formula. [b]Average of the four equatorial M–O distances. [c]The PY-tilt is defined here as the angle between the least squares planes generated by the four equatorial oxygen donors and the atoms of the pyridine ring. [d]The out of plane (OOP) distortion is defined as the displacement of the metal center from the least-squares plane generated by the four equatorial oxygen atoms. [e]The two values correspond to the two inequivalent Co^{3+} complexes found in the crystal structure.

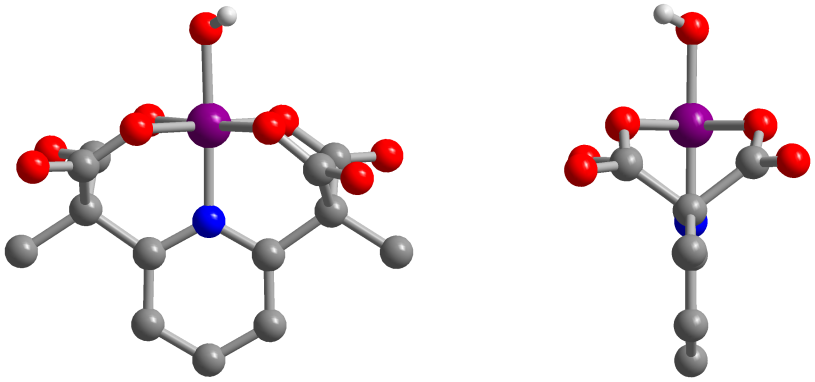


Figure S3.20. X-ray crystal structure of $[(PY(CO_2)_4)Co(OH)]^{2-}$. Purple, red, blue, gray, and small light gray spheres represent Co, O, N, C, and H atoms/ions, respectively. H atoms of hydroxide were identified from the electron density map. All other H atoms, solvent molecules, and two K countercations have been omitted for clarity.

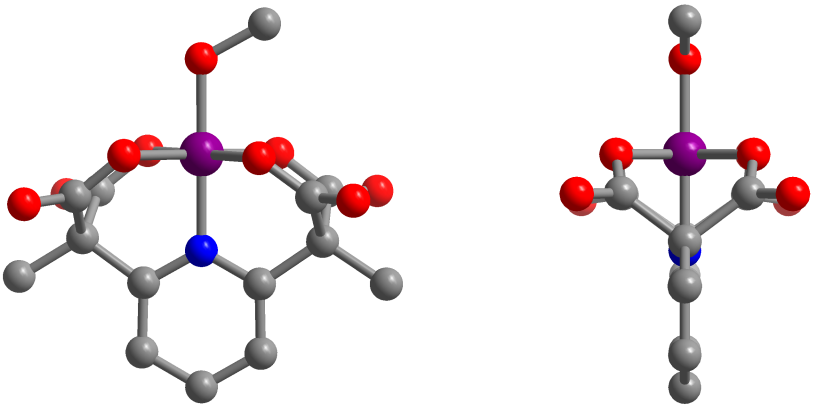


Figure S3.21. X-ray crystal structure of $[(PY(CO_2)_4)Co((OH)_{0.5}(OMe)_{0.5})]^{2-}$. Purple, red, blue, and gray spheres represent Co, O, N, and C atoms/ions, respectively. All H atoms, solvent molecules, and two K countercations have been omitted for clarity. This crystal was obtained during an initial screen of reaction conditions seeking to generate $[(PY(CO_2)_4)Co(H_2O)]^{2-}$. The run which generated this crystal was identical to the synthesis of $[(PY(CO_2)_4)Co(H_2O)]^{2-}$, except that it was performed in MeOH and in air, allowing this product to be collected as a solid by filtration directly from the reaction mixture. Consequently, the structure was found to have only half occupancy for the axial hydroxide with the other half corresponding to methoxide (shown).

Single Crystal X-ray Structure of $(PPN)_2[(PY(CO_2)_4)Zn(H_2O)]$

Table S3.7. Crystallographic data for the complex $(PPN)_2[(PY(CO_2)_4)Zn(H_2O)]$ with selected bond lengths (Å) and angles (deg).

M	$(PPN)_2[(PY(CO_2)_4)Zn(H_2O)]$	$K_2[(PY(CO_2)_4)Zn(H_2O)]$
Formula	$C_{170}H_{238}N_6O_{66}P_8Zn_2$[a]	$C_{13}H_{15}K_2NO_{11}Zn$[a]
FW	3800.30	504.84
Crystal system	Triclinic	Triclinic
Space Group	*P*−1	*P*−1
Z	2	2
a, Å	14.7541(10)	7.5984(16)
b, Å	23.2242(17)	10.346(2)
c, Å	31.783(2)	10.831(7)
α, deg	91.799(5)	81.810(3)
β, deg	101.041(4)	88.158(4)
γ, deg	93.168(5)	86.912(3)
V, Å^3	10662.6(13)	841.3(6)
Temperature, K	100(2)	100(2)
Wavelength, Å	0.8856	0.71073
Reflections collected	77147	21088
Independent reflections	22298	12504
R(int), %	7.79	2.62
Completeness to theta = 25.000°, %	98.5	99.7
Goodness-of-fit on F^2	1.051	1.073
R1(wR2), %	14.06(35.14)	3.07(7.88)
$M–O_1$, Å	2.069(10), 2.059(14)[c,d]	2.067(3)
$M–O_2$, Å	2.050(10), 2.092(13)	2.111(2)
$M–O_3$, Å	2.077(10), 2.036(15)	2.039(3)
$M–O_4$, Å	2.078(10), 2.082(13)	2.079(2)
$M–O_{eq}$, Å[b]	2.071(10), 2.067(14)	2.0790(3)
$M–O_{axial}$, Å	2.115(9), 2.018(15)	2.063(2)
$M–N_{PY}$, Å	2.156(11), 2.110(13)	2.092(3)
$O_{axial}–M–N_{py}$	174.1(4), 177.5(7)	178.83(4)
$O_1–M–O_3$, deg	175.6(4), 172.7(5)	172.36(8)
$O_2–M–O_4$, deg	169.1(4), 169.5(6)	172.63(10)

[a]Hydrogen atoms on water molecules were placed when identified in the electron difference map; however, not all could be located. Missing hydrogen atoms were omitted from the refinement but included in the given formula. [b]Average of the four equatorial M–O distances. [c]The two values correspond to the two inequivalent Zn^{2+} complexes found in the crystal structure. [d]This crystal diffracted poorly beyond 1.00 angstrom resolution, and a resolution of 0.83 angstroms could not be achieved. Consequently, this dataset is of inadequate quality for accurate determination of bond distances and angles, and only the overall connectivity and arrangement of molecules should be interpreted from this structure.

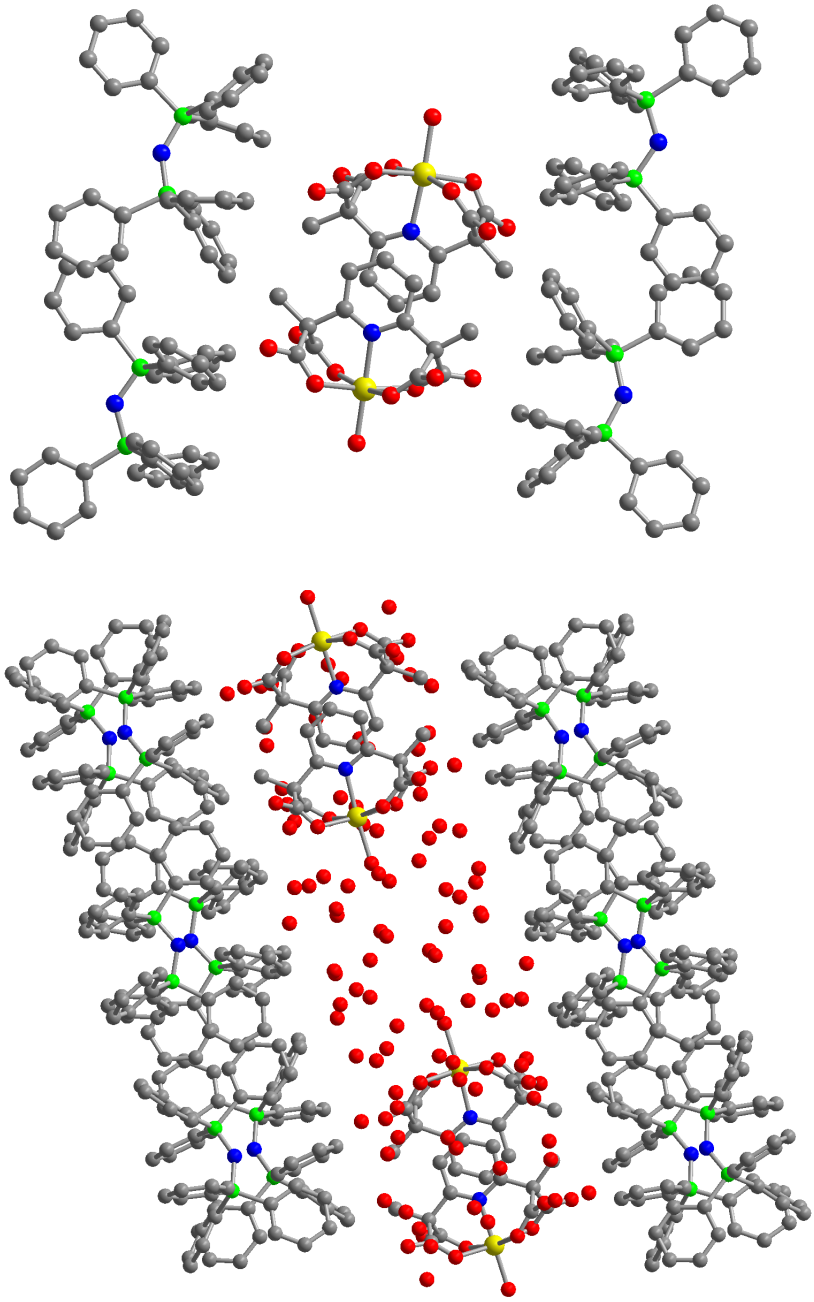


Figure S3.22. X-ray crystal structure of $(PPN)_2[(PY(CO_2)_4)Zn(H_2O)]$ with (bottom) and without (top) water molecules displayed. Yellow, red, blue, green, and gray spheres represent Zn, O, N, P, and C atoms/ions, respectively. H atoms have been omitted for clarity.

Single Crystal X-ray Structures of $A_2[(PY(CO_2)_4)Ni(H_2O)]$ ($A = Li^+, Na^+, K^+, Cs^+$)

Table S3.8. Crystallographic data for metal complexes $A_2[(PY(CO_2)_4)Ni(H_2O)]$ ($A = Li^+, Na^+, K^+, Cs^+$) with selected bond lengths (Å) and angles (deg).

A	Li^+	Na^+	K^+	Cs^+
Formula	$C_{13}H_{16}Li_2NNiO_{11.50}$	$C_{13}H_{23}NNa_2NiO_{15}$	$C_{13}H_{15}K_2NNiO_{11}$[a]	$C_{13}H_{11}Cs_2NNiO_9$
FW	442.86	538.01	498.15	649.76
Crystal system	Monoclinic	Triclinic	Triclinic	Monoclinic
Space Group	*P* 1 2/*n* 1	*P*−1	*P*−1	*P* 1 2_1/*n* 1
Z	4	2	2	4
a, Å	10.940(3)	7.2909(16)	7.5800(2)	10.7371(16)
b, Å	7.3560(18)	10.357(2)	10.3400(3)	7.9321(12)
c, Å	19.736(5)	13.365(3)	10.7590(3)	19.908(3)
α, deg	90	96.831(3)	82.2410(10)	90
β, deg	91.859(4)	91.503(3)	88.3690(10)	100.781(2)
γ, deg	90	90.596(3)	87.1540(10)	90
V, $Å^3$	1587.4(7)	1001.6(4)	834.31(4)	1665.6(4)
Temperature, K	100(2)	100(2)	100(2)	100(2)
Wavelength, Å	0.8856	0.7749	0.71073	0.7749
Reflections collected	19997	14570	11121	23330
Independent reflections	3121	5972	3043	5028
R(int), %	6.13	4.74	2.17	4.67
Completeness to theta = 25.000°, %	99.8	98.1	99.8	98.7
Goodness-of-fit on F^2	1.053	1.086	1.089	1.029
R1(wR2), %	4.20 (10.95)	3.82 (10.99)	2.90 (7.45)	2.07 (5.45)
M–O_1, Å	2.039(3)	2.0365(11)	2.0315(18)	2.0285(14)
M–O_2, Å	2.006(3)	2.0225(11)	2.0122(18)	2.0261(13)
M–O_3, Å	2.058(3)	2.0462(11)	2.0598(18)	2.0471(13)
M–O_4, Å	2.028(3)	2.0365(11)	2.0250(18)	2.0370(13)
M–O_{eq}, Å[b]	2.0328(3)	2.0354(11)	2.0321(18)	2.0347(13)
M–O_{axial}, Å	2.049(3)	2.0603(11)	2.0645(18)	2.0933(14)
M–N_{PY}, Å	1.996(3)	1.9932(13)	2.011(2)	2.0098(15)
O_{axial}–M–N_{py}	174.38(13)	177.81(4)	178.89(8)	176.07(6)
O_1–M–O_3, deg	172.56(11)	175.92(4)	176.12(7)	177.65(5)
O_2–M–O_4, deg	178.00(12)	175.36(4)	176.68(7)	175.40(5)

[a]Hydrogen atoms on water molecules were placed when identified in the electron difference map; however, not all could be located. Four missing hydrogen atoms from this dataset were omitted from the refinement but included in the given formula. [b]Average of the four equatorial M–O distances.

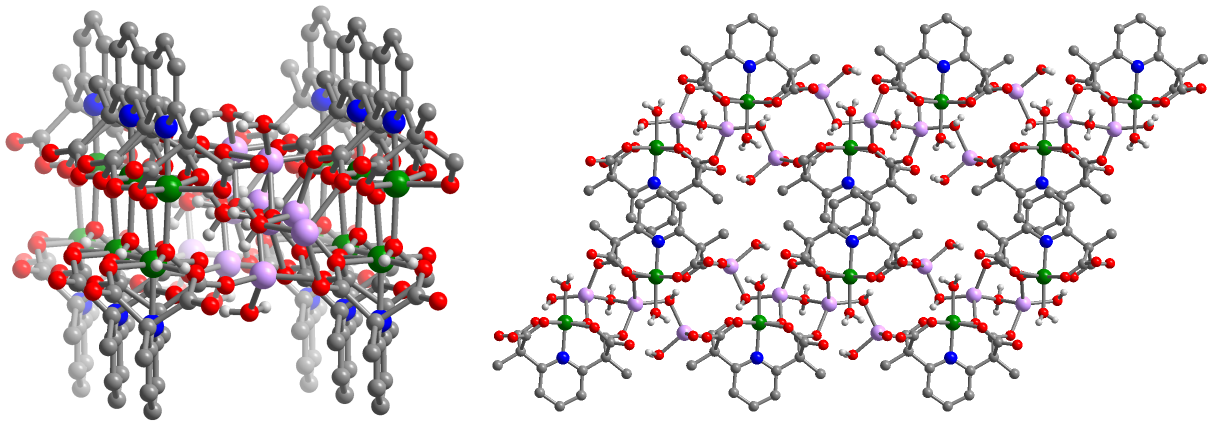


Figure S3.23. X-ray crystal structure of $Li_2[(PY(CO_2)_4)Ni(H_2O)]$. Green, red, blue, light purple, gray, and small gray spheres represent Ni, O, N, Li, C, and H atoms/ions, respectively. H atoms of water were identified from the electron density map. All other H atoms have been omitted for clarity.

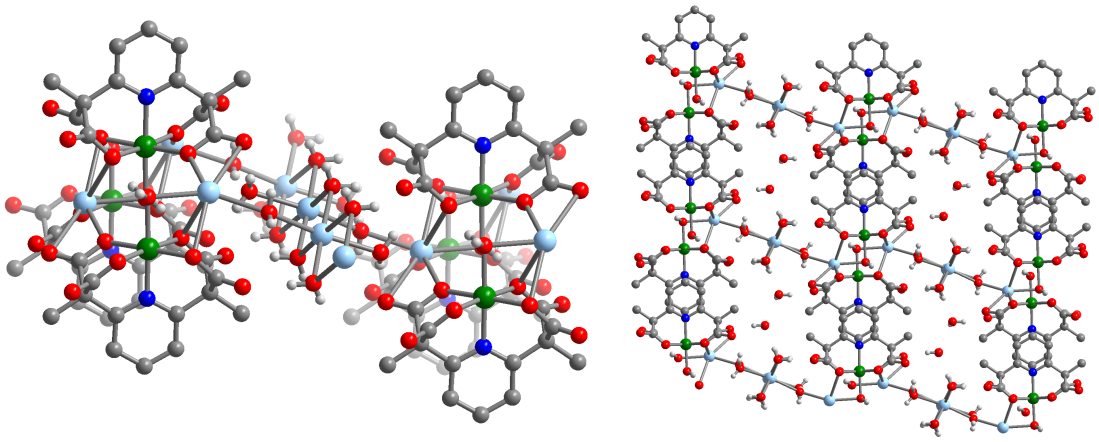


Figure S3.24. X-ray crystal structure of $Na_2[(PY(CO_2)_4)Ni(H_2O)]$. Green, red, blue, light blue, gray, and small gray spheres represent Ni, O, N, Na, C, and H atoms/ions, respectively. H atoms of water were identified from the electron density map. All other H atoms have been omitted for clarity.

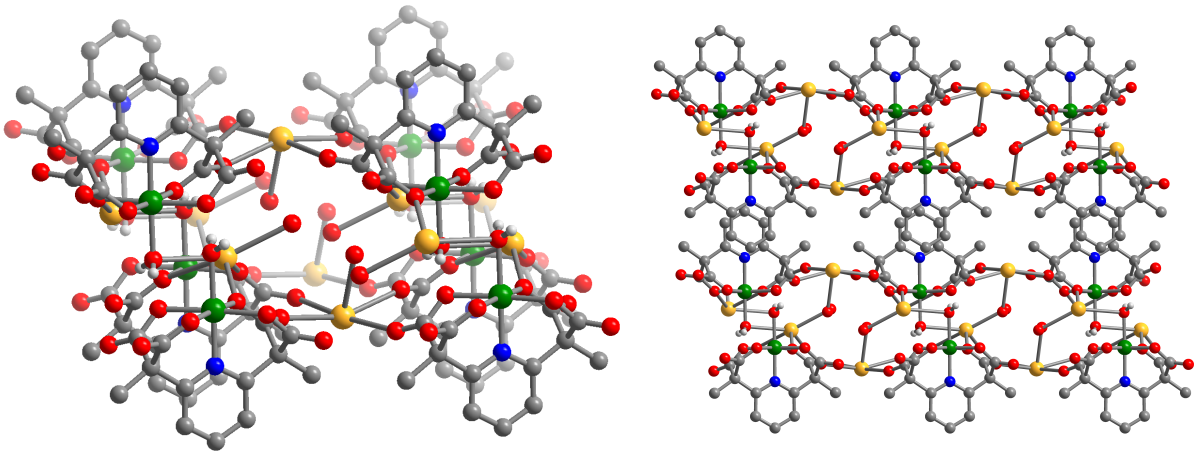


Figure S3.25. X-ray crystal structure of $K_2[(PY(CO_2)_4)Ni(H_2O)]$. Green, red, blue, yellow, gray, and small gray spheres represent Ni, O, N, K, C, and H atoms/ions, respectively. H atoms of water were identified from the electron density map. All other H atoms have been omitted for clarity.

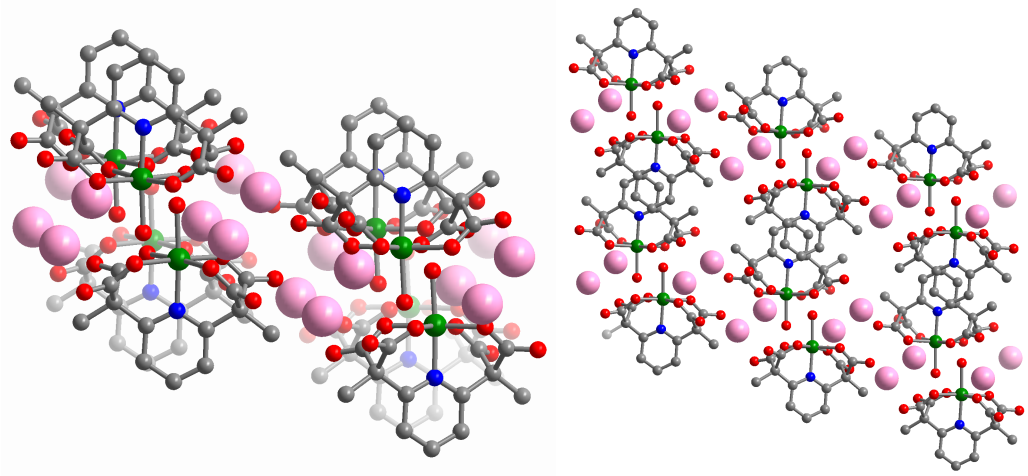


Figure S3.26. X-ray crystal structure of $Cs_2[(PY(CO_2)_4)Ni(H_2O)]$. Green, red, blue, pink, gray, and small gray spheres represent Ni, O, N, Cs, C, and H atoms/ions, respectively. H atoms of water were identified from the electron density map. All other H atoms have been omitted for clarity.

Synthetic Details for $PY4PhXR_2$ Routes

General Information. Unless specified otherwise, all reactions and manipulations were performed under an inert atmosphere using glovebox or Schlenk techniques. Tetrahydrofuran (THF) and ether were dried by passage over activated molecular sieves using a custom-built solvent purification system designed by JC Meyer Solvent Systems. All other solvents and reagents were obtained from commercial vendors and utilized without further purification. 2-Chloro-, 2-bromo, and 2-iodo-1,3-benzenedicarboxylic acid;[41] 2-bromo-1,3-dicyanobenzene;[45] 2-chloro-1,3-dicyanobenzene;[46] di(pyridin-2-yl)methane;[61] 2-chloro-1,3-phenylene bis(trifluoromethanesulfonate);[48] 1,3-dichloro-2-iodobenzene;[62,63] and 1,1-bis(2-pyridyl)ethane[7c] were synthesized as previously described.

Synthesis of Diethyl 2-Bromo-1,3-benzenedicarboxylate. In air, a 100 mL round-bottom flask was charged with 2-bromo-1,3-dicarboxylic acid (1.5 g, 6.2 mmol), concentrated aqueous H_2SO_4 (0.14 mL), and ethanol (60 mL). The mixture was heated at reflux for 5 d and monitored using thin layer chromatography. Any remaining starting material was removed by vacuum filtration, and the solvent was removed by rotary evaporation. The resulting oil was dissolved in 80 mL of ethyl acetate, washed with 3 × 20 mL of concentrated $NaHCO_3$, dried with $MgSO_4$, filtered, and concentrated again using rotary evaporation to yield the product as a clear oil (1.0 g, 54% yield). ^{1}H NMR (DMSO-d_6, 300 MHz,): δ 7.79 (m, 2H), 6.94 (m, 1H), 4.32 (q, J= 7.1 Hz, 4H), 1.29 (t, J= 7.1 Hz, 6H).

Attempted Synthesis of (2-Bromo-1,3-phenylene)bis(pyridin-2-ylmethanone) via Diethyl 2-Bromo-1,3-benzenedicarboxylate. A THF solution (16 mL) of 2-bromopyridine (0.38 mL, 3.9 mmol) was cooled to −78 °C, and 2.5 M *n*-butyllithium in hexanes (1.3 mL,) was added slowly dropwise. After 20 min, a THF solution (3 mL) of diethyl 2-bromo-1,3-benzenedicarboxylate (0.40 g, 1.3 mmol) was added via syringe, and followed 15 min later by quenching with methanol (3 mL). Once the reaction had returned to room temperature, 6 mL of 10% HCl was added (pH 1), and the mixture was extracted with 3 × 5 mL of dichloromethane. Then 10% aqueous NaOH (~8 mL) was added to the aqueous portion until the solution was slightly basic, and an extraction was performed again with 3 × 5 mL of dichloromethane. The organic layer was collected and the crude product was isolated by rotary evaporation as a red-brown oil.

Synthesis of 2-Bromo-1,3-benzenedicarbonyl Dichloride. A 10 mL round-bottom flask was charged with 2-bromo-1,3-dicarboxylic acid (0.25 g, 1.0 mmol) and excess neat oxalyl chloride (1.0 mL). One drop of DMF was then added to the flask via syringe to serve as a catalyst, and the solution immediately began to bubble. After 1 h, the ^{1}H NMR spectrum of an aliquot of the reaction mixture matched that of a previous report,[43] indicating that the reaction had gone to completion. The product was isolated as a white solid by evaporating the oxalyl chloride under reduced pressure, and it was used in the subsequent lithiation step without further purification.

Attempted Synthesis of 1,3-(Bis(bis-2-pyridyl)methoxymethane)-2-bromobenzene (PY4PhBr(OMe)$_2$) via 2-Bromo-1,3-benzenedicarbonyl Dichloride. A THF solution (25 mL) of 2-bromopyridine (0.82 mL, 8.6 mmol) was cooled to −78 °C, and 2.5 M *n*-butyllithium in hexanes (3.5 mL, 8.6 mmol) was added slowly dropwise. After 20 min, a THF solution (5 mL) of the previously made 2-bromo-1,3-benzenedicarbonyl dichloride was added slowly dropwise via syringe, and followed 15 min later by quenching with methanol (3 mL). Once the reaction had returned to room temperature, 10 mL of 10% HCl was added (pH 1), and the mixture was extracted with 3 × 10 mL of dichloromethane. Then 10% aqueous NaOH (~13 mL) was added to the aqueous portion until the solution was slightly basic, and an extraction was performed again with 3 × 10 mL of dichloromethane. The organic layer was collected and the crude product was isolated by rotary evaporation as a brown oil.

Synthesis of (2-Chlorophenyl)(pyridin-2-yl)methanone. A 100 mL Schlenk flask was charged with 2-bromopyridine (0.90 mL, 9.4 mmol) and 40 mL of ether. The solution was cooled to −78 °C, and 1.6 M *n*-butyllithium in hexanes (5.8 mL, 9.3 mmol) was added to the flask slowly dropwise. While this reaction stirred for 10 min, a 50 mL Schlenk flask was charged with 2-chlorobenzonitrile (1.2 g, 8.7 mmol) and 10 mL of THF. The 2-chlorobenzonitrile solution was then added slowly dropwise to the 100 mL flask via cannula. The reaction flask was kept at −78 °C for 1 h, the bath was packed with dry ice, and the reaction was allowed to warm

to room temperature as the dry ice evaporated. After 15 hours, the reaction was poured into a 250 mL beaker containing 50 mL of 3 M HCl at 0 °C. The solution was stirred for 2 h. Then 50 mL of ether was added, the organic layer was removed, and the aqueous portion was washed again with 50 mL of ether. The aqueous layer was transferred to a 125 mL Erlenmeyer flask, and with stirring 60 mL of 3 M NaOH, enough to ensure the solution was slightly basic (pH 8-9), was added. The solution was extracted with 3 × 60 mL of ether, and the organic portions were combined, dried with $MgSO_4$, filtered, and concentrated via rotary evaporation. The crude product was purified by column chromatography on silica (R_f 0.44 4:1 hexanes/ethyl acetate, UV) to give 0.83 g (44% yield) of the product as a yellow oil, which solidified over the course of 1 week. ^{1}H NMR ($CDCl_3$, 300 MHz): δ 8.68 (d, J = 4.9 Hz, 1H), 8.14 (d, J = 7.9 Hz, 1H), 7.91 (td, J = 7.8, 1.8 Hz, 1H), 7.45 (m, J = 11.3, 8.2, 5.3 Hz, 5H). IR (neat, cm^{-1}): 3338w, 3082w, 3057w, 3009w, 2957w, 2922w, 2862w, 1677s, 1583s, 1567m, 1467m, 1435s, 1310s, 1288s, 1263m, 1240s, 1169m, 1127m, 1090m, 1055s, 1031s, 995s, 957m, 934s, 899m, 875m, 814s, 767s, 746s, 736s, 702m, 683s, 637s, 616s, 582m, 557w, 537w, 518w, 504w, 479m, 466w. ESI-MS (*m/z*): $\{C_{12}H_9ClNO\}^+$, 218.0. Anal. Calcd. for $C_{21}H_{29}NO_8$: C, 66.22; H, 3.70; N, 6.44%. Found: C, 66.04; H, 3.57; N, 6.38%.

Synthesis of (2-Chlorophenyl)di(pyridin-2-yl)methanol (PY2PhCl(OH)) A 25 mL Schlenk flask was charged with 2-bromopyridine (0.18 mL, 1.9 mmol) and 3.8 mL of THF. The solution was cooled to −78 °C, and 1.6 M *n*-butyllithium in hexanes (1.1 mL, 1.8 mmol) was added to the flask slowly dropwise. While this reaction stirred for 15 min, (2-chlorophenyl)(pyridin-2-yl)methanone (0.20 g, 0.92 mmol) was dissolved in 1.3 mL of THF in a 20 mL vial. The (2-chlorophenyl)(pyridin-2-yl)methanone solution was then added slowly dropwise to the 100 mL flask via syringe. The reaction flask was kept at −78 °C for 1 h, and then quenched with 1 mL of methanol. Once the reaction had returned to room temperature, 5 mL of deionized water was added, and the mixture was extracted with 3 × 10 mL of dichloromethane. The organic layers were combined, washed with brine, dried with $MgSO_4$, filtered, and concentrated via rotary evaporation. The crude product was purified by recrystallization by layering hexanes over the crude dissolved in a minimal amount of dichloromethane. The final product (34 mg, 16%) was isolated by vacuum filtration as a tan solid. ^{1}H NMR ($CDCl_3$, 300 MHz *d*): δ 8.56 (d, J = 5.1 Hz, 2H), 7.78 (m, 6H), 7.37 (d, J = 7.6 Hz, 1H), 7.12 (t, J = 7.6 Hz, 2H), 6.76 (d, J = 7.5 Hz, 1H). IR (neat, cm^{-1}): 3323w, 3296w, 3283w, 3234w, 3061w, 3009w, 1585s, 1569m, 1463m, 1431s, 1388m, 1299w, 1275w, 1255w, 1179m, 1163w, 1129w, 1107w, 1098w, 1066s, 1042s, 994m, 944w, 933w, 923w, 895w, 792s, 774s, 753s, 728s, 690m, 670s, 637s, 619s, 594m, 566m. ESI-MS (*m/z*): $\{C_{17}H_{14}ClN_2O\}^+$, 297.1. Anal. Calcd. for $C_{21}H_{29}NO_8$: C, 68.81; H, 4.42; N, 9.44%. Found: C, 68.56; H, 4.47; N, 9.27%.

Attempted Synthesis of (2-Chloro-1,3-phenylene)bis(pyridin-2-ylmethanone). A 50 mL Schlenk flask was charged with 2-bromopyridine (0.31 mL, 3.2 mmol) and 16 mL of THF. The flask was cooled to −78 °C, and 1.6 M *n*-butyllithium in hexanes (2.0 mL, 3.2 mmol) was added to the flask slowly dropwise by syringe. While this reaction stirred for 15 min, 2-chloro-1,3-dicyanobenene (0.25 g, 1.5 mmol) was dissolved in 4 mL of THF in a 10 mL round-bottom flask. The 2-chloro-1,3-dicyanobenene solution was then added slowly dropwise to the 50 mL flask via syringe. The reaction was stirred at −78 °C for 1 h and subsequently quenched with 1 mL of methanol. Once it warmed to room temperature, it was poured into 30 mL of 3 M HCl at 0 °C. The mixture was stirred for 20 min and extracted with 3 × 20 mL of dichloromethane. The aqueous portion was made basic with 3 M NaOH (pH 13), and extracted again with 3 × 20 mL of dichloromethane. The organic portions were combined, dried with $MgSO_4$, filtered, and

concentrated via rotary evaporation. Purification by column chromatography on silica was attempted, but only 1,3-phenylenebis(pyridin-2-ylmethanone) was isolated (R_f 0.19 4:1 hexanes/ethyl acetate, UV). ESI-MS (*m/z*): $\{C_{18}H_{13}N_2O_2\}^+$, 289.1.

Attempted Synthesis of 1,3-Bis[bis(2-pyridyl)methyl]-2-halobenzene (PY4PhCl). In a glovebox, a 25 mL Schlenk flask was charged with di(pyridin-2-yl)methane (0.34 g, 2.0 mmol) and 4 mL of THF. A second 25 mL Schlenk flask was charged with anhydrous $ZnCl_2$ (0.41 g, 3.0 mmol). These flasks were transferred to a Schlenk line, and the flask containing di(pyridin-2-yl)methane was cooled to −40 °C in a dry ice and acetonitrile bath before 1.6 M *n*-butyllithium in hexanes (1.3 mL, 2.1 mmol) was added to it dropwise via syringe. After 15 min, the THF solution was cannula transferred with vigorous stirring into the flask containing $ZnCl_2$. The mixture was left to stir at room temperature for 45 min. Meanwhile, $Pd(Ph_3P)_4$ (0.062 g, 0.054 mmol) and LiCl (0.13 g, 3.0 mmol) were added to a third flask under an N_2 purge, and 2-chloro-1,3-phenylene bis(trifluoromethanesulfonate) (0.20 g, 0.49 mmol) and 2 mL of THF were added to it by syringe. Then the organozinc reagent was transferred via cannula into the flask containing the palladium catalyst, and the reaction was heated to reflux for 15 hours. Once the reaction had cooled to room temperature, it was quenched with 30 mL of concentrated $NaHCO_3$. The mixture was extracted with 3 × 20 mL of dichloromethane, and the organic portions were combined, dried with $MgSO_4$, filtered, and concentrated via rotary evaporation. The crude was triturated with ether, and the resulting peach solid was collected by vacuum filtration.

Synthesis of 1,3-Bis[1,1-bis(2-pyridyl)ethyl]-2-iodobenzene (PY4PhIMe$_2$). A 20 mL vial was charged with 1,3-dichloro-2-iodobenzene (0.41 g, 1.9 mmol), 9 mL of THF, and a stirbar and capped with a rubber septum. A 25 mL Schlenk flash was charged with 1,1-bis(2-pyridyl)ethane (1.4 g,7.6 mmol), 6 mL of THF, and a stirbar. Then, both the vial and flask were transferred from the glovebox to a Schlenk line and the Schlenk flask was cooled to −78 °C while the vial was cooled to 0 °C. With stirring, 0.62 mL (1.9 mmol) of 3 M EtMgBr in ether was added dropwise to the vial, and 2.4 mL (7.2 mmol) of EtMgBr was added to the Schlenk flask. Whereas the solution in the vial remained clear, the reaction mixture in the Schlenk flask turned red. Both reaction vessels were removed from the icebaths and stirred at room temperature for 1 h. Then the solution in the vial was cannula transferred dropwise into the flask. After stirring at room temperature for an additional hour, the Schlenk flask was heated to reflux and held at 70 °C for 18 h. As the reaction cooled back to room temperature, a 50 mL Schlenk flask was charged with I_2 (1.4 g, 1.9 mmol) and 6 mL of anhydrous THF and cooled to 0 °C in an icebath. The reaction solution was cannula transferred into the 50 mL flask, and the mixture was left to stir at room temperature for 20 h. Subsequently, $NaSO_3$ (0.38 g, 3.0 mmol in 30 mL of water) was added to the flask and left to stir at room temperature for 15 min followed by NaOH (0.40 g, 10 mmol in 40 mL of water). The solution was extracted with 3 × 20 mL of dichloromethane, and the organic layers were combined, dried with $MgSO_4$, filtered, and concentrated on a rotary evaporator to give a red residue. The residue was dissolved in a minimal amount of dichloromethane and loaded into a 5 mL syringe filled with 4 mL of basic alumina. Additional dichloromethane was used to pass the product through the plug. The yellow filtrate was concentrated, layered with ether and stored at −20 °C overnight. In the morning, the jar was shaken and then returned to the fridge for another 4 h. The pale yellow solids were isolated by vacuum filtration. ^{1}H NMR (acetonitrile-d_3, 400 MHz): δ 8.71 (dt, J = 5.3, 1.4 Hz, 4H), 8.22 (m, 2H), 8.14 (m, 1H), 8.00 (td, J = 8.0, 1.8 Hz, 4H), 7.59 (t, J = 6.6 Hz, 4H), 7.04 (d, J = 8.3 Hz, 4H), 2.15 (s, 6H). ESI-MS (*m/z*): $\{C_{30}H_{26}IN_4\}^+$, 569.1; $\{C_{30}H_{27}IN_4\}^{2+}$, 285.1. The product fails to pass elemental analysis.

Table S3.9. Crystallographic data for the PY4PhIMe$_2$ dataset.

	PY4PhIMe$_2$
Empirical formula	$C_{32.50}H_{27.50}Cl_{7.50}I_4N_4$
Formula weight	1247.56
Temperature	100(2) K
Wavelength	0.71073 Å
Crystal system	Monoclinic
Space group	$P\,2_1/m$
a	14.0132(9) Å
b	14.7317(10) Å
c	20.5562(15) Å
α	90°
β	98.345(4)°
γ	90°
Volume	4198.7(5) Å^3
Z	4
Density (calculated)	1.947 Mg/m^3
Absorption coefficient	1.974 mm^{-1}
F(000)	2360
Crystal size	0.22 × 0.15 × 0.09 mm^3
Theta range for data collection	1.469 to 25.408°
Index ranges	−15<=h<=16, −17<=k<=11, −24<=l<=23
Reflections collected	17857
Independent reflections	7349 [R(int) = 0.0394]
Completeness to theta = 25.00∞	93.4 %[a]
Absorption correction	Semi-empirical from equivalents
Refinement method	Full-matrix least-squares on F^2
Data / restraints / parameters	7349 / 0 / 482
Goodness-of-fit on F^2	1.033
Final R indices [I>2sigma(I)][a]	R1 = 0.0477, wR2 = 0.0847
R indices (all data)	R1 = 0.0797, wR2 = 0.0939
Largest diff. peak and hole	1.665 and -1.109 e.Å^{-3}

[a]The asymmetric unit contained two PY4PhIMe$_2$ molecules and three iodide and one triodide counterions. One of the iodide counterions appeared to be slightly disordered due to large Q-peaks near it (1.410 and 1.665 e.Å^{-3}). Modeling of the disorder by the PART instruction was attempted but resulted in a number of carbon atoms becoming non-positive definite. Thus, the part instruction was removed and the dataset was left as is. The low completeness to theta = 25.00∞, only 93.4%, is likely due to this unmodeled disorder.

Chapter Four

Single-Ion Conducting Polymer Networks with Borate Anions and Flexible Linkers

"In the beginning of the year 1800 the illustrious professor conceived the idea of forming a long column by piling up, in succession, a disc of copper, a disc of zinc, and a disc of wet cloth, with scrupulous attention to not changing this order. What could be expected beforehand from such a combination? Well, I do not hesitate to say, this apparently inert mass, this bizarre assembly, this pile of so many couples of unequal metals separated by a little liquid is, in the singularity of effect, the most marvellous instrument which men have yet invented, the telescope and the steam engine not excepted."

- Count Alessandro Giuseppe Antonio Anastasio Volta

Section 4.1 Introduction

The 2015 U.S. Energy Information Administration Annual Energy Outlook continues to project increased growth in renewable energy technology and capacity over the next few decades.[1] Yet, the ability to harness energy from inconsistent resources like solar or wind alone is insufficient to ensure a consistent and reliable electrical grid, largely as a result of inadequate infrastructure to store the captured energy. Concurrently, the United States and other nations are seeking to transition to an electrically powered transportation fleet that is environmentally sustainable and bolsters future energy security by decreasing dependence on foreign petroleum. Toward these ends, batteries afford the only practical solution.[2,3]

Presently, state of the art battery technology relies on intercalation and insertion of Li-ions into electrodes. One option for improving the gravimetric energy capacity of next-generation lithium batteries is to forgo the insertion electrodes and instead utilize lithium metal electrodes. However, to successfully implement this technology, improvements in lithium electrolyte materials must first be made. Not only should the electrolyte material be mechanically robust and resistant to penetration by dendrites, it must be chemically innocuous toward the lithium metal electrode and support sufficient conductivity of the ions to be suitable for commercial applications (i.e., > 10^{-4} S/cm).[4] Additionally, batteries sold today utilize predominantly liquid electrolyte systems that contain lithium salts and organic solvents.[5] In addition to the safety hazards associated with the organic solvents discussed in Chapter 1, the mobility of the counteranion results in unwanted polarization in the cell[6,7] and a reduction in cycling performance due to anion decomposition at the electrode.[8–10]

One strategy for overcoming the problems associated with the free anions is to develop single-ion conducting electrolytes. In these systems, the anion is physically anchored in the electrolyte. Consequently, Li^+ must hop between the immobilized anions in order to traverse the cell, as opposed to the cation and anion moving as a pair. To date, most single-ion conductors that have been explored have focused on incorporating weakly coordinating carboxylate, sulfonate, or bis((trifluoromethyl)sulfonyl)amide anions into the electrolyte material. On the other hand, only a handful of studies have investigated the use of borate anions.[11–19] Tetraphenylborate in particular is an attractive anion as the low electronegativity of the tetrahedral boron allows for effective delocalization of the negative charge over the four phenyl rings. This attribute, along with the large difference in size between tetraphenylborate and Li^+,

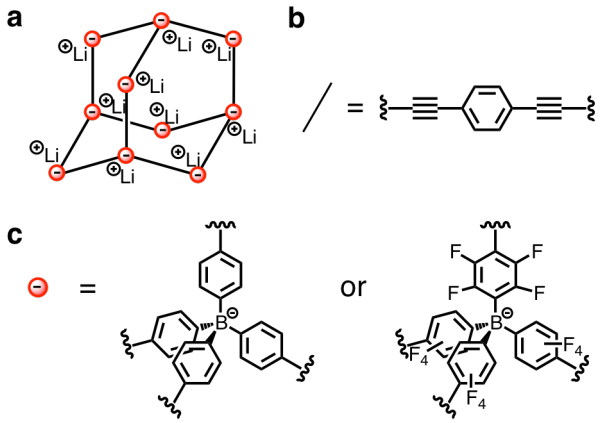


Figure 4.1. Single-ion conducting PAF reported by Van Humbeck and co-workers.[19] (a) Lithium impregnated diamondoid structure. (b) Rigid aromatic linker. (c) Undecorated and fluorinated tetraphenylborate nodes.

should facilitate ion conduction by promoting dissociation of the ion pair and preventing the formation of ion aggregates.[4]

One recent system to utilize the advantageous qualities of tetraphenylborates was a covalent, diamondoid porous organic framework (PAF) composed of anionic tetraphenylborate nodes and rigid aromatic linkers as shown in Figure 4.1.[19] Whereas previous PAFs utilized predominantly neutral nodes,[20–23] incorporation of the anionic borate nodes directly into the framework permitted this material to be impregnated with lithium cations, rendering it a single-ion conductor. The claim that only Li^+ ions are mobile was validated by comparing the current due to Li^+ (i_{Li^+}), to the overall current passed through the cell (i_{total}). The ratio of these two values gives the transference number of the material ($t_{Li^+} = i_{Li^+}/i_{total}$) and is expected to equal unity for a single-ion conductor, though in practice t_{Li^+} for single-ion conductors ranges between 0.9 and 1. As expected, t_{Li^+} was found to be 0.93.[19,24] Conversely, lithium transference numbers for liquid electrolytes are nearly always lower than 0.5.[25] Consequently, unwanted cell polarization and concentration gradients due to anion mobility were eliminated, which is predicted to lead to better overall cell performance.

The modular synthesis of this PAF network allowed for the systematic tailoring of both the linker and node, providing an extra element of control over the properties of the resulting bulk material. For example, pressed pellets of the material made with a perfluorinated tetraphenylborate node exhibited a conductivity of 2.7×10^{-4} S/cm at 28 °C, which was an order of magnitude higher than the analogue made with unfluorinated phenyl rings. The oxidative stability of the material made with the fluorinated tetraphenylborates was found to be 3.5-3.7 V (vs. Li/Li^+) at 90 °C, and it was thermally stable to 300 °C as determined by thermogravimetric analysis. Together, these metrics place this material in line for incorporation into a functional device. Although it still required a small amount of organic solvent to render it conductive, the amount required was significantly less than that needed for standard liquid electrolytes—only about 10 wt % of the material.

While the electrochemical characteristics of this PAF are promising, these brittle powders are not morphologically amenable to cell integration. Moreover, the synthesis of the PAF required a palladium catalyst, which would constitute a significant portion of the cost of the raw materials if it were to be made on an industrial scale. Thus, we have worked to develop a related series of second-generation materials, single-ion conducting polymer networks in which the fluorinated tetraphenylborate node is retained but the rigid aryl linkers have been replaced with flexible linkers. By incorporating a flexible component on the molecular level, it was hoped that the high conductivity would be preserved, but the brittleness of the first-generation PAF material could be alleviated, allowing the conductor to be more easily fashioned into films. Herein, we report the palladium-free synthesis and electrochemical characterization of this new set of polymers, one of which has obtained conductivity values as high as 3.5×10^{-4} S/cm.

Section 4.2 Experimental Section

All syntheses were performed using standard Schlenk techniques unless stated otherwise. Anhydrous diethyl ether and tetrahydrofuran (THF) were dried using a commercial solvent purification system designed by JC Meyer Solvent Systems. Anhydrous 1,4-dioxane purchased from Sigma-Aldrich; propylene carbonate (PC); triethylene glycol dimethyl ether (triglyme); and ethylene carbonate (EC) and dimethyl carbonate (DMC) mixtures were stored over molecular sieves for at least one day before use. Water was removed from PEG400 and PEG1000 by

azeotropic distillation in toluene.[26] Anhydrous methanol was purchased from EMD Chemicals Inc. and used as received. All other solvents and reagents were obtained from commercial vendors and utilized without further purification.

Synthesis of 2,3,5,6-Tetrafluorobenzyl Chloride. A 100 mL oven-dried Schlenk flash was charged with 2,3,5,6-tetrafluorobenzyl alcohol (13.0 g, 72.1 mmol) and tetrabutylammonium chloride (10.0 g, 36.0 mmol). Thionyl chloride (30.0 mL, 411 mmol) was added slowly by syringe. After the bubbling had subsided, the flask was heated to 85 °C for 2 h and then allowed to cool to room temperature. The flask was transferred to a 0 °C ice bath, and the reaction was quenched with 40 mL of deionized water. Next, the solution was brought to pH 6 by the gradual addition of 40 mL of concentrated aqueous Na_2CO_3 followed by 28.8 g of solid Na_2CO_3. The solution was extracted with 4 × 40 mL of diethyl ether. The organic portions were combined, washed with 40 mL of brine, dried with $MgSO_4$, filtered, and concentrated on a rotary evaporator to give a yellow oil. Residual diethyl ether was removed under reduced pressure. It should be noted that the product possesses a relatively low boiling point, and was kept under vacuum only until bubble formation ceased. The pure product was obtained as a clear oil by vacuum distillation at ambient temperature (30 °C) and was collected in a bulb cooled by liquid N_2. In some instances, trace diethyl ether remained after distillation and was not removed prior to the subsequent step. Yield: 13.1 g (92%). ^{1}H NMR (400 MHz, $CDCl_3$) δ 7.09 (tt, J = 9.6, 7.4 Hz, 1H), 4.67 (t, J = 1.4 Hz, 2H). ^{13}C{^{1}H} NMR (151 MHz, $CDCl_3$) δ 146.0 (dddd, J_F = 249.2, 14.0, 9.9, 4.1 Hz), 144.9 (ddt, J_F = 250.7, 14.2, 4.5 Hz), 117.5 (t, J_F = 16.8 Hz), 106.8 (t, J_F = 22.6 Hz), 31.9 (m). ^{19}F NMR (376 MHz, $CDCl_3$) δ −137.5 (ddd, J = 22.1, 13.0, 9.1 Hz), −142.3 (ddd, J = 21.3, 13.2, 7.2 Hz). IR (neat, cm^{-1}): 3084w, 2991w, 1697w, 1626w, 1610w, 1503s, 1462m, 1445m, 1423w, 1392s, 1285s, 1254s, 1187s, 1172s, 1121m, 1024m, 979s, 844s, 756s, 714s, 688s, 660m, 609s, 532m, 477w. Anal. Calcd. for $C_7H_3ClF_4$: C, 42.35; H, 1.52%. Found: C, 42.25; H, 1.44%.

Synthesis of Di(1,2-dimethoxyethane)lithium Tetrakis(4-(chloromethyl)-2,3,5,6-tetrafluorophenyl)borate. A 200 mL oven-dried Schlenk flash was charged with 2,3,5,6-tetrafluorobenzyl chloride (2.00 g, 10.1 mmol) via syringe. Then, 100 mL of anhydrous diethyl ether were added via cannula. The solution was cooled to −78 °C for 10 min before 6.16 mL (9.86 mmol) of 1.6 M *n*-butyllithium in hexanes was added dropwise by syringe over the course of 5 min. The solution was left to stir at −78 °C for 1 h. Then, 2.24 mL of 1.0 M boron trichloride in heptanes was added dropwise via syringe, causing a fog to form in the flask. The flask was kept at −78 °C for 2 h before being allowed to warm to room temperature as the dry ice evaporated. After 18 h, the cloudy solution was quenched with 30 mL of a 0.1 M aqueous LiCl solution. The organic layer was collected and washed with 2 × 30 mL of 0.1 M aqueous LiCl. The organic layer was dried with $MgSO_4$, filtered, and concentrated on a rotary evaporator to give a pale yellow oil. The oil was dissolved in 30 mL of toluene, and the solvent was removed under reduced pressure. The viscous oil was dissolved in 10 mL of dichloromethane before another 20 mL of toluene was added. The solvent was again removed under reduced pressure to give an off-white residue. The residue was transferred to a centrifuge tube and suspended in 30 mL of toluene with the aid of sonication. Centrifugation (5000 rpm, 10 min) was used to separate the mixture and the supernatant was decanted. Again, the solid was suspended in 30 mL of toluene and subjected to a second round of centrifugation. The supernatant was decanted and the white solid was dissolved in a minimal amount of 1,2-dimethoxyethane (~ 5 mL). Hexanes (~ 30 mL) were added to the solution until a layer of oil formed, and the solvent was removed under reduced pressure. The residue was dissolved in 6 mL of dichloromethane followed by 30 mL of

hexanes, and the solvent was again removed under vacuum to yield the final product as a white solid. Yield: 1.02 g (46%). ^{1}H NMR (400 MHz, MeCN-d_3) δ 4.70 (s, 8H), 3.45 (s, 8H), 3.28 (s, 12H). ^{13}C{^{1}H} NMR (151 MHz, MeCN-d_3) δ 149.0 (d, J_F = 241.7 Hz), 144.6 (d, J_F = 243.1 Hz), 113.2 (t, J_F = 17.4 Hz), 72.3, 58.9, 33.8. ^{19}F NMR (376 MHz, MeCN-d_3) δ −132.6, −148.6. IR (neat, cm^{-1}): 2947w, 2841w, 1649w, 1584w, 1449s, 1371w, 1278s, 1252s, 1185m, 1117m, 1074s, 1028w, 990s, 861s, 840w, 771w, 758w, 738w, 716w, 694s, 671s, 651m, 628s, 585m, 566w, 556w, 530w, 522w, 511w, 494w477m, 469w. ESI-MS (m/z): $\{C_{28}H_8BCl_4F_{16}\}^-$, 801. Anal. Calcd. for $C_{36}H_{28}BCl_4F_{16}LiO_4$: C, 43.76; H, 2.86%. Found: C, 43.59; H, 2.80%.

Synthesis of Fluoroborate Network Polymers. In a N_2-filled glovebag, two equivalents of anhydrous linker were measured with a micropipette into a 20 mL vial, a stirbar was added, and the vial was sealed with a rubber septum. 2 mL of anhydrous THF was added via syringe, and four equivalents of 1.6 M *n*-butyllithium in hexanes were added slowly dropwise via syringe with stirring at ambient temperature. This solution was gently stirred at room temperature for 1 h before the solvent was removed under reduced pressure and subsequently replaced by 1 mL of anhydrous 1,4-dioxane. Into a separate vial, one equivalent (300 mg, 0.304 mmol) of di(1,2-dimethoxyethane)lithium tetrakis(4-(chloromethyl)-2,3,5,6-tetrafluorophenyl)borate was weighed in air and suspended with vigorous stirring in 2 mL of anhydrous 1,4-dioxane. After transferring the borate solution to the linker vial via syringe, an additional 0.5 mL of anhydrous 1,4-dioxane was used to rinse the borate vial and then added to the linker vial. At this point, the stopper was removed, the vial threads were wrapped with Teflon tape, and the vial was capped with a Teflon lined vial cap. The reaction mixture was gently stirred for 1 min and then heated to 100 °C for 24 h without stirring. After decanting the 1,4-dioxane, the polymer was subjected to a series of solvent washes. Solvent was exchanged by decanting after periods of at least 6 h: 3 × 6 mL dichloromethane at room temperature; 3 × 6 mL of anhydrous methanol at 55 °C; and finally 3 × 6 mL of anhydrous THF at 55 °C. After the last solvent wash was removed, the product was dried at room temperature for at least 6 h under reduced pressure, and dried at 120 °C under reduced pressure for at least 12 h.

BPEG1 Polymer. Ethylene glycol was used as the linker (1 ethylene glycol unit). 0.146 g (61% yield). IR (neat, cm^{-1}): 3662w, 3618w, 2891w, 1629w, 1486w, 1445s, 1373w, 1355w, 1282w, 1251s1181w, 1079m, 1067m, 1031s, 991m, 936s, 879m, 765w, 743w, 709w, 680w, 666w, 642m, 627w, 618w, 592w, 578w, 567w, 550w, 536w, 527w, 499m, 483m, 470m, 456m. Anal. Calcd. for $C_{32}H_{16}BF_{16}LiO_4 \cdot 1.5C_4H_8O$: C, 50.88; H, 3.10%. Found: C, 51.03; H, 3.16%.

BPEG2 Polymer. Di(ethylene glycol) was used as the linker (2 ethylene glycol units). 0.230 g (87% yield). IR (neat, cm^{-1}): 3672w, 3616w, 3405w, 2925w, 2887w, 1650w, 1625w, 1581w, 1490w, 1444s, 1355m, 1248s, 1072m, 1033s, 991m, 936m, 881m, 825w, 810w, 763m, 745m, 702m, 671m, 639m, 599w, 575w, 556w, 544w, 522w, 511w, 495w, 480w, 459w. Anal. Calcd. for $C_{36}H_{24}BF_{16}LiO_6$: C, 49.46; H, 2.77%. Found: C, 49.50; H, 2.96%.

BPEG3 Polymer. Tri(ethylene glycol) was used as the linker (3 ethylene glycol units). 0.263 g (90% yield). IR (neat, cm^{-1}): 3664w, 3410w, 2927w, 2876w, 1647w, 1488w, 1445s, 1353m, 1249s, 1069s, 1036s, 1005m, 936s, 880m, 823w, 812w, 797w, 787w, 759m, 742w, 717m, 702m, 688m, 675m, 642s, 631m, 624m, 615w, 600w, 592w, 583w, 567w, 555m, 542w, 523m, 508w, 494m, 487m, 478m, 468w, 461m. Anal. Calcd. for $C_{40}H_{32}BF_{16}LiO_8$: C, 49.92; H, 3.35%. Found: C, 50.03; H, 3.26%.

BPEG9 Polymer. Poly(ethylene glycol) 400 was used as the linker (mass range = 380-420 amu, with an average length of 8.7 ethylene glycol units). 0.159 g (72% yield). IR (neat, cm^{-1}): 3458w, 2875m, 1648w, 1488w, 1446s, 1351m, 1282m, 1250s, 1183w, 1081s, 1036s, 989m,

937s, 878m, 762m, 751m, 733m, 702w, 675w, 642m, 603w, 590w, 578w, 568w, 555w, 541w, 530w, 521w, 509w, 500w, 494w, 477w, 469w, 459m. Anal. Calcd. for $C_{62.8}H_{77.6}BF_{16}LiO_{19.4}$: C, 51.50; H, 5.34%. Found: C, 51.53; H, 5.08%.

BPEG22 Polymer. Poly(ethylene glycol) 1000 was used as the linker (mass range = 950-1050 amu, with an average length of 22.3 ethylene glycol units). 0.147 g (36% yield). IR (neat, cm^{-1}): 3451w, 2871m, 1727w, 1648w, 1578w, 1488w, 1449s, 1350m, 1326w, 1295w, 1251s, 1084s, 1036s, 937s, 877m, 849m, 763m, 752m, 736m, 702w, 680w, 643m, 489w, 476w, 468w, 459w. Anal. Calcd. for $C_{117.2}H_{186.4}BF_{16}LiO_{46.6}$: C, 52.86; H, 7.06%. Found: C, 51.64; H, 5.78%.

BPdiol Polymer. 1,5-Pentanediol was used as the linker. 0.213 g (81% yield). IR (neat, cm^{-1}): 3664w, 3616w, 3399w, 2948w, 2879w, 1625w, 1585w, 1490w, 1445s, 1368m, 1280w, 1249s, 1191w, 1077m, 1036s, 990m, 936s, 878s, 813w, 797w, 761m, 747m, 715w, 700w, 671m, 643m, 616w, 599w, 590w, 565w, 556w, 544w, 525w, 495w, 485w, 466w, 459w. Anal. Calcd. for $C_{38}H_{28}BF_{16}LiO_4$: C, 52.44; H, 3.24%. Found: C, 52.73; H, 3.41%.

Physical Measurements. ^{1}H, ^{11}B, ^{13}C, and ^{19}F NMR spectra were collected on a Bruker AVQ-400 MHz or AV-600 instrument and analyzed with MestReNova software (v8.0.2-11021, Mestrelab Research S.L.). All resonances are referenced to the residual solvent signals of $CDCl_3$ (^{1}H, 7.26 ppm; ^{13}C, 77.2 ppm), MeCN-*d*$_3$ (^{1}H, 1.94 ppm; ^{13}C, 1.32 or 118 ppm), and $CFCl_3$ (^{19}F, 0 ppm). IR spectra were collected on a PerkinElmer Spectrum 400 FT-IR/FT-FIR Spectrometer. Mass spectrometry was performed at the QB3/Chemistry Mass Spectrometry Facility at the University of California, Berkeley using an orthogonal acceleration quadrupole time-of-flight (Q-tof) mass spectrometer with an electrospray ionization (ESI) source operated in negative ion mode (Q-tof Premier, Waters, Milford, MA). CHN elemental analyses were performed at the Microanalytical Laboratory of the University of California, Berkeley.

Electrochemical Sample Preparations. After drying the polymers at 120 °C on a Schlenk line, samples were transferred to an argon-filled glovebox. Polymers evaluated in the dry state were used as is. When evaluating the dependence of conductivity on the loading of anhydrous PC or triglyme, ~100 mg of polymer was weighed into a vial and a micropipette was used to add plasticizer in 10, 15, or 20 μL increments. After each addition, the mixture was allowed to sit for 3 minutes and then agitated with a spatula in order to ensure equal distribution of plasticizer through the material prior to loading into the brass impedance cell (see below). After each measurement, the pellet was returned to the sample vial and another aliquot of PC or triglyme was added and the process was repeated.

Samples prepared for all other impedance and electrochemical measurements were loaded with PC or a EC/DMC mixture (1:1 v/v) and allowed to absorb the liquid over 15 h. Although the resulting materials were 68 wt % PC or EC/DMC, they remained free-flowing solids.

Ionic Conductivity Measurements. Electrochemical measurements were performed with an electrochemical impedance spectroscopy capable Bio-Logic VMP-3 multipotentiostat. Impedance spectra were collected between 1 MHz and 1 Hz at 100 mV ac and temperature measurements were determined with a K-type thermocouple. The frequency response curve was fitted to the model circuit shown in Figure 4.2 using the freeware package EC-Lab by Bio-logic Inc. The ionic conductivity was then calculated from the refined cell resistance, R_{bulk}, using Equation 1 in which l is the pellet thickness, A is the electrode area and σ_{bulk} is the bulk ionic conductivity of the sample in S/cm.

Equation 4.1. $$\sigma_{\text{bulk}} = \frac{A}{R_{\text{bulk}} l}$$

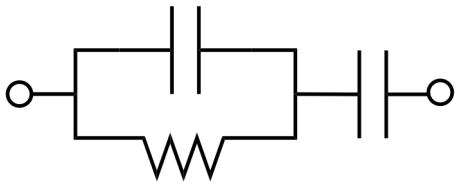


Figure 4.2. Circuit used to model impedance spectra obtained from a cell with stainless steel blocking electrodes. The resistor in parallel with the constant phase elements represents R_{bulk}.

Impedance measurements at ambient temperature were performed in a custom-built brass test cell (Figure S4.1). Assembly of the cell was performed in the following manner. A Garolite washer (thickness 0.25 mm) with a 3.88 mm diameter hole bored in the center was secured to a stainless steal disk using Kapton tape. The disk was placed into the base of the brass cell, and an insulating component with a channel bored through its center was screwed into the brass base, securing the stainless steel washer. Subsequently, 4.0-5.5 mg of polymer material was loaded into the center of the washer. A second stainless steel element was placed into the channel, and the pellet was pressed with a hand press only until resistance was encountered and then the press was released. In this setup, the washer and stainless steel element function as blocking electrodes, and pellet contact is maintained between the two stainless steel electrodes with a 15-lb spring compressed by a brass cell cap.

Variable temperature experiments were performed with a thermocouple inserted into the port at the base of the brass cell. Impedance measurements were taken every 5 °C from 30 °C to 100 °C. Variable temperature conductivity data was fit to the Stokes-Einstein relation[27] in order to determine the energy of activation.

Transference Number Determination. Transference numbers were performed with symmetric Li(s)|electrolyte|Li(s) cells formed by pressing polymer pellets between polished lithium metal smashed onto stainless steel current collectors that served as non-blocking electrodes. A 100 mV dc voltage was applied across the pellet and the current response was recorded as a function of time. The steady state current (I_{ss}) was determined by fitting the resulting curve to the inverse square time law for current decay shown in Equation 4.2. An impedance spectrum was recorded immediately before the voltage step and at the end of the step. The transference number was then calculated using Equation 4.3 as previously reported[24] in which t_{Li+} is the transference number, I_s is the steady state current, I_0 is the initial current following the voltage step, ΔV is the dc voltage applied across the cell, R_0 is the charge transfer resistance for lithium reduction/oxidation measured by impedance spectroscopy before the voltage step, and R_s is the resistance for lithium reduction/oxidation at the end of the voltage step. The cell resistances were determined by fitting the collected impedance spectra to the model circuit in Figure 4.3 using the freeware package EC-Lab.

Equation 4.2. $$I(t) = \frac{1}{\sqrt{c_1(t+c_2)}} + I_{ss}$$

Equation 4.3. $$t_{Li+} = \frac{I_{ss}(\Delta V - I_0 R_0)}{I_0(\Delta V - I_{ss} R_{ss})}$$

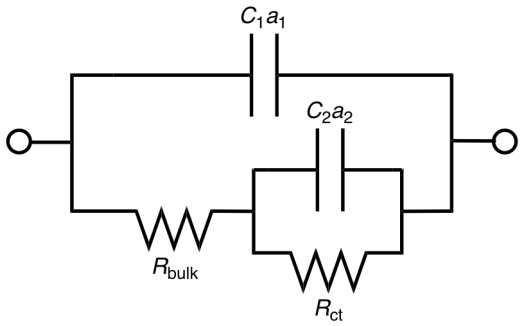


Figure 4.3. Circuit used to model impedance spectra obtained from a cell with non-blocking Li-metal electrodes. The value of R_{ct} was used to determine R^0 and R^s in the transference number calculation.

Section 4.3 Results and Discussion

At the onset of this project, three primary goals were identified for improving upon the first-generation tetraphenylborate PAF: (i) to reduce the brittleness of the material, (ii) to eliminate the need for organic solvents, and (iii) to remove the precious metal catalyst from the synthesis of the polymer. In order to accomplish these goals, the rigid aromatic linker was exchanged for a flexible poly(ethylene glycol) (PEG) linker. By incorporating a flexible component on the molecular level, it was believed that the bulk material would become more malleable and more amenable toward film formation. PEG in particular was chosen as it is well established in its ability to solvate lithium ions and has proven stable in lithium polymer batteries.[28–30] Thus, utilization of PEG could potentially enable the second-generation materials to conduct Li-ions without the need for any organic solvents. Furthermore, PEG linkers terminated in a variety of functional groups are inexpensive and commercially available, which would allow for a variety of synthetic options toward generating the polymer that would avoid the need for a palladium catalyst. However, before polymer synthesis could begin, the borate node first had to be redesigned in order to make it compatible with this new linker.

Because PEG can be purchased with either electrophilic or nucleophilic endgroups, the synthetic strategy planned for the new materials would employ nucleophilc substitution to form new bonds. Although retaining the central fluorinated aryl borate core of the PAF node was desirable due to the high ionic conductivity produced in the resulting PAF, the iodine moieties necessary for the palladium-catalyzed cross-coupling would not be ideal for nucleophilic substitution. In developing the new borate node, special consideration was taken to ensure that future efforts to increase the scale of the synthesis of these polymers would be economically feasible. Thus, 2,3,5,6-tetrafluorobenzyl alcohol was ultimately chosen as the aromatic starting material for the borate, as it is already made commercially as a component of the insecticide transfluthrin.[31,32]

Having identified a suitable starting reagent, two borate targets were investigated, as shown in Figure 4.4. In the first, the alcohols of 2,3,5,6-tetrafluorobenzyl alcohol would be retained and would serve as the nucleophilic component during polymer formation. The synthesis of this target began by protecting the alcohol of 2,3,5,6-tetrafluorobenzyl alcohol with dihydropyran in the presence of catalytic *p*-toluenesulfonic acid. Although the resulting tetrahydropyranyl ether could be isolated, exposing it to *n*-butyllithium and boron trichloride resulted in incomplete conversion to the tetraphenylborate product. In fact, ^{1}H NMR spectroscopy and ESI-MS indicated that the major product was the triarylborane, which was isolated upon aqueous workup as a hydroxytriphenylborate. As an added complication, these two products proved challenging

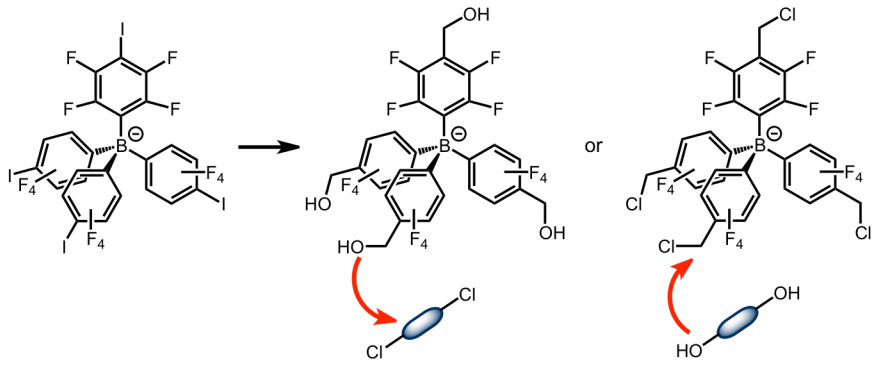
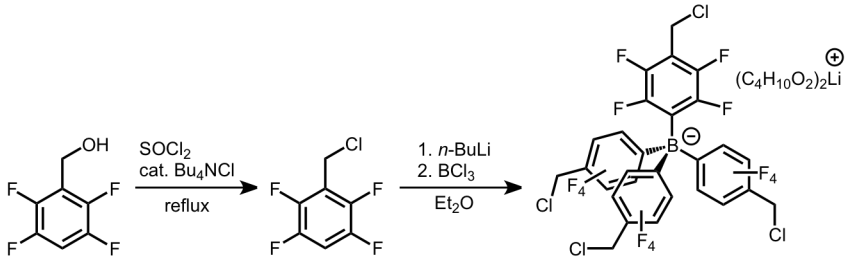


Figure 4.4. Synthetic strategies for generating the second-generation network polymers. Iodine terminated borate node used in the synthesis of the PAF (left). A new nucleophilic borate target possessing benzyl alcohols (center) and a new electrophilic borate target possessing benzyl chlorides (right).



Scheme 4.1. Synthesis of the electrophilic benzyl chloride terminated borate node.

to separate. Consequently, a second borate target in which the benzyl alcohols are converted to chlorides was pursued. As shown in Scheme 4.1, 2,3,5,6-tetrafluorobenzyl alcohol was brought to reflux in neat thionyl chloride and catalytic tetrabutylammonium chloride. Total conversion to the benzyl chloride was complete in less than one hour as verified by ^{1}H NMR spectroscopy, and the final product was isolated as a clear oil in excellent yield (92%) after purification by vacuum distillation. The molecule 2,3,5,6-tetrafluorobenzyl chloride in turn could be selectively deprotonated at the 4-position with *n*-butyllithium and upon exposure to boron trichloride formed the corresponding tetraphenylborate. While the tetraphenylborate can be obtained as a white solid in modest yield (46%), its successful isolation requires that the crude white residue obtained prior to centrifugation be thoroughly dried. Residual diethyl ether or dichloromethane in the residue increases the solubility of the product in toluene and can dramatically reduce the yield of the isolated material.

With the chlorinated tetraphenylborate in hand, screening of reaction conditions for polymer formation began by mixing the borate with tri(ethylene glycol) in THF (65 °C), dimethoxyethane (85 °C), dimethyl formamide (100 °C), or dimethyl sulfoxide (100 °C). Tri(ethylene glycol), a short PEG chain, was chosen for the screens, such that proton signals in the ^{1}H NMR spectrum could be clearly resolved for both borate and PEG components, allowing this characterization technique to serve as a probe for new bond formation. Unfortunately, these reaction conditions only returned starting materials. Next, the tri(ethylene glycol) linker was deprotonated with *n*-butyllithium prior to addition of the borate. Performing the reaction in THF at ambient temperature again returned the starting materials. However, when the reaction was carried out in 1,4-dioxane and heated to 100 °C for 15 h, an insoluble gelatinous material formed in the bottom of the reaction vial. No remaining reactants were identified in an NMR spectrum of the supernatant, and an IR spectrum of the dried product indicated that the strong bands in the C–Cl

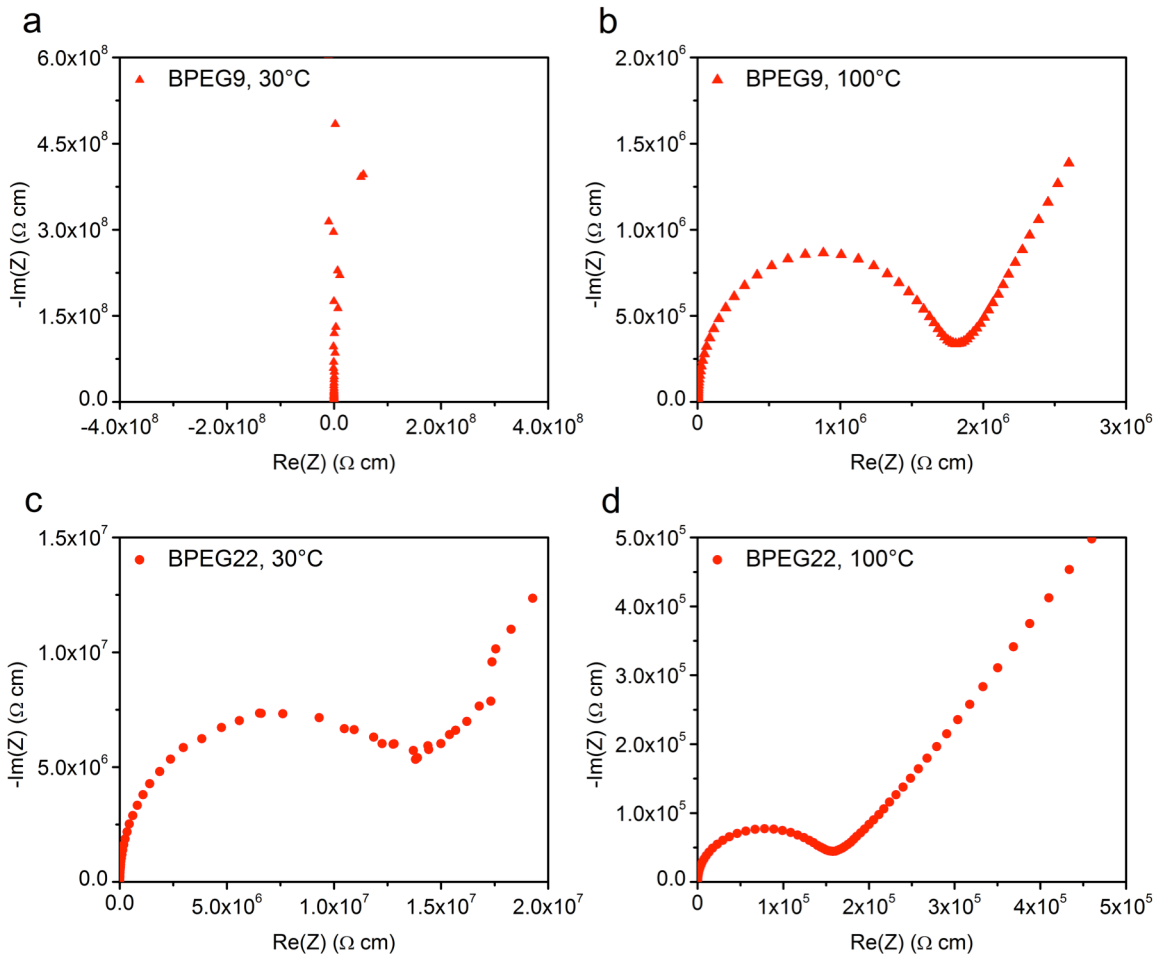


Figure 4.5. Nyquist impedance plots of solid polymer electrolytes BPEG9 and BPEG22 at ambient temperature and 100°C.

frequency range (800-600 cm^{-1}) had been lost, suggesting that the benzyl chloride had been effectively displaced (Figure S4.10). Upon optimization of the reaction conditions, a series of five polymers were made with various PEG chain lengths in good yields: BPEG1, BPEG2, BPEG3, BPEG9, and BPEG22 were synthesized using ethylene glycol (61% yield), di(ethylene glycol) (87%), tri(ethylene glycol) (90%), poly(ethylene glycol) 400 (72%), and poly(ethylene glycol) 1000 (36%), respectively.[33] The low yield for BPEG22 was likely due to the fact that this material has a tendency to form small particles as well as a bulk mass at the bottom of the reaction vessel. Although these polymers are insoluble in all common organic solvents (chlorinated organic solvents, etheric solvents, acetonitrile, acetone, methanol, and dimethyl sulfoxide), allowing them to be cleaned by subsequent washes, the small particles of BPEG22 are often lost when the washes are decanted.

Drying the polymers at 120 °C for 12 h results in the materials made with shorter linkers (BPEG1, BPEG2, and BPEG3) breaking into brittle powders. However, BPEG9 and BPEG22 remain intact and are flexible. In particular, BPEG22 can be stretched to a small extent. If synthesized without stirring, BPEG9 and BPEG22 appear film-like, though optimization of film formation has not yet been extensively investigated.

Linker length also exerts a strong effect on the conductive properties of the polymer networks. While the brittle powders incorporating short linkers were not at all conductive in the

dry state, BPEG9 and BPEG22 were indeed conductive at elevated temperatures (up to 6.3 × 10^{-6} S/cm at 100 °C for BPEG22) as shown in the Nyquist impedance plots in Figure 4.5, thus qualifying these two materials as solid polymer electrolytes. It is unsurprising that BPEG22 exhibits higher conductivity than BPEG9, as it has been shown that longer linkers tend to enhance conductivity by allowing for more flexibility and better segmental motion of the solvating ethylene glycol chains, which in turn facilitates the movement of ions through the material.[11] Because the borate anions are locked into the polymer backbone, Li^+ must hop between anions as it moves through the electrolyte. Figure 4.6 shows a fit of the Stokes-Einstein relation[27] to variable-temperature conductivity data between 30 and 100 °C. These experiments found that the activation energy for the hopping mechanism in BPEG9 (1.30 eV) and BPEG22 (0.66 eV) is high compared to the first-generation materials (0.25 eV) and to other values typically observed for solid polymer electrolytes.[27]

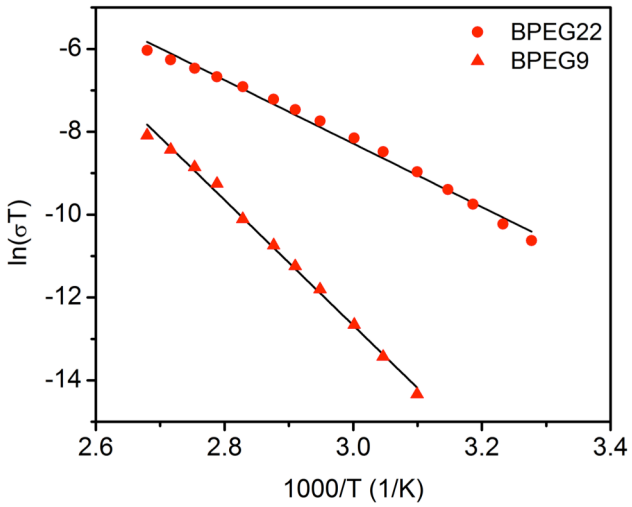


Figure 4.6. Variable temperature data from 30-100 °C for BPEG9 and BPEG22.

Although the network polymers possessing the longer PEG linkers were conductive without the addition of any solvent at elevated temperatures, they remained two orders of magnitude less conductive than the first-generation electrolyte. In order to amplify the conductivity, propylene carbonate (PC) or triethylene glycol dimethyl ether (triglyme) were added to the polymers as plasticizers, a common practice for enhancing conductivity in PEG-based electrolytes.[34] When only PEG is present to solvate Li^+, the movement of the PEG chains can be inhibited due to ionic cross-linking of the glycol chains by coordinated Li^+. The addition of plasticizer provides better solvation of Li^+, which disrupts ionic cross-linking and assists in alleviating any ion pairing effects between Li^+ and the borate anions.[12,35] Additionally, after exposure to solvent, the particles swell noticeably. When compressed into pellets, this swelling likely has the added benefit of improving particle-particle contacts, which would in turn improves the overall conductivity values obtained. Initial screens evaluating the effect of plasticizer loading on conductivity established that polymers loaded with PC performed slightly better than those loaded with triethylene glycol dimethyl ether (triglyme) (Figure S4.11 and S4.12) and that maximum conductivity was achieved when the materials were loaded with 65-69 wt % PC, causing these materials to fall into the category of single-ion conducting polymer gels rather than solid polymer electrolytes. Interestingly, they remained free-flowing powders despite the high plasticizer loading.

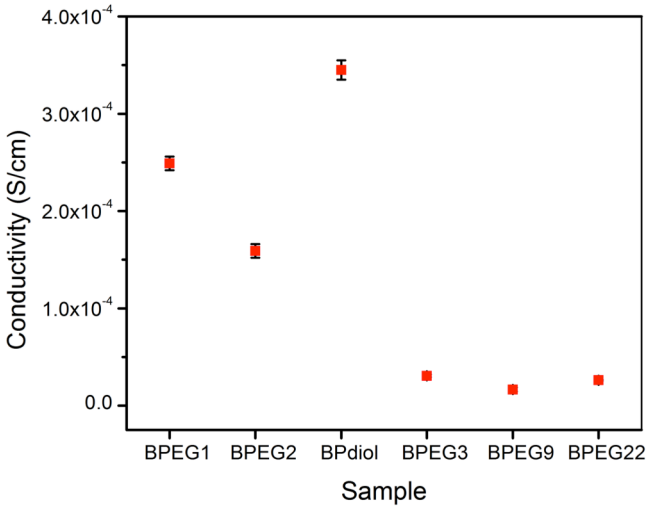


Figure 4.7. Average conductivity of gel polymer electrolytes loaded with 68 wt % PC. Each data point corresponds to $n = 10$ pellets, and standard error bars are shown in black.

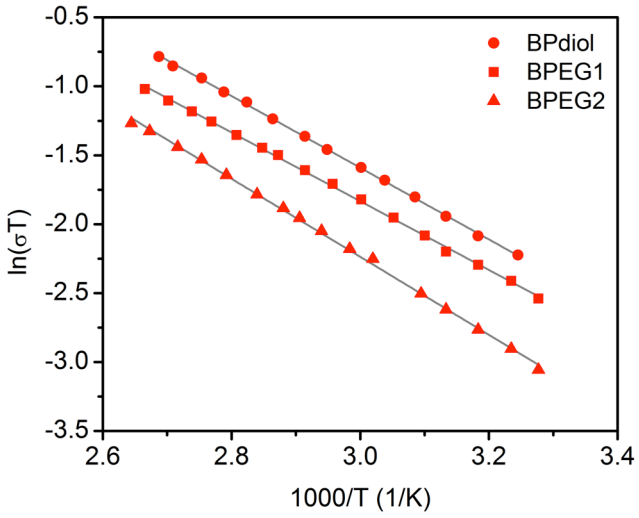


Figure 4.8. Variable temperature data from 30-100 °C for BPEG1, BPEG2, and BPdiol loaded with 68 wt % PC.

Whereas longer linkers were found to increase conductivity when the polymers were dry, the trend was reversed once plasticizer was added. Figure 4.7 illustrates that the materials with shorter linkers exhibited the highest conductivity values when the series was loaded with 68 wt % PC. This change is likely due to two factors; shortening the linker effectively increases the relative concentration of Li^+ in the material and decreases the distance Li^+ must hop between borate anions. Indeed, BPEG1 exhibited the highest conductivity value of 2.5×10^{-4} S/cm at ambient temperature (30 °C), placing it on equal footing with the conductivity of the first-generation PAF. While BPEG2 provided a slightly lower value of 1.6×10^{-4} S/cm, BPEG3, BPEG9, and BPEG22 were an order of magnitude less conductive ($1.7\text{-}3.1 \times 10^{-5}$ S/cm).

With the addition of PC, the Li^+-solvating properties of PEG were no longer vital to the performance of the polymer. In fact, interactions between Li^+ and the stationary PEG support could potentially hinder ion transport. To test if conductivity could be improved by reducing the number of coordinating moieties in the linker chain, a new polymer (BPdiol) was generated with

1,5-pentanediol serving as the linker. This particular unit was chosen as it possesses a comparable chain length to BPEG2 but the central ether oxygen is substituted by a non-coordinating methylene group. After loading BPdiol with 68 wt % PC, ac impedance spectroscopy revealed a jump in conductivity to 3.5×10^{-4} S/cm—over a two-fold enhancement compared to the original BPEG2 polymer.

Subsequently, BPEG1, BPEG2, and BPdiol were evaluated to determine if the activation energy for ion transport differed between these three highest performing gel electrolytes. Variable temperature conductivity data between 30-100 °C resulted in activation energies of 0.22 eV for BPEG1 and 0.24 eV for BPEG2. Though slight, this difference is in agreement with BPEG1 possessing the shorter borate-borate distance over which a Li^+ must hop. In comparing the values obtained for BPEG2 and BPdiol to see if switching to a less coordinating linker would facilitate ion transport, this strategy did indeed appear to have a beneficial effect, as BPdiol exhibited a slightly lower activation energy (0.22 eV) than BPEG2 even though these two linkers were of the same length.

Keeping in mind the ultimate goal of incorporating these materials into cells possessing Li-metal electrodes, BPEG1 was inserted into a symmetric Li(s)|electrolyte|Li(s) cell and its transference number was evaluated using the potentiostatic polarization method proposed by Bruce, Evans, and Vincent.[24] In this technique, a small potential is applied to the cell and the resulting current is tracked over time. Whereas the current decays significantly for a liquid electrolyte due to concentration gradients resulting from mobile anions, a single-ion conductor exhibits a negligible change between the initial (I_0) and steady state current (I_{ss}) values. Using these values, a t_{Li^+} can be calculated, and as expected, immobilization of the borate anions in BPEG1 gives t_{Li^+} = 1.01 (Figure 4.9). As a result of the non-blocking Li-metal electrodes, two processes are observed in the Nyquist impedance plot of this cell. The higher frequency feature corresponds to the ionic resistance, and the lower frequency feature represents the charge transfer resistance of Li^+ crossing the electrolyte|Li(s) interface. Figure 4.10 shows the data from impedance experiments performed before the potential step is applied and after a steady-state current is reached and demonstrates that there is no change in these processes over the course of the experiment. Longer runs (Figure S4.16) also show that while settling of the pellet and

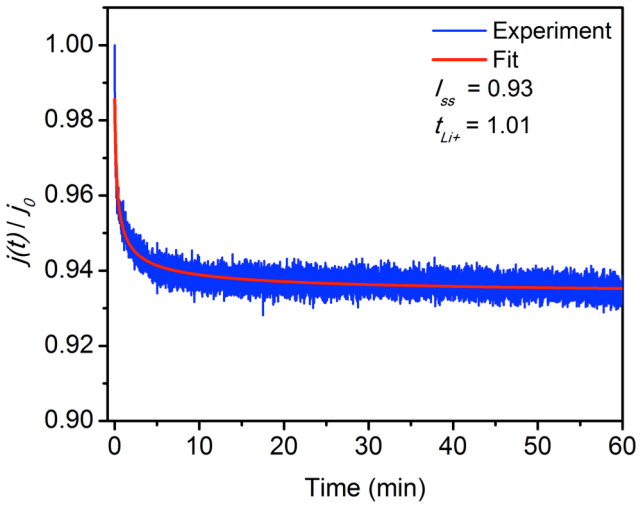


Figure 4.9. Current decay curve and fit for a Li(s)|BPEG1|Li(s) cell after applying a potential of 100 mV.

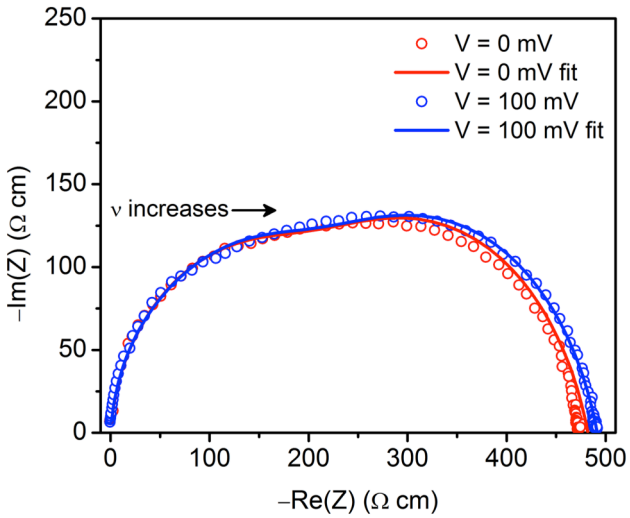


Figure 4.10. Nyquist impedance plots of a Li(s)|BPEG1|Li(s) cell before and after applying a potential of 100 mV.

evolution of the electrolyte|Li(s) interface does occur immediately after cell assembly, both processes stabilize over time. Importantly, the charge transfer resistance remains constant indicating that BPEG1 remains stable and does not foul the interface over time.

Section 4.4 Conclusions and Outlook

A new series of borate-based single-ion conducting polymer electrolytes possessing flexible linkers have been synthesized without the aid of a precious metal catalyst and instead are generated via nucleophilic substitution reactions. Two of these materials, BPEG9 and BPEG22, are flexible and exhibit conductivity in the range of 10^{-6} S/cm at 100 °C. Although these two solid polymer electrolytes are conductive without the addition of any solvent, their conductivity is two orders of magnitude too low for practical implementation into a commercial device. As a result, the addition of PC to the network polymers was explored, yielding three polymer gel electrolytes (BPdiol, BPEG1, and BPEG2) that exhibit low activation energies and high conductivities of 10^{-4} S/cm that qualify them for implementation into functional battery devices. Additionally, these electrolytes show good stability toward Li-metal electrodes and high transference numbers, supporting the expectation that they do indeed behave as single-ion conducting electrolytes.

There is yet more work to be done to move these materials forward. Although the gel electrolytes in particular show high conductivities, forming films with these materials has yet to be achieved and electrochemical measurements have thus far been restricted to pressed pellets. On the other hand, BPEG9 and BPEG22 have the desirable property of being flexible and appear to hold potential for being fashioned into films. In order for these polymer networks to be truly commercially viable, the mechanical properties of the materials formed with long linkers must be merged with the conductivity of the materials made with short linkers. Such a marriage might be accomplished by investigating systems generated by mixtures of short and long linkers. Once adequate films have been obtained, measurements to evaluate the mechanical strength of the films can be performed.

Structure-property relationships between conductivity and linker composition have provided an additional insight during the course of this study. Based on the enhancement in conductivity

observed by reducing the number of coordinating moieties in the linker, it is proposed that a polymer network in which all oxygen moieties are removed and replaced by alkane units might offer even higher conductivity. However, in order for such a material to be achieved, the bond forming chemistry between the linker and borate node must be amended. As a more accessible alternative, alkane chains terminated by less coordinating functional groups that are still compatible with the nucleophilic substitution chemistry established here (e.g. thiols) could be incorporated into the polymer networks.

Section 4.5 Acknowledgements

This research was supported by the National Science Foundation Graduate Research Fellowship Grant No. DGE-1106400 to the author and by Robert Bosch LLC. The author thanks Prof. Jeffrey F. Van Humbeck for synthetic direction and Dr. Zachary Smith for characterization advice. Michael L. Aubrey performed the cycling and transference number experiments. Support in screening reaction conditions for 2,3,5,6-tetrafluorobenzyl chloride was provided by Prof. Robert G. Bergman's Spring 2015 CHEM 115 class (Kersti Caddell Haatveit, Tiffany Chen, Khaled Jami, and Zhenfeng Yu).

Section 4.6 References

(1) Conti, J. J. *Annual Energy Outlook 2015 with projections to 2040*; AEO2015; U.S. Energy Information Administration, Office of Integrated and International Energy Analysis, 2015.
(2) Huggins, R. A. *Advanced Batteries: Materials Science Aspects*; Springer US: Boston, MA, 2009.
(3) Larcher, D.; Tarascon, J.-M. *Nat. Chem.* **2015**, *7*, 19–29.
(4) Liang, S.; Choi, U. H.; Liu, W.; Runt, J.; Colby, R. H. *Chem. Mater.* **2012**, *24*, 2316–2323.
(5) *Electrolytes for Lithium and Lithium-Ion Batteries*, 1st ed.; Jow, T. R., Xu, K., Borodin, O., Ue, M., Eds.; Modern Aspects of Electrochemistry; Springer: New York, New York, 2014; Vol. 58.
(6) Chazalviel, J. N. *Phys. Rev. At. Mol. Opt. Phys.* **1990**, *42*, 7355–7367.
(7) Rosso, M.; Gobron, T.; Brissot, C.; Chazalviel, J. N.; Lascaud, S. *J. Power Sources* **2001**, *97–98*, 804–806.
(8) Lian, F.; Guan, H.; Wen, Y.; Pan, X. *J. Membr. Sci.* **2014**, *469*, 67–72.
(9) Sumathipala, H. H.; Hassoun, J.; Panero, S.; Scrosati, B. *Ionics* **2007**, *13*, 281–286.
(10) Bouchet, R.; Maria, S.; Meziane, R.; Aboulaich, A.; Lienafa, L.; Bonnet, J.-P.; Phan, T. N. T.; Bertin, D.; Gigmes, D.; Devaux, D.; Denoyel, R.; Armand, M. *Nat. Mater.* **2013**, *12*, 452–457.
(11) Sun, X.-G.; Reeder, C. L.; Kerr, J. B. *Macromolecules* **2004**, *37*, 2219–2227.
(12) Sun, X.-G.; Liu, G.; Xie, J.; Han, Y.; Kerr, J. B. *Solid State Ion.* **2004**, *175*, 713–716.
(13) Sun, X.-G.; Kerr, J. B. *Macromolecules* **2006**, *39*, 362–372.
(14) Cakmak, G.; Verhoeven, A.; Jansen, M. *J. Mater. Chem.* **2009**, *19*, 4310.
(15) Driscoll, P. F.; Yang, L.; Gervais, M.; Kerr, J. B. *ECS Trans.* **2011**, *33*, 33–53.
(16) Zhu, Y. S.; Gao, X. W.; Wang, X. J.; Hou, Y. Y.; Liu, L. L.; Wu, Y. P. *Electrochem. Commun.* **2012**, *22*, 29–32.
(17) Xu, G.; Zhang, Y.; Rohan, R.; Cai, W.; Cheng, H. *Electrochim. Acta* **2014**, *139*, 264–269.

(18) Wang, X.; Liu, Z.; Kong, Q.; Jiang, W.; Yao, J.; Zhang, C.; Cui, G. *Solid State Ionics* **2014**, *262*, 747–753.
(19) Van Humbeck, J. F.; Aubrey, M. L.; Alsbaiee, A.; Ameloot, R.; Coates, G. W.; Dichtel, W. R.; Long, J. R. *Chem. Sci.* **2015**, *6*, 5499–5505.
(20) Ding, S.-Y.; Wang, W. *Chem. Soc. Rev.* **2012**, *42*, 548–568.
(21) Ben, T.; Qiu, S. *CrystEngComm* **2013**, *15*, 17–26.
(22) Fischer, S.; Schmidt, J.; Strauch, P.; Thomas, A. *Angew. Chem. Int. Ed.* **2013**, *52*, 12174–12178.
(23) Zhu, G.; Ren, H. *Porous Organic Frameworks: Design, Synthesis and Their Advanced Applications*; SpringerBriefs in Molecular Science; Springer: New York, 2015.
(24) Bruce, P. G.; Evans, J.; Vincent, C. A. *Solid State Ionics* **1988**, *28–30*, 918–922.
(25) Zugmann, S.; Gores, H. J. In *Encyclopedia of Applied Electrochemistry*; Kreysa, G., Ota, K., Savinell, R. F., Eds.; Springer New York, 2014; pp 2086–2091.
(26) Kinard, L.; Kasper, K.; Mikos, A. *Protoc. Exch.* **2012**.
(27) Linford, R. G.; Hackwood, S. *Chem. Rev.* **1981**, *81*, 327–364.
(28) Xu, K. *Chem. Rev.* **2004**, *104*, 4303–4418.
(29) Agrawal, R. C.; Pandey, G. P. *J. Phys. Appl. Phys.* **2008**, *41*, 223001–223019.
(30) Quartarone, E.; Mustarelli, P. *Chem. Soc. Rev.* **2011**, *40*, 2525–2540.
(31) *TRANSFLUTHRIN*; WHO Specifications and Evaluations for Public Health Pesticides; World Health Organization, 2006; p 20.
(32) Paranjape, K.; Gowariker, V.; Krishnamurthy, V. N.; Gowariker, S. *The Pesticide Encyclopedia*; CABI: Boston, MA, 2015.
(33) The numeral designation for each material signifies the number of ethylene glycol units in the linker. The numbers for BPEG9 and BPEG22 give the average number of ethylene glycol units, as these reagents are purchased as mixtures of chains ranging from 380-420 and 950-1050 amu, respectively.
(34) Xu, W.; Angell, C. A. *Electrochim. Acta* **2003**, *48*, 2029–2035.
(35) Choi, U. H.; Liang, S.; O'Reilly, M. V.; Winey, K. I.; Runt, J.; Colby, R. H. *Macromolecules* **2014**, *47*, 3145–3153.

Section 4.7 Supporting Information

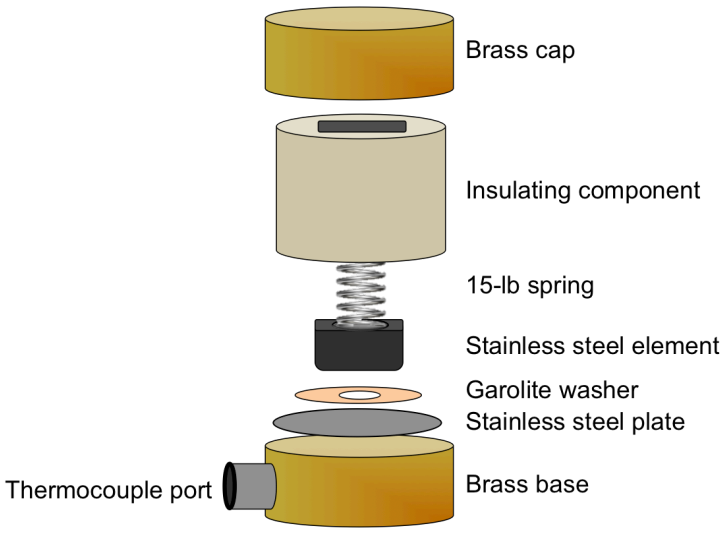


Figure S4.1. Brass cell used to house pellets of polymer during impedance measurments.

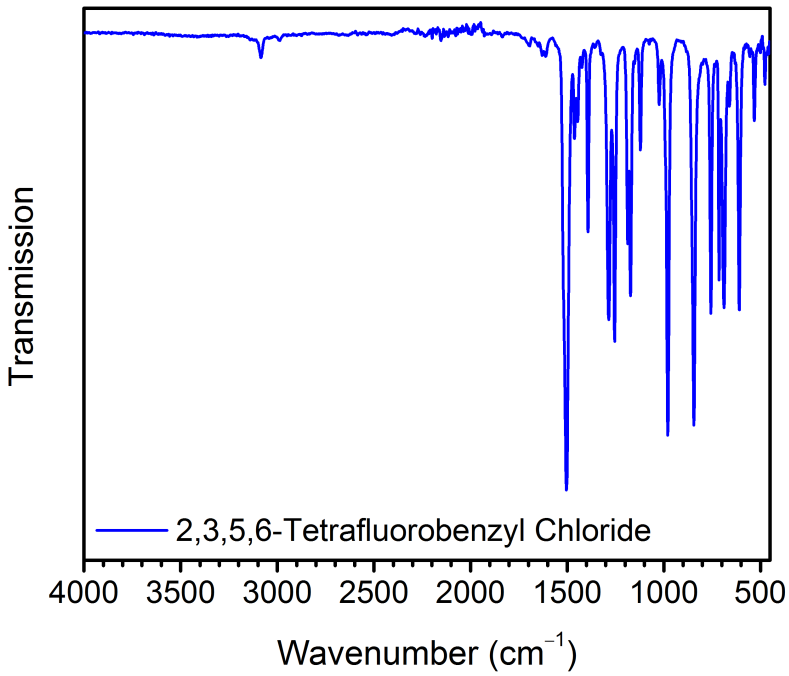


Figure S4.2. FT-IR spectrum of 2,3,5,6-tetrafluorobenzyl chloride.

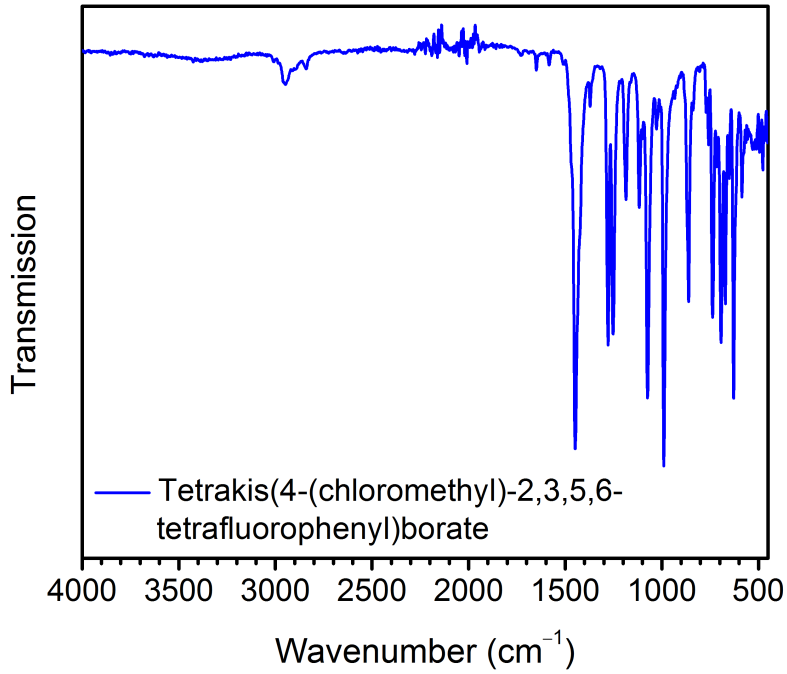


Figure S4.3. FT-IR spectrum of di(1,2-dimethoxyethane)lithium tetrakis(4-(chloromethyl)-2,3,5,6-tetrafluorobenzyl chloride.

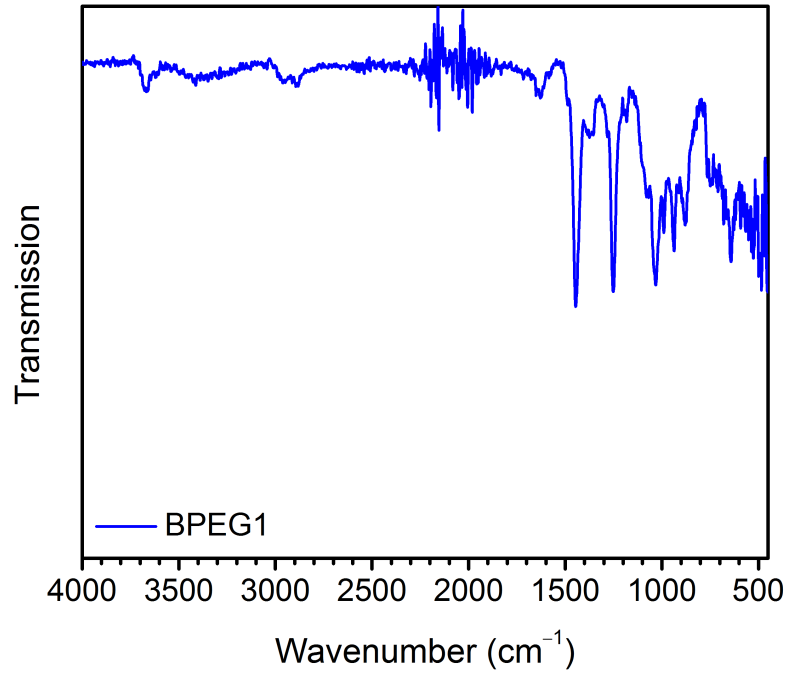


Figure S4.4. FT-IR spectrum of BPEG1.

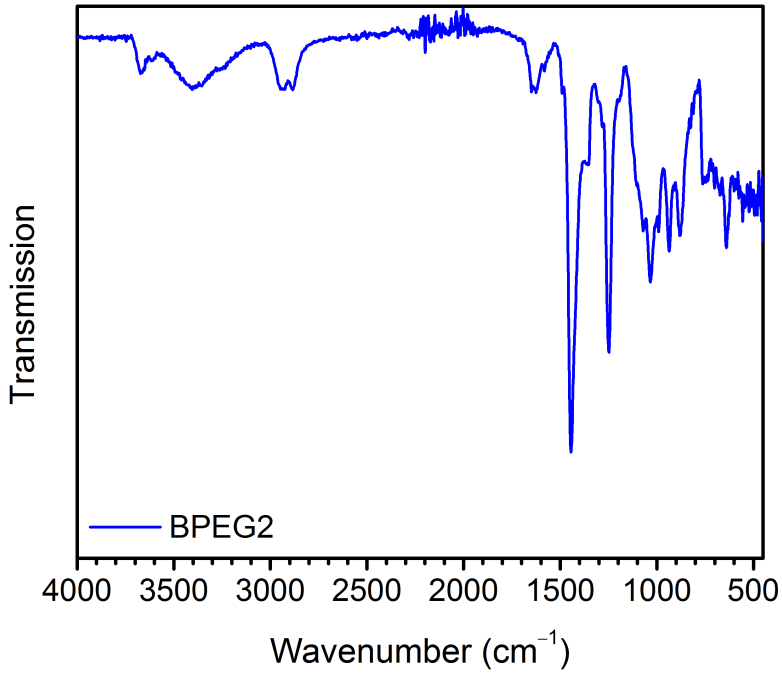


Figure S4.5. FT-IR spectrum of BPEG2.

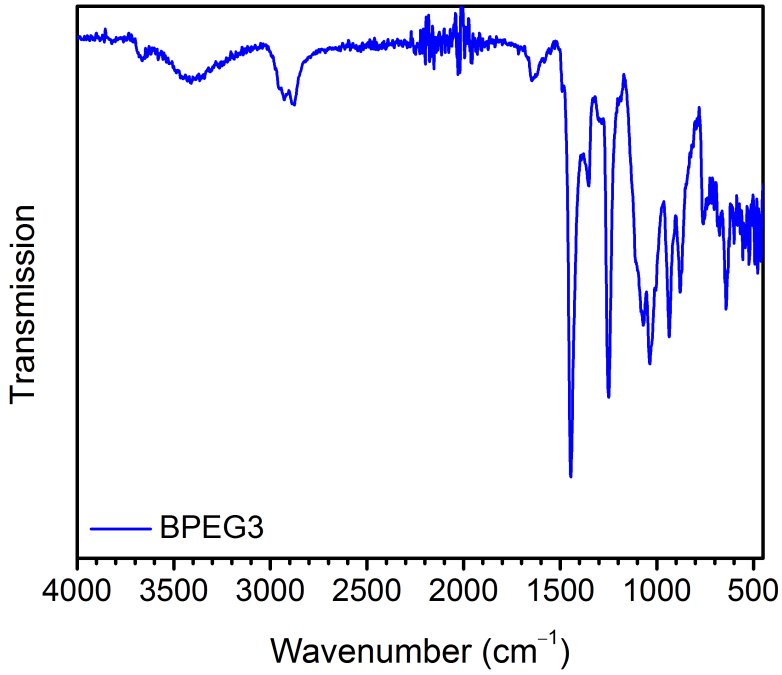


Figure S4.6. FT-IR spectrum of BPEG3.

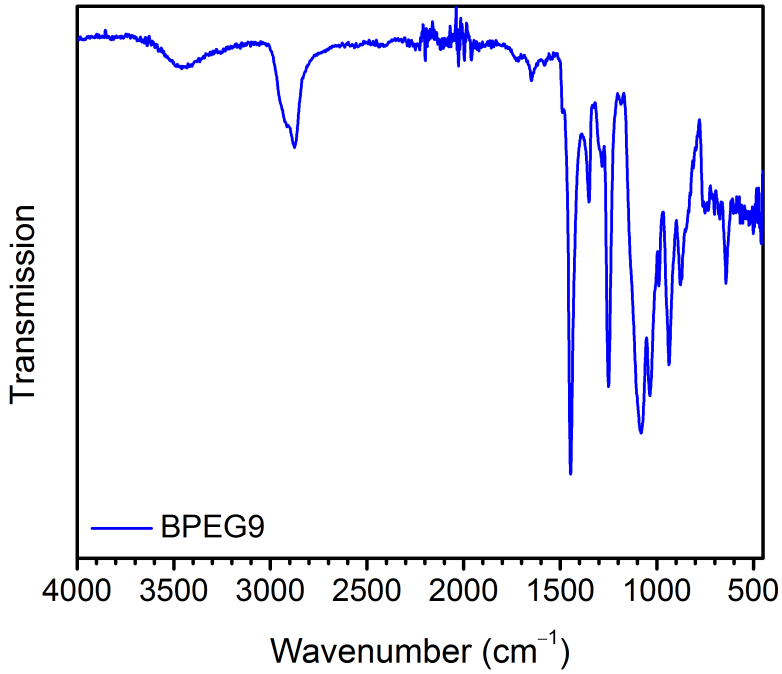


Figure S4.7. FT-IR spectrum of BPEG9.

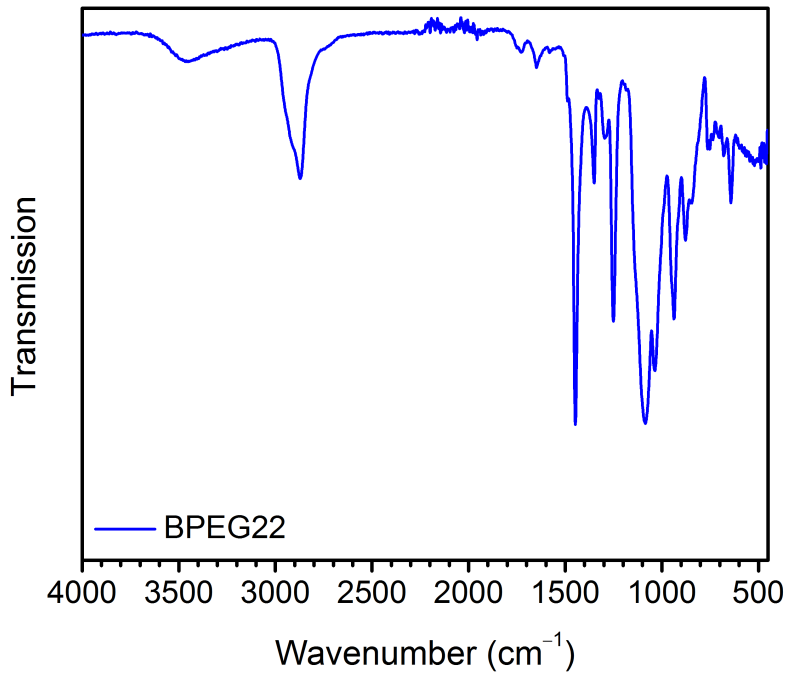


Figure S4.8. FT-IR spectrum of BPEG22.

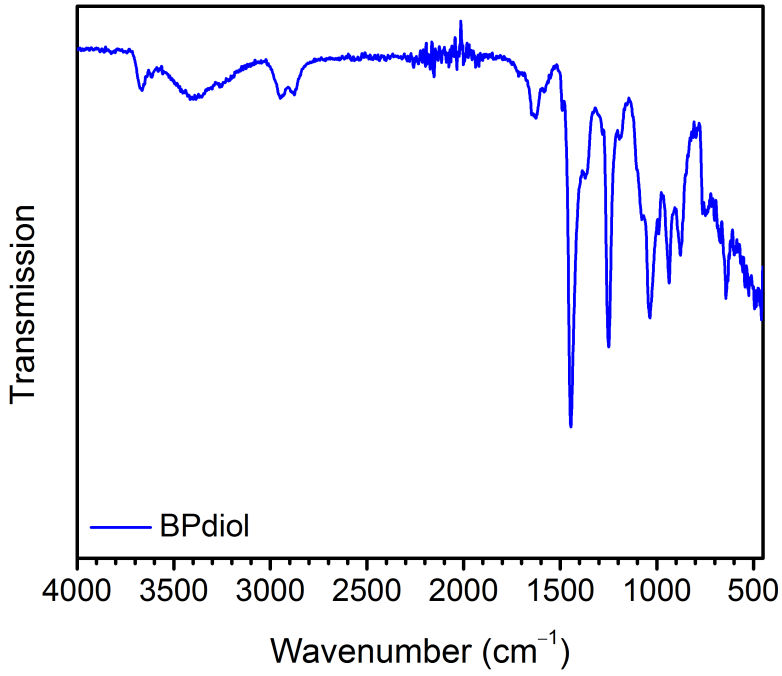


Figure S4.9. FT-IR spectrum of BPdiol.

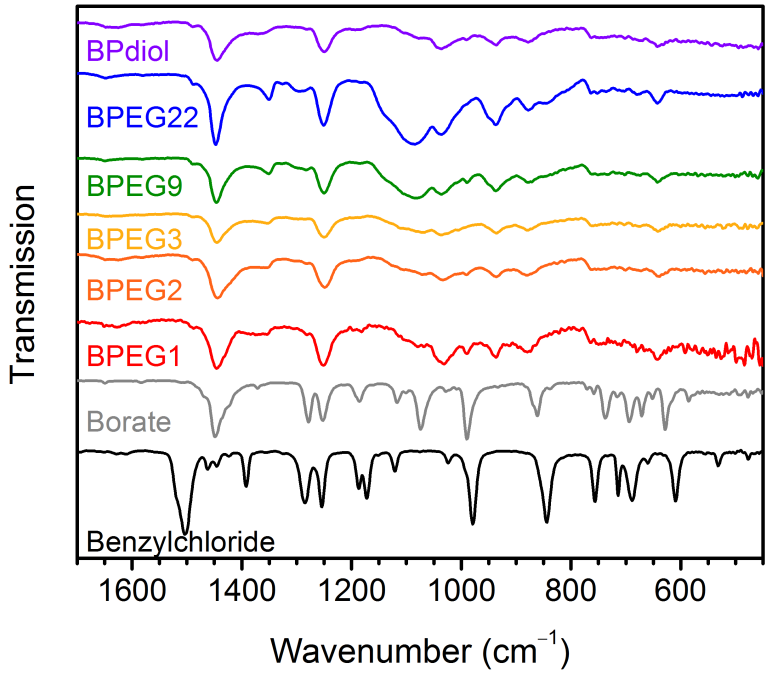


Figure S4.10. FT-IR spectrum of all materials from 450-1700 cm^{-1}. Note that the strong bands in the C–Cl frenquency range (600-800 cm^{-1}) are no longer present in the polymer materials.

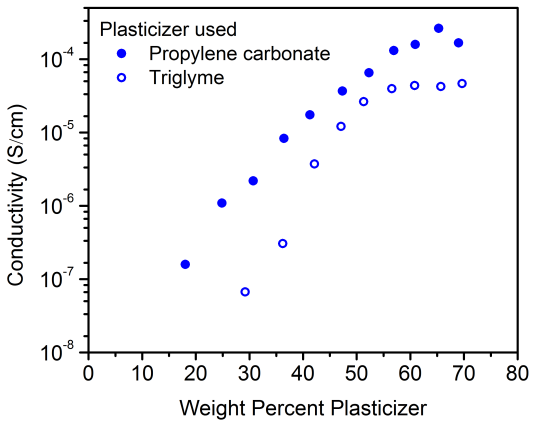


Figure S4.11. Dependence of conductivity in BPEG1 on plasticizer loading with propylene carbonate and triglyme.

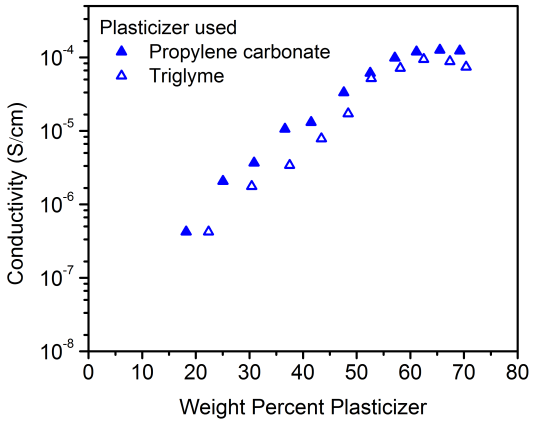


Figure SI 12. Dependence of conductivity in BPEG2 on plasticizer loading with propylene carbonate and triglyme.

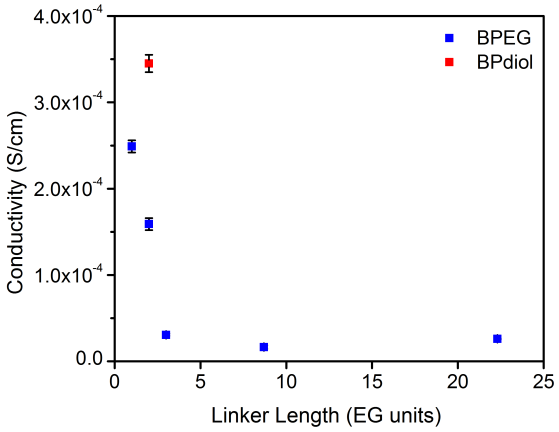


Figure S4.13. Dependence of conductivity on linker length in the gel polymer electrolytes loaded with 68 wt% PC.

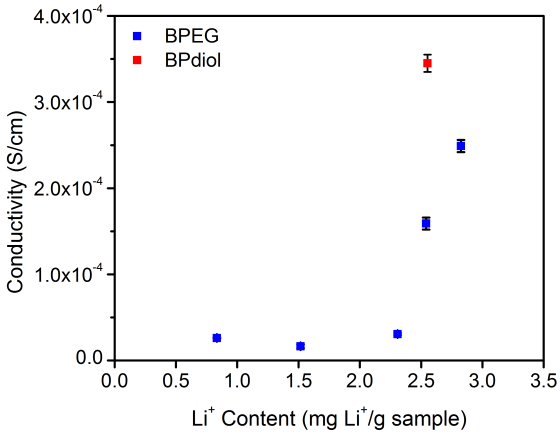


Figure S4.14. Dependence of conductivity on the concentration of Li^+ in the gel polymer electrolytes loaded with 68 wt% PC.

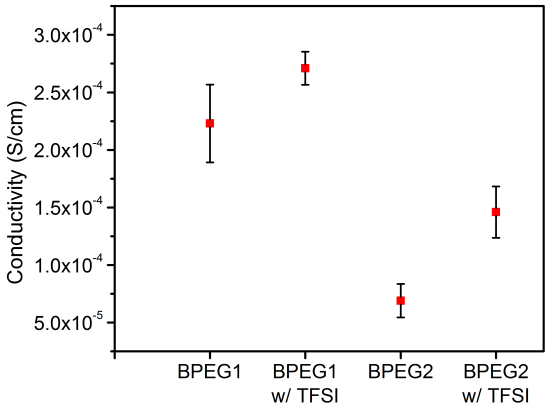


Figure S4.15. Average conductivity of the gel polymer electrolytes BPEG1 and BPEG2 loaded with 65 wt% PC or an equivalent volume of 1.0 M Li(TFSI). Each data point corresponds to $n = 3$ pellets, and standard error bars are shown in black.

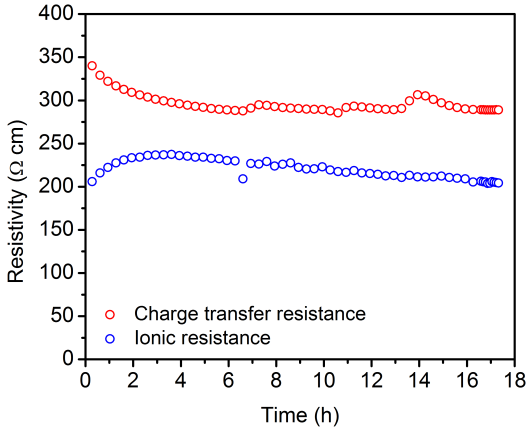


Figure S4.16. Charge transfer resistance and ionic resistance for a Li(s)|BPEG1|Li(s) cell over the course of 18 hours with an applied potential of 100 mV.